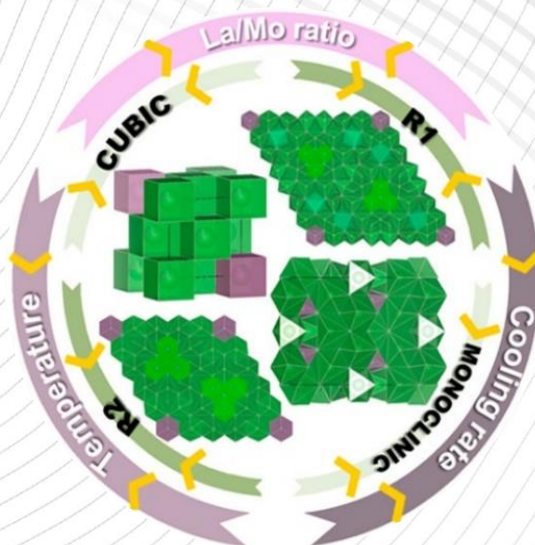


TESIS DOCTORAL

Lanthanum Molybdates: a comprehensive study for hydrogen separation membranes



Adrián López Vergara

Directores

Enrique Ramírez Losilla y José Manuel Porras Vázquez

Programa de Doctorado

Química y Tecnologías Químicas: Materiales y Nanotecnología


Facultad de Ciencias

Universidad de Málaga, 2022



UNIVERSIDAD
DE MÁLAGA

AUTOR: Adrián López Vergara

 <https://orcid.org/0000-0001-5948-5952>

EDITA: Publicaciones y Divulgación Científica. Universidad de Málaga



Esta obra está bajo una licencia de Creative Commons Reconocimiento-NoComercial-SinObraDerivada 4.0 Internacional:

<http://creativecommons.org/licenses/by-nc-nd/4.0/legalcode>

Cualquier parte de esta obra se puede reproducir sin autorización pero con el reconocimiento y atribución de los autores.

No se puede hacer uso comercial de la obra y no se puede alterar, transformar o hacer obras derivadas.

Esta Tesis Doctoral está depositada en el Repositorio Institucional de la Universidad de Málaga (RIUMA): riuma.uma.es





UNIVERSIDAD
DE MÁLAGA

Lanthanum Molybdates: a comprehensive study for hydrogen separation membranes.

Memoria presentada para optar al título de

**Doctor en Química y Tecnologías Químicas. Materiales y
Nanotecnología “Mención Internacional”**

Fdo: Adrián López Vergara

Directores:

Fdo: Dr. Enrique Ramírez Losilla
Catedrático Química Inorgánica
Universidad de Málaga

Fdo: Dr. José Manuel Porras Vázquez
Profesor titular Química Inorgánica
Universidad de Málaga

Universidad de Málaga
Facultad de Ciencias
Departamento de Química Inorgánica, Cristalografía y Mineralogía
Málaga, 2022





UNIVERSIDAD
DE MÁLAGA



Escuela de Doctorado

DECLARACIÓN DE AUTORÍA Y ORIGINALIDAD DE LA TESIS PRESENTADA PARA OBTENER EL TÍTULO DE DOCTOR

D./Dña ADRIÁN LÓPEZ VERGARA

Estudiante del programa de doctorado CIENCIAS Y TECNOLOGÍAS QUÍMICAS. MATERIALES Y NANOTECNOLOGÍA de la Universidad de Málaga, autor/a de la tesis, presentada para la obtención del título de doctor por la Universidad de Málaga, titulada: LANTHANUM MOLYBDATES: A COMPREHENSIVE STUDY FOR HYDROGEN SEPARATION MEMBRANES.

Realizada bajo la tutorización de ENRIQUE RAMÍREZ LOSILLA y dirección de ENRIQUE RAMÍREZ LOSILLA y JOSÉ MANUEL PORRAS VÁZQUEZ (si tuviera varios directores deberá hacer constar el nombre de todos)

DECLARO QUE:

La tesis presentada es una obra original que no infringe los derechos de propiedad intelectual ni los derechos de propiedad industrial u otros, conforme al ordenamiento jurídico vigente (Real Decreto Legislativo 1/1996, de 12 de abril, por el que se aprueba el texto refundido de la Ley de Propiedad Intelectual, regularizando, aclarando y armonizando las disposiciones legales vigentes sobre la materia), modificado por la Ley 2/2019, de 1 de marzo.

Igualmente asumo, ante a la Universidad de Málaga y ante cualquier otra instancia, la responsabilidad que pudiera derivarse en caso de plagio de contenidos en la tesis presentada, conforme al ordenamiento jurídico vigente.

En Málaga, a 17 de OCTUBRE de 2022

<p>Fdo.: ADRIÁN LÓPEZ VERGARA Doctorando/a</p>	<p>Fdo.: ENRIQUE RAMÍREZ LOSILLA Tutor/a</p>
<p>Fdo.: ENRIQUE RAMÍREZ LOSILLA Y JOSE MANUEL PORRAS VAZQUEZ Director/es de tesis</p>	



EFQM AENOR



Ministerio de Gobierno. Campus El Ejido.
29071
10 28 / 952 13 14 61 / 952 13 71 10
E-mail: doctorado@uma.es



Agradecimientos.

Al fin, aquí está la famosa Tesis por la que tanto me preguntabais. El camino ha sido largo y duro, y toda la gente que me ha apoyado se merece unas palabritas por lo que han tenido que soportar.

Primero, quiero dar las gracias a Enrique y José por enseñarme tanto, confiar en mí y respaldarme desde que empecé mi TFG, soy muy afortunado por haberos tenido como directores de Tesis. Dar también las gracias a Aurelio, David y al resto del grupo por su buen trato, sus consejos y ayudarme a crecer como investigador. Y a Lucia, Javi y Marta por ayudarme con las publicaciones que hemos realizado en común. Agradecer también a Pedro por mantener toda la maquinaria del departamento funcionando. A Antonio, por entenderme y saber cuándo necesitaba un correctivo, y por asistirnos en cualquier momento que lo necesitamos, facilitándonos mucho el trabajo, sobre todo el de los viernes al mediodía. Te echaremos de menos.

También, agradecer al resto de los miembros del Departamento de Química Inorgánica por todo su apoyo y buen hacer, os llevo en el corazón, sobre todo a mi gente del consejo de sabios que han hecho que todo sea más ameno, cualquier cosa que necesitéis contad conmigo. Y a la gente del SCAI, por su dedicación analizando todas muestras que se prepararon durante estos años.

Sobretudo agradecer a Carlos, el que nunca falla pase lo que pase, gracias a ti no me he hundido, la vida nos pone frente a desafíos complicados pero esa lucha dará sus frutos y podrás estar aquí con nosotros, te esperamos hermano. Guille, Heber, Neus y gente del Spaceblock y del Roao, muchas gracias por hacerme disfrutar tanto con vuestra compañía y también hacerme tanto disfrutar de la escalada. También gracias a mi psicóloga, el último tirón ha sido el más duro y no hubiese podido luchar sin tus consejos y tu ayuda.

A Rocío, con la cual compartí toda mi trayectoria académica y evolución personal, desde prácticamente el principio hasta el final. Gracias por todo lo que hemos pasado (tanto bueno como malo) y que me ha llevado a descubrir como soy y ser mejor persona. Media Tesis es tuya, y de Melón. Y a mi familia, los más importantes, que me enseñaron a ser paciente y a pelear por lo que quería, sin importar las circunstancias. Gracias Papa, Mama, Susana, Nuria, Rubén, Lucia, titos, abuelos... Os quiero.

Finalmente, agradecer a la financiación recibida a la Junta de Andalucía, la European Social Fund y la Universidad de Málaga por los distintos contratos de investigación que me han permitido realizar la Tesis.

Cosas que pasan.

INDEX

Abbreviations.....	1
Phase labels summary.....	3
RESUMEN	5
1. INTRODUCTION	23
1.1. Classic energy sources and their effect on the global climate.....	23
1.2. Hydrogen the possible solution.....	26
1.3. Perspectives on developing proton-electron conducting ceramic materials.....	30
1.4. Principles of H ₂ separation in ceramic membranes.....	31
1.4.1. Hydrogen separation process.....	31
1.4.2. Theoretical understanding of H ₂ transport mechanisms.....	33
1.5. Perspectives and development of dense proton-electron ceramic materials.....	35
1.5.1. Perovskite-type structure materials: Synthesis, characterization and membrane performance.....	36
1.5.2. Fluorite-type structure materials: Synthesis, characterization and membrane performance.....	38
1.5.3. Tungstate-based materials: Synthesis, characterization and membrane performance.....	40
1.6. Doping of lanthanide tungstate.....	45
1.6.1. Effect of doping on the lanthanum site.....	45
1.6.2. Effect of doping on tungsten site.....	46

1.6.3. Total substitution of tungsten with molybdenum in lanthanum tungstates.....	48
1.6.4. Influence of fluorine doping on the structural and electrical properties of materials.....	52
1.6.5. The fluorination process	54
1.7. Materials and methods.....	56
1.7.1. Synthesis by the freeze-drying method	56
1.8. Characterization of materials.....	61
1.8.1. X-Ray powder diffraction (XRPD)	61
1.8.1.1. The Rietveld method	63
1.8.1.2 The Le Bail method.....	64
1.8.1.3. Experimental devices.....	66
1.8.2. Neutron powder diffraction (NPD)	68
1.8.2.1. Experimental device.....	68
1.8.3. Transmission electron microscopy (TEM)	70
1.8.3.1. Experimental device.....	72
1.8.4. Scanning electron microscopy (SEM)	74
1.8.4.1. Experimental device.....	75
1.8.5. X-Ray photoelectronic spectroscopy (XPS)	76
1.8.5.1. Experimental device.....	76
1.8.6. Electrochemical Characterization.....	77
1.8.6.1. Complex impedance spectroscopy	79
1.8.6.2. Experimental device.....	81
1.8.6.3. Conductivity vs oxygen partial pressure	82
1.8.6.4. Experimental device.....	83

2. OBJECTIVES	87
3. ARTICLES	89
3.1. Effect of Preparation Conditions on the Polymorphism and Transport Properties of $\text{La}_{6-x}\text{MoO}_{12-\delta}$ ($0 \leq x \leq 0.8$)	89
3.2. Metal-Doping of $\text{La}_{5.4}\text{MoO}_{11.1}$ Proton Conductors: Impact on the Structure and Electrical Properties	90
3.3. Synergic Effect of Metal and Fluorine Doping on the Structural and Electrical Properties of $\text{La}_{5.4}\text{MoO}_{11.1}$ -Based Materials	91
3.4. Unravelling Crystal Superstructures and Transformations in the $\text{La}_{6-x}\text{MoO}_{12-\delta}$ ($0.6 \leq x \leq 3.0$) Series: A System with Tailored Ionic/Electronic Conductivity	92
4. DISCUSSION	95
4.1. Influence of the preparation conditions on the structure and properties of $\text{La}_{6-x}\text{MoO}_{12-\delta}$ ($0 \leq x \leq 3$)	95
4.1.1. Optimization of the sintering temperature	95
4.1.2. Cooling rate influence	97
4.1.3. Single-phase existence range	99
4.2. Structural characterization of $\text{La}_{6-x}\text{MoO}_{12-\delta}$ single phases	105
4.2.1. Preliminary studies	105
4.2.2. Study in depth of the rhombohedral structures	116
4.3. General characterization and trends of $\text{La}_{6-x}\text{MoO}_{12-\delta}$ single phases ...	131
4.3.1. Structural characterization	131
4.3.2. Microstructure of materials	134
4.3.3. Electrical characterization	137

4.4. Modification of the cationic-anionic framework. Influence of the preparation conditions	144
4.4.1. Substitution in the lanthanum position, $\text{La}_{5.3}\text{A}_{0.1}\text{MoO}_{11.05}$ (A = Ca, Sr and Ba) series	144
4.4.2. Substitution in the molybdenum position, $\text{La}_{5.4}\text{Mo}_{0.9}\text{B}_{0.1}\text{O}_{11.1-\delta}$ (B = Ti, Zr and Nb) series	147
4.4.3. Study of $\text{La}_{5.4}\text{Mo}_{1-x}\text{Nb}_x\text{O}_{11.1-x/2}$ ($0 \leq x \leq 0.25$) series	152
4.4.4. Substitution in the oxygen position via fluorination, $\text{La}_{5.4}\text{Mo}_{1-x}\text{B}_x\text{O}_{11.1-y/2-\delta}\text{F}_y$. (x = 0 and 0.10; B = Ti, Zr and Nb; y = 1, 3 and 6)	162
4.4.5. Microstructural characterization of doped materials	173
4.5. Electrical characterization of doped materials	177
5. CONCLUSIONS	183
6. APPENDIXES	185
6.1. Phase stability and thermal characterization of $\text{La}_{5.4}\text{MoO}_{11.1}$	185
6.2. X-ray photoelectronic spectroscopy characterization	189
6.3. Phase stability of doped compounds under reducing conditions	192
6.4. Hydrogen separation membrane test	194
7. BIBLIOGRAPHY	197
Permissions	211

FIGURES INDEX.

RESUMEN

Figura 1. Difractogramas de rayos-X del $\text{La}_{5.4}\text{MoO}_{11.1}$ sinterizado a $1500\text{ }^{\circ}\text{C}$ 1h y enfriado a diferentes velocidades (*quenching*, 50, 5, 2.5, and $0.5\text{ }^{\circ}\text{C}\cdot\text{min}^{-1}$). 10

1. INTRODUCTION

Figure 1.1. World primary energy consumption..... 23

Figure 1.2. Regions where natural disasters will occur caused by climate change 24

Figure 1.3. Scheme of hydrogen fuel cell car functioning 27

Figure 1.4. Pressure Swing Adsorption (PSA) system scheme..... 29

Figure 1.5. Scheme of H_2 separation process using a dense proton-electron conducting ceramic membrane 32

Figure 1.6. BZCY and BZCYZn permeation studies at different temperatures..... 37

Figure 1.7. Electron conductivity of $\text{La}_{1.95}\text{Ca}_{0.05}\text{Ce}_2\text{O}_{6.975}$ and $\text{La}_{1.95}\text{Ca}_{0.05}\text{Zr}_2\text{O}_{6.975}$ under different atmospheres..... 40

Figure 1.8. Total conductivity of $\text{Ln}_6\text{WO}_{12}$ ($\text{Ln} = \text{La}, \text{Nd}, \text{Gd}, \text{and Er}$) measured in wet H_2 41

Figure 1.9. Phase diagram of $\text{La}_2\text{O}_3\text{-WO}_3$ 42

Figure 1.10. Variation of lattice parameters obtained by XRPD as a function of nominal La/W ratio after calcination at 1500 °C	43
Figure 1.11. Structure of $\text{La}_{28-y}\text{W}_{4+y}\text{O}_{54+\delta}$ (for $y = 1$)	44
Figure 1.12. Open circuit voltage of a Pt// $(\text{Mo})\text{La}_{5.4}\text{WO}_{12-\delta}$ //Pt fuel cell as a function of temperature	48
Figure 1.13. La_2O_3 - MoO_3 phase diagram.....	49
Figure 1.14. Scanvac® Coolsave™ 110–4Pro freeze-dryer used in samples preparation.....	57
Figure 1.15. General scheme of freeze-drying method synthesis process ..	58
Figure 1.16. Aqueous solution phase diagram	59
Figure 1.17. Brown powder obtained at 300 °C 1h	60
Figure 1.18. Bragg’s Law representation.	62
Figure 1.19. Pictures of (left) PANalytical Empyrean diffractometer and (right) PANalytical X’Pert PRO MPD diffractometer used in this thesis....	66
Figure 1.20. (Top) Aerial picture of Paul Scherrer Institute (PSI) in Switzerland and (bottom) the HRPT diffractometer	69
Figure 1.21. Example of HRTEM images for a multilayer sample CGO and LSC that are easily differenced by the local microstructure regions and the SAED obtained by Fourier transformed of the structure CGO	72
Figure 1.22. HRTEM instrument that was used for characterizing the materials	72
Figure 1.23. Components of a scanning electron microscope.....	73

Figure 1.24. Picture of scanning electronic microscope used in this thesis	75
Figure 1.25. Picture of PHI 5700 XPS spectrophotometer used in this thesis	77
Figure 1.26. Nyquist diagram of material with a unique contribution (a) and different contributions from total impedance (b)	80
Figure 1.27. Experimental assembly and electrochemical cell of complex impedance spectroscopy equipment	82
Figure 1.28. Dependence of total conductivity and different contribution ionic/electronics for a mixed conductor.....	83
Figure 1.29. a) Diagram of the different parts of the variable pressure partial impedance spectroscopy measuring device. b) Photograph of the furnace and the cell.....	83
Figure 1.30. Variation of oxygen partial pressure vs time at 1173 K.....	86

4. DISCUSSION.

Figure 4.1. XRPD patterns of $\text{La}_{5.4}\text{MoO}_{11.1}$ obtained by heating 1h between 800 and 1500 °C and cooled down at 5 °C min^{-1}	96
Figure 4.2. XRPD patterns of $\text{La}_{5.4}\text{MoO}_{11.1}$ obtained by heating at 1500 °C 1h and cooled down at different rates (quenching, 50, 5, 2.5, and 0.5 °C $\cdot\text{min}^{-1}$)	97
Figure 4.3. XRPD patterns for selected $\text{La}_{6-x}\text{MoO}_{12-\delta}$ ($x = 1.0, 1.5, 2.0$ and 2.5) samples, obtained by heating 1h between 800 and 1500 °C and cooled down at 5 °C $\cdot\text{min}^{-1}$	100

Figure 4.4. XRPD patterns of $\text{La}_{6-x}\text{MoO}_{12-\delta}$ ($x = 0, 0.4, 0.6, 1.0, 1.5, 2.0, 2.5$ and 3.0) series obtained by heating at $1500\text{ }^\circ\text{C}$ 1h and cooled down at different rates (quenching, 5 and $0.5\text{ }^\circ\text{C}\cdot\text{min}^{-1}$)	103
Figure 4.5. Rietveld XRPD plot of $\text{La}_{5.4}\text{MoO}_{11.1}$ obtained by heating at $1500\text{ }^\circ\text{C}$ 1h and cooled down by quenching	105
Figure 4.6. c-axis view of the cubic structure of $\text{La}_{5.4}\text{MoO}_{11.1}$ heated at $1500\text{ }^\circ\text{C}$ 1h and cooled down by quenching	105
Figure 4.7. SAED patterns (a and b) and HRTEM image (c) of $\text{La}_{5.4}\text{MoO}_{11.1}$ obtained by heating at $1500\text{ }^\circ\text{C}$ 1h and cooled down by quenching along different zone axes.....	107
Figure 4.8. Le Bail XRPD plot of $\text{La}_{5.4}\text{MoO}_{11.1}$ obtained by heating at $1500\text{ }^\circ\text{C}$ 1h and cooled down at $50\text{ }^\circ\text{C}\cdot\text{min}^{-1}$ (rhombohedral structure R1)	108
Figure 4.9. Le Bail XRPD plot of $\text{La}_{5.4}\text{MoO}_{11.1}$ obtained by heating at $1500\text{ }^\circ\text{C}$ 1h and cooled down at $0.5\text{ }^\circ\text{C}\cdot\text{min}^{-1}$ (rhombohedral structure R2)	109
Figure 4.10. SAED patterns (a, b, and c) and HRTEM (d and e) images of $\text{La}_{5.4}\text{MoO}_{11.1}$ obtained by heating at $1500\text{ }^\circ\text{C}$ 1h and cooled down at $50\text{ }^\circ\text{C}\cdot\text{min}^{-1}$ (rhombohedral structure R1)	110
Figure 4.11. SAED patterns (a, b, and c) and HRTEM (d and e) images of $\text{La}_{5.4}\text{MoO}_{11.1}$ obtained by heating $1500\text{ }^\circ\text{C}$ 1h and cooled down at $0.5\text{ }^\circ\text{C}\cdot\text{min}^{-1}$ (rhombohedral structure R2)	110
Figure 4.12. Rietveld XRPD plot of La_4MoO_9 obtained by heating at $1500\text{ }^\circ\text{C}$ 1h and cooled down at $0.5\text{ }^\circ\text{C}\cdot\text{min}^{-1}$	112

- Figure 4.13.** c-axis view of the monoclinic structure of La_4MoO_9 obtained by heating at 1500°C 1h and cooled down at $0.5^\circ\text{C}\cdot\text{min}^{-1}$ 112
- Figure 4.14.** SAED patterns (left) and HRTEM (right) images of La_4MoO_9 obtained by heating at 1500°C 1h and cooled down at $0.5^\circ\text{C}\cdot\text{min}^{-1}$ 115
- Figure 4.15.** SAED patterns of $\text{La}_{5.4}\text{MoO}_{11.1}$; left with an R1 symmetry along the $[002]_F$ zone axis where modulation vectors are of the type $q_{F1} = 1/7 (220)$, and right with an R2 symmetry along the $[111]_F$ zone axis, where modulation vectors are of the type $q_{F1} = 1/5 (220)$ 117
- Figure 4.16.** Rietveld NPD plot of $\text{La}_{5.4}\text{MoO}_{11.1}$ obtained by heating at 1500°C 1h and cooled down at $50^\circ\text{C}\cdot\text{min}^{-1}$ (R1) 122
- Figure 4.17.** Rietveld NPD plot of $\text{La}_{5.4}\text{MoO}_{11.1}$ obtained by heating at 1500°C 1h and cooled down at $0.5^\circ\text{C}\cdot\text{min}^{-1}$ (R2) 126
- Figure 4.18.** c-axis view of the rhombohedral structures of $\text{La}_{5.4}\text{MoO}_{11.1}$ obtained by heating at 1500°C 1h and cooled down at 50 and $0.5^\circ\text{C}\cdot\text{min}^{-1}$, R1, and R2, respectively 130
- Figure 4.19.** HRTEM images and SAED patterns of $\text{La}_{4.5}\text{MoO}_{9.75}$ and La_4MoO_9 compositions obtained by heating at 1500°C 1h and cooled down at $5^\circ\text{C}\cdot\text{min}^{-1}$ 133
- Figure 4.20.** SEM micrographs of $\text{La}_{6-x}\text{MoO}_{12-\delta}$ ($x = 0.6, 1.5, 2$) obtained by heating at 1500°C 1h and cooled down at different rates, comparing the grain size with each structure obtained 135
- Figure 4.21.** EDS images of surfaces and La, Mo elemental mappings of $\text{La}_{6-x}\text{MoO}_{12-\delta}$ ($x = 0.6, 1.5, 2$) obtained by heating at 1500°C for 1h and cooled down at different rates 136

Figure 4.22. Representative impedance spectra at 400 °C of $\text{La}_{6-x}\text{MoO}_{12-\delta}$ ($x = 0.6, 1.5, \text{ and } 2.0$) obtained by heating at 1500 °C 1h and cooled down by quenching, under dry and wet N_2 atmospheres	138
Figure 4.23. Arrhenius plots of (a) $\text{La}_{5.4}\text{MoO}_{11.1}$, (b) $\text{La}_{4.5}\text{MoO}_{9.75}$ and (c) La_4MoO_9 obtained by heating at 1500 °C 1h and cooled down at different rates under dry and wet N_2 and wet 5% H_2 -Ar atmospheres.....	139
Figure 4.24. Conductivity vs oxygen partial pressure at 800 °C for $\text{La}_{5.4}1500\text{-Q}$, $\text{La}_{4.5}1500\text{-Q}$, and $\text{La}_{4.0}1500\text{-Q}$	143
Figure 4.25. XRPD patterns of $\text{La}_{5.3}\text{A}_{0.10}\text{MoO}_{11.05}$ ($\text{A} = \text{Ca}, \text{Sr and Ba}$) series obtained by heating at 1500 °C 1h and cooled down at different rates (quenching, 50 and 0.5 °C·min ⁻¹)	145
Figure 4.26. XRPD patterns of $\text{La}_{5.4}\text{Mo}_{0.90}\text{B}_{0.10}\text{O}_{11.1-\delta}$ ($\text{B} = \text{Ti}, \text{Zr and Nb}$) samples obtained by heating 1h between 1200 and 1500°C and cooled down at 50 °C·min ⁻¹	148
Figure 4.27. XRPD patterns of $\text{La}_{5.4}\text{Mo}_{0.90}\text{B}_{0.10}\text{O}_{11.1-\delta}$ ($\text{B} = \text{Ti}, \text{Zr and Nb}$) series obtained by heating at 1500°C 1h and cooled down at different rates (quenching, 50 and 0.5 °C·min ⁻¹)	149
Figure 4.28. Le Bail XRPD plots of $\text{La}_{5.4}\text{Mo}_{0.90}\text{Ti}_{0.10}\text{O}_{11.05}$ obtained by heating at 1500 °C 1h and cooled down at 50 °C·min ⁻¹ with rhombohedral structure R1	151
Figure 4.29. XRPD patterns of $\text{La}_{5.4}\text{Mo}_{1-x}\text{Nb}_x\text{O}_{11.1-x/2}$ ($x = 0, 0.05, 0.10, 0.15, 0.20 \text{ and } 0.25$) series obtained by heating at 1500 °C 1h and cooled down at different rates (quenching, 50 and 0.5 °C·min ⁻¹)	153
Figure 4.30. Unit cell volume versus niobium content of $\text{La}_{5.4}\text{Mo}_{1-x}\text{Nb}_x\text{O}_{11.1-x/2}$ series cooled down at different rates (quenching, 50 and 0.5 °C·min ⁻¹)	156

Figure 4.31. Rietveld XRPD (top) and TOF-NPD (bottom) plots of $\text{La}_{5.4}\text{Mo}_{0.90}\text{Nb}_{0.10}\text{O}_{11.05}$ obtained by heating at 1500 °C 1h and cooled down by quenching.....	158
Figure 4.32. SAED patterns of $\text{La}_{5.4}\text{Mo}_{0.90}\text{Nb}_{0.10}\text{O}_{11.05}$ obtained by heating at 1500 °C 1h and cooled down by quenching along a) $[11\bar{0}]$ and b) $[21\bar{0}]$ zone axes	161
Figure 4.33. SAED patterns and HRTEM images of $\text{La}_{5.4}\text{Mo}_{0.90}\text{Nb}_{0.10}\text{O}_{11.05}$ obtained by heating at 1500 °C 1h and cooled down at 0.5 °C·min ⁻¹ along (a,b) $[001]$, (c,d) $[72\bar{7}]$ and (e,f) $[22\bar{1}]$ zone axes	162
Figure 4.34. a) XRPD patterns of $\text{La}_{5.4}\text{MoO}_{11.1-y/2}\text{F}_y$ (y = 0, 1, 3 and 6) series obtained by heating at 1500 °C 1h and cooled down at 5 °C·min ⁻¹ . b) XRPD patterns of $\text{La}_{5.4}\text{MoO}_{11.1-y/2}\text{F}_y$ (y = 3) heated at 1500 °C 1h and cooled down at different rates (quenching, 50, 5 and 0.5 °C·min ⁻¹)	163
Figure 4.35. XRPD patterns of $\text{La}_{5.4}\text{MoO}_{11.1-y/2}\text{F}_y$ (y = 3) obtained by heating 1h between 800 and 1500 °C and cooled down at 5 °C·min ⁻¹	164
Figure 4.36. XRPD patterns of $\text{La}_{5.4}\text{Mo}_{0.90}\text{B}_{0.10}\text{O}_{11.05-y/2-8}\text{F}_y$ (B= Ti, Zr and Nb, y = 3) obtained by heating 1h between 1200 and 1500 °C and cooled down at 5 °C·min ⁻¹	166
Figure 4.37. Rietveld XRPD (top) and NPD (bottom) plots of $\text{La}_{5.4}\text{Mo}_{0.90}\text{Nb}_{0.10}\text{O}_{11.05}\text{F}_3$ obtained by heating at 1200 1h and cooled down at 5 °C·min ⁻¹	169
Figure 4.38. SAED patterns and HRTEM images of: (a-c) $\text{La}_{5.4}\text{MoO}_{11.1-y/2}\text{F}_y$ (y = 3) obtained by heating at 1500 °C 1h and cooled down at 5 °C·min ⁻¹ ; and (d-f) $\text{La}_{5.4}\text{Mo}_{0.90}\text{Nb}_{0.10}\text{O}_{10.05-y/2}\text{F}_y$ (y = 3) obtained by heating at 1200 °C 1h and cooled down at 5 °C·min ⁻¹ along different zone axes	172

Figure 4.39. SEM images of $\text{La}_{5.4}\text{Mo}_{1-x}\text{Nb}_x\text{O}_{11.1-x/2}$ ($x = 0$ and 0.10) obtained by heating at $1500\text{ }^\circ\text{C}$ 1h and cooled down by quenching and $0.5\text{ }^\circ\text{C}\cdot\text{min}^{-1}$, comparing the grain size with each treatment and showing that the Nb content increases the grain size	174
Figure 4.40. SEM micrographs of $\text{La}_{5.4}\text{Mo}_{1-x}\text{Nb}_x\text{O}_{11.1-y/2-\delta}\text{F}_y$ ($x = 0, 0.10$ and $y = 3$) obtained by heating at different temperatures 1h and cooled down at $5\text{ }^\circ\text{C}\text{ min}^{-1}$	175
Figure 4.41. SEM-EDS elemental mappings of the surface of $\text{La}_{5.4}\text{Mo}_{0.90}\text{Nb}_{0.10}\text{O}_{11.05-y/2}\text{F}_y$ ($y = 3$) sintered at $1200\text{ }^\circ\text{C}$ for 1h	176
Figure 4.42. Representative impedance spectra at $400\text{ }^\circ\text{C}$ of $\text{La}_{5.4}\text{Mo}_{1-x}\text{Nb}_x\text{O}_{11.1-y/2-\delta}\text{F}_y$ ($x = 0, 0.10$ and $y = 0, 3$) obtained by heating at $1500\text{ }^\circ\text{C}$ 1h and cooled down by quenching ($5\text{ }^\circ\text{C}\cdot\text{min}^{-1}$ in case of fluorinated samples) under dry/wet N_2 and wet $5\%\text{ H}_2\text{-Ar}$ gases at $400\text{ }^\circ\text{C}$	177
Figure 4.43. Arrhenius plots of the overall conductivity of $\text{La}_{5.4}\text{Mo}_{1-x}\text{Nb}_x\text{O}_{11.1-x/2}$ ($x = 0, 0.10$) obtained by heating at $1500\text{ }^\circ\text{C}$ 1h and cooled down by quenching, measured in dry/wet N_2 and wet $5\%\text{ H}_2\text{-Ar}$	178
Figure 4.44. Conductivity of $\text{La}_{5.4}\text{Mo}_{1-x}\text{Nb}_x\text{O}_{11.1-x/2}$ ($x = 0, 0.10$) obtained by heating $1500\text{ }^\circ\text{C}$ 1h and cooled by quenching, 50 and $0.5\text{ }^\circ\text{C}\cdot\text{min}^{-1}$ measured at $800\text{ }^\circ\text{C}$ in dry/wet N_2 and wet $5\%\text{ H}_2\text{-Ar}$	179
Figure 4.45. Arrhenius plots of the overall conductivity $\text{La}_{5.4}\text{Mo}_{0.90}\text{Nb}_{0.10}\text{O}_{11.05-y/2}\text{F}_y$ ($y = 3$) were sintered at $1500\text{ }^\circ\text{C}$ for 1h and cooled at $5\text{ }^\circ\text{C}\cdot\text{min}^{-1}$ under different flowing atmospheres	181

6. APPENDIXES.

- Figure 6.1.** XRPD patterns of $\text{La}_{5.4}\text{MoO}_{11.1}$ obtained by heating at 1500 °C 1h and cooled down at different rates (quenching, 50 and 0.5 °C·min⁻¹) after annealing for 48 h in air at 800 °C, 5% H₂-Ar at 800 °C and air at 1000 °C..... 186
- Figure 6.2.** HT-XRPD for $\text{La}_{5.4}\text{MoO}_{11.1}$ that were cooled down by (a) 50 °C·min⁻¹ and (b) quenching, measured at temperatures between 30°C and 1000 °C..... 187
- Figure 6.3.** Thermogravimetric curves for $\text{La}_{5.4}\text{MoO}_{11.1}$ calcinated at 1500 °C 1h and cooled down at different rates (quenching, 50 and 0.5 °C·min⁻¹) performed under humidified air from room temperature to 1000 °C on cooling..... 188
- Figure 6.4.** XPS spectra for O 1s, Mo 3d and La 3d_{5/2} for samples $\text{La}_{5.4}\text{1500-Q}$, $\text{La}_{5.4}\text{1500-50}$, $\text{La}_{5.4}\text{1500-0.5}$ 190
- Figure 6.5.** XPS spectra of Mo 3d core level for $\text{La}_{5.4}\text{1500-Q}$ treated in 5%H₂-Ar for 24h. Mo⁶⁺ is only observed 192
- Figure 6.6.** XRPD patterns of cubic [$\text{La}_{5.4}\text{Mo}_{1-x}\text{Nb}_x\text{O}_{11.1-(x+y)/2}\text{F}_y$ ($x=0, 0.10$; and $y=3$)] and rhombohedral [$\text{La}_{5.4}\text{Mo}_{1-x}\text{B}_x\text{O}_{11.1-(x+y)/2}\text{F}_y$ ($x=0, 0.10$; B = Ti, Zr, Nb; $y=3$)] samples, obtained at 1200 and 1500 °C, respectively; after annealing the powders at 800 °C for 48h in 5%H₂-Ar..... 193
- Figure 6.7.** Hydrogen permeation for $\text{La}_{5.4}\text{Mo}_{0.9}\text{Nb}_{0.1}\text{O}_{11.05}$ obtained by heating at 1500 °C 1h and cooled down at 50 °C·min⁻¹ compared with $\text{La}_{5.5}\text{W}_{0.8}\text{Mo}_{0.2}\text{O}_{11.25-\delta}$ 194

TABLES INDEX.

RESUMEN.

Tabla 1. Velocidades de enfriamiento necesarias para obtener compuestos monofásicos en la serie $\text{La}_{6-x}\text{MoO}_{12-\delta}$ ($0 \leq x \leq 3$) al sinterizar a 1500 °C 1h.....	11
Tabla 2. Conductividades obtenidas para las muestras más representativas que se han estudiado en esta tesis doctoral medidas en atmosfera de N_2 seco y húmedo y en 5% H_2 -Ar húmedo a 700 °C.....	19

1. INTRODUCTION

Table 1.1. Selected lanthanide molybdates with their crystalline structures and conductivity	52
Table 1.2. Different characteristics and problems of typical fluorination agents.....	55

4. DISCUSSION.

Table 4.1. Summary of $\text{La}_{6-x}\text{MoO}_{12-\delta}$ ($x = 0, 0.4, 0.6, 1.0, 1.5, 2.0, 2.5$ and 3.0) samples obtained by heating 1h between 800 and 1500 °C and cooled down at $5 \text{ °C} \cdot \text{min}^{-1}$	101
Table 4.2. Summary of cooling rates needed to obtain $\text{La}_{6-x}\text{MoO}_{12-\delta}$ ($0 \leq x \leq 2$) single phases by heating the precursors at 1500 °C 1h.....	104
Table 4.3. Refined atomic positions, and isotropic atomic displacement parameters of La_4MoO_9 with a monoclinic symmetry from XRPD	113
Table 4.4. Interatomic distances of La_4MoO_9 with a monoclinic symmetry	114
Table 4.5. Independent atoms of the ideal fluorite crystal structure in the $R\bar{3}m$ space group of the $7 \times 7 \times 1$ supercell.....	119

Table 4.6. Independent atoms of the ideal fluorite crystal structure in the $R\bar{3}m$ space group of the $5 \times 5 \times 1$ supercell	121
Table 4.7. Refined atomic positions, occupancy factors and isotropic atomic displacement parameters of $La_{5.4}MoO_{11.1}$ obtained by heating at 1500 °C 1h and cooled down at 50 °C·min ⁻¹ (R1) from NPD in $R\bar{3}m$ space group	123
Table 4.8. Interatomic distances of $La_{5.4}MoO_{11.1}$ obtained by heating at 1500 °C 1h and cooled down at 50 °C·min ⁻¹ (R1) from NPD in $R\bar{3}m$ space group	124
Table 4.9. Refined atomic positions, occupancy factors and isotropic atomic displacement parameters of $La_{5.4}MoO_{11.1}$ obtained by heating at 1500 °C 1h and cooled down at 0.5 °C·min ⁻¹ (R2) from NPD in $R\bar{3}m$ space group	127
Table 4.10. Interatomic distances of $La_{5.4}MoO_{11.1}$ obtained by heating at 1500 °C 1h and cooled down at 0.5 °C·min ⁻¹ (R2) from NPD in $R\bar{3}m$ space group	128
Table 4.11. Unit cell parameters, cell volumes and agreement factors of $La_{6-x}MoO_{12-\delta}$ ($x = 0.6, 1, 1.5,$ and 2.0) obtained by heating at 1500 °C 1h and cooled down at different rates (quenching, 5 and 0.5 °C·min ⁻¹) determined by Rietveld refinements of XRPD data	132
Table 4.12. Bulk cation concentration (at. %) determined by EDX for $La_{5.4}MoO_{11.1}$ obtained by heating at 1500 °C 1h and cooled down at different rates (quenching, 50, and 0.5 °C·min ⁻¹)	137
Table 4.13. Conductivity data obtained for $La_{6-x}MoO_{12-\sigma}$ ($x = 0.6, 1.5,$ and 2.0) obtained by heating at 1500 °C 1h and cooled down at different rates (quenching, 50, 5 and 0.5 °C·min ⁻¹), measured at 700 and 400 °C	140
Table 4.14. Summary of $La_{5.3}A_{0.10}MoO_{11.05}$ ($A = Ca, Sr,$ and Ba) phases obtained by heating at 1500 °C 1h and cooling down at different rates (quenching, 50 and 0.5 °C·min ⁻¹)	146
Table 4.15. Summary of $La_{5.4}Mo_{0.90}B_{0.10}O_{11.1-\delta}$ ($B = Ti, Zr,$ and Nb) phases obtained by heating at 1500 °C 1h and cooled down at different rates (quenching, 50 and 0.5 °C·min ⁻¹)	150

Table 4.16. Summary of cooling rates needed to obtain $\text{La}_{5.4}\text{Mo}_{1-x}\text{Nb}_x\text{O}_{11.1-x/2}$ ($0 \leq x \leq 0.20$) single phases by heating the precursors at 1500 °C 1h..... 154

Table 4.17. Unit cell parameters, volumes and agreement factors of $\text{La}_{5.4}\text{Mo}_{1-x}\text{Nb}_x\text{O}_{11.1-x/2}$ ($x = 0, 0.05, 0.10, 0.15$ and 0.20) series obtained by heating at 1500 °C 1h and cooled down at different rates (quenching, 50 and $0.5 \text{ °C}\cdot\text{min}^{-1}$) determined by Rietveld (cubic) and Le Bail (rhombohedral) refinements of XRPD data 155

Table 4.18. Unit cell parameters, cell volumes, Rietveld agreement factors, atomic positions, isotropic atomic displacement parameters and occupancy factors of $\text{La}_{5.4}\text{Mo}_{1-x}\text{Nb}_x\text{O}_{11.1-x/2}$ ($x = 0, 0.10,$ and 0.20) obtained by heating at 1500 °C 1h and cooled down by quenching determined by TOF-NPD Rietveld refinements using different data banks (4, 5, and 6) 159

Table 4.19. Atomic and weight percentage of fluorine obtained by ion-chromatography and calculated formulas for $\text{La}_{5.4}\text{Mo}_{1-x}\text{B}_x\text{O}_{11.1-y/2-\delta}\text{F}_y$ ($x = 0, 0.10$; $\text{B} = \text{Ti}, \text{Zr}, \text{Nb}$; $y = 3$) heated 1h between 1200-1400 °C and cooled down at $5 \text{ °C}\cdot\text{min}^{-1}$ 167

Table 4.20. Unit cell parameters, cell volumes, agreement factors, atomic displacement, occupancy factors, and O(F)-O(F) distances determined from a combined XRPD-NPD Rietveld refinement of $\text{La}_{5.4}\text{Mo}_{0.90}\text{Nb}_{0.10}\text{O}_{11.05-y/2}\text{F}_y$ ($y = 3$) obtained by heating at 1200 °C 1h and cooled at $5 \text{ °C}\cdot\text{min}^{-1}$. Data for $\text{Nb}_{0.10}1500\text{-Q}$ are also included 170

Table 4.21. Unit cell parameters, cell volumes and agreement factors of $\text{La}_{5.4}\text{Mo}_{1-x}\text{B}_x\text{O}_{11.1-y/2-\delta}\text{F}_y$ ($x = 0, 0.1$; $\text{B} = \text{Ti}, \text{Zr}$ and Nb ; $y = 3$) series obtained by heating between 1200-1400 °C 1h and cooled down at $5 \text{ °C}\cdot\text{min}^{-1}$ determined by Le Bail refinements of XRPD data..... 171

6. APPENDIXES.

Table 6.1. Unit cell parameters of $\text{La}_{5.4}\text{MoO}_{11.1}$ heated at 1500 °C 1h and cooled down at different rates (quenching, 50 and $0.5 \text{ °C}\cdot\text{min}^{-1}$) after annealing the powders at 800 °C 48h in air and 5% $\text{H}_2\text{-Ar}$ 185

Table 6.2. Surface atomic concentration (at. %) of $\text{La}_{5.4}\text{MoO}_{11.1}$ heated at 1500 °C 1h and cooled down at different rates (Q, 50 and $0.5 \text{ °C}\cdot\text{min}^{-1}$) 189

ABBREVIATIONS.

BZCY	$\text{BaZr}_{0.1}\text{Ce}_{0.7}\text{Y}_{0.2}\text{O}_3$	NPD	Neutron Powder Diffraction
BZCYZn	$\text{BaZr}_{0.3}\text{Ce}_{0.6}\text{Y}_{0.1}\text{Zn}_{0.05}\text{O}_3$	PDF	Powder Diffraction File
COP	Conference of the parts	PLD	Pulsed Laser Deposition
CVD	Chemical vapor deposition	pO₂	Partial Pressure of Oxygen
EDS	Energy-dispersive X-Ray Spectroscopy	PSA	Pressure Swing Adsorption
EDTA	Ethylenediaminetetraacetic acid	PSI	Paul Scherrer Institute
EMF	Synchronous impedance method	PVDF	Polyvinylidene Fluoride
EIS	Electrochemical Impedance Spectroscopy	Q	Quenching
FESEM	Field Emission Scanning Electron Microscopy	SAED	Selected Area Electron Diffraction
FIB	Focused Ion Beam	SCY	$\text{SrCe}_{0.95}\text{Y}_{0.05}\text{O}_{3-\delta}$
HR	High Resolution	SDC	$\text{Ce}_{0.8}\text{Sm}_{0.2}\text{O}_{2-\delta}$
HRPT	High Resolution Powder Diffractometer for Thermal Neutrons	SEM	Scanning Electron Microscopy
HT	High Temperature	SG	Space Group
ICSD	Inorganic Crystal Structure Database	SOFC	Solid Oxide Fuel Cell
LAMOX	$\text{La}_2\text{Mo}_2\text{O}_9$	STFC	Science and Technology Facilities Council
LN	Lanthanide	TEM	Transmission Electron Microscopy
MONO	Monoclinic		



PHASE LABELS SUMMARY.

□	Cubic
○	R1
△	R2
*	La ₂ O ₃
∅	Monoclinic
Π	La ₆ Mo ₂ O ₁₅
#	BaMoO ₄
◇	La ₂ B ₄ O ₇
+	La(OH) ₃
▼	LaNbO ₄
⦿	La ₂ MoO ₆
λ	LaOF
△	La ₃ Mo ₂ O ₁₀
⋈	TiO ₂



RESUMEN.

En la actualidad, el desarrollo de la ciencia y la tecnología relacionada con la energía limpia, incluyendo su almacenamiento y conversión, es clave en la lucha contra la contaminación global y el futuro agotamiento de los combustibles fósiles. Si el cambio climático no se frena, se producirán numerosos problemas económicos, sociales y ambientales que pueden afectar incluso a la preservación de la vida en la Tierra.

Para evitar este dramático futuro, la ciencia y la tecnología se han centrado en mejorar la eficiencia del proceso actual de generación de energía (sobre todo basado en combustibles fósiles), el desarrollo de los procesos de obtención de energía limpia y la sustitución de combustibles fósiles por otros que no tengan emisiones nocivas.

A su vez, se tiene en cuenta el uso de tecnologías como las energías renovables (solar, eólica, etc...) que producen energía limpia sin generar ningún residuo durante el proceso. Pero para ello es necesario el apoyo de toda la sociedad para enfrentarse al enorme problema medioambiental.

Para ello se han reunido la mayoría de países del mundo en la Conferencia del Cambio Climático de Glasgow (2022), donde los expertos estimaron que la temperatura ascendería entre unos 1.8 y 2.4 °C dentro de 50 años, proponiendo medidas para disminuir este efecto que puede ser devastador para la sociedad. Estas propuestas deben llevarse a cabo debiendo modificarse los hábitos de consumo de la sociedad actual y buscar nuevos combustibles mucho más limpios y eficientes.

El hidrógeno se considera un vector energético muy atractivo ya que su densidad de energía es mucho mayor que la de cualquier otro combustible. El máximo rendimiento de energía se consigue por conversión directa en una

pila de combustible generando únicamente agua como subproducto. Los altos costes y las dificultades técnicas están retrasando la implantación de una economía basada en H₂ (verde) siendo necesario superar una serie de desafíos tecnológicos antes de obtenerlo por procesos renovables; por ejemplo, mediante una electrolisis del agua con energía procedente de una central hidroeléctrica, solar, eólica y/o geotérmica (Ho *et al.*, 2011; Ji *et al.*, 2013; Niknam *et al.*, 2013; Sorensen *et al.*, 2007; Wang D. *et al.*, 2013).

Actualmente, la generación de hidrógeno se hace mayoritariamente a través del reformado del gas natural y/o de la gasificación del carbón, que son económicamente más favorables, pero mucho más contaminantes. Uno de los inconvenientes asociados a estos procesos es que el gas está impurificado con otros compuestos; por ejemplo, CO₂, CO, H₂O, NO_x y SO_x lo que hace necesario una purificación preferentemente con sistemas que sean de bajo coste, simples y eficientes.

Entre las distintas tecnologías desarrolladas al respecto, se encuentran las membranas de separación de hidrógeno que actúan como barreras selectivas que sólo permiten el paso del hidrógeno. Existen muchos tipos de membranas de separación de hidrógeno, las más prometedoras son las cerámicas que se caracterizan por ser baratas, estables en atmósferas de CO, CO₂ y H₂S, trabajan a elevada temperatura (~800 °C) y tienen una alta permeación. La elevada temperatura de trabajo es clave ya que acelera la cinética de disociación de H₂ lo que las hace aplicables industrialmente (Amewaza *et al.*, 2005; Katahira *et al.*, 2000; Kitamura *et al.*, 2003). Los materiales empleados para su fabricación son el SrCeO₃ y BaCeO₃ debido a su elevada conductividad protónica a alta temperatura. El principal inconveniente que presentan es que no son estables en atmósferas de CO y CO₂, reaccionando y formando un carbonato metálico que expande la celda y

origina su fractura, por ello es necesario buscar otros compuestos que sean más estables.

Entre los materiales cerámicos que pueden usarse como membranas de separación de hidrogeno, se encuentran el SrCeO_3 y BaCeO_3 con estructura tipo perovskita que tienen elevada conductividad protónica a alta temperatura. El principal inconveniente que tienen es que no son estables en atmósferas de CO y CO_2 , dado que se segrega el correspondiente carbonato metálico que produce la expansión de la celda y por ello su fractura. Por ello, los materiales no pueden emplearse para purificar el H_2 obtenido del reformado de hidrocarburos lo que hace necesario buscar otros compuestos que sean más estables en corrientes ácidas.

Otros materiales alternativos son los wolframatos de elementos lantánidos con fórmula general $\text{Ln}_6\text{WO}_{12-\delta}$, $\text{Ln} = \text{La}, \text{Nd}, \text{Sm}$ y Gd , que tienen buena conductividad iónica y son estables en atmósferas ácidas. La conductividad disminuye al disminuir el radio del lantánido debido a que se produce un cambio de simetría cristalina; por ello los más estudiados son los derivados del lantano, $\text{La}_{6-x}\text{WO}_{12-\delta}$. Numerosos trabajos analizan la influencia del contenido de lantano en la estructura y en las propiedades eléctricas. Está aceptado que para relaciones La/W menores de 5.3 se segrega $\text{La}_6\text{W}_2\text{O}_{15}$ y por encima de 5.7, La_2O_3 . Solo las composiciones comprendidas entre 5.3 y 5.7 son monofásicas con estructura cúbica tipo fluorita (Magrasó *et al.* 2009). Utilizando métodos directos y mapas de diferencias de Fourier con datos de difracción de rayos-X (XRPD) y de neutrones (NPD), se ha propuesto que el wolframio ocupa parcialmente la posición del lantano y que las vacantes de ion oxido aumentan al disminuir el contenido de lantano (Magrasó *et al.* 2012), siendo más adecuado reescribir la fórmula general de la serie de la forma $\text{La}_{28-x}\text{W}_{4+x}\text{O}_{54+\delta}\square_{10-\delta}$.

Para aumentar el rendimiento de las membranas construidas con estos materiales se recurre normalmente al dopaje. Entre todos los dopantes estudiados, los mejores resultados se obtienen con el Mo, en materiales con fórmula general $\text{La}_{5.5}\text{W}_{1-x}\text{Mo}_x\text{O}_{12-\delta}$ ($0 \leq x \leq 1$), debido a su mayor facilidad de reducción a otros estados de oxidación inferiores (Amsif *et al.* 2012). Puesto que al aumentar el contenido en Mo se consiguen mejores valores de conductividad total, parece lógico pensar que el material puro de Mo sería el mejor. Este hecho constituye nuestra hipótesis de partida para la realización de la Tesis Doctoral, en la que surge una nueva serie de fórmula general $\text{La}_{6-x}\text{MoO}_{12-\delta}$ a explorar. La bibliografía existente en su momento se publica que el molibdato de lantano, $\text{La}_{5.5}\text{MoO}_{11.25}$, es el que presenta mayor conductividad ($2 \cdot 10^{-4} \text{ S} \cdot \text{cm}^{-1}$) frente a sus homólogos de otros lantánidos ($\sim 1 \cdot 10^{-4} \text{ S} \cdot \text{cm}^{-1}$). Sin embargo, los resultados son confusos, escasos y algunas veces contradictorios.

Para facilitar la lectura de la memoria los resultados más significativos se presentan de forma diferente al cronológico de la investigación. Primero se exponen los resultados publicados en los artículos *Chemistry of Materials* **2017**, 29, 6966-6975 y **2020**, 32, 7052-7062 donde se optimizan las condiciones sintéticas, se resuelve la estructura de las distintas fases y se correlaciona la estructura con las propiedades en materiales con fórmula general $\text{La}_{6-x}\text{MoO}_{12-\delta}$ ($0 \leq x \leq 3.0$). En segundo lugar, se presentan los resultados publicados en *Inorganic Chemistry* **2018**, 57, 12811-12819 y **2020**, 59, 1444-1452 donde se realiza una modificación del entramado catiónico y/o aniónico para optimizar sus propiedades. Respecto al resumen y para simplificar, se ha realizado unificando los estudios de optimización sintética, determinación estructural y posteriormente, la correlación entre la

microestructura y propiedades eléctricas (el mismo esquema se seguirá en el acto de defensa).

La Tesis comienza con la optimización de las condiciones de síntesis-sinterización de la composición $\text{La}_{5.4}\text{MoO}_{11.1}$. Entre todas las posibles composiciones se elige ésta por tener la misma estequiometría que la del sistema relacionado, $\text{La}_{5.4}\text{WO}_{11.1}$, pensando en que tendrá ciertas similitudes. La síntesis se realiza mediante el método del precursor liofilizado¹ mezclando disoluciones de los cationes en cantidades estequiométricas en presencia de un agente complejante (ácido etilendiaminotetraacético). La disolución resultante se congela en N_2 líquido obteniendo pequeñas esferas del material que se someten posteriormente a un proceso de liofilización (~48 h) para eliminar el agua.

Una vez seco, el precursor se calcina rápidamente a $300\text{ }^\circ\text{C}$ 1h liberándose una gran cantidad de gases debido a la autoignición de nitratos y especies orgánicas contenidas en el material, obteniéndose un sólido poroso y de gran volumen que se calcina a $800\text{ }^\circ\text{C}$ durante 1h calentando/enfriando a $5\text{ }^\circ\text{C}\cdot\text{min}^{-1}$ para completar la descomposición térmica y dejar el precursor libre de restos carbonosos. Por último, el polvo a $800\text{ }^\circ\text{C}$ se prensa en pastillas de 10 mm de diámetro y 1 mm de espesor a $2\text{ MPa}\cdot\text{cm}^{-2}$ y se calcina a temperaturas comprendidas entre 1100 y $1500\text{ }^\circ\text{C}$.

Mediante difracción de rayos-X se detecta la presencia de una fase romboédrica tipo $\text{La}_6\text{MoO}_{12}$ (PDF 00-34-1220) denominada a partir de ahora R1, otra hexagonal tipo La_4MoO_9 (PDF 00-023-1144) denominada a partir de ahora R2 y La_2O_3 (PDF 01-073-2141). Para evitar la segregación de La_2O_3 , se calcina a $1500\text{ }^\circ\text{C}$; sin embargo, en ningún caso se aíslan como fases puras.

¹Este procedimiento se utiliza para todos los materiales de la Tesis Doctoral variando únicamente las condiciones necesarias para preparar las disoluciones de los diferentes metales.

Para evitar la segregación de varias fases de forma simultánea se optimiza la velocidad de enfriamiento, una vez fijada la temperatura de sinterización a 1500 °C durante 1h. Para ello, las muestras se enfrían a 5 velocidades distintas: *quenching* (un enfriamiento súbito desde 1500 °C hasta temperatura ambiente en un horno de ascensor), 50, 5, 2.5 y 0.5 °C·min⁻¹ (Figura 1).

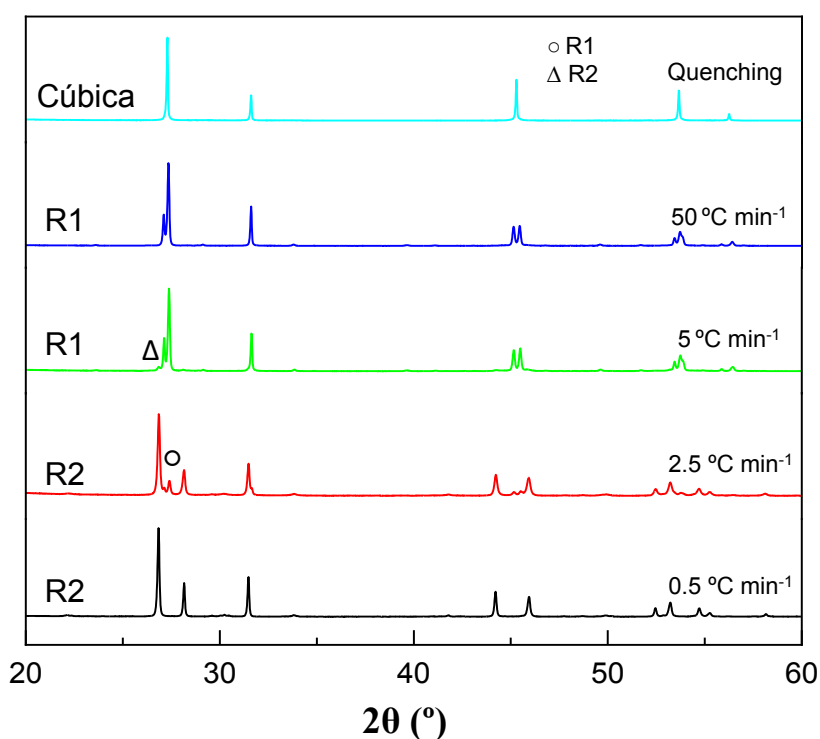


Figura 1. Difractogramas de rayos-X del La_{5.4}MoO_{11.1} sinterizado a 1500 °C 1h y enfriado a diferentes velocidades (*quenching*, 50, 5, 2.5, and 0.5 °C·min⁻¹). La fase mayoritaria se denota en la parte inferior a la izquierda del difractograma, y también se marcan las fases secundarias minoritarias.

Las muestras obtenidas por *quenching* son cúbicas tipo fluorita, al disminuir la velocidad de enfriamiento se obtiene la fase R1 a 50 °C·min⁻¹ que evoluciona progresivamente, hasta obtenerse la fase R2 al enfriar a

0.5 °C·min⁻¹. Una vez optimizadas las condiciones sintéticas para La_{5.4}MoO_{11.1}, el estudio se extiende a los materiales de la serie La_{6-x}MoO_{12-δ} (x = 0, 0.4, 0.6, 1, 1.5, 2, 2.5 y 3). Primero, se analiza la influencia de la temperatura de sinterización (800-1500 °C) enfriando a 5 °C·min⁻¹, donde solo la muestra La₄MoO₉ es monofásica independientemente de la temperatura empleada.

De forma más general se concluye que es necesario alta temperatura (1400-1500 °C) y un contenido en lantano comprendido entre $4 \leq x \leq 4.5$ para obtener compuestos monofásicos. Este estrecho rango de composiciones puede ampliarse modificando la velocidad de enfriamiento (Tabla 1). Así, para contenidos de lantano comprendidos entre $5.4 \leq x \leq 4$, se obtiene la estructura tipo fluorita mediante *quenching*, análogamente cuando la velocidad se hace muy pequeña (0.5 °C·min⁻¹) se favorece la formación de una nueva fase monoclinica.

Tabla 1. Velocidades de enfriamiento necesarias para obtener compuestos monofásicos en la serie La_{6-x}MoO_{12-δ} (0 ≤ x ≤ 3) al sinterizar a 1500 °C 1h. Las celdas vacías implican condiciones en las que no se obtienen monofases.

Muestra	Velocidad de enfriamiento			
	<i>Quenching</i>	50 °C·min ⁻¹	5 °C·min ⁻¹	0.5 °C·min ⁻¹
La_{5.4}	Cúbico	R1	-	R2
La₅	Cúbico	R1	-	R2
La_{4.5}	Cúbico	-	Cúbico	-
La₄	Cúbico	-	Cúbico	Monoclinico

El estudio sistemático realizado demuestra que se puede controlar la estructura final (cúbica, R1, R2 o monoclinica), en función del contenido de lantano, temperatura y velocidad de enfriamiento.

Una vez aisladas e identificadas las diferentes fases puras se realiza una caracterización estructural utilizando todas las técnicas disponibles: XRPD, NPD y HRTEM-SAED.

- (i) La muestra cúbica se refinó por el método de Rietveld utilizando difracción de rayos-X de laboratorio (g.e. $Fm\bar{3}m$, $Z = 4$, $a = 5.6676(1) \text{ \AA}$, $V = 45.51 \text{ \AA}^3$) obteniéndose buenos valores de factores de acuerdo $R_{wp} = 6.9\%$ y $R_F = 3.2\%$. En esta estructura los átomos de La y Mo comparten la misma posición cristalográfica.

La estructura cúbica simple se confirma por HRTEM y SAED, y solamente, a lo largo de algunos ejes de zona, los patrones muestran tenues reflexiones satélite debido a pequeñas modulaciones estructurales por ligeras variaciones en el entramado de los átomos de oxígeno.

- (ii) El estudio de las estructuras romboédricas es mucho más complejo, puesto que no existe un modelo estructural de partida que permita realizar un refinamiento de Rietveld. Para caracterizar estructuralmente las fases $La_{5.4}MoO_{11.1}$ inicialmente se realizó un refinamiento por el método de Le Bail utilizando datos de difracción de rayos-X de laboratorio en el grupo espacial $R\bar{3}$ (que no tiene restricciones) para las estructuras R1 ($a = 3.99 \text{ \AA}$, $c = 9.87 \text{ \AA}$, $R_{wp} = 10.35\%$) y R2 ($a = 4.10 \text{ \AA}$, $c = 9.52 \text{ \AA}$, $R_{wp} = 9.39\%$). Los resultados son aceptables; sin embargo, tanto en R1 como en R2 se observan picos no indexados que no corresponden a fases secundarias y que se pueden asociar a la presencia de superestructuras. Mediante HRTEM-SAED se identifican dos superestructuras $7a \times 7a \times c$ para R1 y otra $5a \times 5a \times c$ para R2 que se correlacionan adecuadamente con las distancias interplanares y con los datos obtenidos por XRPD.

Debido a la enorme complejidad de la estructura, el presumiblemente elevado número de átomos en la celdilla unidad y de volumen de celda, todos los intentos de resolver la estructura por metodología “*ab initio*” usando datos de difracción de rayos-X de laboratorio y/o de neutrones resultan infructuosos. Para realizar la resolución estructural se recurrió al formalismo del superespacio (teoría de De Wolff, Janner A. *et. al.*, 1983) utilizando imágenes HRTEM-SAED en colaboración con el profesor Gianguido Baldinozzi de la Universidad Paris-Saclay. Con esta metodología se obtienen unas posiciones atómicas preliminares de las superceldas $7a \times 7a \times c$ y $5a \times 5a \times c$ transformando la estructura de la fluorita en un subgrupo trigonal $R\bar{3}$ a la que se aplican diferentes vectores de modulación. A continuación, las posiciones atómicas deducidas teóricamente se utilizan como modelo de partida para realizar un refinamiento de Rietveld con datos de difracción de neutrones obteniéndose buenos resultados: R1 (g.e. $R\bar{3}m$, $Z = 3$, $a = 27.9510(9)\text{Å}$, $c = 9.8998(9)\text{Å}$, $V = 6698.1(9)\text{Å}^3$, $R_{wp} = 4.09\%$, $R_F = 3.56\%$, fórmula experimental: $\text{La}_{5.48}\text{MoO}_{11.265}$ y densidad cristalografica = $5.834\text{ g}\cdot\text{cm}^{-3}$) y R2 (g.e. $R\bar{3}m$, $Z = 3$, $a = 20.4941(5)\text{Å}$, $c = 9.5183(5)\text{Å}$, $V = 3463.1(8)\text{Å}^3$, $R_{wp} = 6.52\%$, $R_F = 3.84\%$, fórmula experimental: $\text{La}_{5.52}\text{MoO}_{11.7}$ y densidad cristalográfica = $5.793\text{ g}\cdot\text{cm}^{-3}$). La validez de los modelos estructurales se confirma por su similitud con la fórmula nominal ($\text{La}_{5.4}\text{MoO}_{11.1}$), con los de la densidad experimental ($R1 = 5.811(3)\text{ g}\cdot\text{cm}^{-3}$, $R2 = 5.717(7)\text{ g}\cdot\text{cm}^{-3}$) y por los valores razonables de distancias de enlace. Ambas estructuras tienen entornos de coordinación del lantano y molibdeno cúbicos que justifican la interconversión a alta temperatura.

- (iii) La estructura monoclinica de La_4MoO_9 se refinó con datos de difracción de rayos-X de laboratorio utilizando como modelo de partida la estructura descrita por Dan Vu *et al.*, 2019 para $\text{La}_{34}\text{Mo}_8\text{O}_{75}$ obteniéndose buenos resultados: g.e. $C12/m1$, $Z = 1$, $a = 17.0611(1)\text{Å}$, $b = 12.2095(1)\text{Å}$, $c = 9.7479(1)\text{Å}$, $V = 45.54(1)\text{Å}^3$, $R_{wp} = 6.42\%$ y $R_F = 9.19\%$. Los resultados del refinamiento son aceptables con buenos

valores de factores de acuerdo, a pesar de que se trata de una estructura compleja con 7 posiciones cristalinas independientes para el La y una coordinación piramidal para el Mo. Los estudios HRTEM-SAED descartan la existencia de un ordenamiento de átomos de oxígeno a larga distancia que dé lugar a una superestructura.

Las muestras obtenidas por *quenching*, $\text{La}_{6-x}\text{MoO}_{12-\delta}$, $x = 0.6, 1, 1.5, 2$ se caracterizaron por XRPD y HRTEM-SAED. De forma general se observa un ligero incremento del volumen al disminuir el contenido en La (desde 45.51 hasta 45.58 Å³) como consecuencia del efecto conjunto de dos factores: por un lado, la disminución del contenido de lantano que contrae la estructura; y, por otra parte, la disminución del contenido de oxígeno que debilita el entramado y expande la celda. Las muestras con un contenido en lantano $x = 1.5$ y 2, $\text{La}_{4.5}\text{MoO}_{10.12}$ y La_4MoO_9 obtenidas enfriando a 5 °C·min⁻¹, parecen cúbicas monofásicas por XRPD, pero al estudiarse por HRTEM-SAED se comprueba que en ellas cohabitan dominios cúbicos y romboédricos.

Una vez optimizadas las condiciones sintéticas del sistema $\text{La}_{6-x}\text{MoO}_{12-\delta}$ ($0 \leq x \leq 3$) se ha dopado aliovalentemente el entramado catiónico y/o aniónico para mejorar las propiedades. El dopaje se ha realizado en las 2 posiciones posibles, es decir, en la de los metales (La y Mo) y en la del oxígeno, tanto aislada como simultáneamente.

- (i) Dopaje en la posición del lantano, $\text{La}_{5.3}\text{A}_{0.1}\text{MoO}_{11.05}$ (A = Ca, Sr, Ba). Todos los intentos para obtener materiales monofásicos variando la temperatura (de 800 a 1500 °C) y velocidad de enfriamiento (*quenching*, 50 y 0.5 °C·min⁻¹) resultaron infructuosos segregándose óxidos, por ejemplo, La_2O_3 , $\text{La}_2\text{Ba}_4\text{O}_7$, BaMoO_4 cuya proporción se incrementa al aumentar el tamaño del catión.

- (ii) Dopaje en la posición del molibdeno, $\text{La}_{5.4}\text{Mo}_{0.9}\text{B}_{0.1}\text{O}_{11.05}$ (B = Ti, Zr, Nb). Los estudios sistemáticos realizados, variando la temperatura y velocidad de enfriamiento permiten obtener compuestos monofásicos para Ti y Nb. Las fases son romboédricas R1 para Ti (*quenching* y $50\text{ }^\circ\text{C}\cdot\text{min}^{-1}$) y Nb (50 y $0.5\text{ }^\circ\text{C}\cdot\text{min}^{-1}$); resultando cúbicas únicamente cuando se dopa con Nb y se enfrían súbitamente. Dado que el dopaje con Ti y Zr no estabiliza ninguna fase cúbica bajo estas condiciones experimentales el estudio se centró en analizar el rango de existencia y la influencia del contenido en Nb en la estructura y propiedades eléctricas (ver siguiente apartado).
- (iii) Dopaje con niobio, $\text{La}_{5.4}\text{Mo}_{1-x}\text{Nb}_x\text{O}_{11.1-x/2}$ ($0 \leq x \leq 0.25$). Los mejores resultados del dopaje catiónico se obtienen para esta familia de materiales, resultando compuestos cúbicos y romboédricos R1 monofásicos para $x \leq 0.20$ cuando se enfrían mediante *quenching* o $50\text{ }^\circ\text{C}\cdot\text{min}^{-1}$, respectivamente. La fase romboédrica R2 deja de ser estable al enfriar a $0.5\text{ }^\circ\text{C}\cdot\text{min}^{-1}$, obteniéndose solo una fase R1 pura² para el caso $x = 0.1$. Las imágenes HRTEM-SAED confirman una superestructura $7a \times 7a \times c$ en todos los casos. La variación de los parámetros de red en estos compuestos sigue la Ley de Vegard observándose una disminución homogénea y monótona debido al menor tamaño del Nb^{5+} (0.71 \AA) en comparación con el La^{3+} (1.16 \AA) y Mo^{6+} (1.02 \AA) en la misma coordinación. Refinamientos combinados de rayos-X de laboratorio y neutrones de tiempo de vuelo de las fases cúbicas confirman el modelo estructural propuesto obteniéndose una mayor concentración de vacantes de oxígeno al aumentar el contenido de Nb.

²Posteriormente a la publicación, se pudo comprobar que la introducción de Nb en la estructura estabiliza la fase R1 enfriando como mínimo a una velocidad de $5\text{ }^\circ\text{C}\cdot\text{min}^{-1}$, lo que demuestra el efecto beneficioso de este catión.

(iv) Fluoración, $\text{La}_{5.4}\text{Mo}_{1-x}\text{B}_x\text{O}_{12-y/2-\delta}\text{F}_y$ ($x = 0, 0.1$; $y = 0, 1, 3, 6$; $B = \text{Ti, Zr, Nb}$). Como es bien sabido, la sustitución de oxígeno por otros elementos puede producir una modificación en la estructura y propiedades de los materiales. La fluoración se realizó mediante reacción en estado sólido de los precursores a $360\text{ }^\circ\text{C}$ con PVDF debido a su simplicidad y a los buenos resultados obtenidos en compuestos relacionados.

En primer lugar, se optimizó el contenido en flúor en los materiales sin dopaje catiónico resultando un mayor efecto estabilizador cuando el contenido de flúor es $y = 3$.

Respecto a la influencia de la velocidad de enfriamiento se obtiene preferentemente la fase R1, excepto si se utiliza un enfriamiento súbito, que da lugar a una estructura tipo fluorita. Una vez demostrado el efecto beneficioso del flúor, el estudio se amplió a los materiales con dopaje catiónico, utilizando las condiciones previamente optimizadas y variando la temperatura de sinterización entre 1200 y $1500\text{ }^\circ\text{C}$.

En los difractogramas se puede observar que las muestras calentadas a $1300\text{-}1500\text{ }^\circ\text{C}$ 1h tienen estructura R1 sin segregaciones de fases, en lugar de las no fluoradas. Las muestras calentadas a $1200\text{ }^\circ\text{C}$, los dopados con Ti presentan mezcla de fases secundarias de LaOF y $\text{La}_3\text{Mo}_2\text{O}_{10}$ y las dopadas con Zr tienen estructura R1 con segregados La_2MoO_6 . Sin embargo, los materiales con Nb cambian su estructura con mezcla R1 y R2 con segregados de La_2O_3 , a una estructura cubica monofásica.

A $1200\text{ }^\circ\text{C}$, solo las muestras con Nb son cúbicas monofásicas, mientras que entre $1300\text{-}1400$ todas son R1. Al igual que en todos los casos anteriores, estas simetrías están confirmadas con imágenes HRTEM-SAED. Se realizó un estudio estructural más detallado de las muestras dopadas. Se confirmó por Le Bail que los molibdatos de lantano dopados con Ti y Nb tienen estructura romboédrica con grupo espacial $R\bar{3}$ característica de la estructura R1 como ocurría con las muestras sin dopar.

También, se observa una disminución del tamaño de celda con la sustitución en la posición del molibdeno con respecto a las muestras sin dopar, algo que era de esperar ya que se sustituye el Mo^{6+} (1.02Å) por elementos como el Ti^{4+} (0.74Å), Zr^{4+} (0.84Å) y Nb^{5+} (0.74Å) que tienen menores valores de radio iónico. Cabe destacar que, aunque Ti^{4+} y Nb^{5+} tienen el mismo tamaño de radio iónico, las estructuras obtenidas no tienen el mismo volumen de celda, esto es debido a que la sustitución aliovalente de Mo^{6+} por Ti^{4+} da lugar a la formación de una vacante de ion oxido por mol de dopante.

Por otra parte, la estructura cubica obtenida para la muestra enfriada por quenching y dopada con Nb se estudió por un refinamiento combinado de Rietveld de XRPD y NPD de tiempo de vuelo, usando una estructura tipo fluorita con grupo espacial $Fm\bar{3}m$ como modelo inicial. Se refinaron todos los parámetros y se obtuvieron buenos valores de factores de acuerdo. Además, puede observarse la tendencia de la disminución del volumen de celda unidad con la entrada de más Nb en la estructura. Esto se explica ya que a más sustitución de Mo^{6+} por Nb^{5+} , se generan más vacantes ion oxido en el entramado aniónico.

Mediante cromatografía iónica se pudo comprobar que al aumentar la temperatura se produce una pérdida de flúor por evaporación de forma que a 1500 °C el contenido de flúor está por debajo del límite de detección de la técnica. Mediante un refinamiento combinado de rayos-X y de neutrones se confirmó la sustitución de los átomos de oxígeno por flúor ya que se produce una ligera expansión de la celda (de 45.35(1) sin flúor a 46.28(1) Å³ con flúor) debido a las mayores repulsiones electrostáticas del entramado aniónico que puede demostrarse por el aumento de la distancia interatómica O(F)-O(F) (de 2.83(1) sin flúor a 2.85(1) Å con flúor) y de los factores de ocupación (de 0.732(3) sin flúor a 0.767(2) con flúor).

Todas las estructuras obtenidas por las muestras dopadas se analizaron también por SAED y HRTEM para confirmar también por esta vía que cristalizan en cada estructura. Estos análisis clarifican que las

estructuras R1 estabilizadas por el dopaje con Nb y F son realmente R1, ya que presentan la superestructura característica $7a \times 7a \times c$, y que la estructura obtenida con el dopaje doble Nb y F calentada a 1200 °C es realmente cubica.

La microestructura y tamaño de grano de los materiales monofásicos se estudió por microscopía electrónica de barrido (SEM) en forma de pastillas sinterizadas. En general todos los materiales presentan una densidad muy elevada, con una porosidad prácticamente despreciable y sin fases secundarias en las fronteras de grano. Para las composiciones sin dopar, $\text{La}_{6-x}\text{MoO}_{12-\delta}$ ($0.4 \leq x \leq 2$), se observó una disminución del tamaño de grano al aumentar el contenido de lantano, donde los valores decrecen de 19.2 a 15.8 μm para las composiciones La_4MoO_9 y $\text{La}_{5.4}\text{MoO}_{11.1}$, respectivamente, ambas enfriadas mediante *quenching* desde 1500 °C. Por otro lado, condiciones de enfriamiento más lentas conducen a tamaños de grano superiores debido al mayor tiempo de residencia del material a alta temperatura, permitiendo que el grano crezca más. Así, la composición $\text{La}_{5.4}\text{MoO}_{11.1}$ enfriada a $0.5 \text{ }^\circ\text{C min}^{-1}$ presenta un tamaño de grano medio de 21.2 μm . Para las composiciones con modificaciones en su entramado iónico, se aprecia en general un aumento del tamaño de grano medio con el dopaje, por ejemplo, de 15.8 a 33.5 μm para las composiciones $\text{La}_{5.4}\text{MoO}_{11.1}$ y $\text{La}_{5.4}\text{Mo}_{0.90}\text{Nb}_{0.10}\text{O}_{11}$, respectivamente, ambas enfriadas mediante *quenching* desde 1500 °C. Por último, las muestras se analizaron también mediante espectroscopía dispersiva de rayos-X (EDS), confirmando la homogeneidad catiónica de todos los materiales y la ausencia de fases secundarias.

Finalmente, las propiedades eléctricas de los materiales se estudiaron en forma de pastillas sinterizadas mediante espectroscopía de impedancias en diferentes atmósferas (N_2 seco y húmedo y 5% H_2 -Ar húmedo), para analizar

las diferentes contribuciones a la conductividad total: iónica, electrónica y protónica. En la Tabla 2, se resumen los valores de conductividad de las muestras estudiadas. Todas las composiciones (sin dopar o dopadas) muestran gráficos de Nyquist muy similares, con dos contribuciones: una debida al interior del grano, y otra a los procesos de electrodo, con capacidades del orden de los $\sim\text{pF}\cdot\text{cm}^{-1}$ y $\sim\mu\text{F}\cdot\text{cm}^{-1}$, respectivamente. Este comportamiento se debe al elevado tamaño de grano de los materiales y a la ausencia de fases secundarias.

Tabla 2. Conductividades obtenidas para las muestras más representativas* que se han estudiado en esta tesis doctoral medidas en atmosfera de N_2 seco y húmedo y en 5% H_2 -Ar húmedo a $700\text{ }^\circ\text{C}$.

Muestras	N_2 seco ($\text{mS}\cdot\text{cm}^{-1}$) $\sigma_{700\text{ }^\circ\text{C}}$	N_2 húmedo ($\text{mS}\cdot\text{cm}^{-1}$) $\sigma_{700\text{ }^\circ\text{C}}$	5% H_2-Ar húmedo ($\text{mS}\cdot\text{cm}^{-1}$) $\sigma_{700\text{ }^\circ\text{C}}$
La_{5,4}1500-Q	$1.7\cdot 10^{-1}$	$2.5\cdot 10^{-1}$	5.0
La_{5,4}1500-50	$7.1\cdot 10^{-2}$	$1.4\cdot 10^{-1}$	$4.5\cdot 10^{-1}$
La_{5,4}1500-0.5	$9.0\cdot 10^{-2}$	$1.8\cdot 10^{-1}$	$4.5\cdot 10^{-1}$
La_{4,0}1500-Q	$1.4\cdot 10^{-1}$	$1.5\cdot 10^{-1}$	9.5
La_{4,0}1500-5	$1.3\cdot 10^{-2}$	$4.6\cdot 10^{-2}$	6.0
La_{4,0}1500-0.5	$1.8\cdot 10^{-1}$	$2.6\cdot 10^{-1}$	1.6
Nb_{0,10}1500-Q	$4.4\cdot 10^{-1}$	$5.1\cdot 10^{-2}$	5.1
Nb_{0,10}1500-50	$2.1\cdot 10^{-1}$	$2.9\cdot 10^{-1}$	6.4
Nb_{0,10}1500-0.5	$8.8\cdot 10^{-2}$	$1.5\cdot 10^{-1}$	6.2
La_{5,4}1500-F₃	-	-	5.2
Nb_{0,10}1500-F₃	$2.1\cdot 10^{-2}$	$4.1\cdot 10^{-2}$	5.1
Nb_{0,10}1200-F₃	-	-	2.3

*Las muestras fluoradas no se midieron en atmosferas de N_2 .

La representación de los datos de conductividad frente a la temperatura en formato tipo Arrhenius desvela para todas las composiciones una importante contribución protónica a la conductividad en atmósferas húmedas, especialmente por debajo de 650 °C. A temperaturas superiores esta contribución se pierde y la movilidad iónica se encuentra dominada por la de ion óxido. Este comportamiento se refleja en los valores de energías de activación, que disminuyen de ~1.05 a 0.80 eV en atmósferas de N₂ seco y húmedo, respectivamente.

Para las composiciones no dopadas, La_{6-x}MoO_{12-δ} (0.6 ≤ x ≤ 2), en atmósferas de N₂, ya sea seco o húmedo, se observa una disminución de la conductividad para menores contenidos de lantano, con valores de 2.5·10⁻¹, 1.9·10⁻¹ y 1.5·10⁻¹ mS·cm⁻¹, para La_{5.4}MoO_{11.1}, La_{4.5}MoO_{9.75} y La₄MoO₉, respectivamente, todas enfriadas mediante *quenching* desde 1500 °C, a 700 °C en N₂ húmedo. Esto es debido a que el excesivo número de vacantes de ion óxido generado al disminuir el contenido de lantano dificulta el movimiento de los iones óxidos y los protones por los canales de conducción iónicos. También es importante mencionar que, para una misma composición, pero con diferentes simetrías, aspecto controlable con las condiciones de preparación, las muestras con mayor simetría siempre presentan los mejores valores de conductividad.

Por otro lado, las composiciones dopadas catiónicamente, La_{5.4}Mo_{0.9}B_{0.1}O_{11.1-δ} (B = Ti, Zr, Nb), presentan un aumento de la conductividad iónica, determinadas en atmósferas de N₂, debido al hecho de que la sustitución aliovalente de Mo⁶⁺ por cationes con menor estado de oxidación conlleva a la generación de vacantes de ion óxido y a una mejora de la movilidad de éste. Esto se puede ver claramente para La_{5.4}MoO_{11.1} y La_{5.4}Mo_{0.9}Nb_{0.1}O_{11.05}, ambos obtenidos mediante *quenching* desde 1500 °C,

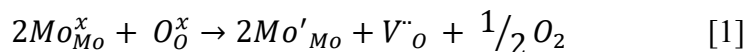
donde los valores de conductividad se doblan desde $2.5 \cdot 10^{-1}$ a $5.1 \cdot 10^{-1} \text{ mS} \cdot \text{cm}^{-1}$ a $700 \text{ }^\circ\text{C}$ en N_2 húmedo.

Por otra parte, se realizó el estudio de la influencia del dopaje de flúor en la conductividad observándose el mismo comportamiento frente a atmosferas húmedas y secas y con la temperatura. Así, para la misma composición que se ha comentado anteriormente, $\text{La}_{5.4}\text{Mo}_{0.9}\text{Nb}_{0.1}\text{O}_{11.05}$, se observa una disminución de la conductividad de la muestra fluorada respecto a la sin fluorar, de 0.21 a 0.01 mS cm^{-1} , a $700 \text{ }^\circ\text{C}$ en N_2 seco. Destacar también que las energías de activación aumentan con la fluoración, de 0.81 a 1.07 eV . Esto es debido al llenado de las vacantes de ion óxido por átomos de flúor (por cada átomo de oxígeno entran dos de flúor), lo que dificulta el movimiento de iones óxido por la pérdida de vacantes. Pero la entrada de flúor en los materiales disminuye la conductividad, debido a un aumento de la energía de activación del sistema debido a la ocupación de las vacantes ion oxido por fluoruros que disminuye la cantidad de huecos oxido, lo que dificulta el transporte de iones oxido a través del entramado aniónico.

Estos corroboran dichos efectos y también demuestran que el dopaje de Zr y Ti no incrementan la conductividad tanto como lo hace el dopaje con Nb. El fluoruro, aunque puede estabilizar incluso la estructura cubica para la muestra dopada con Nb a baja temperatura, el que este material este preparado a únicamente $1200 \text{ }^\circ\text{C}$ disminuye drásticamente sus valores de conductividad porque el material es muy poroso. El estudio de la conductividad en función del pO_2 resulta en los mismos resultados que las muestras sin dopar, teniéndose contribución mayoritaria tipo-n en condiciones reductoras y tipo-p en condiciones oxidantes.

Finalmente, en condiciones muy reductoras (atmósfera de $5\% \text{ H}_2\text{-Ar}$ húmedo), para todas las muestras se observa un aumento muy importante de

la conductividad debido a una contribución electrónica a la conductividad tipo n, causada por la reducción de Mo^{6+} a Mo^{5+} , según la siguiente ecuación redox:



En condiciones reductoras, para muestras preparadas en las mismas condiciones, los valores de conductividad aumentan al disminuir el contenido de lantano. Por ejemplo, para $\text{La}_{5.4}\text{MoO}_{11.1}$, $\text{La}_{4.5}\text{MoO}_{9.75}$ y La_4MoO_9 , todas enfriadas mediante *quenching* desde 1500 °C, los valores de conductividad son 5.0, 7.5 y 9.5 $\text{mS}\cdot\text{cm}^{-1}$, a 700 °C en 5% H_2 -Ar húmedo. También se observa una disminución de las energías de activación, con valores de 0.72, 0.55 y 0.51 eV, respectivamente. Esto es debido a que al reducir la relación La/Mo se produce, como se comentó anteriormente, una disminución de los volúmenes de celda, lo que se hace que los átomos de molibdeno están más cerca unos de otros, facilitando los saltos electrónicos y aumentando la conductividad de este tipo.

Finalmente, se puede afirmar que estos materiales son prometedores para aplicarlos como membranas de separación de hidrógeno. Por lo que se realizó un estudio de las prestaciones de algunos de estos materiales, demostrando que son estables en las condiciones de trabajo. Sin embargo, se obtuvieron valores de permeación de hidrógeno demasiado bajos, siendo necesario realizar un estudio más en profundidad en el futuro.

1. INTRODUCTION.

1.1. Classic energy sources and their effect on the global climate.

The Industrial Revolution in the XVIII century brought one of the greatest economic, social, and technological transformations in society. This revolution revolved around carbon, used as the principal fuel, developing new technologies such as the railway and steamboat.

These transport technologies were the origin of the mechanization of production, the competition between companies and to a more aggressive exploitation of natural resources. This economy has remained and generates an enormous quantity of waste and contamination, which is modifying the climate, weather patterns and causing extreme events.

The perspectives for the future hold no good. Energy consumption will duplicate by 2050 and, if the actual tendency is not changed, the consequences will be irreversible (Figure 1.1).

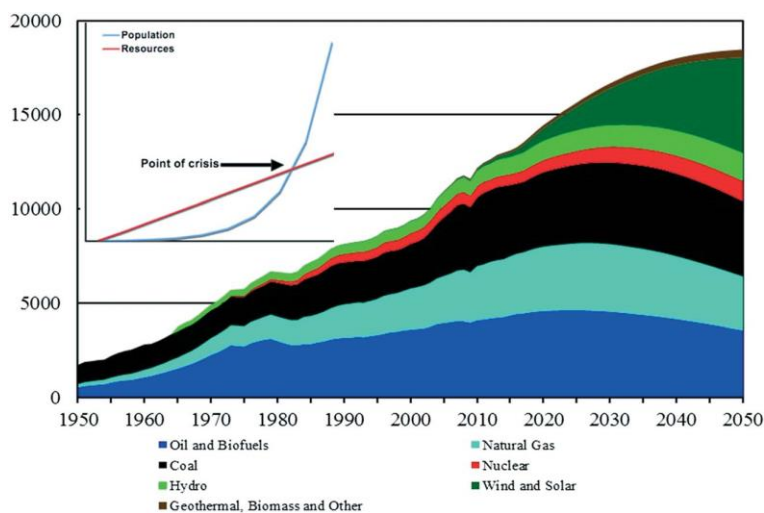


Figure 1.1. World primary energy consumption (million tons of oil equivalent 1950-2050) (Environment, Energy, Sustainability: Journal- ES Energy & Environment, Qinglong J. *et al.*, 2018).

Global warming implies serious climatic problems that modify the habitats of millions of different species and could lead to their extinction. This global warming also will generate a significant number of extreme meteorological phenomena in many zones as well as an increase in natural disasters like tornados, fires, and floods (Figure 1.2). For example, the temperature increase will cause wildfires in forests and droughts (at the end of the century the average temperature will increase by 3 degrees). High temperatures will also produce the thaw of the poles and increase the thermal expansion of water, rising the sea level up to 2 meters, flooding coast zones. At the same time, the thaw will liberate gases such as CH₄ and CO₂ from permafrost, increasing the seawater acidity.

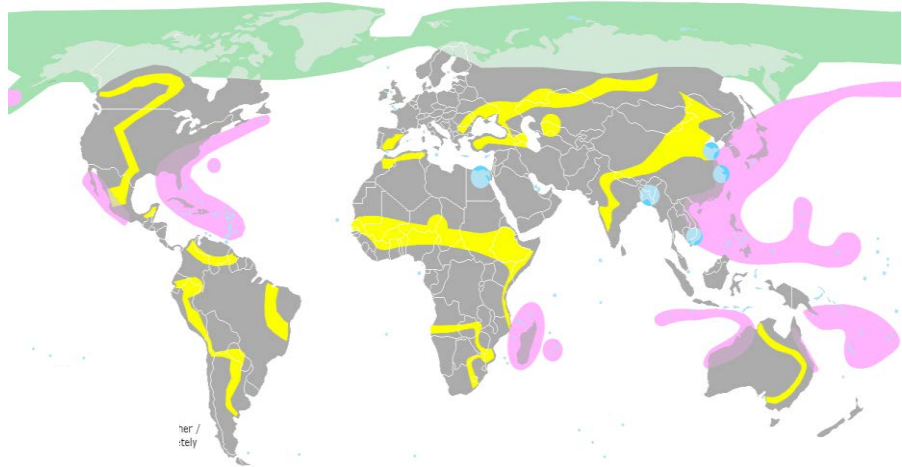


Figure 1.2. Regions where natural disasters will occur caused by climate change. In pink hurricanes, in yellow desertification or drought, and in blue floods that will submerge these zones (KVDP, Natural disasters caused by climate change, Creative Commons Wikipedia 2015).

The economic and social impact will be enormous, causing starving and food problems (that will be more drastic in a world with overpopulation), and changes in the frontiers of countries for the rising of the sea level. At the same

time, it will produce more conflicts for the lack of resources, increasing tensions between countries, and more social differences.

To prevent that future, science and technology are focused on improving the efficiency of the current energy generation methods (based on fossil fuels), the development of processes for the obtention of clean energy, or the substitution of fossil fuels by others that do not produce harmful emissions.

Furthermore, some technologies could substitute fossil fuels, for example, wind and solar energy (inexhaustible sources), which produce clean energy, and that do not generate waste. However, they need support from governments, companies, and society to face the enormous environmental problems.

Under the Paris Agreement (2016), 195 countries set a target to keep average global temperature change below 2 °C and as close as possible to 1.5 °C. Before the Glasgow Climate Change Conference the planet was headed to a dangerous rise of 2.7 °C of the temperature (COP26, <https://ukcop26.org/>). Based on new announcements made during the Conference, experts estimate that we are now on a path to between 1.8 °C and 2.4 °C. Countries have now agreed to revisit their commitments, as necessary, by the end of 2022 to put us on track for 1.5 °C of warming, maintaining the ambitions of the Paris Agreement. To deliver on these promises, COP26 also agreed for the first time to accelerate efforts towards the phase-down of unabated coal power and inefficient fossil fuel subsidies and recognized the need for support towards a just transition.

COP26 also completed the technical negotiations on the so-called Paris Agreement Rulebook, which fixes the transparency and reporting

requirements for all parties to track progress against their emission reduction targets. The Rulebook also includes the Article 6 mechanisms, which set out the functioning of international carbon markets to support further global cooperation on emission reductions.

On climate finances, the agreed text commits developed countries to double the collective share of adaptation finance within the \$100 billion annual targets for 2021-2025. Parties also commit to a process to agree on long-term climate finance beyond 2025. The COP also decided to establish a dialogue between parties, stakeholders, and relevant organizations to support efforts to avert, minimize and address losses and damages associated with climate change.

1.2. Hydrogen, the possible solution.

One of the most promising and clean energy sources is hydrogen (H₂). Its oxidation releases water vapor and generates a large amount of energy 241 kJ·gr⁻¹ (higher than the 45.5 kJ·gr⁻¹ produced by diesel). The use of this type of fuel would drastically change the current situation. In addition, it has been shown by numerous studies (BMW company, 2013; Ho *et al.*, 2011; Ji *et al.*, 2013; Niknam *et al.*, 2013; Sorensen *et al.*, 2007; Wang *et al.*, 2013) that the use of H₂ as fuel is completely plausible and can be used to replace current engines and power generators with fossil fuels. Therefore, they can be applied in vehicles of all types (from cars to submarines, Figure 1.3) and the energy storage or extra generators.

Fuel cell electric technology explained

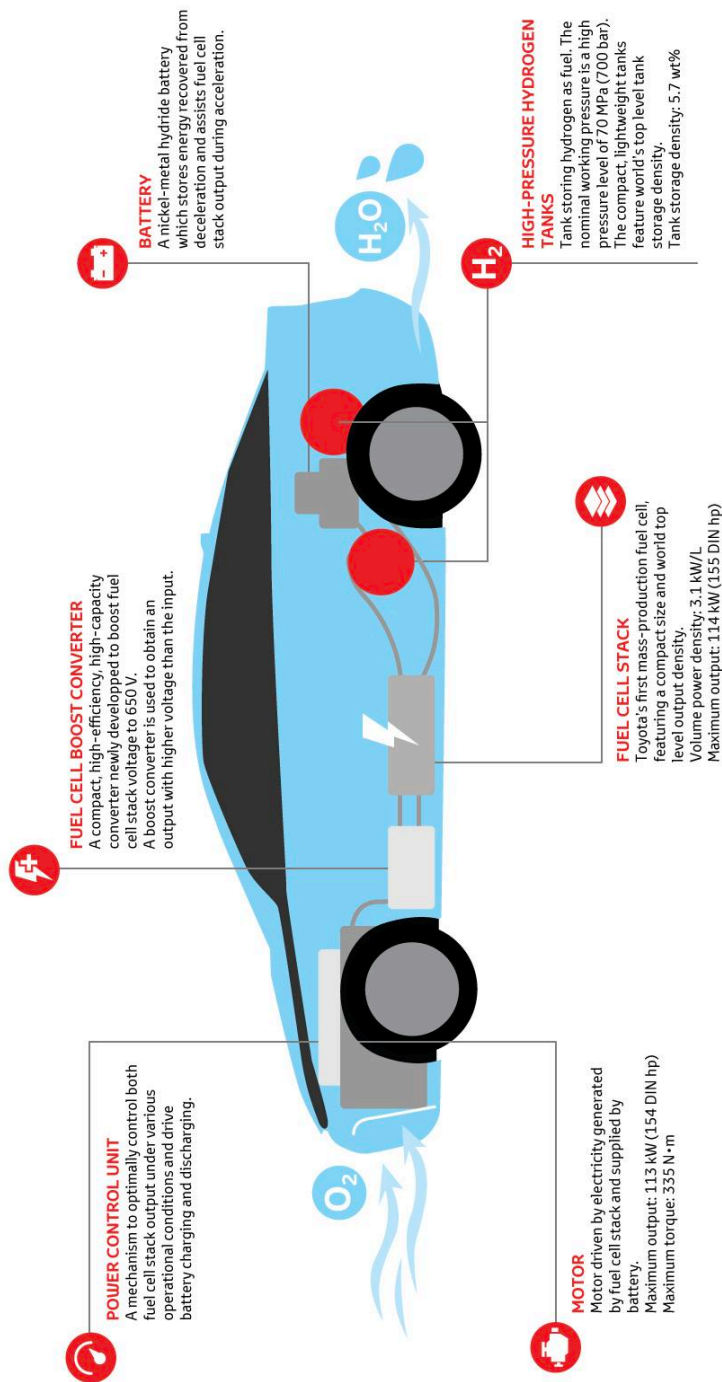
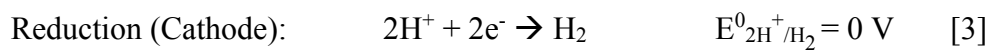
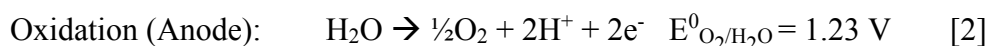


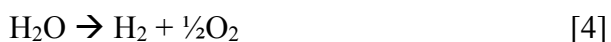
Figure 1.3. Scheme of hydrogen fuel cell car functioning (Toyota® Mirai operating principles, 2015).

Hydrogen (H₂) can be obtained either by the electrolysis of water (I) or by fossil fuel reforming (II) (Bolland, 2003; Penner *et al.*, 2006; Riter *et al.*, 2007; Speight, 2019).

I) Water electrolysis is a process that split H₂O into hydrogen and oxygen, produced in a cell consisting of an anode and a cathode separated by an electrolyte (such as Nafion[®]). The reactions involved in the process are:



The global reaction in ideal conditions needs to apply 1.23 V of energy, because the process is non-spontaneous.



Real water electrolyzers require higher voltages for the reaction to proceed. The energy that exceeds 1.23 V is called overpotential or overvoltage and represents any kind of loss and nonideality in the electrochemical process. Usually, the higher overpotential is for the four-electron oxidation of water to oxygen at the anode, using Pt as the electrode.

II) Nowadays, the easiest and cheapest process to obtain hydrogen is the reforming of fossil fuels. However, this produces other gases such as CO₂, CO, O₂, H₂O, SO_x, and NO_x, which need to be separated from H₂.

The steam reforming reaction involved is:



Currently, the hydrogen separation is performed with the pressure swing adsorption technique (PSA, Figure 1.4). This process consists of a closed system with controllable pressure that forces gases to be adsorbed

using different materials such as activated carbon, silica gel, alumina, or zeolites, which separates gases at high pressures and room temperature. Also, this process is used in the production of ammonia or hypoxic air technology, also known as an oxygen reduction system (ORS), which reduces the concentration of oxygen in protected rooms to minimize the risk of fires. However, PSA has some drawbacks such as high energy consumption and the need to maintain high pressure to perform the gas separation.

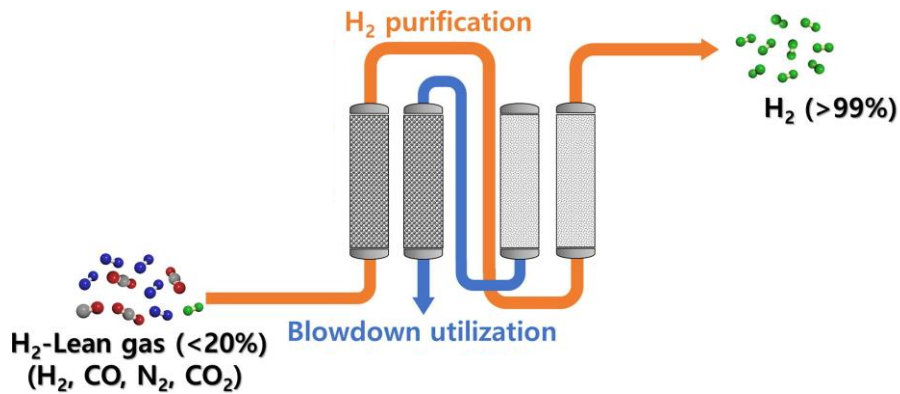


Figure 1.4. Pressure Swing Adsorption (PSA) system scheme (Modified with permission from Elsevier, Park, *et al.*, Copyright 2021).

To overcome these problems alternative technologies has been developed such the hydrogen separation membranes, with great energy efficiency and without the need to generate high pressures, making the process less expensive.

1.3. Perspectives on developing proton-electron conducting ceramic materials.

In recent years, scientists have produced extensive efforts to develop proton-electron conducting ceramic materials and their associated membranes for H₂ separation, which allows the purification of the hydrogen by applying the reaction:



Only protons and electrons pass through the membrane and will recombine on the other side. However, several challenges must be overcome before commercialization, including the improvement of those properties that now are insufficient:

1. Chemical stability of the materials in acidic gas atmospheres at high temperatures.
2. Proton and electron conductivities of the materials for high H₂ fluxes.
3. H₂ dissociation/reassociation reaction rates at the membrane surfaces.
4. Mechanical strength and durability for long-term operation.
5. Thermal stability for long-term operation.
6. Fundamental understanding of material/membrane performance and degradation.

The conductivity of the membrane is also important, pure proton-conducting materials cannot be used as hydrogen separation membrane because have insufficient electron conduction, and it is necessary to apply across the membrane an auxiliary external electrical circuit that creates a hydrogen chemical gradient to drive the flow of hydrogen. Membrane materials with mixed electron and proton conductivity will be more effective due to the migration of electrons and protons through the membrane to

recombine on the other side which makes possible to carry out the process in a non-galvanic mode without using an external electrical circuit.

Overcoming these challenges could finish in the final commercialization of these membranes. Evidence of the interest in these materials is the great number of researchers working on this task for the last two decades (approximately more than 7000 articles in Web of Science).

1.4. Principles of H₂ separation in ceramic membranes.

Understanding the process of hydrogen separation is essential to improving the performance of materials and membranes. In this section, the principles of the H₂ separation process and the exploitation of these in current devices will be discussed.

1.4.1. Hydrogen separation process.

The H₂ separation process using a dense proton-electron conducting ceramic membrane under a concentration gradient is schematically illustrated in Figure 1.5.

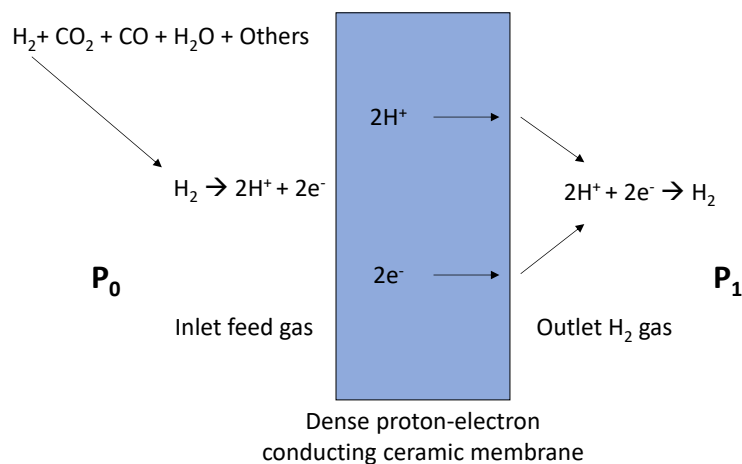


Figure. 1.5. Scheme of H₂ separation process using a dense proton-electron conducting ceramic membrane.

In this membrane, H₂ moves from the high partial pressure side (P₀) to the low partial pressure side (P₁). The process of H₂ separation through this membrane mainly involves three steps: 1) H₂ is first adsorbed into the surface of dense proton-electron conducting ceramic membranes, then dissociates into proton and electrons; 2) protons and electrons diffuse together to the other side of the membrane surface; 3) protons and electrons recombine to form molecular H₂ again (Shusil, *et al.*, 2006; Phair *et al.*, 2006). To obtain a practical H₂ separation rate, both surfaces of the membrane should have catalytic effects for H₂ dissociation and reassociation.

As mentioned above, the process of hydrogen permeation is controlled by two processes: the surface process and bulk diffusion. If the permeation process is controlled by bulk membrane transport, decreasing the thickness of the membrane can boost the transport rate; if it is controlled by the surface process, modifying the membrane surface may increase the hydrogen permeation flux. For example, it was reported that the hydrogen permeation flux increased significantly when a Pd-modified surface was used on a Ni-BCY membrane, due to the excellent ability of Pd to catalyse the H₂ dissociation (Zhang *et al.*, 2002).

For the bulk controlled process, the transport of protons through the membrane is the rate-determining step if the electron conductivity is much higher than the proton conductivity. According to the chemical/electrochemical potentials and conductivities of both protons and electrons within the membrane, the H₂ flux (j_{H₂}) during the separation process can be written as this equation:

$$j_{H_2} = \frac{RT}{4F^2L} \frac{\sigma_{H^+} \cdot \sigma_{el}}{\sigma_{H^+} + \sigma_{el}} \ln \left(\frac{P_0}{P_1} \right) \quad [7]$$

This is the Wagner equation, where R is the universal gas constant, T is temperature, F is the Faraday constant, L is the thickness of the ceramic membrane, σ_{H^+} is the proton conductivity within the membrane, σ_{el} is the sum of electron and hole conductivities, P_0 is the H_2 pressure at the inlet gas chamber as was indicated in Figure 1.5, and P_1 is the H_2 pressure at the outlet H_2 gas chamber. Note that σ_{H^+} and σ_{el} are both independent of hydrogen pressure in this equation.

Equation [7] shows that the hydrogen flux is inversely proportional to the thickness of the membrane, therefore, a high hydrogen flux can be obtained by reducing its thickness, thereby lowering the bulk diffusion resistance. This can be done by supporting a thin proton-electron conducting ceramic membrane onto an inert porous support using various technical methods, such as co-pressing (Zhu Z.W. *et al.*, 2012; Escolástico *et al.*, 2011), spin coating (Hamawaka *et al.*, 2002), dip coating, spray coating, sputtering, sol-gel methods, pulsed laser deposition (PLD) and chemical vapor deposition (CVD) (Verweij, 2003).

From [7] it can also be seen that the H_2 flux is controlled by the proton and electron conductivities, the temperature, and the hydrogen pressure on both sides of the membrane. Also, increasing the temperature and pressure at the inlet gas side and pressure at the outlet gas side can effectively improve the H_2 flux. If the proton conductivity within the membrane is much smaller than the electron conductivity, that is, $\sigma_{H^+} \ll \sigma_{el}$, [7] can be rewritten as:

$$j_{H_2} = \frac{RT}{4F^2L} \sigma_{H^+} \ln\left(\frac{P_0}{P_1}\right) \quad [8]$$

In this case, developing highly conductive proton-conducting ceramic membranes is important for achieving a high H_2 flux, although doing so is challenging with the current state of technology. If the proton conductivity

within the membrane is much larger than the electron conductivity ($\sigma_{H^+} \ll \sigma_{el}$), [8] can be rewritten as:

$$j_{H_2} = \frac{RT}{4F^2L} \sigma_{el} \ln\left(\frac{P_0}{P_1}\right) \quad [9]$$

In this case, developing ceramic membranes with dense proton-electron conducting ceramic membrane becomes critical in achieving a high H₂ flux during the separation process. Normally, it is hard to obtain both high proton and high electron conductivities, although some attempts have been reported (Song *et al.*, 2004).

1.4.2. Theoretical understanding of H₂ transport mechanisms.

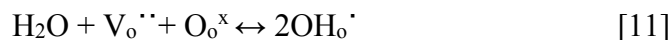
The major driving force behind H₂ transport within a dense proton-electron conductor ceramic membrane is the pressure difference across the membrane. The difference can induce a Nernstian potential (E) across the membrane, according to the following equation (Roark *et al.*, 2002):

$$E = \frac{RT}{nF} \ln\left(\frac{P_1}{P_0}\right) \quad [10]$$

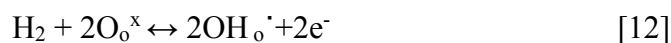
Where R, T, P₀, and P₁ have the same meaning as in [7] and n is the electron number in the H₂ dissociation/reassociation reaction (H₂ ↔ 2H⁺ + 2e⁻), equal to 2. The value of this potential is in the range of 50-500 mV, depending on the temperature and H₂ pressure difference across the membrane. Under this potential difference, the dissociated protons and electrons move from the inlet gas side to the outlet gas side, and the transport rate is determined by the magnitude of the potential difference.

During H₂ dissociation/reassociation at the ceramic membrane surfaces, the oxygen vacancy and the oxygen anion sites inside the surface oxide materials play a critical role (Phair *et al.*, 2006). Normally, the feed gas

mixture contains moisture; the oxygen vacancies, expressed in the literature as $V_o^{\cdot\cdot}$, will react with water to fill the lattice positions with oxide ions (expressed as O_o^x), forming proton-retaining oxide ions (also called proton charge carriers, expressed as OH_o^{\cdot}) at normal lattice sites:



That reaction indicates that more oxygen vacancies in the crystal structure of oxides will induce more proton-retaining oxide ions, leading to a higher proton conductivity. This equation also indicates the importance of water in proton conductivity. Furthermore, H_2 in the inlet feed gas can also directly react with the oxide ions to produce proton-retaining oxide ions:



Where OH_o^{\cdot} is the major intermediate for proton conduction within the membrane, under the driving force of a potential difference. It is generally accepted that the proton inside the OH_o^{\cdot} species can transfer between oxygen ions in the normal position, producing proton conductivity (Norby *et al.*, 1996).

1.5. Perspectives and development of dense proton-electron ceramic materials.

As discussed above, developing dense proton-electron conducting ceramic materials and their associated membranes is key to obtaining a high-performance H_2 separation technology. To achieve this goal, it is necessary to address the synthesis, characterization, and performance to improve and optimize the proton-electron conductivity, and chemical and mechanical stability, maintaining at the same time a low cost (Tao *et al.*, 2015). In the

next sections, the principal materials for hydrogen separation materials are discussed.

1.5.1. Perovskite-type structure materials: Synthesis, characterization and membrane performance.

This section will present materials for membrane applications with a perovskite structure. On one hand, single-phase ceramics materials based on SrCeO_3 show proton conductivity at high temperatures. One of the compositions studied was a $\text{SrCe}_{0.95}\text{Y}_{0.05}\text{O}_{3-\delta}$ (SCY)-based membrane, with a hydrogen permeation flux of $0.04 \text{ mL}\cdot\text{cm}^{-2}\cdot\text{min}^{-1}$ in a membrane of 1.5 mm at $900 \text{ }^\circ\text{C}$ obtaining a lower value than the estimated by proton conductivity measurements (Guan *et al.*, 1998). The difference between calculated and observed permeation rates was attributed to interfacial polarization, being necessary to improve the conductivity and interfacial properties of these materials.

Other samples studied were $\text{SrCe}_{1-x}\text{M}_x\text{O}_{3-\delta}$ based proton-conducting perovskites, where $M = \text{Eu}, \text{Tm}, \text{or Sm}$ (Song *et al.*, 2004; Qi *et al.*, 2000). The introduction of an element with a variable oxidation number can increase electron conductivity and modify the hydrogen permeability depending on the type and ionization potential of dopants. $\text{SrCe}_{0.95}\text{Eu}_{0.05}\text{O}_{3-\delta}$ has a higher hydrogen permeability than $\text{SrCe}_{0.95}\text{Sm}_{0.05}\text{O}_{3-\delta}$ in all conditions. The most remarkable value is for the Eu-doped sample with $0.017 \text{ mL}\cdot\text{cm}^{-2}\cdot\text{min}^{-1}$, higher than the permeability of $0.012 \text{ mL}\cdot\text{cm}^{-2}\cdot\text{min}^{-1}$ for Sm-doped material under dry hydrogen at $850 \text{ }^\circ\text{C}$ with membranes of 1.6 mm thickness (Song *et al.*, 2003). Also, a 5% Tm-doped material was studied and showed that the electron hopping mechanism played the dominant role, and the charge transfer between two neighbouring ions of different valences could result in

an increase of the electron conduction with values of $0.17 \text{ mL}\cdot\text{cm}^{-2}\cdot\text{min}^{-1}$ at $900 \text{ }^\circ\text{C}$ with 5% H_2 -He as gas inlet and membranes with 1.5 mm of thickness.

On the other hand, other materials of interest are single-phase ceramics materials based on BaCeO_3 , which also present high proton conductivity at high temperatures. To improve the electron conductivity of perovskite oxides, the materials were doped with different cations, increasing the hydrogen flux due to a higher ambipolar diffusion associated with hole conduction. For example, $\text{BaCe}_{0.9}\text{Mn}_{0.1}\text{O}_{3-\delta}$ produces a hydrogen permeation flux of $0.009 \text{ mL}\cdot\text{cm}^{-2}\cdot\text{min}^{-1}$ and $\text{BaCe}_{0.95}\text{Nd}_{0.05}\text{O}_{3-\delta}$ a flux of $0.016 \text{ mL}\cdot\text{cm}^{-2}\cdot\text{min}^{-1}$, both at $900 \text{ }^\circ\text{C}$ using 15 vol.% hydrogen as feed gas (Cai *et al.*, 2009).

Another possibility is the introduction of transition metals, like Zr, as a partial substitute for Ce in Y-doped BaCeO_3 , as can be seen in Figure 1.6, these doping can slightly improve the hydrogen permeation performance of proton-conducting $\text{BaZr}_{0.3}\text{Ce}_{0.6}\text{Y}_{0.1}\text{Zn}_{0.05}\text{O}_3$ (BZCYZn) perovskite membranes (Zhang *et al.*, 2014).

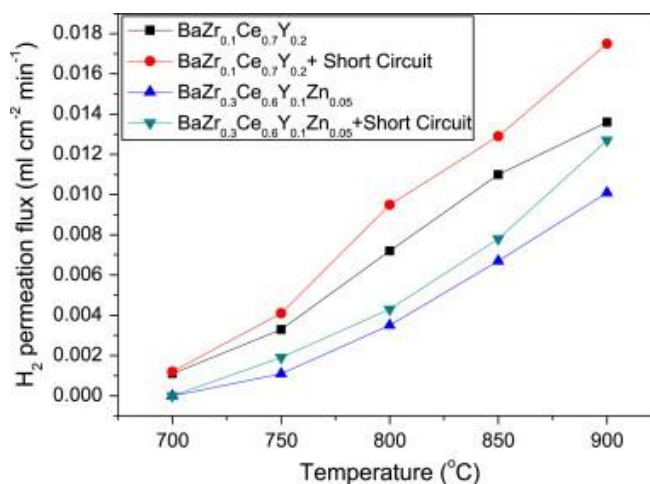


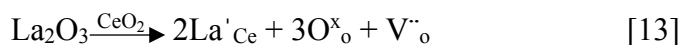
Figure 1.6. BZCY and BZCYZn permeation studies at different temperatures. The materials were studied also by shelf-short-circuited (applying external electrical power) to provide electron conduction that is low in these materials, improving the hydrogen permeation flux. (Reprinted with permission from Elsevier, Zhang *et al.* Copyright 2014).

Adding water vapor to the sweep gas led to a slight increase in H₂ permeation fluxes for both membranes, most likely because the water vapor facilitated hydrogen adsorption and/or an association process. The values obtained were 0.013 mL·cm⁻²·min⁻¹ for BZCY and 0.009 mL·cm⁻²·min⁻¹ for BZCYZn at 900°C.

One of the most important problems of these materials is their low stability in CO₂ and CO, both produced in the reforming of fossil fuels due to Sr and Ba being basic ions that react easily with these gases. Therefore, it is necessary to study more materials to improve their stability in acid currents generated in the H₂ obtention process and maximize electron conductivity by optimizing the doping level and element.

1.5.2. Fluorite-type structure materials: Synthesis, characterization and membrane performance.

Oxides with fluorite-type structures can increase the hydrogen conductivity by doping. For example, La-doping in CeO₂ increases the hydrogen permeation flux to values of 0.042 mL·min⁻¹·cm⁻² at 850 °C in ceramic membranes (Zhu *et al.*, 2012) due to oxide vacancies generation:



According to this reaction, doping with a high concentration of La into the CeO₂ structure will increase the oxygen vacancy. But a vacancy content too high would decrease the mobility of the oxygen ions in the structure and reduce the oxygen conductivity. However, the experimental results showed the increase of proton conductivity with an increment of lanthanum doping reaching a maximum at 0.5, decreasing by adding more La. This was probably due to the blocking effect of La₂O₃.

In addition, other lanthanides can modify the conductivity of the materials. For example, Sm-doped materials, $\text{Ce}_{0.8}\text{Sm}_{0.2}\text{O}_{1.9}$, reach conductivities higher than $0.1 \text{ S}\cdot\text{cm}^{-1}$ at $600 \text{ }^\circ\text{C}$ (Ding *et al.*, 2010). Usually, these materials have been used for oxygen separation membranes and intermediate-temperature solid oxide fuel cells (Ding *et al.*, 2008 and 2009; Yi *et al.*, 2006; Wang D. *et al.*, 2006) because of present low proton conductivity. Doped $\text{Ce}_{0.8}\text{Yb}_{0.2}\text{O}_{2-\delta}$ had a proton conductivity of only about $10^{-6} \text{ S}\cdot\text{cm}^{-1}$ at $800 \text{ }^\circ\text{C}$, which is higher than the proton conductivity of single-crystal YSZ with values of $10^{-8} \text{ S}\cdot\text{cm}^{-1}$ (Nigara *et al.*, 2000, 2003 and 2004).

This type of fluorite-structure material seems to have low proton conductivity for H_2 separation membranes. Therefore, structural modifications are necessary. A study discovered that $\text{La}_{1.95}\text{Ca}_{0.05}\text{Ce}_2\text{O}_{6.975}$ has a fluorite structure, showing an excellent electron conductivity (about $1.0\text{-}1.5 \text{ S}\cdot\text{cm}^{-1}$ at 800°C) and good values of proton conductivity ($\sim 0.2 \text{ S}\cdot\text{cm}^{-1}$ at 800°C) as shown in Figure 1.7 (Wang J.D. *et al.*, 2005). Also, it was found that $\text{Ce}_{0.8}\text{Sm}_{0.2}\text{O}_{2-\delta}$ (SDC) had a considerable hydrogen permeation flux as a hydrogen separation membrane, $0.192 \text{ mL}\cdot\text{min}^{-1}\cdot\text{cm}^{-2}$ in an 80% $\text{H}_2\text{-N}_2$ atmosphere at $800 \text{ }^\circ\text{C}$ (Sun *et al.*, 2013).

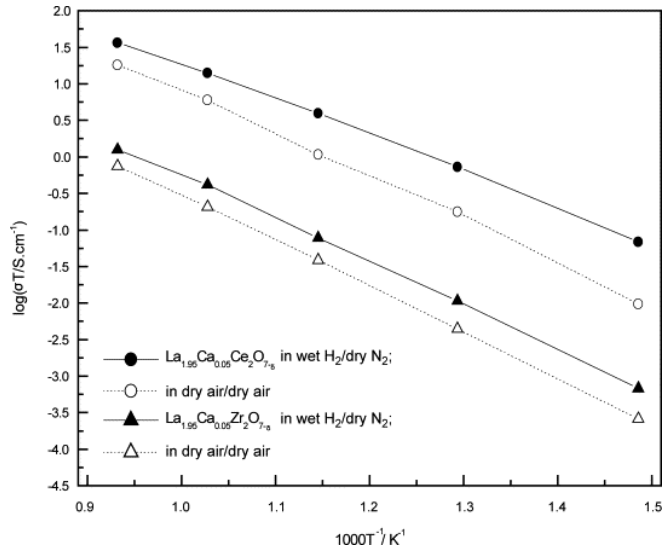


Figure 1.7. Electron conductivity of $\text{La}_{1.95}\text{Ca}_{0.05}\text{Ce}_2\text{O}_{6.975}$ and $\text{La}_{1.95}\text{Ca}_{0.05}\text{Zr}_2\text{O}_{6.975}$ under different atmospheres. (Reprinted with permission from Elsevier, Wang J.D. *et al.* Copyright 2005).

1.5.3. Tungstate-based materials: Synthesis, characterization and membrane performance.

Rare-earth tungstates $\text{Ln}_6\text{WO}_{12-\delta}$ ($\text{Ln} = \text{La}, \text{Nd}, \text{Sm}, \text{etc.}$) are promising materials for H_2 separation membranes at high temperatures and solid oxide fuel cell electrolytes due to their sufficient mixed conductivity and stability in CO_2 and sulphur-containing environments. To determine the applicability of these materials, the conductivity of the $\text{Ln}_{6-x}\text{WO}_{12}$ series was studied and is shown in Figure 1.8.

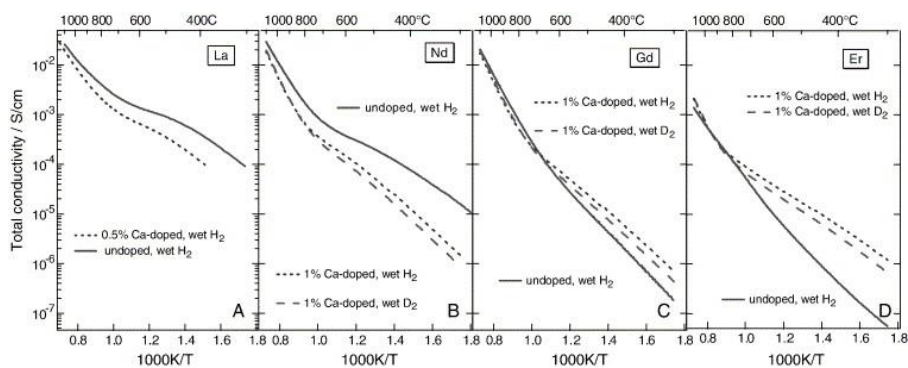


Figure 1.8. Total conductivity of $\text{Ln}_6\text{WO}_{12}$ ($\text{Ln} = \text{La}, \text{Nd}, \text{Gd}, \text{and Er}$) measured in wet H_2 . (Modified with permission from Elsevier, Haugsrud, Copyright 2007).

The conductivity decreases with the Ln ionic radius in the order of $\text{La} > \text{Nd} > \text{Sm} > \text{Gd}$ due to a decrease in crystal symmetry from cubic, tetragonal and rhombohedral as the ionic radius of rare-earth becomes smaller, being lanthanum tungstate the most conductor with a conductivity of $7.5 \cdot 10^{-4} \text{ S} \cdot \text{cm}^{-1}$ at $750 \text{ }^\circ\text{C}$ in wet air (Escolástico *et al.*, 2009; Shimura *et al.*, 2001; Haugsrud *et al.*, 2007).

To understand deeply the $\text{La}_{6-x}\text{WO}_{12-\delta}$ behaviour, the phase diagram of the $\text{La}_2\text{O}_3\text{-WO}_3$ system was studied (Figure 1.9) showing that the ratio 3:1 phase ($\text{La}_6\text{WO}_{12}$) prepared by the ceramic method, is a material that needs high synthesis temperatures to be obtained, between 1750 and $1960 \text{ }^\circ\text{C}$ (Haugsrud *et al.*, 2007). Furthermore, it is possible to modify the lanthanum content to generate vacancies that can influence the final structure and electrical properties of the materials.

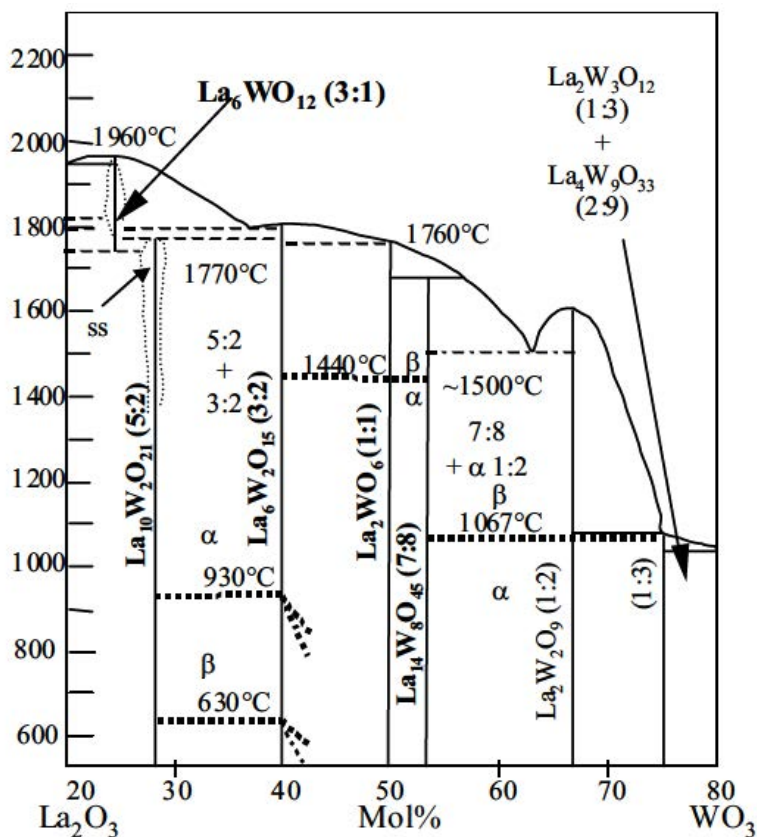


Figure 1.9. Phase diagram of La₂O₃-WO₃ (Extracted with permission from Elsevier, Yoshimura *et al.* Copyright 1976). Arrow indicates the La/W = 6 ratio that appears between 1750 and 1960 °C.

Lanthanum tungstates with La/W ratios between 4.8 (~5:2, La₁₀W₂O₂₁) and 6.0 (3:1, La₆WO₁₂) were prepared by the freeze-drying method obtaining cubic fluorite structures for all of them. However, single phases only could be obtained for ratios between 5.3 and 5.7 at a sintering temperature of 1500 °C (Magrasó *et al.*, 2009). For La/W ratios lower than 5.3 the samples are not monophasic, with segregations of La₆W₂O₁₅. For ratios higher than 5.7, La₂O₃ segregates as secondary phase, as can be seen in Figure 1.10.

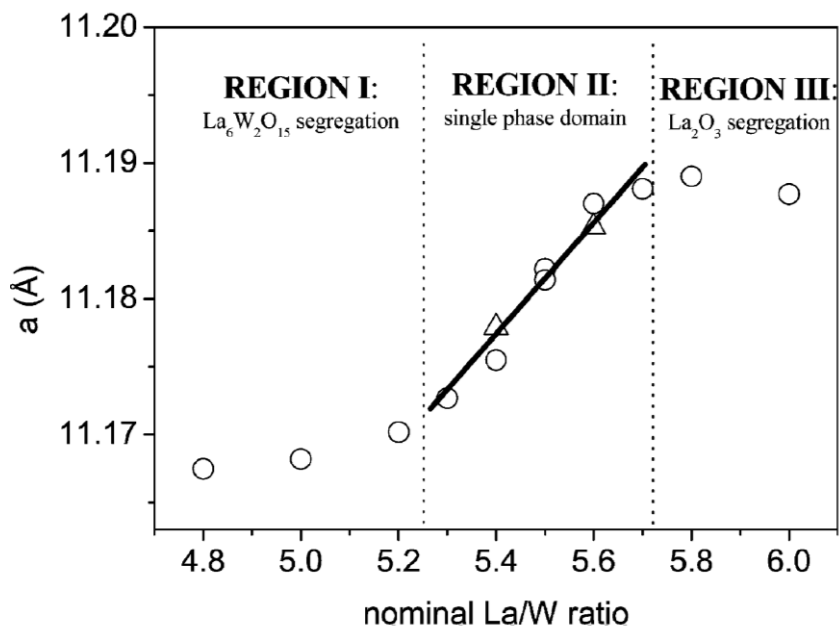


Figure 1.10. Variation of lattice parameters obtained by XRPD as a function of nominal La/W ratio after calcination at 1500 °C (Added with permission from Royal Society of Chemistry, Magrasó *et al.* Copyright 2009).

La_{5.6}WO_{11.4} was structurally studied, due to the unexpected influence of the ratio La/Mo the density of the samples measured by He-pycnometry. The density of single-phase materials has to be independent of composition, but this did not happen with different La/W relations. The structural study was performed by combining direct methods and Fourier analysis of XRPD and NPD data in the $F\bar{4}3m$ cubic space group.

The data obtained by the structural characterization studies allow to create a structural model that is shown in Figure 1.11.

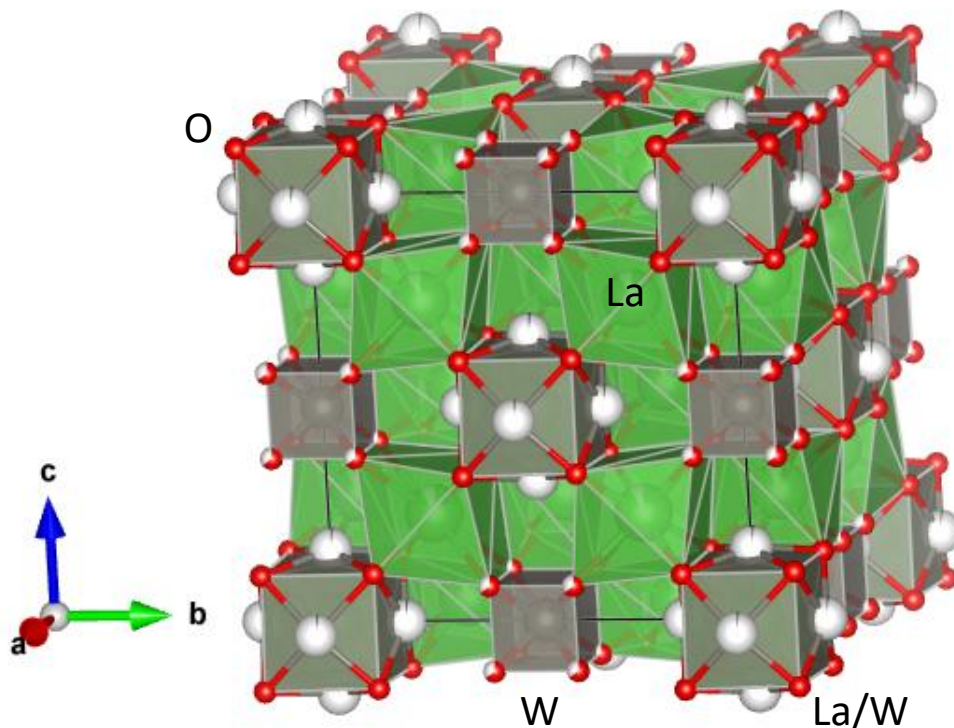


Figure 1.11. Structure of $\text{La}_{28-y}\text{W}_{4+y}\text{O}_{54+\delta}$ (for $y = 1$), La is represented with green spheres, and W is represented with grey spheres and their coordination environment with grey polyhedron (Based of American Journal Society, Magrasó *et al.* Copyright 2012).

In this structure, W sites ($4b$) are fully occupied, and they are surrounded by eight oxygen sites that are partially filled. The average coordination of W ($4b$) is 5.2. In addition, La ions ($4a$) are also coordinated with eight oxygen sites having the eight positions fully occupied, while for La ($24f$), only half of these sites are occupied. The effective coordination for La ($24f$) is 6.6 and it has a more distorted environment compared to La ($4a$). The concentration of oxygen vacancies in this material is 11.2 per unit cell, ~ 3 positions per formula unit. However, to reduce the number of vacancies to about $\frac{1}{2}$ per unit cell, approximately one W is positioned in La ($24f$) sites per

formula unit as donor dopant, $W_{La}^{\cdot\cdot}$. The overall stoichiometry of these materials is $La_{28-x}W_{4+x}O_{54+\delta}\square_{2-\delta}$ ($\delta = 3x/2$).

The conduction mechanism of $La_{5.6}WO_{11.4}$ is dependent on the temperature, due to dehydration at 800 °C. At 600-700 °C, the ionic conductivity is higher, making the materials suitable for SOFC applications. But at 1000 °C, the proton conductivity is lost by dehydration, enhancing the electronic conductivity, so the material is suitable for hydrogen separation membranes application at intermediate temperatures (Magrasó *et al.*, 2014).

In later works, $La_{5.5}WO_{12-\delta}$ was tested for separation membrane applications with a $0.136 \text{ mL}\cdot\text{min}^{-1}\cdot\text{cm}^{-2}$ hydrogen permeation flux at 1000 °C and high stability (≈ 400 hours) in CO_2 , H_2S , CO , and H_2 atmospheres (Escolástico *et al.*, 2013a). Looking to improve the performance of these materials, the cationic doping in the La and W-sites was studied, to increase the ionic and protonic conductivity.

1.6. Doping of lanthanide tungstate.

In 2010, a patent claimed the use of mixed conductive oxides based on $Ln_6WO_{12.31}$ reporting higher conductivities and H_2 flux levels for several substituted or doped compounds. The range of compounds covered is $(Ln_{1-x}A_x)_6(W_{1-y}B_y)_zO_{12-\delta}$ being $Ln = La, Pr, Nd, Sm$, $A = La, Ce, Pr, Nd, Eu, Gd, Tb, Er, Yb, Ca, Mg, Sr, Ba, Th, In, Pb$, $B = Mo, Re, U, Cr, Nb$, $0 \leq x \leq 0.7$, $0 \leq y \leq 0.5$, x or $y > 0$, $1 \leq z \leq 1.25$, and $0 \leq \delta \leq 0.3$ (Serra *et al.*, 2010).

1.6.1. Effect of doping on the lanthanum site.

To improve the electrical properties of lanthanum tungstates, doping was tested with Zr and Nd on the lanthanum position. These materials are monophasic with a fluorite-type structure, but doping did not increase the

conductivity with values of $2 \cdot 10^{-3}$, $8 \cdot 10^{-4}$, and $5 \cdot 10^{-3}$ $\text{S} \cdot \text{cm}^{-1}$ for $\text{La}_{5.8}\text{WO}_{11.7}$ (undoped), $\text{La}_{5.45}\text{Zr}_{0.35}\text{WO}_{11.9}$ and $\text{La}_{5.22}\text{Nd}_{0.58}\text{WO}_{11.7}$, respectively, at 800 °C in wet H_2 (Shimura *et al.*, 2001).

Also, doping with Ca, Ba and Sr was studied. The $\text{La}_{5.45-x}\text{M}_x\text{WO}_{12-\delta}\square_{2-\delta}$ ($\text{M} = \text{Ca}, \text{Ba}$ and Sr ; $0 \leq x \leq 0.2$) series were studied by XRPD and all samples presented a fluorite-type structure. This doping also led to the generation of oxygen vacancies, with the exception of Ba^{2+} , which is not incorporated into the structure. Although, it is shown that doping with low contents of the cations ($x < 0.1$) improves the conductivity of these materials. The maximum value of conductivity is obtained for $\text{La}_{5.425}\text{Sr}_{0.025}\text{WO}_{12-\delta}\square_{2-\delta}$ under wet N_2 at 500 °C ($1.3 \cdot 10^{-3}$ $\text{S} \cdot \text{cm}^{-1}$), and the minimum value for $\text{La}_{5.3}\text{Ca}_{0.15}\text{WO}_{12-\delta}\square_{2-\delta}$ under dry N_2 at 500 °C ($0.52 \cdot 10^{-3}$ $\text{S} \cdot \text{cm}^{-1}$). However, if the doping is higher than 0.1 ($x > 0.1$) the conductivity decreases due to a proton trapping mechanism that makes their mobility more difficult. (Zayas-Rey *et al.*, 2014).

Finally, other dopants like Ce, Nd, Tb, and Y were tested in the lanthanum site. These dopants decrease the conductivity or modify the crystalline structure of the tungstates and were not further studied. The poor improvement in the electrical properties by doping in lanthanum sites shifted the focus to substitution in the tungsten site (Seeger *et al.*, 2013).

1.6.2. Effect of doping on tungsten site.

The substitution of tungsten with other cations results in changes in the electrical properties. For example, 20 % substitution with Re in $\text{La}_6\text{WO}_{12}$ led to an improvement in their conductivity values of $1.63 \cdot 10^{-3}$ $\text{S} \cdot \text{cm}^{-1}$ versus the undoped material with values of $7.5 \cdot 10^{-4}$ $\text{S} \cdot \text{cm}^{-1}$ at 600 °C in wet 5% H_2 -Ar (Seeger *et al.*, 2013).

Doping with Nb^{5+} in $\text{La}_{5.5}\text{W}_{1-x}\text{Nb}_x\text{O}_{12-\delta}$ enhances the conductivity one order of magnitude, from 0.004 for the undoped compound to $0.01 \text{ S}\cdot\text{cm}^{-1}$ for a sample with a 10% in Nb, at 800 °C in 5% H_2 -Ar (Zayas-Rey *et al.*, 2013). That increase is due to the aliovalent substitution of W^{6+} by Nb^{5+} and the generation of oxide vacancies that enhance the ionic conductivity.

Different studies prove that Mo-doping increase the electronic conductivity as the reducibility of Mo^{6+} is higher than that of W^{6+} . $\text{La}_{5.5}\text{W}_{1-x}\text{Mo}_x\text{O}_{12-\delta}$ with $x \leq 0.4$ crystallizes in a cubic structure, and for $x \geq 0.6$ in a rhombohedral structure. The study of the electrical properties indicated that the electronic conductivity increases without altering the protonic conductivity significantly. The ambipolar proton-electron conductivity has values of $1.6 \cdot 10^{-3} \text{ S}\cdot\text{cm}^{-1}$ with a substitution of 40% Mo ($\text{La}_{5.5}\text{W}_{0.6}\text{Mo}_{0.4}\text{O}_{12-\delta}$) at 600 °C and these values were stable over more than 60 h at 900 °C in wet reducing conditions (Amsif *et al.*, 2012).

On the other hand, a fuel testing was developed using the EMF method to extract proton-electron transport numbers, with values from 0.9 (900 °C) to 1 (500 °C) under oxidizing conditions for $\text{La}_{5.4}\text{WO}_{12-\delta}$ confirming that the main charge carriers are ions. Electron holes only contribute at high temperatures. The partial substitution of Mo (30%) in lanthanum tungstates, maintains the transport number but increases the electronic conductivity compared with $\text{La}_{5.4}\text{WO}_{12-\delta}$ (Figure 1.12). The measurements show a mixed proton-oxide ion-electron/electron-hole with values of $\sim 2\text{-}3 \cdot 10^{-3} \text{ S}\cdot\text{cm}^{-1}$ in wet 5% H_2 -Ar at 700 °C (Magrasó, 2013).

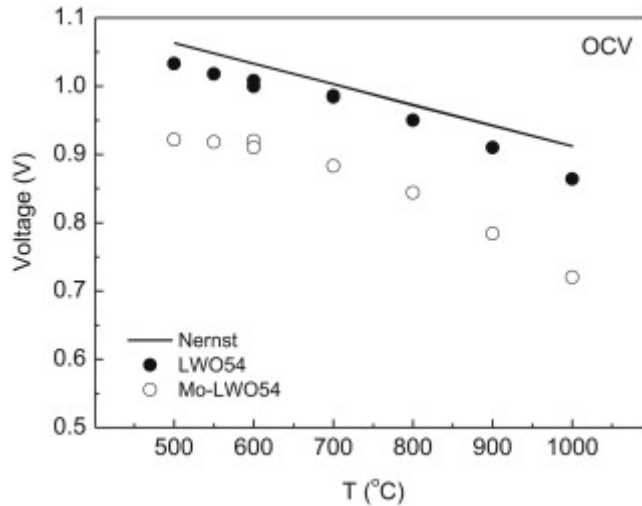


Figure 1.12. Open circuit voltage of a Pt/(Mo)La_{5.4}WO_{12-δ}//Pt fuel cell as a function of temperature. Gases: wet air (cathode) and wet 5% H₂-Ar (anode). (Modified with permission from Elsevier, Magrasó Copyright 2013).

Finally, the influence of doping with Mo was also tested in hydrogen separation experiments. La_{5.5}W_{0.3}Mo_{0.7}O_{7.55-δ} present values of 0.6·10⁻³ mL·min⁻¹·cm⁻² at 700 °C (Vøllestad *et al.*, 2014). The best results are for La_{5.5}W_{0.6}Mo_{0.4}O_{11.25-δ} with 0.195 mL·min⁻¹·cm⁻² at 1000 °C (Chen *et al.*, 2015).

1.6.3. Total substitution of tungsten with molybdenum in lanthanum tungstates.

Due to the improvement of electronic conductivity by the introduction of Mo in lanthanum tungstates, new materials were studied where W was completely substituted by Mo. In Figure 1.13 it is shown the La₂O₃-MoO₃ phase diagram (Cros *et al.* 1978).

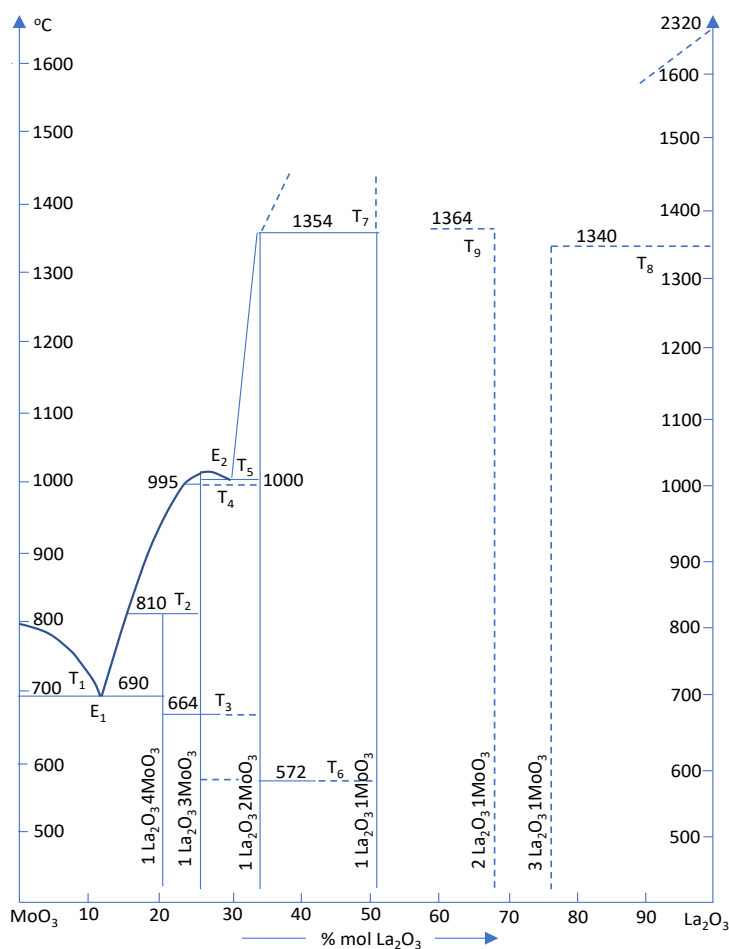


Figure 1.13. La₂O₃-MoO₃ phase diagram (Attached from Cross *et al.*, 1978).

As can be seen in the phase diagram, La₆MoO₁₂ is stable from room temperature to high temperatures, unlike La₆WO₁₂ which is thermodynamically unstable at room temperature.

The series Ln_{6-x}MoO_{12-δ} (x = 0, 0.5; Ln = La, Gd, Dy, Ho, Er, Tm, Yb, and Lu) was prepared by mechanical activation of their respective oxides followed by high-temperature synthesis (Shlyakhtina *et al.*, 2017A). At low temperatures, between 900-1100 °C, the ionic radii of Ln influence the final structure: fluorite, rhombohedral, bixbyite, or tetragonal, which is metastable.

Above 1200 °C, a mixture of bixbyite and rhombohedral phases is obtained. At high temperatures (1400-1600 °C), the rhombohedral structure is predominant for the bigger lanthanides but the stabilization of cubic structure as the size of the rare-earth decreases is observed. In general, the conductivity of materials decreases as the rare-earth radii decreases, being the most promising sample $\text{La}_{5.5}\text{MoO}_{11.25}$, with values of $2 \cdot 10^{-4} \text{ S} \cdot \text{cm}^{-1}$ at 600 °C in wet air. Although this material crystallizes with a fluorite structure at 900 °C, it is metastable, transiting to a rhombohedral phase at high temperatures and decreasing the conductivity. So, it is essential to obtain this structure at higher temperatures, to improve the conductivity of the materials (Shlyakhtina *et al.*, 2017A).

At the onset of this Thesis (2017), there was almost no knowledge of the materials belonging to this series, especially La. What follows is a summary of the best works published to present day.

$\text{La}_{5.5}\text{MoO}_{11.25}$ and $\text{Nd}_6\text{MoO}_{12}$ were studied in depth by HT-NPD. The analysis confirms that $\text{La}_{5.5}\text{MoO}_{11.25}$ evolves from rhombohedral to cubic on heating at 1270 °C, segregating La_2O_3 in the process. On cooling the sample returns to a rhombohedral symmetry. In addition, this material is stable in dry and wet conditions. On other hand, $\text{Nd}_6\text{MoO}_{12}$ evolves from rhombohedral to cubic at 1140 °C (Savvin *et al.*, 2018 and Shlyakhtina *et al.*, 2019).

$\text{Sm}_{6-x}\text{MoO}_{12-\delta}$ ($x = 0, 0.5$) were also prepared by mechanical activation, obtaining a fluorite-type structure for $\text{Sm}_6\text{MoO}_{12}$ after heating at 1600 °C for 3h, and a rhombohedral symmetry for $\text{Sm}_{5.5}\text{MoO}_{11.25}$ with same treatment. At lower sintering temperatures Sm_2O_3 segregates. The higher conductivity values are for the cubic $\text{Sm}_6\text{MoO}_{12}$, with $1.48 \cdot 10^{-3} \text{ S} \cdot \text{cm}^{-1}$ at 750°C in air. It was also observed that the proton conductivity decreases with temperature.

Doping strategies were also performed in the rare-earth position of these molybdates in order to stabilize the cubic phase and improve the electrical properties. The materials were doped with zirconium, $\text{Ln}_{6-x}\text{Zr}_x\text{MoO}_{12-\delta}$ ($x = 0.2, 0.6, \text{ and } 1$; $\text{Ln} = \text{La, Nd, Sm, and Dy}$) and prepared by mechanical activation at different sintering temperatures. At $1600\text{ }^\circ\text{C}$ 3h, the Zr stabilizes cubic structure instead of $R\bar{3}$. In addition, $\text{La}_{5.8}\text{Zr}_{0.2}\text{MoO}_{12-\delta}$, with a rhombohedral structure, presents reflections attributed to superstructures (Shlyakhtina *et al.*, 2016).

For $\text{Nd}_{5.4}\text{Zr}_{0.6}\text{MoO}_{12.3}$ the cubic structure is stable at all range studied and the cell parameters become smaller due to the partial reduction of Mo^{6+} and the disordering on the Ln/Mo sites. The reducibility of Nd and Mo also decreases the protonic conductivity (Shlyakhtina *et al.*, 2019).

In addition, $\text{Sm}_{5.4}\text{Zr}_{0.6}\text{MoO}_{12.3-\delta}$ and $\text{Sm}_5\text{Zr}_1\text{MoO}_{12-\delta}$ prepared by mechanical activation and sintered at $1600\text{ }^\circ\text{C}$ 3h present a fluorite structure, with total conductivities of $5 \cdot 10^{-4}\text{ S}\cdot\text{cm}^{-1}$ at $800\text{ }^\circ\text{C}$ in air for both. Although, at lower temperatures, $\text{Sm}_{5.4}\text{Zr}_{0.6}\text{MoO}_{12-\delta}$ has better electron conductivity due to the donor effect³. Also, the proton conductivity of the materials decreases for smaller cations (Savvin *et al.*, 2014 and 2015).

Finally, $\text{Ho}_{5.4}\text{Zr}_{0.6}\text{MoO}_{12.3}$ and $\text{Nd}_{5.4}\text{Zr}_{0.6}\text{MoO}_{12.3}$ were studied by HT-NPD. $\text{Ho}_{5.4}\text{Zr}_{0.6}\text{MoO}_{12.3}$ adopted a cubic structure from room temperature to $1400\text{ }^\circ\text{C}$. Although, $\text{Nd}_{5.4}\text{Zr}_{0.6}\text{MoO}_{12.3}$ present a mix of cubic and rhombohedral phases treated at same conditions (Savvin *et al.*, 2018).

³Donor effect: The introduction of a cation with higher oxidation state in a crystalline structure create the donor energy level. As energy gap between donor energy level and conduction band is very small, electrons can easily cross it and the conductivity of the n-type semiconductor is greatly improved.

In summary, an increase of the radius of lanthanides stabilizes the fluorite structure. In addition, Zr-doping also stabilizes the fluorite structure but decreases the conductivity. In Table 1.1, the structure and bulk conductivity of the different lanthanide molybdates studied are summarized.

Table 1.1. Selected lanthanide molybdates with their crystalline structures and conductivity. (Added with permission from Savvin *et al.* Copyright 2018 Elsevier.)

Composition	Structure	Bulk conductivity in wet air at 400 °C (S·cm⁻¹)
La_{5.5}MoO_{11.25}	Fluorite-like, rhombohedral	1·10 ⁻⁵
La_{5.8}Zr_{0.2}MoO_{12.1}	Fluorite-like, rhombohedral	6·10 ⁻⁶
Nd_{5.4}Zr_{0.6}MoO_{12.1}	Fluorite, 2 phases	7·10 ⁻⁶
Sm₆MoO₁₂	Fluorite	1·10 ⁻⁵
Sm_{5.4}Zr_{0.6}MoO_{12.3}	Fluorite	4·10 ⁻⁶
Dy_{5.4}Zr_{0.6}MoO_{12.3}	Fluorite	4·10 ⁻⁶
Ho_{5.4}Zr_{0.6}MoO_{12.3}	Fluorite	3·10 ⁻⁷
Yb₆MoO₁₂	Bixbyite	2·10 ⁻⁷

On the other hand, to avoid a high-temperature treatment the Nd₂O₃ content decreased, obtaining Nd₁₀Mo₂O₂₁ that has a complex rhombohedral structure without segregations with a mixed electronic/protonic conductivity. The conductivities of Nd₁₀Mo₂O₂₁ were 8.5·10⁻³ S·cm⁻¹ at 800 °C and 8·10⁻⁴ S·cm⁻¹ at 600 °C in wet air (Shlyakhtina *et al.*, 2019).

1.6.4. Influence of fluorine doping on the structural and electrical properties of materials.

The anionic framework can be modified to improve the structural and electrical properties of the materials and one of the most common strategies used is the substitution of oxygen for fluorine. The first studies dealt with the modification of Sr_2CuO_3 , a superconducting material with a transition temperature of 70 K at high-pressure conditions. By the introduction of fluorine (fluorination), this temperature can be modified to 46 K at ambient pressure (Al-Mamouri *et al.*, 1994).

Another example were materials such as Ba_2ZrO_4 and Sr_2TiO_4 . In these cases, the fluorination was performed using NH_4F at 250 °C, confirming that one oxygen can be substituted with two fluorine, increasing the anion content and expanding the unit cell and modifying the titanium environment for $\text{Sr}_2\text{TiO}_3\text{F}_2$ from an octahedral to a semi-pyramidal coordination. In addition, the use of poly (vinylidene fluoride) gives higher quality samples than other fluorinating agents (Slater, 2002).

The fluorination can also change the oxidation state of the materials, for instance, for $\text{SrFe}_{1-x}\text{Sn}_x\text{O}_{3-\delta}$ ($x = 0.31$ and 0.54), Fe^{4+} is reduced to Fe^{3+} after fluorination with CH_2CF_2 . (Berry *et al.*, 2009). In addition, $\text{SrFe}_{0.9}\text{Ti}_{0.1}\text{O}_{3-x}\text{F}_x$ ($x = 0.05$ and 0.10) were prepared by the sol-gel method, and studies confirms that anion doping is a feasible way to improve the transport numbers (Zhang *et al.*, 2017). Also, fluorine can enhance the oxygen transport without modifying the structure of materials, obtaining values of oxygen permeation of $\sim 1.2 \text{ mL} \cdot \text{min}^{-1} \cdot \text{cm}^{-2}$ for $\text{SrCo}_{0.9}\text{Nb}_{0.1}\text{O}_{3-\delta}\text{F}_{0.1}$ at 700 °C (Zhu J. *et al.*, 2016).

Fluorine doping was also tested with brownmillerite-type materials ($\text{Ba}_2\text{In}_2\text{O}_5$) and it was observed an improvement in the electrical properties after the incorporation of a low amount of fluorine. Total conductivities improved from $6 \cdot 10^{-5}$ to $4 \cdot 10^{-4} \text{ S} \cdot \text{cm}^{-1}$ for the fluorinated $\text{Ba}_{0.5}\text{In}_2\text{O}_{4.7}\text{F}_{0.3}$, at 700°C in wet air (Animitsa *et al.*, 2012 and 2018).

Finally, the fluorination of lanthanum tungstates was studied to improve their electrical properties. Materials with the formula $\text{La}_{5.5}\text{W}_{0.6}\text{Mo}_{0.4}\text{O}_{11.25-8}\text{F}_x$ ($x = 0, 0.02, 0.05, 0.1, 0.2, 0.5,$ and 1) were prepared by using LaF_3 as fluorinating agent in a traditional solid-state reaction method. The hydrogen permeability is enhanced from $0.10 \text{ mL} \cdot \text{min}^{-1} \cdot \text{cm}^{-2}$ for the undoped material to $0.16 \text{ mL} \cdot \text{min}^{-1} \cdot \text{cm}^{-2}$ for $\text{La}_{5.5}\text{W}_{0.6}\text{Mo}_{0.4}\text{O}_{11.25-8}\text{F}_{0.05}$ (Chen *et al.*, 2017). In addition, proton conductivity increases for the sample with 0.05 content in fluorine, from $1 \cdot 10^{-3} \text{ S} \cdot \text{cm}^{-1}$ for the undoped material, to $1.5 \cdot 10^{-3} \text{ S} \cdot \text{cm}^{-1}$ at 650°C . This conductivity contribution changes drastically at high temperatures due to the enhancement of the electronic conductivity obtaining similar conductivity values for both samples.

1.6.5. The fluorination process.

The fluorination with F_2 gas at high temperatures is not adequate due to the difficulty to control the amount incorporated into the structure. In addition, F_2 is a dangerous gas that can attack the reaction systems and be toxic to the users. Therefore, alternative fluorination methods were devised for inorganic materials. Table 1.2 shows a comparison between different fluorination agents.

Table 1.2. Different characteristics and problems of typical fluorination agents.

Fluorinating agent	Characteristic	Problems
F₂ gas	Fluorine insertion gives high oxidation states.	Toxicity and hard fluorination control.
NH₄F	Substitution maintaining oxidation state.	Tendency to form alkaline fluoride AF ₂ (A: alkaline earth) or rare-earth fluoride LnOF (Ln: rare earth) impurities.
XeF₂	Can give both fluorine substitution and insertion.	Need to employ sealed tubes and give the same impurities as NH ₄ F.
CuF₂, ZnF₂	Can give both fluorine substitution and insertion.	CuO and ZnO impurities

In general, these fluorinating agents present important toxicity and purification problems. This can be avoided by using organic products that can be burnt off during the fluorination process, improving the purification of materials. Perfluoropentane (C₅F₁₂), perfluorodecane (C₁₀F₂₂), and polyvinylidene fluoride (-(C₂H₂F₂)_n-, PVDF) are interesting because are solid at room temperature and in thermally stable with a large percentage of fluorine content. Different studies consider that poly (vinylidene fluoride) is the best fluorinating agent due to the minimization of impurities and simplicity of the process, which consists of adding PVDF to the sample at 360°C in a stoichiometric amount (Zhang *et al.*, 2001; Slater, 2002).

1.7. Materials and methods.

In this thesis, all the materials were prepared by the freeze-drying method which presents advantages in comparison to traditional solid-state synthesis methods such as high control of stoichiometry, particle size, homogeneity, and synthesis at low temperature that prevent the degradation of the materials.

1.7.1. Synthesis by the freeze-drying method.

The freeze-drying method has been used for many years to dehydrate in the pharmaceutical and food industry without the use of heating, to avoid the spoiling of the desired product.

The process consists in freezing with liquid nitrogen (-196 °C) an aqueous solution that contains cations in stoichiometric proportions and the presence of a complexing agent and removing the solvent by vacuum sublimation at low temperature, obtaining a homogeneous material. Experimentally, this process is performed in a Scanvac® Coolsave™ 110-4Pro freeze-dryer (Figure 1.14).



Figure 1.14. Scanvac® Coolsave™ 110-4Pro freeze-dryer used in samples preparation.

Each cation solution, in stoichiometric proportions, was prepared in different ways:

- **La, Ca, Sr and Ba.** The solutions were prepared by dissolving La_2O_3 (99.99% Aldrich), CaCO_3 (99%, Alfa Aesar), SrCO_3 (99.99%, Alfa Aesar), and BaCO_3 (99%, Alfa Aesar), in diluted HNO_3 (1:1). La_2O_3 needs to be previously calcinated to 1000 °C 1h to dehydrate and decarbonate.
- **Mo.** The solution was prepared by dissolving MoO_3 (99%, Fluka) in diluted NH_3 (1:1).
- **Ti.** The solution was obtained by dissolving titanium isopropoxide, $\text{Ti}[\text{OCH}(\text{CH}_3)_2]_4$ (99%, Aldrich) in pure ethanol. When the solid is dissolved and mixed with rest of compounds, it is needed to heat the solution to extract the ethanol.

-
- **Zr and Nb.** The solutions are prepared by dissolving zirconium oxonitrate hexahydrate, $\text{ZrO}(\text{NO}_3)_2 \cdot 6\text{H}_2\text{O}$ (99% Aldrich) and niobium oxalate, $\text{Nb}(\text{HC}_2\text{O}_4)_5 \cdot \text{H}_2\text{C}_2\text{O}_4$ (97% ABCR), in distilled water.

Finally, to each cation solution, ethylenediaminetetraacetic acid (EDTA, Sigma-Aldrich), is added in a 1:1 metal:ligand ratio to complex the cations and facilitate their mixture. Later, the pH of the combined solution is adjusted to 7-8 and the final volume to ~ 100 mL. The resulting solution goes through the following processes as is shown in Figure 1.15.

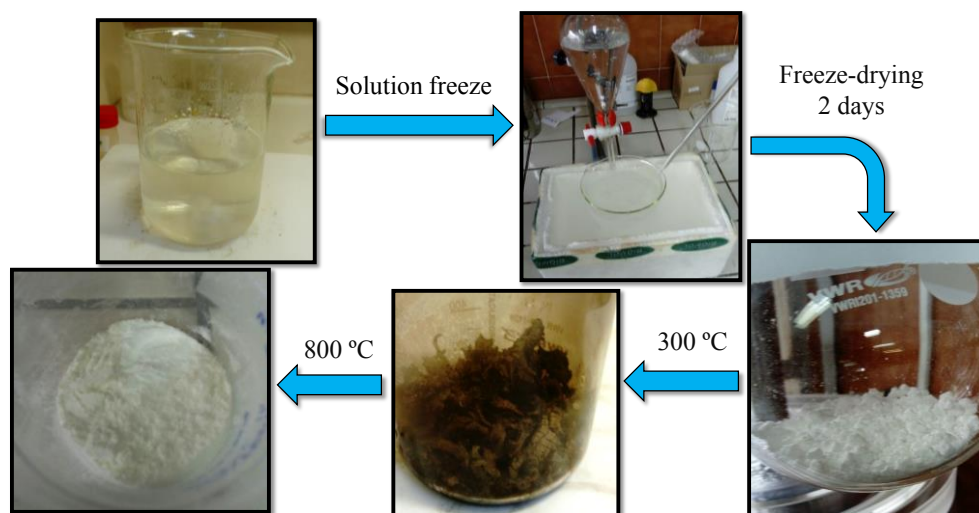


Figure 1.15. General scheme of freeze-drying method synthesis process.

The freezing step should be fast to avoid concentration gradients due to the different solubilities of the reagents and maintain the homogeneity and stoichiometry of the cations. The mixed solution is dripped slowly with a separatory funnel over liquid nitrogen while stirring vigorously with a glass rod, so that drops do not agglomerate with each other, maximizing the efficiency of sublimation by increasing the superficial area of the sample. After the freezing process, water is removed by vacuum sublimation in a

freeze-drier that captures all condensable gases. This method allows for the transformation of water from solid to gas instantly due to the conditions having less temperature and pressure than the triple point of water, as can be seen in Figure 1.16.

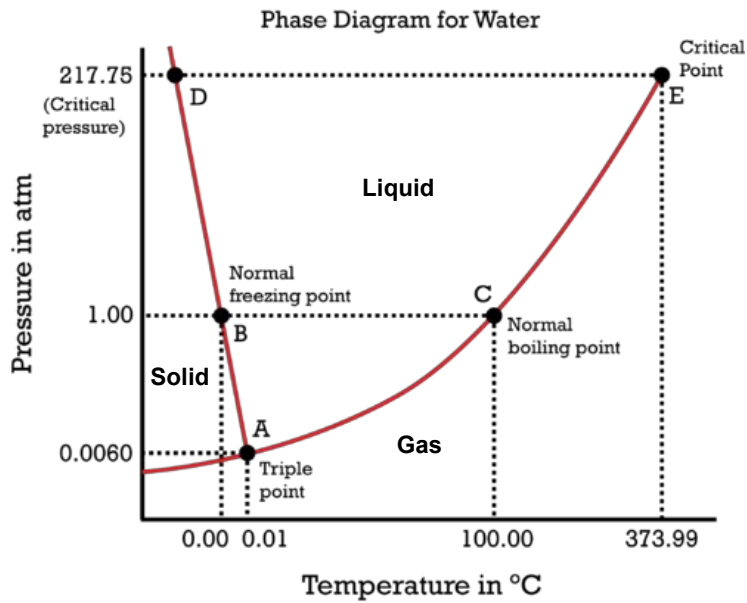


Figure 1.16. Aqueous solution phase diagram, the objective of freeze-drying is to decrease the temperature of the system and apply a vacuum to dry the materials without heat (something that could destroy the material).

While the temperature of the material is increased to room temperature, the remaining water is removed. This process takes place at the same time as the primary drying because the sample absorbs external heat and reaches room temperature while sublimation happens. In our case, the whole freeze-drying process takes place in two days. The dried powder obtained is rapidly calcinated at 300°C for 1 hour to prevent rehydration. A brown powder (Figure 1.17) is obtained due to fact that the material still contains organic residues, so a second calcination at 800°C for 1 hour (with heating and cooling

rates of $5\text{ }^{\circ}\text{C}\cdot\text{min}^{-1}$), assures the complete removal of all organic compounds obtaining a precursor of each material



Figure 1.17. Brown powder obtained at $300\text{ }^{\circ}\text{C}$ 1h. This powder is ground and heated at $800\text{ }^{\circ}\text{C}$ 1h with a rate of $5\text{ }^{\circ}\text{C}\cdot\text{min}^{-1}$ to remove all organic wastes.

To prepare fluorinated compounds, the precursor powders obtained at $800\text{ }^{\circ}\text{C}$ are mixed and ground with different stoichiometric proportions of polyvinylidene difluoride $(-\text{CH}_2-\text{CF}_2-)_n$ (PVDF) for 15 min in an agate mortar and then heated at $360\text{ }^{\circ}\text{C}$ for 12h (heating and cooling rate of 1 and $10\text{ }^{\circ}\text{C}\cdot\text{min}^{-1}$, respectively).

Finally, these materials are sintered with different thermal treatments: heating at temperatures between 1200 and $1500\text{ }^{\circ}\text{C}$ for 1h and cooling at different rates (quenching³, 50, 5, and $0.5\text{ }^{\circ}\text{C}\cdot\text{min}^{-1}$) to evaluate the effects of synthesis-sintering conditions in the structural, microstructural and electrical properties of the materials.

³Sudden cooling from high temperature to room temperature in a lift furnace. This strategy is widely used to stabilize high temperatures structures at room temperature.

1.8. Characterization of the materials.

1.8.1. X-ray Powder Diffraction (XRPD).

XRPD is a non-destructive technique used in many disciplines, for example in materials science for determining the atomic and molecular structure. X-rays are electromagnetic waves in the wavelength range from 0.01 to 10 nm. When X-rays with a wavelength λ and an intensity I_0 interact with matter, they become attenuated (μ), absorbed (τ), scattered (σ), and undergo the so-called “pair-building” (π). Diffraction occurs when X-rays are scattered by a material. Regarding the scattering process, two main interactions can be distinguished: coherent (Thomson scattering, where X-rays are scattered elastically without changing their energy values) and incoherent scatter (Compton scattering and fluorescence). X-rays are commonly generated by (i) deflecting high-energy electrons by electromagnetic fields, typically used in synchrotrons, or (ii) bombarding an anode with a focused electron beam. Electrons are emitted by a hot filament (cathode) and accelerated by the high voltage difference between the anode and the cathode. The kinetic energy of electrons is converted into heat (99%) and X-ray radiation (1%). When a monochromatic X-ray beam with a wavelength of λ falls on a regular arrangement of atoms with an angle of θ , it undergoes constructive interference leading to diffraction (Bragg’s Law, Figure 1.18). This wavelength, λ , must be comparable to the interatomic spacing of a crystal.

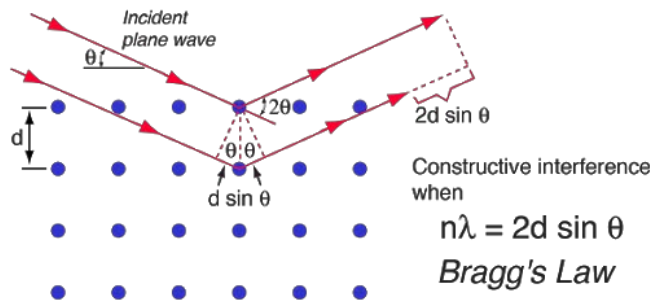


Figure 1.18. Bragg's Law representation.

Lattice planes are defined by Miller indices ($h\ k\ l$). The separation of these planes depends on the dimensionality and symmetry of the unit cell, which is the smallest unit that has the full symmetry of the crystal and can build it up by translational displacements. The unit cell is defined by its lattice parameters: the length of the cell edges (a , b , and c) and the angles between them (α , β , and γ).

The intensity of the reflections is principally influenced by the structure factor (F_{hkl}), the amount of material, and the absorption in the material while the shape of the diffraction peaks can be influenced by instrument and sample-related effects. The structure factor, F_{hkl} , is the sum of all the scattering of an X-ray beam by all the electrons in the crystal. The expression for the structure factor is:

$$F_{hkl} = \sum_j f_j e^{2\pi i(hx+ky+lz)} \quad [14]$$

where f_j is the scattering factor for an atom j located at (x, y, z) position. Each scattered X-ray is defined by its amplitude, $|F_{hkl}|$, and the phase of the diffracted wave, ϕ_{hkl} .

$$F_{hkl} = |F_{hkl}| e^{i\phi_{hkl}} \quad [15]$$

The intensity of a reflection, I_{hkl} , is proportional to the structure factor squared, being C_{hkl} a calculable constant dependent on the sample absorption and instrumental factors:

$$I_{hkl} = C_{hkl}F_{hkl}^2 \quad [16]$$

It is not possible to directly obtain the crystal structure from a diffraction experiment because the phases cannot be measured. However, it can be obtained indirectly from a set of amplitude values, $|F_{hkl}|$.

There are two main X-ray diffraction techniques:

-Single Crystal X-ray Diffraction (SCXRD). The sample is a single crystal that is rotated around various axes to find many different reflections. The crystal structure can be obtained from the angular positions and the intensity of these reflections.

-XRPD: Polycrystalline or powdered samples contain many small crystallites with a random full range of possible orientations, being necessary to vary the incidence and diffraction angles. This technique can be used for different applications such as qualitative and quantitative phase identification, particle size characterization or structural determination of new phases, etc.

1.8.1.1. The Rietveld method.

Rietveld refinement is employed when the crystallographic structure of the material is known. It consists of minimizing the difference between an experimental and a calculated diffraction pattern, employing an approximated structural model and parameters that allow distributing the intensities of the different reflections in the diffraction pattern. Initial parameters must be as close as possible to the final parameters. This method employs the entire diffraction pattern instead of the integrated intensities of the diffraction peaks,

allowing to solve the overlap peak problem and extract the maximum information from the diffraction pattern.

Two types of data are necessary to obtain the calculated intensities, (i) atomic parameters such as atomic positions, atomic displacement parameters, and site occupancies, and (ii) global parameters such as scale factors of each phase for crystalline compounds mixtures, background parameters, zero shift, profile function, unit cell parameters, preferred orientation, extinction, and absorption parameters. Both types of parameters are optimized during the refinement process until the best fit is obtained.

In a Rietveld refinement, it is important to use high-quality diffraction data. There are three influencing factors of data quality: (i) the crystallinity of the sample, (ii) measurement conditions, and (iii) the radiation employed (preferably monochromatic radiation, $K\alpha_1$). Furthermore, soft constraints, such as angles or bond distances, can be added to decrease the number of observations for the refinement. Soft constraints can be used when part of the geometry is known or the structure consists of rigid building units, e.g. SiO_4^{4-} or PO_4^{3-} .

1.8.1.2. The Le Bail method.

The Le Bail method extracts intensities (I_{hkl}) from powder diffraction data. This is done to find intensities that are suitable to determine the atomic structure of a crystalline material, to determine lattice parameters, and has the added advantage of checking phase purity with certain limitations. For the Le Bail method, the unit cell and the approximate space group (there are some groups that have restrictions) of the sample must be predetermined because they are included as a part of the fitting technique. It is not necessary to know the structural factor and associated structural parameters, since they are not

considered in this type of analysis. The Le Bail method can be used to find phase transitions in high pressure and temperature experiments. It generally provides a quick method to determine the lattice parameters, which allows for better experimental planning. Le Bail analysis provides a reliable estimation for the intensities of allowed reflections for different crystal symmetries.

Le Bail analysis fits parameters using a steepest descent minimization process. The parameters being fitted include the unit-cell parameters, the instrumental zero error and peak width and shape parameters. First, the Le Bail method defines an arbitrary starting value for the intensities (I_{obs}). This value is ordinarily set to one, but other values may be used. While peak positions are constrained by the unit cell parameters, intensities are unconstrained. The equation to calculate intensities is:

$$I_{obs} = \frac{\sum y_i(obs)y_i(1)}{y_i(calc)} \quad [17]$$

In equation [17], I_{obs} is the intensity observed at a particular step, and $y_i(obs)$ is the observed profile point. $y_i(calc)$ is the single intensity value that may contain more than one peak. Other peaks may be calculated similarly. The final intensity for a peak is calculated as $y(calc) = y_i(1) + y_i(2)$. The summation is carried out over all contributing profile points for a particular 2θ ($^\circ$). This process is known as profile intensity partitioning, and it works over any number of peaks. The Le Bail technique works especially well with overlapping intensities since in this method the intensity is allotted based on the multiplicity of the intensities that contribute to a particular peak.

There exist other procedures similar to Le Bail called the Pawley method that allow to fit a powder pattern without a structural model. Altomare *et al.* (1996), considered that pattern-decomposition programs based on the Le Bail algorithm can exploit the prior information in a more effective way

than Pawley-method-based decomposition programs. However, Le Bail method could as well lead to negative intensities in ranges of the pattern where the background is overestimated. The fact is that both the Pawley and Le Bail methods can estimate structure factor amplitudes which can lead to solve structures from powder diffraction data in a quite more efficient way than was previously possible, even if the overlapping handicap precludes forever attainment of the single crystal data quality level (Le Bail, 2005). Therefore, we employ the Le Bail method because the program that we use to refine data is GSAS and it works with this method.

1.8.1.3. Experimental devices.

The X-ray powder diffraction studies have been carried out with two instruments: an Empyrean and an X'Pert Pro MPD (PANalytical) diffractometers, both from the *Servicios Centrales de Apoyo a la Investigación* (SCAI) at the *Universidad de Malaga* (Figure 1.19).



Figure 1.19. Pictures of (left) PANalytical Empyrean diffractometer and (right) PANalytical X'Pert PRO MPD diffractometer used in this thesis, belonging to the *Servicios Centrales de Apoyo a la Investigación* (SCAI) at the *Universidad de Malaga*.

The PANalytical Empyrean diffractometer, used for routine analysis, present interchangeable Cu $K\alpha_{1,2}$ and Mo X-ray tubes and a PIXcel 3D ultrafast detector that allow 1D and 2D measurements (microstructural analysis and preferred orientation). The routine 1D measure is the most used in this thesis with a Bragg-Brentano configuration, with programmable and fixed anti-scatter and divergence slit without using a monochromator to maximize the number of measures to make the analysis faster as possible. A Ni or Zr filter is used to eliminate the $K\beta$ radiation of Cu or Mo, respectively.

In addition, this diffractometer can work in reflection and transmission modes with flat samples and capillaries, with high-resolution measurements using a Ge (111) monochromator to index crystalline materials and structural and textural analysis. The X-ray laboratory also provides Anton Paar high and low-temperature chambers: (i) HTK1200N that works from ambient temperature to 1200 °C, at vacuum or inert gases conditions; and (ii) a TTK450N chamber that allows working at temperatures between -180 °C and 450 °C, at vacuum or inert gases conditions. This temperature is obtained with a flux of liquid N₂ supplied with a 10L Dewar.

The PANalytical X'Pert PRO, used for structural studies, consists of an automatic loader and sample holder and allows to obtain high-resolution data since it only uses Cu $K\alpha_1$ monochromatic radiation. In the path of the incident beam, the optical system is formed by a primary monochromator of the Johansson type with a Ge (111) crystal, a Soller slit system, a programmable divergent slit, a mask that limits the beam width, and a slit of anti-divergence.

In the path of the diffracted beam, the optics are formed by a programmable anti-divergence reception slit, a Soller slit system, and an X'Celerator RTMS (Real-Time Multiple Strip) detectors consisting of 128 Si detectors placed in line. The X'Celerator detector provides several advantages

over scintillation detectors. Thanks to its design and operation, the time required to obtain a diffractogram can be reduced to less than one minute without compromising the resolution of the measurement.

The sample holders available for the diffractometers are made of steel, nickel, aluminium, or methacrylate; in each case, the most appropriate one is used depending on the number of samples available. The experimental conditions used have been 45 kV of voltage and 40 mA of current intensity for both devices. The diffractograms were made between 15 and 120° (2 θ), with a step size of 0.0167° and for a total measurement time of 0.5-2 hours depending on the quality needed. Routine measurements take less time than the Rietveld ones, which are more precise.

1.8.2. Neutron Powder Diffraction (NPD).

Diffraction experiments can be performed using neutrons instead of X-rays. Neutrons, unlike X-rays, which interact primarily with the electron cloud surrounding each atom, interact with the atom nuclei, providing complementary information not accessible with X-rays. For example, scattering length are isotope dependent, such as hydrogen and boron, and capable of distinguishing between elements with adjacent atomic numbers, such as iron and cobalt, isotopes of the same element, or element groups whose atomic numbers are wide apart, such as palladium and hydrogen (deuterium).

1.8.2.1. Experimental device.

To perform NPD experiments, it is necessary to apply for beamtime, making a proposal that has to be accepted by a scientific panel of the institution. In our case the measurements were made in 2 different facilities: GemXPress in the ISIS Neutron and Muon Sources at the STFC Rutherford

Appleton Laboratory (United Kingdom), and HRPT in SINQ at the Paul Scherrer Institute (PSI) in Switzerland.

A preliminary study of the samples with the simplest symmetries was performed in GemXPress, an available and fast system, where the researchers load the samples in a vanadium can and send them by courier to ISIS, where they are measured. The instrument has high intensity, high-resolution neutron diffraction and can study pairs distribution function to determine the structure of crystalline powders and amorphous materials. However, the GemXPress diffractometer does not have enough resolution for a deep study of materials depending on the symmetry of materials.

On the other hand, at PSI the materials were studied in the HRPT diffractometer (Figure 1.20) designed as a flexible instrument for efficient neutron powder diffraction studies at RT.



Figure 1.20. (Top) Aerial picture of Paul Scherrer Institute (PSI) in Switzerland and (bottom) the HRPT diffractometer.

It has high resolution ($\delta d/d < 0.001$) by thermal neutrons, and large scattering angles of the monochromator and the sample (up to 165°). Using primary collimators, a secondary slit system, and by an appropriate choice of the sample diameter, resolution and intensity can be optimized. A wide range of neutron wavelengths $\lambda = 0.84\text{-}2.96 \text{ \AA}$ is available. Due to the use of a large position-sensitive (PSD) He detector is possible for simultaneous measurements within a scattering angle range of 160 degrees with an angular step of 0.1° . The detector can be positioned on air cushions also at intermediate positions and the angular step can be e.g., 0.05° or less. The detector can run in a stroboscopic mode for the measurements of the crystal structures as a function of the time the periodic processes (for example, charging/discharging) with a maximal time resolution of 10ms. An oscillating radial collimator suppresses Bragg peaks from the sample environment such as cryostats, furnaces, magnets, or high-pressure cells ($<14 \text{ kbar}$) and ($<100 \text{ kbar}$). The HRPT instrument is also equipped with a computer-controlled sample changer for eight samples for room temperature, and a sample changer for five samples with sample rotation for the temperature range of 1.5-315 K.

1.8.3. Transmission electron microscopy (TEM).

Transmission electron microscopy (TEM) uses an electron beam that is transmitted to a thin layer that magnifies objects up to 2 million times obtaining an image at an atomic scale. The principal advantage of this technique is that can determine the atomic organization of materials from scattering (collisions interactions between electrons and samples atoms). This technique can be used for different purposes:

- SAED: Selected area electron diffraction represents the reciprocal network of materials. A periodic crystal structure leads to electron

diffraction that satisfies Bragg conditions. A family of crystallographic planes will diffract with electrons beam. Therefore, reciprocal space distances can be transformed to direct space d_{hkl} by [18]:

$$d^* = \frac{\lambda \cdot l}{d_{hkl}} \quad [18]$$

Where l is the camera constant, that depends on the electron wavelength, λ (0.0251 Å, when are working at 200 kV). The camera constant is determined using a patron sample with a known ionic framework.

Electron diffraction works similarly to XRPD and can be used for determining cell parameters and atomic positions. It presents the advantage that has more accuracy to determine superstructures and is more sensitive to lighter elements. In addition, SAED gives information of the local ionic framework, and XRPD of the average structure of the material. That makes electron diffraction and high-resolution images a useful tool to study defects, textures of microdomains, etc. In addition, is an interesting tool to determine space groups, because it can differentiate between reflection families.

- HRTEM: High-resolution transmission electron microscopy images allow the study of regions by images, for the search of defects or local microstructural changes. In addition, it can be obtained the electron diffraction pattern from the image by Fourier transformation, which can be compared from the obtained in SAED, as can be seen in Figure 1.21.

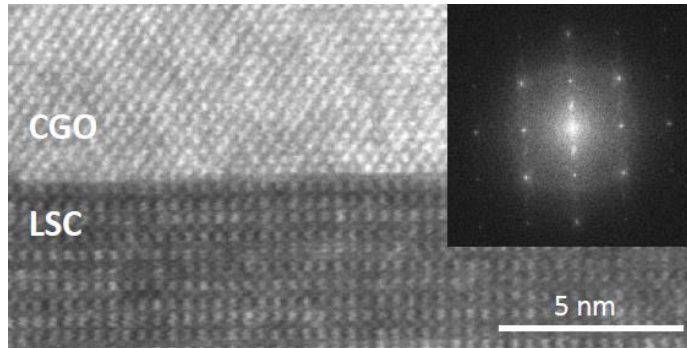


Figure 1.21. Example of HRTEM images for a multilayer sample CGO and LSC that are easily differentiated by the local microstructure regions and the SAED obtained by Fourier transformed of the structure CGO.

1.8.3.1. Experimental device.

The experimental device used in this thesis was a Jeol JEM 2100 HRTEM from the *Renewable Energy Research Institute at the University of Castilla-La Mancha* and is shown in Figure 1.22.



Figure 1.22. HRTEM instrument that was used for characterizing the materials belonging to the *Renewable Energy Research Institute at the University of Castilla-La Mancha*.

1.8.4. Scanning electron microscopy (SEM).

SEM provides high magnification images of the surface of the materials. The applications of the technique are numerous, both in materials sciences and in biomedicine. Within materials science, applications in metallurgy, mineralogy, construction and ceramic materials, electronics, fracture studies, surfaces, and elementary composition stand out. The basic components of a scanning electron microscope are shown in Figure 1.23.

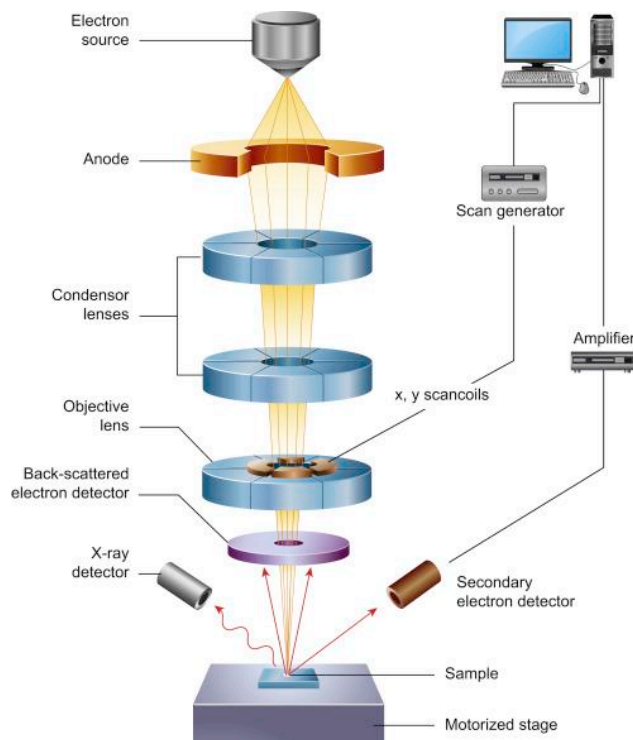


Figure 1.23. Components of a scanning electron microscope.

The operation of SEM is based on the bombardment of a surface by high-speed electrons that are generated by a LaB_6 or W filament subjected to a high voltage. A charged anode located in front starts the electrons of the

LaB₆ cathode increasing its speed. The electron beam is collimated using different lenses and magnetic coils to focus it on the sample, which needs to be measured under vacuum and coated with gold, graphite, or iridium because needs to be conductive to prevent it from overcharging, which could make it difficult to take pictures. The vacuum is made to give better stability to the electron beam because they are absorbed by the atmosphere and to avoid gas ionization. The beam moves over the sample by scanning in the X and Y directions, such that the position in which the beam is at each moment coincides with the appearance of brightness proportionally to the signal emitted at a given point of a screen. The electrons that interact with the sample are collected in different sensors depending on the analysis to be performed.

When an electron beam strikes the surface of a solid, several phenomena happen on the remission of a portion of the incident radiation, light emission, secondary and Auger electrons, X-rays, etc. All these signals can be used to obtain information about the nature of the sample (morphology, composition, crystalline structure, electronic structure, etc.). The images obtained in the scanning electron microscope correspond to secondary electrons or backscattered electrons emitted after the interaction with the sample of an incident beam between 5 and 30 KeV.

These devices can also perform other analysis techniques, as electron dispersed spectroscopy (EDS), based on the characteristic X-ray emission of each element. The electron beam energy interacts with the sample and generates X-ray radiation. This radiation is characteristic of each element of the periodic table and is captured by a semiconductor Si detector. The X-ray radiation interact with the detector producing an electronic jump from the valence band to the conduction band, generating electron-gap pairs. The number of electron-gap pairs depends on each element and semiconductor

gap. The detector charges and converts it into voltage giving the corresponded EDS spectra. This technique allows to know the composition and elemental quantities in a specific region of the sample studied. It makes the technique useful for impurities determination in polycrystalline samples that are not detectable by XRPD, without the need to know the exact composition of the sample.

1.8.4.1. Experimental device.

Figure 1.24 shows the device used in this thesis, a Helios Nanolab 650 located in *Centro de Bioinnovación y Nanotecnología* of *Universidad de Málaga*. Also, this device has a FESEM-FIB system with these particularities:

- The FESEM uses electrons generated in a tungstate monocrystal with a peak form of 2 nm forming a high electron flux and low extraction voltages. The energy obtained is highly focused resulting in higher resolution than SEM.
- The FIB uses a Ga^+ beam (130000 times heavier than electrons) that interacts with samples. Ion beams can ionize the surface of the sample and can be used to modify it at a nanometric scale.



Figure 1.24. Picture of scanning electronic microscope used in this thesis, a Helios Nanolab 650 belonging to *Centro de Bioinnovación y Nanotecnología* of *Universidad de Málaga*.

1.8.5. X-ray photoelectronic spectroscopy (XPS).

The XPS technique is based on the application of a radiation to the solid sample. The process is made in a high vacuum with monoenergetic X-rays. The energy emission of electrons from atoms due to the photoelectric effect can be described in the next formula:

$$E = hv - BE - \phi \quad [19]$$

Where hv is photon energy, BE is the binding energy for electrons prior to ionization with respect to the vacuum level and ϕ is work spectrophotometer function.

The BE of an internal electron depends on the oxidation state of the element and the peak position can change various eV depending on different oxidation states. Also, BE can be shifted depending on the chemical environment.

XPS is a superficial technique since X-rays only interact with the more external atomic layers. Any element has its unique bond energy; therefore, this technique is a tool to identify and determine the proportions and oxidation states of surface elements.

1.8.5.1. Experimental device.

Figure 1.25 shows the spectrophotometer used in this thesis, a Physical Electronics PHI-5700 that belong to the *Servicio Central de Apoyo a la Investigación* (SCAI) in *Universidad de Málaga*. The machine has a dual-beam of X-ray radiation of Mg-K $_{\alpha}$ ($h\nu = 1253.6$ eV) and Al-K $_{\alpha}$ ($h\nu = 1483.6$ eV). Spectra was registered with a 45° angle using a hemispheric multichannel analyser electronic model 80-365B, which works with a 25.9 eV constant energy. These measurements were done at low pressure ($<1.3 \cdot 10^{-}$

⁷ Pa) at the ionization chamber. Bond energy was obtained with a ± 0.1 eV precision guiding with the C(1s) reference from adventitious carbon at 284.4 eV.



Figure 1.25. Picture of PHI 5700 XPS spectrophotometer used in this thesis, in *Servicio Central de Apoyo a la Investigación (SCAI)* of *Universidad de Málaga*.

1.8.6. Electrochemical characterization.

The electrochemical characterization of the materials is essential to studying the possible application as hydrogen separation membranes. Generally, the total conductivity of an ionic conductor is the sum of several contributions: ionic (oxide and/or proton ions) and electronic (p and n-type). For hydrogen separation membranes the material must have high dual proton-electron conductivity to allow the electrons and protons travel through the membrane from one side to the other side with the lowest resistance possible. The electrical conductivity is a characteristic magnitude of each material that can be determined by knowing the electrical resistance to the passage of a current. For a material with a certain geometry (e.g., cylindrical, rectangular,

etc.), the electrical resistance can be calculated with Ohm's law, applying a potential difference (V) to the sample, and measuring the current passing through it (I).

$$R = \frac{V}{I} \quad [20]$$

Being the conductivity:

$$\sigma = \frac{L}{S \cdot R} \quad [21]$$

Where L is thickness and S surface of sample.

However, for an ionic conductor, this two-contact method cannot be applied to measure the total conductivity. When a constant potential is applied, the O^{2-} ions and the vacancies move towards the positive and negative electrodes, respectively. This movement causes the polarization of the material due to the accumulation of opposite charges at the electrodes that causes the resistance of the electrolyte to add to the polarization resistance so that the resistance determined with a 2-pointed dc method is greater than the real one.

For the study of ionic conductivity there exist different measurement methods, for example, the complex impedance spectroscopy. This method has some applications ranging from material transport determination, diffusion measurements, corrosion studies, and electrical properties analysis, to studying the microstructural defects and the influence of the composition on conductivity. In addition, it can be used to study systems as varied as chemical sensors, and fuel cells or to investigate the behaviour of membranes in living cells.

1.8.6.1. Complex impedance spectroscopy.

Electrochemical impedance spectroscopy (EIS) is a very useful tool to determine the physical-chemical phenomena that occur at an electrode-electrode interface of an electrochemical cell. From the information provided by the EIS measurements, material properties can be known, such as conductivity, dielectric constant, charge mobility, the concentration of charged species, the rate constants of absorption reactions, the value of the capacity of the interface region or the diffusion coefficient of a natural species in the electrode. The impedance of the system, Z , is related to the applied potential, E , and the current generated, I , by Ohm's law:

$$E=I \cdot Z \quad [22]$$

The applied voltage can be written as follows,

$$E(t) = E_0 \cdot \sin(\omega t) \quad [23]$$

$E(t)$ is the voltage (Volts), as a function of time, E_0 is the amplitude of the voltage (Volts), ω is the angular frequency (rad/s), f is the frequency (Hz) and t is the time (s).

The current obtained after the application of the potential can be written as:

$$I(t) = I_0 \cdot \sin(\omega t + \Phi) \quad [24]$$

$I(t)$ is the current (A) as a function of time and Φ the offset of the current concerning the applied potential.

The impedance of the system can be determined:

$$Z(t) = \frac{E(t)}{I(t)} = \frac{E_o \cdot \sin(\omega t)}{I_o \cdot \sin(\omega t + \Phi)} = \frac{E_o}{I_o} \left(\frac{e^{i\omega t}}{e^{i\omega t + \Phi}} \right) = \frac{E_o}{I_o} e^{-j\Phi} = Z_o e^{-j\Phi} \quad [25]$$

The impedance is, therefore, a complex magnitude that can be expressed in the real component and imaginary:

$$Z(\omega) = |Z|(\cos \varphi + j \sin \varphi) = Z'(w) + jZ''(w) \quad [26]$$

The representation of the imaginary part of the impedance $Z''(w)$ versus the real part $Z'(w)$ is known as Nyquist diagrams. The simplest Nyquist diagram is found in monocrystalline materials with a single driving mechanism. In this case, the representation in the complex impedance plane is a semicircle of radius R_b , equal to the resistance of the material and centred on the real axis ($R_b/2$). The points to the right of the diagram correspond to those of lower frequency so that R_b is the ohmic resistance in a direct current of the material (Figure 1.26).

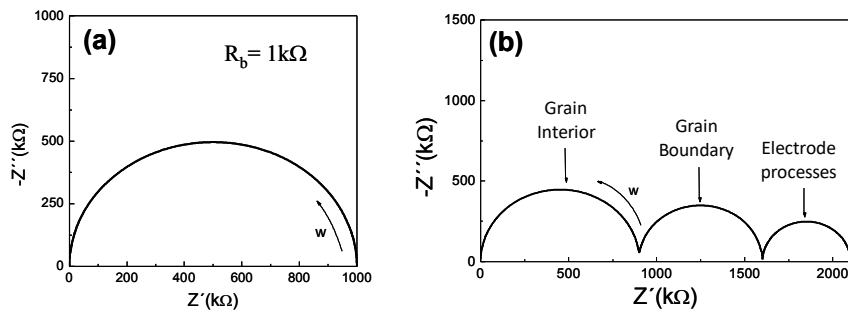


Figure 1.26. Nyquist diagram of material with a unique contribution (a) and different contributions from total impedance (b).

In polycrystalline materials, the conductive species must move through the interior of the grains and the interfaces between them. The resistance that the ions meet in the grain limit is different from the grain inside and they also have a different capacity associated. This causes two arcs to appear in the impedance spectra, one associated with the interior of the grain (bulk) and the other with the grain border (grain-boundary). Other processes often also appear at a very low frequency, due to the diffusion of the oxide ions and the charge transfer processes that occur at the electrode/electrolyte interface. For the ideal case shown in Figure 1.27b, where the processes appear separated, the resistance of each of these contributions can be easily obtained from the cut-off point of each semicircle with the real axis. The capacity of these processes can also be determined, based on the frequencies of the maximum impedance spectrum, according to the following relation:

$$f_{\max} = \frac{1}{2\pi RC} \quad [27]$$

Generally, the different processes do not appear as separate, as shown in this ideal case, so an adjustment with equivalent circuits is necessary.

1.8.6.2. Experimental device.

The impedance measurements are performed with a frequency analyser, Solartron 1260 model, which has a useful frequency range between 1 mHz and 1 MHz. The ac-disturbances range from a few millivolts to 0.5 V. The impedance analyser is controlled through a computer. For data acquisition, the ZPlot and SetTemp 3.1 programs are available for the Eurotherm 2408 temperature controller that runs externally from the ZPlot. This allows measurements to be made in a fully automated manner. In this Thesis, the measurements were made from 800 to 200 °C every 20 or 50 °C, at different

atmospheres as N_2 , O_2 , and 5% H_2 -Ar in dry and wet conditions, stabilizing the temperature before the measurement for 10 minutes. Figure 1.27. shows the distribution and parts of this system.

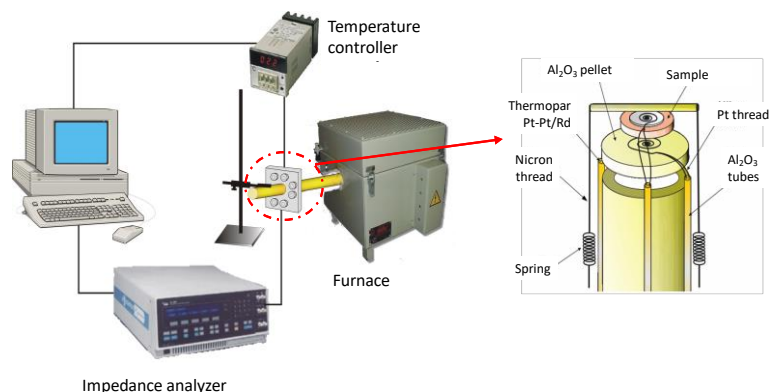


Figure 1.27. Experimental assembly and electrochemical cell of complex impedance spectroscopy equipment.

1.8.6.3. Conductivity vs oxygen partial pressure.

In ionic-electronic conductors, it is critical to identify crystalline defects based on parameters such as temperature and partial pressure of oxygen (pO_2). Studying the dependence of these parameters on conductivity it is easy to know what defects dominate under certain conditions.

In order to know if a material exhibits mostly ionic or electronic conductivity, the study of its variation with the partial pressure of oxygen is one of the most used methods. If a material exhibits mostly ionic contribution over a wide range of partial oxygen pressures, in general, the conductivity will be independent of the partial oxygen pressure.

The different contributions to conductivity for a mixed conductor are presented in Figure 1.28. As can be seen, the n-type conductivity is predominant at low partial oxygen pressures, while the p-type prevails at high

O₂ pressures. In the intermediate region of pO₂, the conductivity is mainly ionic, being the minor electronic contribution for this case simulated from [23].

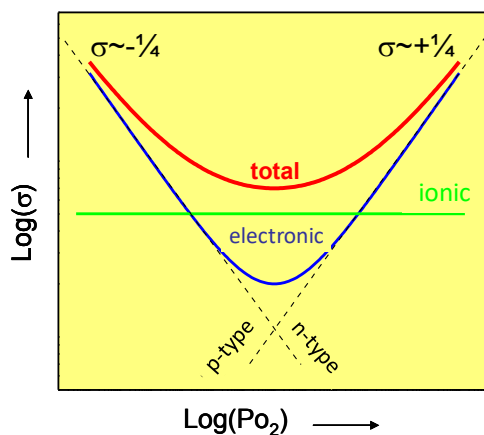


Figure 1.28. Dependence of total conductivity and different contribution ionic/electronics for a mixed conductor (Brouwer approximation).

1.8.6.4. Experimental device.

The conductivity determination as a function of the partial pressure of oxygen has been carried out in a sealed gas flow system, specially designed for this purpose. A picture of the device used is shown in Figure 1.29.

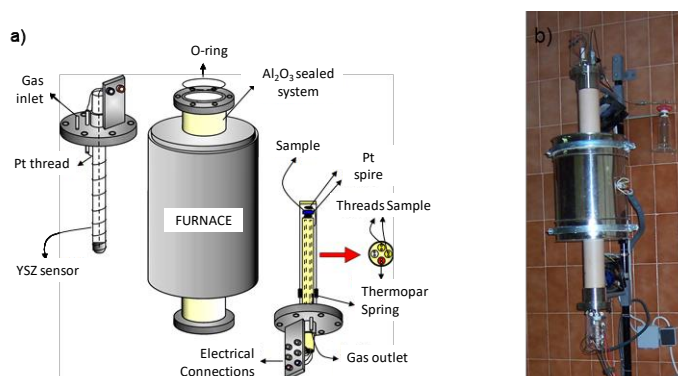


Figure 1.29. a) Diagram of the different parts of the variable pressure partial impedance spectroscopy measuring device. b) Photograph of the furnace and the cell.

It consists of a measuring cell, a tubular furnace, and an oxygen sensor. Electrical measurements were recorded with an HP4284A impedance analyzer with these characteristics:

- The measuring cell is built on a stainless-steel support with an alumina shaft of 13 mm in diameter and 25 cm in length with 4 holes through which 3 two-hole pyrometric rods are used to isolate electrically to the wires. One of them is the thermocouple holder, which is located very close to the tablet, and the other two are used to house the 4 Pt wires (the four-pointed procedure is used) that reach the electrodes.
- The tubular furnace was constructed by winding around a tube of dense alumina (99.7% Al_2O_3) Kanthal® wire (type A1). The ends of the tube have two stainless steel pieces attached that allow the measuring cell and an oxygen sensor to be practically adjusted. These two pieces are attached to the terminals with screws and an O-ring to prevent gas leakage, achieving a virtually watertight system. Each of the steel supports (of the measuring cell and the sensor) has a key that allows the internal air to be purged from the gas chamber.
- The oxygen sensor is built on a non-porous YSZ sheath of 10 mm in diameter and 20 cm in length open only by one end. To construct the sensor, at the closed end it is applied inside, and out, Pt paint covering approximately 2 cm in height and serves to glue two Pt wires that connect to a voltmeter. The closed end of the sheath is inside the oven while the open part is outside it and is always at atmospheric pressure. As a result of the difference in partial pressures of oxygen in and out of the gas cell, a potential difference has generated those results in a partial pressure value of oxygen using the Nernst equation.

To reduce the partial pressure of oxygen inside the chamber, a gas that can be inert (N_2 , Ar, etc.) or a reactive mixture, for example, 5% H_2 - N_2 or 5% H_2 -Ar, is flowed. These mixtures are more effective since, at the temperature at which the process is carried out, H_2 is combined with O_2 , reducing the oxygen content in the chamber to a greater extent. For example, if purging with N_2 a partial pressure of 10^{-5} atm is reached at 900°C , while if the gas used is 5% H_2 -Ar, the value decreases to 10^{-20} atm at the same temperature. To experiment with variable oxygen pressure, once the tablet is placed in the cell, the system is closed and slowly heated (at $5^\circ\text{C}\cdot\text{min}^{-1}$) to the temperature at which the experiment is to be carried out. When it is stable, a small gas flow (approximately $20\text{ cm}^3\cdot\text{min}^{-1}$) is passed long enough to reach equilibrium. This situation is recognized when the voltage remains constant, and the electrical resistance of the material does not vary. Next, the gas inlet and outlet are closed, and the impedance spectra and sensor potential readings begin to be recorded simultaneously every 15 min. As the system is not completely airtight, the air enters very slowly by diffusion, increasing the value of the partial pressure of oxygen progressively.

The total duration of the measurement depends on the working temperature and the speed with which the oxygen re-enters the measurement chamber, being in most cases 48h. Figure 1.30. shows as an example the variation of $p\text{O}_2$ over time.

In these types of measurements, there are two important limitations, on the one hand, it should be noted that the sensor response is only linear at very low (between 10^{-25} and 10^{-15} atm) or relatively high ($>10^{-5}$ atm) partial oxygen pressures.

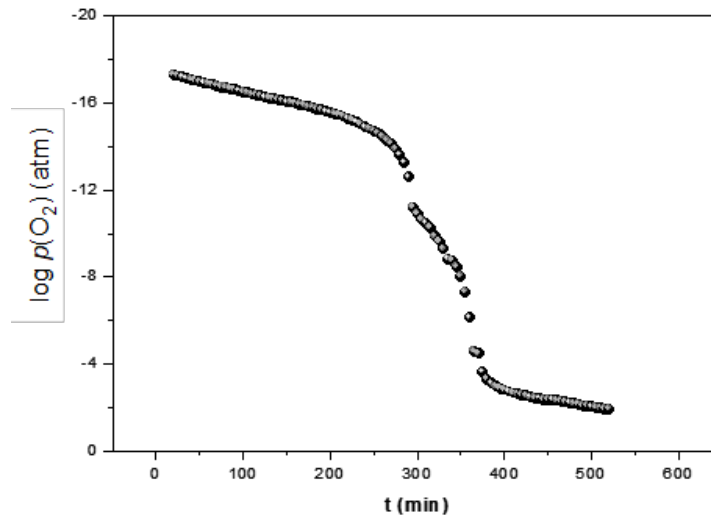


Figure 1.30. Variation of oxygen partial pressure vs time at 1173 K.

At intermediate pressures (between 10^{-14} and 10^{-5} atm) there is a small variation in a very short period that prevents us from making accurate readings. It should be considered that the jump is lower the higher the working temperature, hence, the measurements are usually carried out between 800-1000 °C. On the other hand, there is an experimental limitation in the working temperature that must be at least 600 °C. Below this temperature, the oxide ion conductivity of the YSZ is very small and cannot be used as an oxygen sensor. Finally, it is important to note that these measures are essentially "non-equilibrium", and in some cases, the results may be affected by reasons of kinetic nature.

2. OBJECTIVES.

The main objective of this thesis is the study of lanthanum molybdates, ceramic materials with ionic and electronic conductivity, stable at high temperatures in CO₂, CO, SO_x-containing atmospheres, for their use as hydrogen separation membranes. The following subobjectives have been established:

- 1) Synthesis by the freeze-drying method of the La_{6-x}MoO_{12-δ} (0 ≤ x ≤ 3) series and study the influence of the synthesis-sintering conditions on the single-phase existence range and polymorphism of these materials.
- 2) Perform a comprehensive structural and microstructural analysis of the obtained materials using a wide range of techniques such as X-ray, neutron diffraction, transmission electron microscopy, selected area electron diffraction and scanning electron microscopy.
- 3) Optimize the properties of the materials by aliovalent doping on the cationic and anionic framework, performing a substitution in lanthanum position, according to formula La_{5.3}A_{0.10}MoO_{11.05} (A = Ca, Sr, and Ba), and in the molybdenum position followed by a fluorination, according to the formula La_{5.4}Mo_{1-x}B_xO_{11.1-y/2-δ}F_y. (x = 0, and 0.10; B = Ti, Zr, and Nb; and y = 1, 3, and 6).
- 4) Conduct a thorough analysis of the electrochemical properties by impedance spectroscopy, in order to evaluate the contribution to the overall conductivity of different charge carriers: oxide ion, proton and electrons, establishing the relationship between structure, lanthanum content, doping and the conduction properties.



3. ARTICLES.

Article 1

-“Effect of Preparation Conditions on the Polymorphism and Transport Properties of $\text{La}_{6-x}\text{MoO}_{12-\delta}$ ($0 \leq x \leq 0.8$)”, Adrián López-Vergara, Jose M. Porras-Vázquez, Antonia Infantes-Molina, Jesús Canales-Vázquez, Aurelio Cabeza, Enrique R. Losilla and David Marrero-López. *Chemistry of Materials* 2017, 29, 6966-6975. DOI: 10.1021/acs.chemmater.7b02481.

In this work, $\text{La}_{6-x}\text{MoO}_{12-\delta}$ ($0 \leq x \leq 0.8$) materials are investigated as a new family of ceramic proton conductors. Different polymorphic phases with rhombohedral and cubic structure are obtained, depending on the cooling rate applied during the synthesis process. The materials have been thoroughly characterized by different techniques, including X-ray powder diffraction, transmission electron microscopy, and X-ray photoelectron spectroscopy in order to fully understand the structural features of the samples. Thermogravimetric analysis and impedance spectroscopy in dry/wet gases (N_2 , O_2 , and 5% H_2 -Ar) confirmed the existence of proton conductivity at low temperature. Under a reducing atmosphere, the materials are mixed ionic-electronic conductors. The sample prepared at the fastest cooling rate exhibits cubic structure and higher n-type electronic conductivity compared to those prepared at a slower cooling rate with rhombohedral structure.

Article 2

-“Metal-Doping of La_{5.4}MoO_{11.1} Proton Conductors: Impact on the Structure and Electrical Properties”, Adrián López-Vergara, José M. Porrás-Vázquez, Einar Vøllestad, Jesús Canales-Vázquez, Enrique R. Losilla, and David Marrero-López. *Inorganic Chemistry* 2018, 57, 20, 12811-12819. DOI: 10.1021/acs.inorgchem.8b02010.

La_{5.4}MoO_{11.1} proton conductors with different metal doping (Ca²⁺, Sr²⁺, Ba²⁺, Ti⁴⁺, Zr⁴⁺, and Nb⁵⁺) have been prepared and structurally and electrically characterized. Different polymorphs are stabilized depending on the doping and cooling rate used during the synthesis process. The most interesting results are obtained for Nb-doping, La_{5.4}Mo_{1-x}Nb_xO_{11.1-x/2}, where single compounds are obtained in the compositional range $0 \leq x \leq 0.2$. These materials are fully characterized by structural techniques such as X-ray and neutron powder diffraction and transmission electron microscopy, which independently confirm the changes of polymorphism. Scanning electron microscopy and impedance spectroscopy measurements in dry/wet gases (N₂, O₂, and 5% H₂-Ar) showed an enhancement of the sinterability and electrical properties of the materials after Nb-doping. Conductivity measurements under very reducing conditions revealed that these materials are mixed ionic-electronic conductors, making them potential candidates for hydrogen separation membranes.

Article 3

-“Synergic Effect of Metal and Fluorine Doping on the Structural and Electrical Properties of La_{5.4}MoO_{11.1}-Based Materials”, Adrián López-Vergara, Marta Bergillos-Ruiz, Javier Zamudio-García, José M. Porrás-Vázquez, Jesús Canales-Vázquez, David Marrero-López, and Enrique R. Losilla. *Inorganic Chemistry* 2020, 59, 2, 1444–1452. DOI: 10.1021/acs.inorgchem.9b03194.

Cationic and anionic frameworks of La_{5.4}MoO_{11.1} proton conductors have been modified by means of metal (Ti⁴⁺, Zr⁴⁺, and Nb⁵⁺) and fluorine (F⁻) doping. This synergic effect leads to the stabilization of high symmetry and single-phase polymorphs. The materials have been fully characterized by structural techniques, such as X-ray and neutron powder diffraction and transmission electron microscopy. The fluorine content was determined by ion chromatography. Impedance spectroscopy analysis under different atmospheres (dry and wet N₂ and O₂ and wet 5% H₂-Ar) showed an improvement in the electronic conductivity under reducing conditions, making these materials potential candidates for hydrogen separation membranes.

Article 4

-“Unravelling crystal structures and transformations in the $\text{La}_{6-x}\text{MoO}_{12-\delta}$ ($0.6 \leq x \leq 0.3$) series. A system with tailored ionic/electronic conductivity. Adrián López-Vergara, Lucía Vizcaíno-Anaya, José M. Porras-Vázquez, Gianguido Baldinozzi, Lucía dos Santos-Gómez, Jesús Canales-Vázquez, David Marrero-López, and Enrique R. Losilla. *Chemistry of Materials* 2020, 32, 16, 7052–7062. DOI: 10.1021/acs.chemmater.0c02673.

Crystalline $\text{La}_{6-x}\text{MoO}_{12-\delta}$ materials with different lanthanum/molybdenum ratios ($0.6 \leq x \leq 3.0$) have been prepared via a freeze-drying precursor route. The influence of the lanthanum content, sintering temperature, and cooling rate on the phase existence range and polymorphism was evaluated. Lanthanum-rich compounds present three different polymorphs: a cubic (disordered) fluorite and two complex rhombohedral superstructures related to the fluorite. For the first time, the structural resolution of these rhombohedral superstructures, $7 \times 7 \times 1$ and $5 \times 5 \times 1$, has been successfully accomplished by neutron powder diffraction and transmission electron microscopy studies. As the La/Mo ratio decreases, the cubic symmetry is stabilized, although a phase transformation from cubic to monoclinic occurs at a low cooling rate. Impedance spectroscopy measurements under different atmospheres (dry and wet N_2 and 5% H_2 -Ar) show that all materials exhibit mixed proton–electronic conductivity. The n-type electronic conductivity is attributed to Mo^{6+} reduction and increases for those phases with lower lanthanum content, i.e., for quenched samples, from 5 mS cm^{-1} for $\text{La}_{5.4}\text{MoO}_{11.1}$ to 9.5 mS cm^{-1} for La_4MoO_9 at 700°C in very reducing and wet conditions, which are significantly better than the values published to date for mixed lanthanum tungstates/molybdates. This makes these materials potential candidates for hydrogen separation membranes.



4. DISCUSSION.

In this thesis it has been carried out a complete study of the $\text{La}_{6-x}\text{MoO}_{12-\delta}$ ($0 \leq x \leq 3$) nominal series. Firstly, it was determined the influence of the sintering temperature and cooling rate in the synthesis of the materials and its effect on the single-phase existence range and polymorphism. Secondly, a complex structural analysis was performed to determine the structures of different polymorphs using TEM and NPD data. Finally, it was tested how modifications in the cationic and anionic frameworks by doping change the textural and electrical properties of the materials, with the final goal of employing them as hydrogen separation membranes.

4.1. Influence of the preparation conditions on the structure and properties of $\text{La}_{6-x}\text{MoO}_{12-\delta}$ ($0 \leq x \leq 3$).

4.1.1. Optimization of the sintering temperature.

A preliminary study was performed with the composition $\text{La}_{5.4}\text{MoO}_{11.1}$, a work not previously reported in the literature. Precursors were prepared by the freeze-drying method (as described in section 1.7.1.). The powders obtained at 800 °C were compacted into pellets with 10 mm of diameter and 1 mm of thickness, and then sintered at different temperatures. XRPD patterns of $\text{La}_{5.4}\text{MoO}_{11.1}$ heated between 800-1500 °C for 1h and cooled down at 5 °C·min⁻¹ (that can be considered a standard cooling rate in many laboratories) are shown in Figure 4.1.

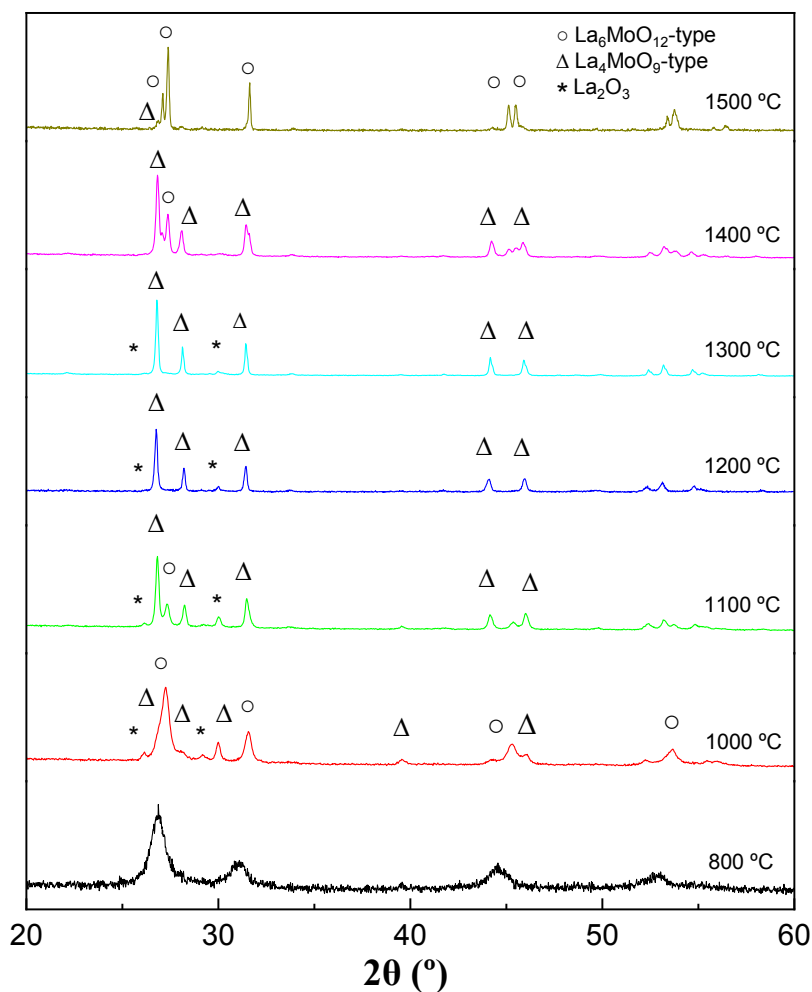


Figure 4.1. XRPD patterns of $\text{La}_{5.4}\text{MoO}_{11.1}$ obtained by heating 1 h between 800 and 1500 °C and cooled down at 5 °C min^{-1} . The main peaks of the different phases are labeled.

At 800 °C, XRPD patterns show broad peaks that can be indexed as a cubic fluorite-type structure because of the nanocrystalline nature of the powders. Increasing the temperature to 1000-1300 °C leads to the appearance of different phases: a rhombohedral $\text{La}_6\text{MoO}_{12}$ -type structure (PDF 00-34-1220), a hexagonal La_4MoO_9 -type structure (PDF 00-023-1144), and La_2O_3 (PDF 01-073-2141). It is important to remark that the structure of these two lanthanum molybdates phases was unknown in this initial part of the research.

Above 1300 °C, the samples are a mixture of the $\text{La}_6\text{MoO}_{12}$ -type and La_4MoO_9 -type structures, whereas at 1500 °C $\text{La}_6\text{MoO}_{12}$ is formed preferably. These results were reproducible in different syntheses and no single phase can be obtained under these synthetic conditions. Therefore, in order to isolate each structure, it was studied the influence of the cooling rate in the synthesis.

4.1.2. Cooling rate influence.

XRPD patterns of $\text{La}_{5.4}\text{MoO}_{11.1}$ heated at 1500 °C for 1h and cooled down at different rates: quenching, 50, 5, 2.5, and 0.5 °C min^{-1} in air, are shown in Figure 4.2.

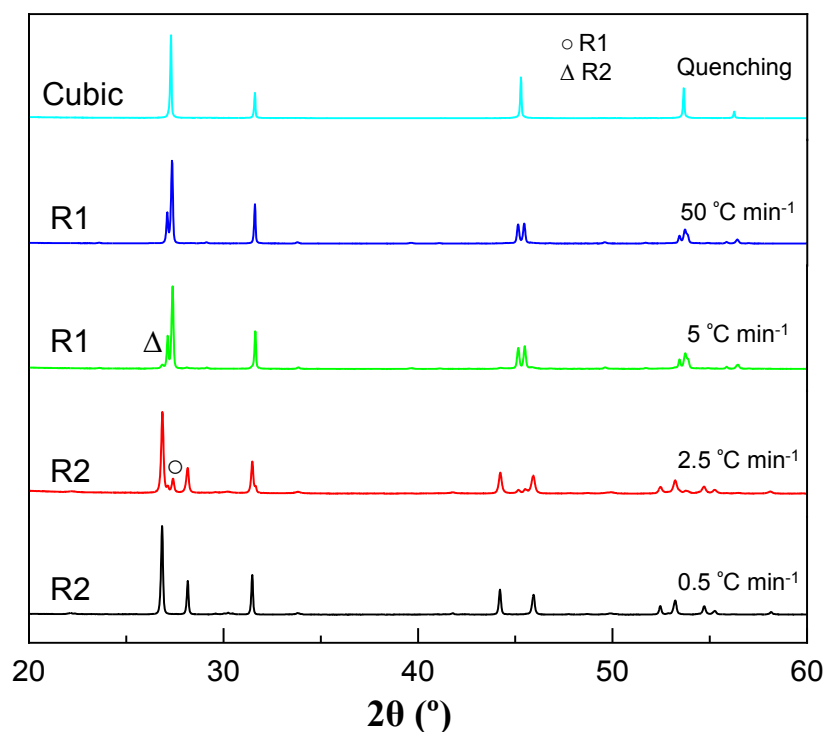


Figure 4.2. XRPD patterns of $\text{La}_{5.4}\text{MoO}_{11.1}$ obtained by heating at 1500 °C 1h and cooled down at different rates (quenching, 50, 5, 2.5, and 0.5 °C \cdot min^{-1}). The major phase is denoted at the bottom left of the diffraction pattern and the minor secondary phases are labeled.

The samples cooled by quenching present a cubic fluorite-type structure without any secondary phases. This structure is kinetically stable at room temperature and, as it has been shown later, does not evolve over time (years).

On the other hand, at lower cooling rates phases thermodynamically more stable are obtained. Samples cooled at $50\text{ }^{\circ}\text{C}\cdot\text{min}^{-1}$ crystallize in a single-phase $\text{La}_6\text{MoO}_{12}$ -type rhombohedral structure (named R1 from now on). Samples cooled down at 5 and $2.5\text{ }^{\circ}\text{C}\cdot\text{min}^{-1}$ are not monophasic, showing mixtures of the $\text{La}_6\text{MoO}_{12}$ -type and La_4MoO_9 -type structures. Finally, samples cooled at the lowest cooling rate, $0.5\text{ }^{\circ}\text{C}\cdot\text{min}^{-1}$, lead to a single phase with a La_4MoO_9 -type rhombohedral structure (named R2 from now on). Therefore, only samples cooled down by quenching, 50 and $0.5\text{ }^{\circ}\text{C}\cdot\text{min}^{-1}$ are monophasic.

For this composition, the use of a cooling rate of $50\text{ }^{\circ}\text{C}\cdot\text{min}^{-1}$ has turned out to be the key to isolating the R1 phase. In our case, the furnace maintains the cooling rate until it reaches $1100\text{ }^{\circ}\text{C}$, from then on, the cooling rate is slower. However, from this temperature the desired phase has already been obtained, the control of the cooling rate is not being so important from this point. But it is experimentally very complicated since it requires a furnace with very concrete technical specifications, which means that it cannot be easily reproduced in other laboratories. For this reason, from now on in other compositions we have tried to avoid these conditions as much as possible.

To simplify this section, Appendix 6.1 shows other results regarding stability studies and thermal analysis of these materials.

4.1.3. Single-phase existence range.

Once the synthesis temperatures and cooling rates are established, the study was extended to the $\text{La}_{6-x}\text{MoO}_{12-\delta}$ ($0 \leq x \leq 3$) series to analyze how the cationic content influences the structure of the materials.

$\text{La}_{6-x}\text{MoO}_{12-\delta}$ ($x = 0, 0.4, 0.6, 1.0, 1.5, 2.0, 2.5$ and 3.0) compounds were synthesized by heating the precursors from 800 to 1500 °C for 1h and cooling down at 5 °C·min⁻¹. The materials from now on will be named as $\text{La}_{6-x}\text{T-C}$, where 6-x represents the lanthanum content, T is the sintering temperature and C is the cooling rate. XRPD patterns for selected samples and a summary of the phases obtained are shown in Figure 4.3 and Table 4.1, respectively.

Generally, all samples at 800 °C show broad diffraction peaks, due to the nanocrystalline nature of powders that can be indexed using a cubic fluorite as the main phase. At 1000-1300 °C, samples with lanthanum content between $\text{La}_{6.0}$ and $\text{La}_{4.5}$ are a mixture of a cubic fluorite, R1, R2, La_2MoO_6 , and La_2O_3 , except for $\text{La}_{4.5}\text{1100-5}$, which crystallizes as R2 and a monoclinic structure, a composition similar to $\text{La}_{34}\text{Mo}_8\text{O}_{75}$, reported by Dan Vu *et al.*, 2019. For low La/Mo ratios, the monoclinic phase presence is predominant, being monophasic for $\text{La}_{4.0}$ and monoclinic with secondary phases of La_2MoO_6 and $\text{La}_6\text{Mo}_2\text{O}_{15}$ for lower lanthanum contents.

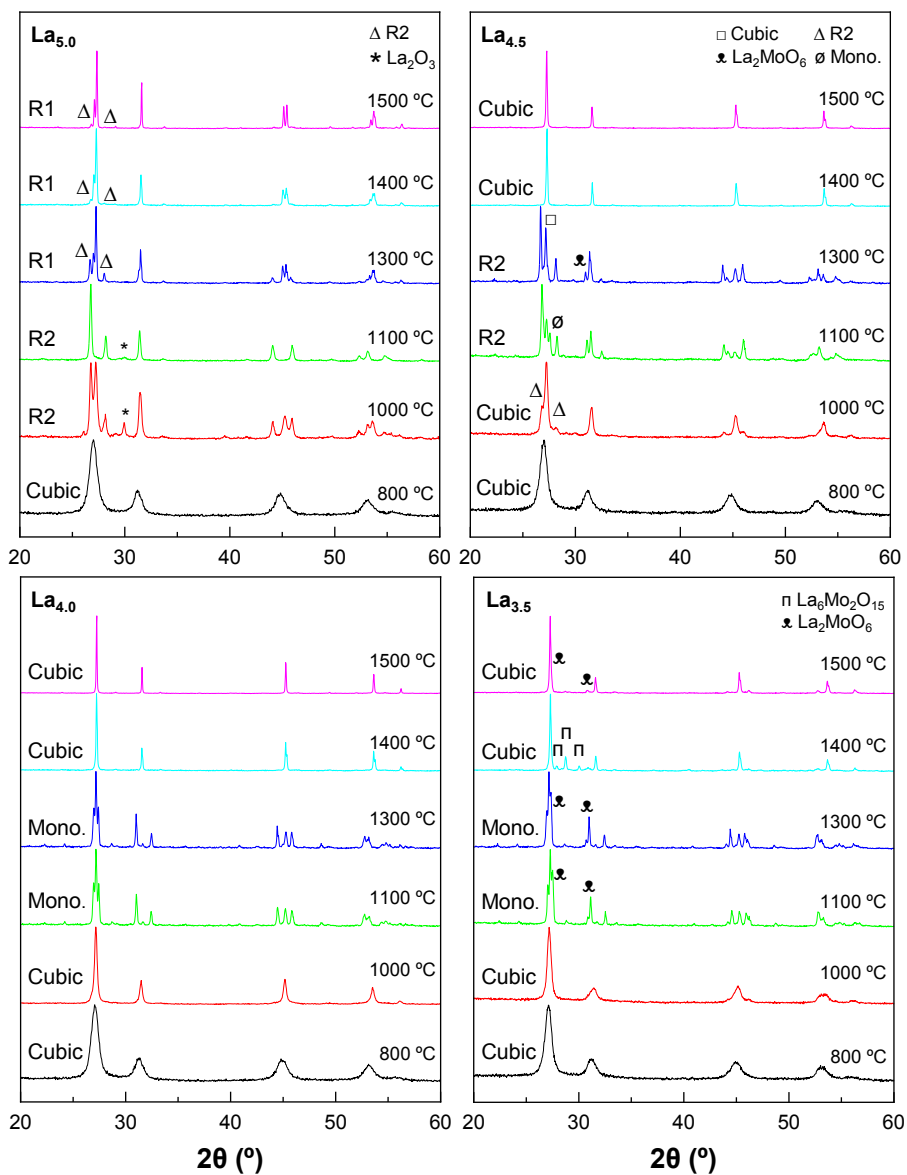


Figure 4.3. XRPD patterns for selected $\text{La}_{6-x}\text{MoO}_{12-\delta}$ ($x = 1.0, 1.5, 2.0$ and 2.5) samples, obtained by heating 1h between 800 and 1500 °C and cooled down at $5\text{ }^\circ\text{C}\cdot\text{min}^{-1}$. The major phase for each sample is denoted at the bottom left of the diffraction patterns and the minor secondary phases are labeled.

Table 4.1. Summary of $\text{La}_{6-x}\text{MoO}_{12-8}$ ($x = 0, 0.4, 0.6, 1.0, 1.5, 2.0, 2.5$ and 3.0) samples obtained by heating 1h between 800 and 1500 °C and cooled down at 5 °C·min⁻¹. The major phase is in bold letters.

La_{6-x}	Sintering Temperature (°C)					
	800	1000	1100	1300	1400	1500
$\text{La}_{6.0}$	R1 Cubic	Cubic R2 La_2O_3	R1 R2 La_2O_3	R2 La_2O_3	R1 R2 La_2O_3	R1 R2 La_2O_3
$\text{La}_{5.6}$	R1 Cubic	Cubic R2 La_2O_3	R1 R2 La_2O_3	R2 La_2O_3	R1 R2 La_2O_3	R1 R2 La_2O_3
$\text{La}_{5.4}$	Cubic	R1 R2 La_2O_3	R1 R2 La_2O_3	R2 La_2O_3	R1 R2	R1 R2
$\text{La}_{5.0}$	Cubic	R2 La_2O_3	R2 La_2O_3	R1 R2	R1 R2	R1 R2
$\text{La}_{4.5}$	Cubic	Cubic R2	R2 Mono.	R2 Cubic La_2MoO_6	Cubic	Cubic
$\text{La}_{4.0}$	Cubic	Cubic	Mono.	Mono.	Cubic	Cubic
$\text{La}_{3.5}$	Cubic	Cubic	Mono. La_2MoO_6	Mono. La_2MoO_6	Cubic $\text{La}_6\text{Mo}_2\text{O}_{15}$	Cubic La_2MoO_6
$\text{La}_{3.0}$	Mono. La_2MoO_6	Mono. La_2MoO_6	Mono. La_2MoO_6	Mono. La_2MoO_6	Mono. $\text{La}_6\text{Mo}_2\text{O}_{15}$ La_2MoO_6	Mono. $\text{La}_6\text{Mo}_2\text{O}_{15}$ La_2MoO_6

At higher temperatures (1400-1500 °C), lanthanum contents of $\text{La}_{6.0}$ and $\text{La}_{5.6}$ present R1 and R2 structures with La_2O_3 segregations, but from $\text{La}_{5.4}$ to $\text{La}_{3.0}$ the samples did not present La_2O_3 . Nevertheless, at these temperatures, $\text{La}_{5.4}$ and $\text{La}_{5.0}$ are mixtures of the R1 and R2 rhombohedral structures. $\text{La}_{4.5}$ and $\text{La}_{4.0}$ crystallize in a cubic structure without side phases.

However, when the lanthanum content is lower than 4, although the main phase is cubic, they are mixed with two additional low La/Mo ratio phases, $\text{La}_6\text{Mo}_2\text{O}_{15}$ (PDF 00-034-1134) and La_2MoO_6 (PDF 01-080-0437), which appear due to the high number of cationic vacancies.

As can be seen in the XRPD analysis, there exist a direct relationship between the lanthanum content and the final structure of the materials. The decrease of the lanthanum content leads to the crystallization of the materials as single phases with cubic symmetry due to the smaller mismatch in the ionic Shannon radii in coordination 8 of La (1.16 Å) and Mo (1.02 Å), not being necessary to use a sudden cooling from high temperature or a rate of $50\text{ }^\circ\text{C}\cdot\text{min}^{-1}$. Nevertheless, a high number of cationic vacancies makes the phases unstable and low La/Mo ratio compounds can segregate. It must be noted that the ionic radii of Mo^{6+} in 8-fold coordination is not reported in Shannon's database; therefore, it has been estimated from the Mo-O distances of several molybdenum-containing compounds: $\text{La}_{2.4}\text{Mo}_{1.6}\text{O}_8$ (ICSD 27006), $\text{Ho}_2\text{MoO}_{4.8}$ (ICSD 261709), $\text{Bi}_{3.2}\text{Mo}_{0.8}\text{O}_{7.5}$ (ICSD 38357) and Mo_3O (ICSD 15903), all of them with a $Fm\bar{3}m$ space group.

The influence of the cooling rate was also analyzed. XRPD patterns of the $\text{La}_{6-x}\text{MoO}_{12-\delta}$ ($x = 0, 0.4, 0.6, 1.0, 1.5, 2.0, 2.5$ and 3.0) series heated at $1500\text{ }^\circ\text{C}$ for 1h and cooled down at different rates (quenching, 5, and $0.5\text{ }^\circ\text{C}\cdot\text{min}^{-1}$) and a summary of the conditions employed to obtain single phases are shown in Figure 4.4 and Table 4.2, respectively.

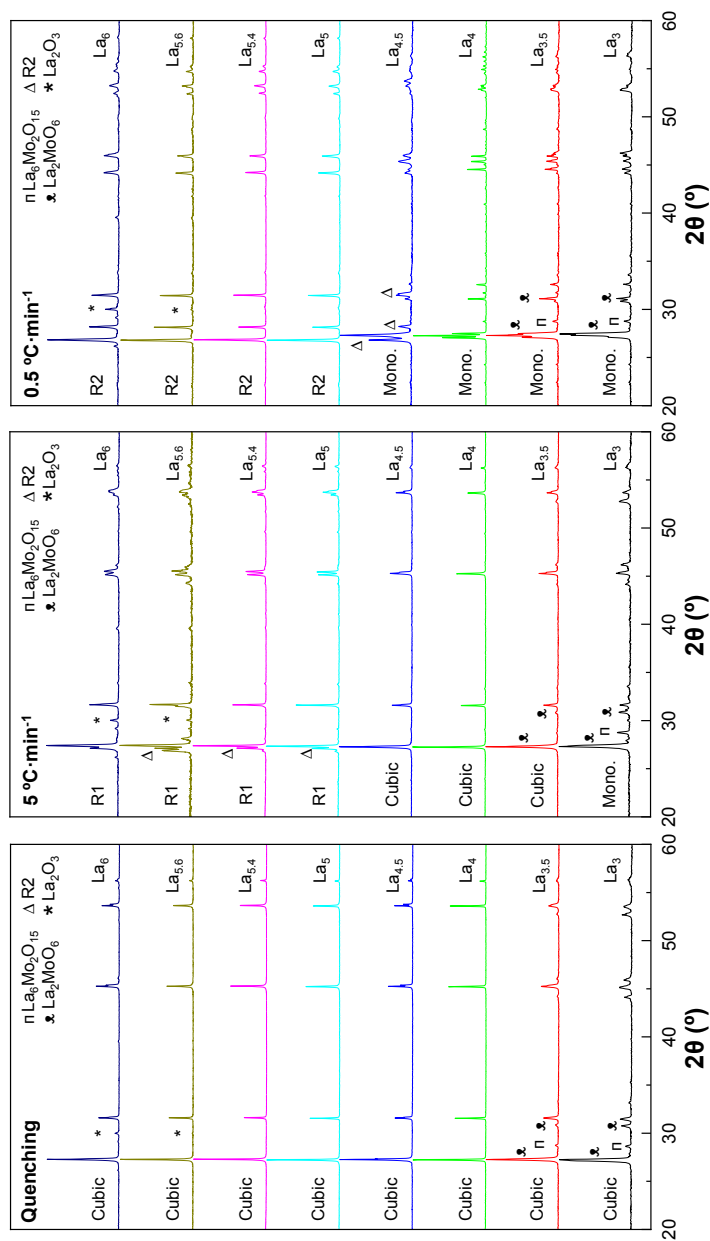


Figure 4.4. XRPD patterns of $\text{La}_{6-x}\text{Mo}_{2-x}\text{O}_{12-3}$ ($x = 0, 0.4, 0.6, 1.0, 1.5, 2.0, 2.5$ and 3.0) series obtained by heating at $1500\text{ }^\circ\text{C}$ 1h and cooled down at different rates (quenching, 5 and $0.5\text{ }^\circ\text{C}\cdot\text{min}^{-1}$). The major phase for each sample is denoted at the bottom left of the diffraction patterns and the minor secondary phases are labelled.

Table 4.2. Summary of cooling rates needed to obtain $\text{La}_{6-x}\text{MoO}_{12-\delta}$ ($0.6 \leq x \leq 2$) single phases by heating the precursors at 1500 °C 1h. Empty cells correspond to conditions that did not lead to single phases*.

Sample	Cooling rate			
	Quenching	50 °C·min ⁻¹	5 °C·min ⁻¹	0.5 °C·min ⁻¹
La_{5.4}	Cubic	R1	-	R2
La_{5.0}	Cubic	R1	-	R2
La_{4.5}	Cubic	-	Cubic	-
La_{4.0}	Cubic	-	Cubic	Monoclinic

*The composition range is reduced compared to the original series. Only monophasic samples are shown in this Table.

All materials cooled down by quenching present a cubic structure but only the samples with lanthanum content between $\text{La}_{5.4}$ to $\text{La}_{4.0}$ are monophasic. Higher lanthanum contents present La_2O_3 segregations and low ones leads to the segregation of secondary phases such as $\text{La}_6\text{Mo}_2\text{O}_{15}$ and La_2MoO_6 .

$\text{La}_{4.5}$ and $\text{La}_{4.0}$ cooled down at 5 °C·min⁻¹ present an average cubic structure by XRPD, however, the materials show cubic and rhombohedral domains by TEM that will be deeply studied in the next section.

Samples cooled down at 0.5 °C·min⁻¹ with high lanthanum contents (between $\text{La}_{6.0}$ to $\text{La}_{5.0}$) crystallize in the R2 structure but only $\text{La}_{5.4}$ and $\text{La}_{5.0}$ are monophasic without La_2O_3 segregation. On the other hand, lanthanum contents between $\text{La}_{4.5}$ to $\text{La}_{3.0}$ present a monoclinic-type structure, although only $\text{La}_{4.0}$ is monophasic without segregations of $\text{La}_6\text{Mo}_2\text{O}_{15}$, La_2MoO_6 , and R2.

Therefore, the control of the synthesis conditions (lanthanum content, heating temperature and cooling rate) results in four different single phases: cubic, R1, R2, and monoclinic. These structures will be studied deeply by different structural characterization techniques in the next sections.

4.2. Structural characterization of $\text{La}_{6-x}\text{MoO}_{12-\delta}$ single phases.

4.2.1. Preliminary studies.

A preliminary structural determination of selected single phases was carried out for the $\text{La}_{5.4}\text{MoO}_{11.1}$ (cubic, R1, and R2) and La_4MoO_9 (monoclinic) compositions in order to acquire a deeper knowledge of these structures and the optimization of the synthesis conditions.

a) Cubic structure.

The cubic structure was studied by the Rietveld method using a fluorite-type structure with the $Fm\bar{3}m$ space group as starting structural model. Firstly, overall parameters were fitted (histogram, scale factors, background, and peak shape coefficients). La and Mo were located in the same crystallographic position, and their contents were fixed to the nominal stoichiometry. The isotropic thermal factors were also constrained to be equal.

The final refinement (s.g. $Fm\bar{3}m$, $Z = 4$, $a = 5.6676(1) \text{ \AA}$; $V = 45.51 \text{ \AA}^3$) converged to $R_{\text{wp}} = 6.9\%$ and $R_{\text{F}} = 3.2\%$, good values that confirm that the adjustment with this model is correct. A Rietveld XRPD plot and a three-dimensional representation of the c-axis view of the structure are shown in Figure 4.5 and 4.6, respectively.

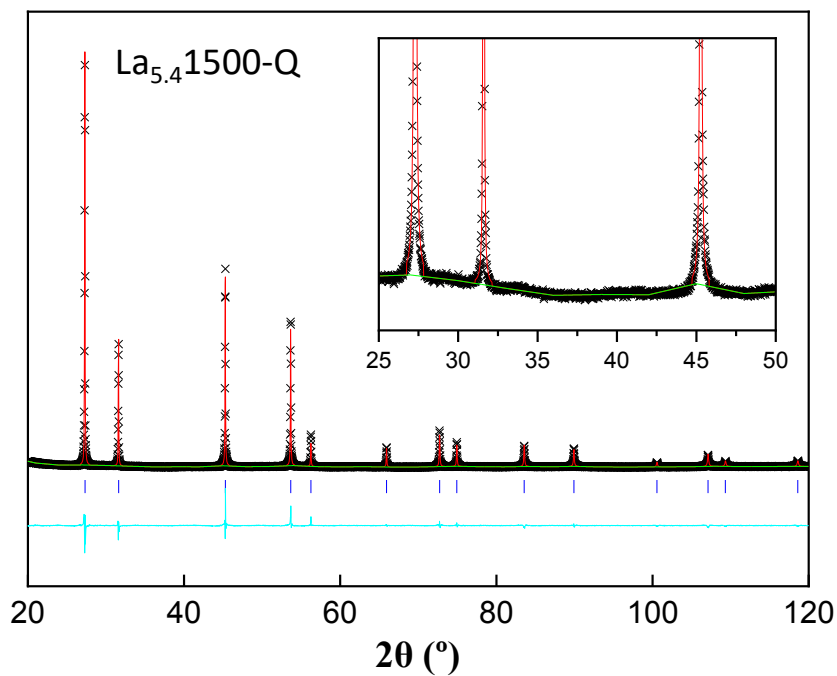


Figure 4.5. Rietveld XRPD plot of $\text{La}_{5.4}\text{MoO}_{11.1}$ obtained by heating at 1500 °C 1h and cooled down by quenching. In the image are represented the experimental data (×××), calculated pattern (—), and difference curve (cyan at the bottom).

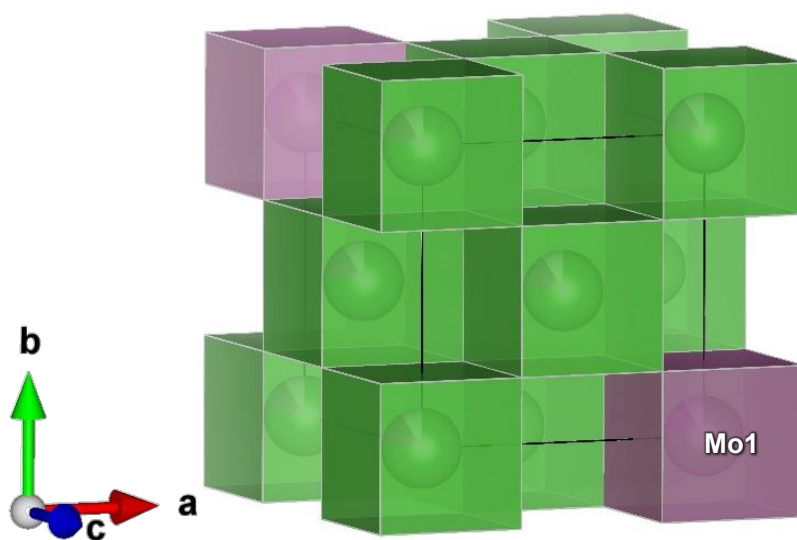


Figure 4.6. c-axis view of the cubic structure of $\text{La}_{5.4}\text{MoO}_{11.1}$ heated at 1500 °C 1h and cooled down by quenching. La and Mo coordination spheres are coloured with green and purple cubes, respectively.

To further confirm the cubic structure of this sample, selected area electron diffraction (SAED) and HRTEM images were obtained (Figure 4.7).

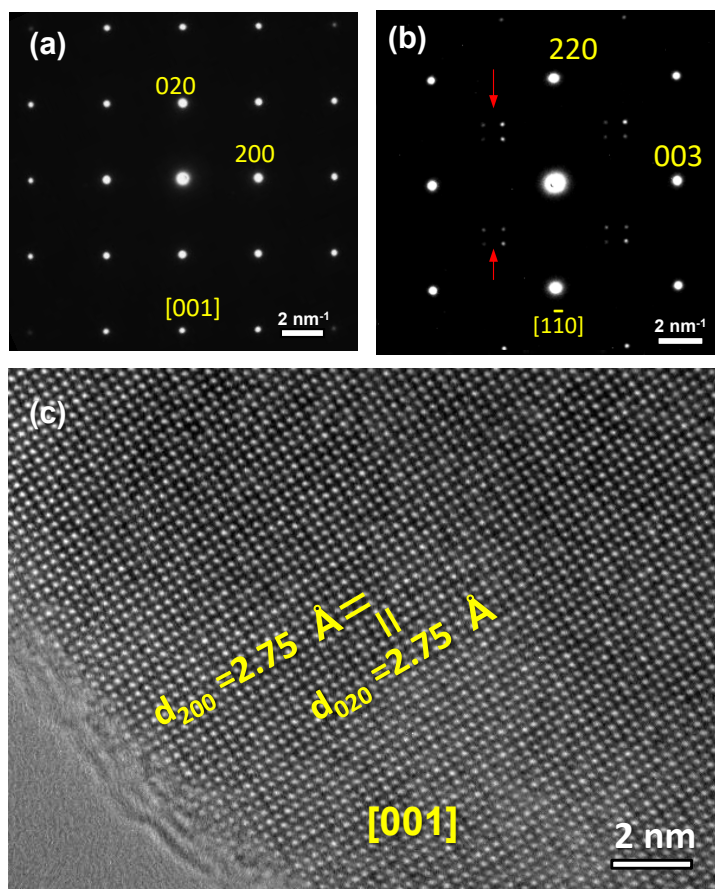


Figure 4.7. SAED patterns (a and b) and HRTEM image (c) of $\text{La}_{5.4}\text{MoO}_{11.1}$ obtained by heating at $1500\text{ }^\circ\text{C}$ 1h and cooled down by quenching along different zone axes. The arrows indicate diffuse scattering due to the structure modulation. The SAEDs are indexed by considering a cubic fluorite-type structure.

The SAED patterns of the quenched samples can be indexed as a cubic fluorite structure, in good agreement with the unit cell parameters determined by XRPD. Nevertheless, in some axes, the SAEDs show faint satellite reflections, which are ascribed to structure modulations due to minor variations in the oxygen sublattice.

b) Rhombohedral structures.

Rhombohedral phases (R1 and R2) have no initial structural models available in the literature. Therefore, the XRPD patterns of $\text{La}_{5.4}\text{1500-50}$ and $\text{La}_{5.4}\text{1500-0.5}$ were indexed using the Dicvol software to determine the basic unit cell from the most intense diffraction peaks (Boultif, 2004). The obtained $R\bar{3}$ cell parameters were used as initial model for the Le Bail analysis of $\text{La}_{5.4}\text{1500-50}$ (R1) and $\text{La}_{5.4}\text{1500-0.5}$ (R2) (Figure 4.8 and 4.9).

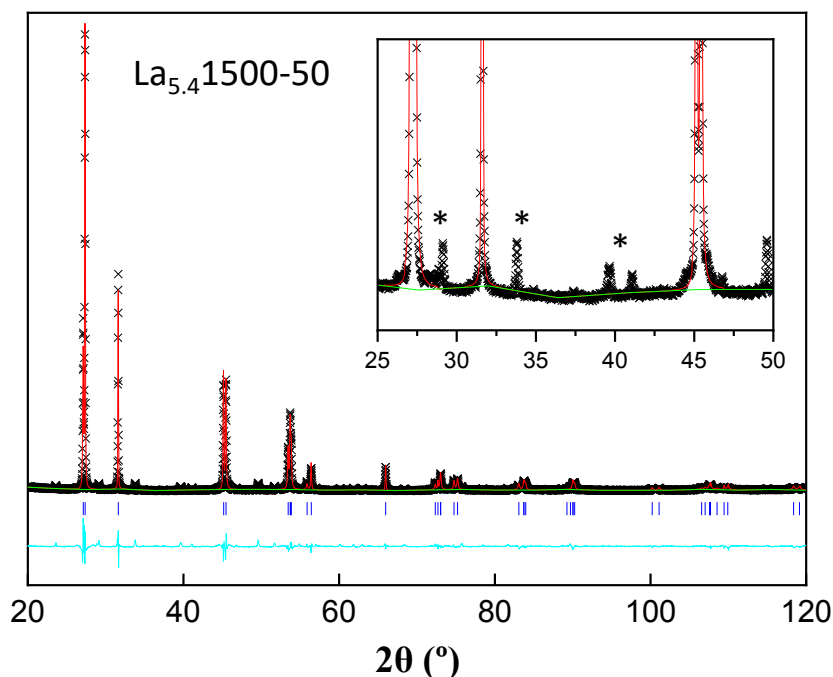


Figure 4.8. Le Bail XRPD plot of $\text{La}_{5.4}\text{MoO}_{11.1}$ obtained by heating at 1500°C 1h and cooled down at $50^\circ\text{C}\cdot\text{min}^{-1}$ (rhombohedral structure R1). In the image are represented the experimental data ($\times\times\times$), calculated pattern (—), and difference curve (cyan at the bottom). Asterisks show the superstructure reflections.

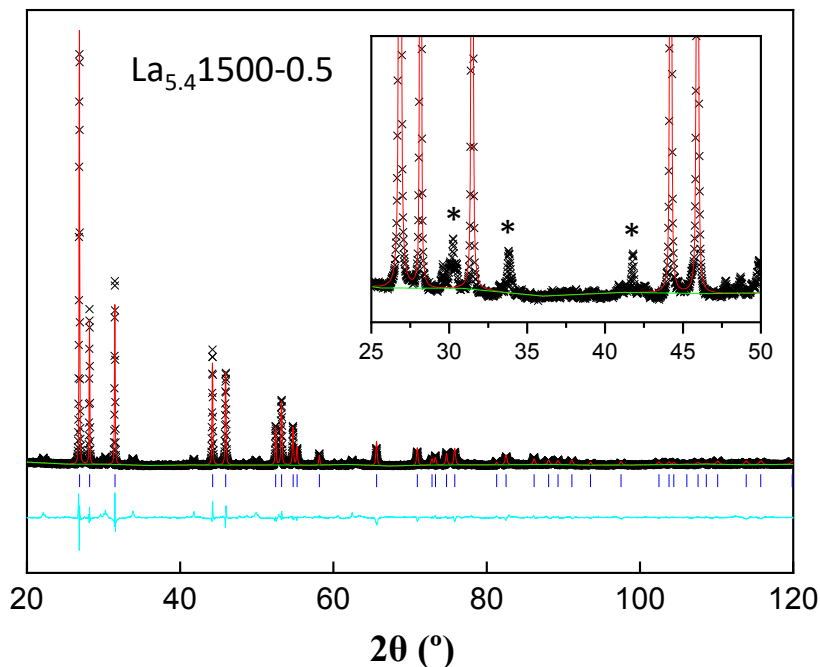


Figure 4.9. Le Bail XRPD plot of $\text{La}_{5.4}\text{MoO}_{11.1}$ obtained by heating at 1500 °C 1h and cooled down at 0.5 °C·min⁻¹ (rhombohedral structure R2). In the image are represented the experimental data (xxx), calculated pattern (—), and difference curve (cyan at the bottom). Asterisks show the superstructure reflections.

The study suggests the presence of superstructures for the R1 and R2 phases due to the presence of some small intensity peaks that could not be indexed (see marks at insets in Figure 4.8 and 4.9). These peaks were also observed in related $\text{La}_{5.5}\text{W}_{0.4}\text{Mo}_{0.6}\text{O}_{12-\delta}$ phases, attributed to superstructure reflections (Amsif *et al.*, 2012). To confirm the presence of the superstructures suggested by the Le Bail analysis, a HRTEM-SAED study was performed (Figure 4.10 and 4.11).

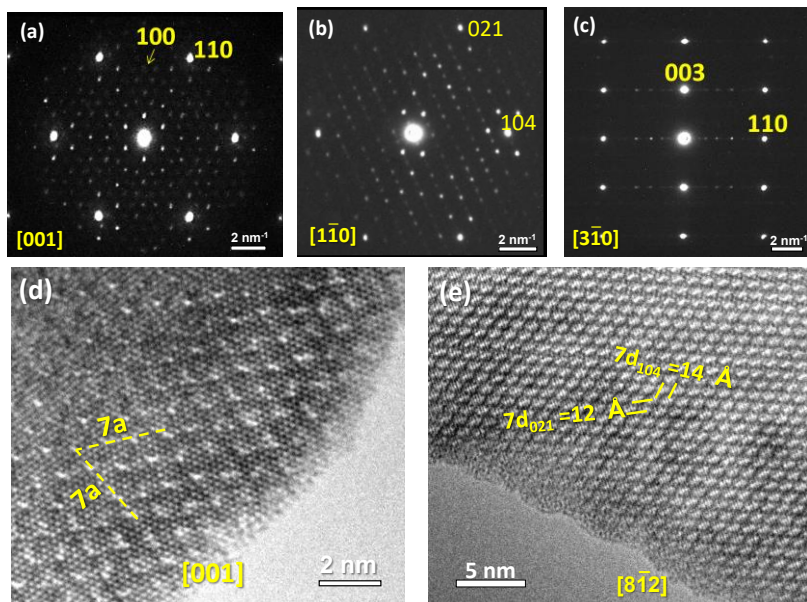


Figure 4.10. SAED patterns (a, b, and c) and HRTEM (d and e) images of $\text{La}_{5.4}\text{MoO}_{11.1}$ obtained by heating at $1500\text{ }^\circ\text{C}$ 1h and cooled down at $50\text{ }^\circ\text{C}\cdot\text{min}^{-1}$ (rhombohedral structure R1). In the pictures appears the $7a \times 7a \times c$ superstructure relative to the basic single unit cell determined by XRPD data.

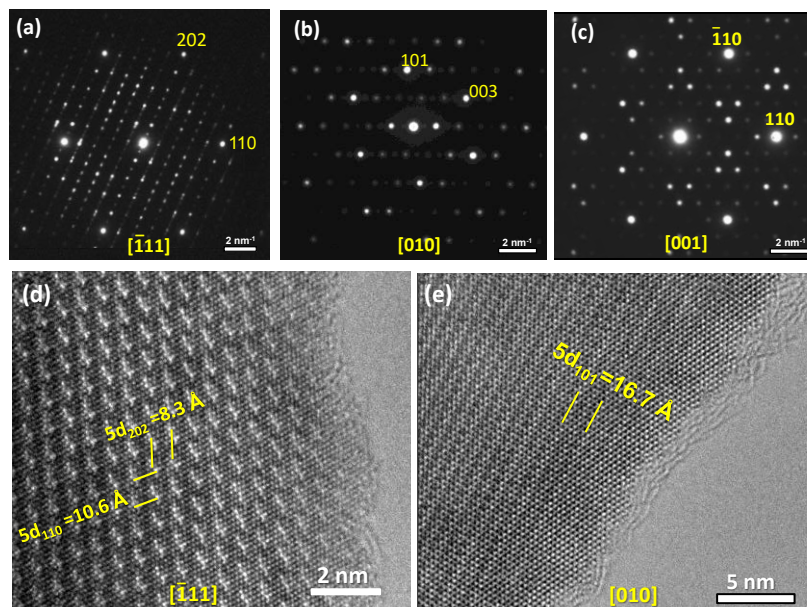


Figure 4.11. SAED patterns (a, b, and c) and HRTEM (d and e) images of $\text{La}_{5.4}\text{MoO}_{11.1}$ obtained by heating $1500\text{ }^\circ\text{C}$ 1h and cooled down at $0.5\text{ }^\circ\text{C}\cdot\text{min}^{-1}$ (rhombohedral structure R2). In the pictures appears the $5a \times 5a \times c$ superstructure relative to the basic single unit cell determined by XRPD data.

For samples cooled down at $50\text{ }^{\circ}\text{C}\cdot\text{min}^{-1}$, some zone axes exhibit superstructure reflections along different directions, which can be induced by some atomic arrangement, likely oxygen variation. The superstructure is reminiscent of that reported by Amsif *et al.* (2012) and can be indexed considering a $7a \times 7a \times c$ superstructure from the basic cell parameters determined by XRPD ($a = 3.99\text{ \AA}$ and $c = 9.87\text{ \AA}$). The HRTEM image in the [001] zones-axis clearly shows the superstructure, and the interplanar spaces are in good agreement with the XRPD data and the proposed $7a \times 7a \times c$ supercell.

The samples cooled down at $0.5\text{ }^{\circ}\text{C}\cdot\text{min}^{-1}$, also present superstructures in some zone axes with different reflections. The patterns can be indexed as a $5a \times 5a \times c$ superstructure from the basic cell parameters determined by XRPD ($a = 4.10\text{ \AA}$ and $c = 9.52\text{ \AA}$). The HRTEM images clearly show the superstructure, and the interplanar distances are in good agreement with the XRPD data and the proposed $5a \times 5a \times c$ supercell.

c) Monoclinic structure.

Monoclinic La_4MoO_9 was studied by the Rietveld method using the structure of $\text{La}_{34}\text{Mo}_8\text{O}_{75}$ as starting model (Dan Vu *et al.*, 2019). Firstly, overall parameters were fitted as usual and occupancy factors were conveniently modified to reflect the theoretical stoichiometry. Isotropic thermal factors were constrained to be equal for different atoms on the same crystallographic site.

Final refinement (s.g. $C12/m1$, $Z = 1$, $a = 17.0611(1)\text{ \AA}$, $b = 12.2095(1)\text{ \AA}$, $c = 9.7479(1)\text{ \AA}$; $V = 45.54(1)\text{ \AA}^3$) converged to $R_{\text{wp}} = 6.42\%$ and $R_{\text{F}} = 9.19\%$. The Rietveld XRPD plot, a three-dimensional representation of the c-

axis view of the structure, refined atomic parameters and atomic distances are shown in Figure 4.12 and 4.13, and Table 4.3 and 4.4, respectively.

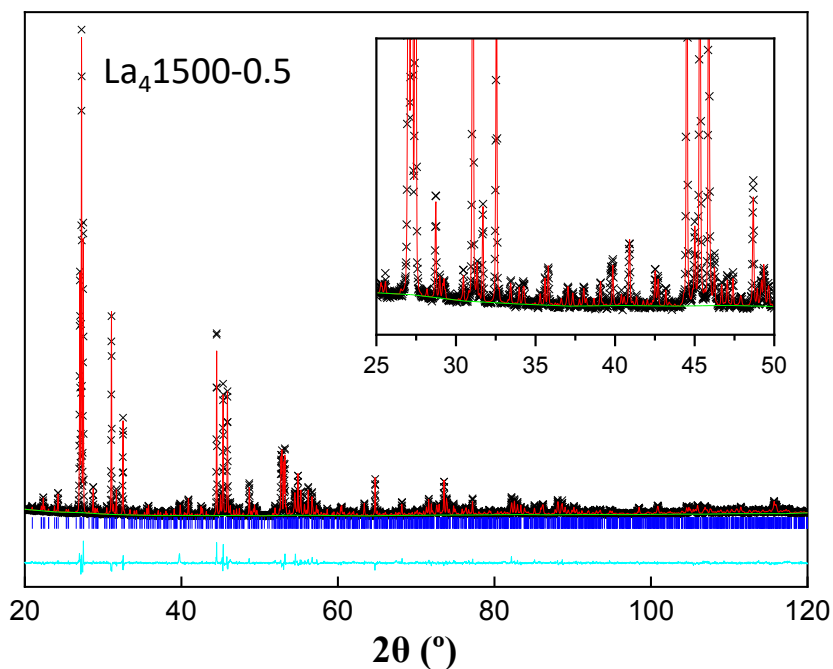


Figure 4.12. Rietveld XRPD plot of La_4MoO_9 obtained by heating at $1500\text{ }^\circ\text{C}$ 1h and cooled down at $0.5\text{ }^\circ\text{C}\cdot\text{min}^{-1}$. In the images are represented the experimental data ($\times\times\times$), calculated pattern (—), and difference curve (cyan at the bottom).

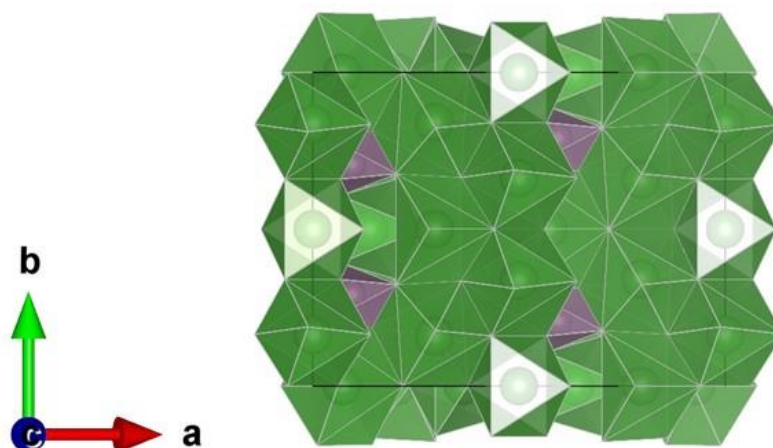


Figure 4.13. c-axis view of the monoclinic structure of La_4MoO_9 obtained by heating at $1500\text{ }^\circ\text{C}$ 1h and cooled down at $0.5\text{ }^\circ\text{C}\cdot\text{min}^{-1}$. The coordination spheres are represented by green and purple cubes, respectively, being the purple one pyramidal molybdenum.

Table 4.3. Refined atomic positions, and isotropic atomic displacement parameters of La₄MoO₉ obtained by heating at 1500 °C 1h and cooled down at 0.5 °C·min⁻¹ (monoclinic structure) from XRPD* in C12/m1 space group.

Atom	x	y	z	Uiso× 100 (Å²)
La1	0.1558(1)	0.1546(2)	0.4197(2)	0.6(-)
La2	0.2038(2)	0	0.1150(2)	0.6(-)
La3	0.36398(2)	0	0.5561(2)	1.3(-)
La4	0.2050(1)	0.3410(2)	0.1550(2)	0.6(-)
La5	0.0708(2)	0	0.6994(3)	0.5(-)
La6	0	0.1631(2)	0	0.5(-)
La7	0	½	0	1.1(-)
Mo1	0.4055(2)	0.2079(2)	0.2378(2)	1.1(-)
O1	0.077(2)	0	0.458(2)	1.3(-)
O2	0.061(1)	0	0.940(2)	1.3(-)
O3	0.234(1)	0	0.375(2)	1.3(-)
O4	0.218(1)	0	0.877(2)	1.3(-)
O5	0.140(1)	0.165(1)	0.167(2)	1.3(-)
O6	0.124(1)	½	0.193(2)	1.3(-)
O7	0.298(1)	0.841(1)	0.598(2)	1.3(-)
O8	0.489(1)	0.311(1)	0.261(2)	1.3(-)
O9	0.356(1)	0.313(1)	0.323(1)	1.3(-)
O10	0.433(1)	0.160(1)	0.070(2)	1.3(-)
O11	0.433(1)	0.107(1)	0.367(1)	1.3(-)
O12	0.298(1)	0.177(2)	0.117(2)	1.3(-)

*These values have been fixed and not refined.

Table 4.4. Interatomic distances of La₄MoO₉ obtained by heating at 1500 °C 1h and cooled down at 0.5 °C·min⁻¹ (monoclinic structure) from XRPD* in C12/m1 space group.

Bond	Distance (Å)	Bond	Distance (Å)
La1-O1	2.41(1)	La4-O4	2.42(2)
La1-O3	2.43(1)	La4-O5	2.43(2)
La1-O5	2.38(1)	La4-O6	2.48(2)
La1-O7	2.43(2)	La4-O7	2.42(1)
La1-O7	2.46(1)	La4-O9	2.56(2)
La1-O8	2.77(1)	La4-O10	2.62(2)
La1-O9	2.61(2)	La4-O12	2.64(2)
La2-O2	2.46(1)	La4-O12	2.65(2)
La2-O3	2.41(2)	La5-O1	2.39(2)
La2-O4	2.41(1)	La5-O1	2.47(2)
(La2-O5)×2	2.42(2)	La5-O2	2.40(2)
(La2-O12)×2	2.68(2)	La5-O4	2.52(2)
La3-O3	2.32(2)	(La5-O8)×2	2.60(2)
La3-O6	2.38(2)	(La5-O9)×2	2.64(2)
(La3-O7)×2	2.34(2)	(La6-O2)×2	2.40(2)
(La3-O11)×2	2.82(2)	(La6-O5)×2	2.39(2)
Mo1-O8	1.85(1)	(La6-O8)×2	2.63(1)
Mo1-O9	1.87(1)	(La6-O10)×2	2.63(2)
Mo1-O10	1.93(1)	(La7-O6)×2	2.31(2)
Mo1-O11	1.71(1)	(La7-O10)×4	2.47(2)
Mo1-O12	1.85(2)		

*These values have been fixed and not refined

For this sample, despite the profile being adequately fit, the refinement does not lead to good R_{wp} and R_F values (6.42% and 9.19%, respectively). This is due to the high structural complexity of the sample and neutron powder diffraction data are required. This structure possesses 7 independent crystallographic positions for lanthanum (three 8-fold, two 7-fold, and two 6-fold) and 1 molybdenum with an unusual 5-fold coordination with pyramidal symmetry.

SAED and HRTEM patterns (Figure 4.14) were registered to analyze the possibility of a superstructure not previously described in the literature. Intense reflections were observed, corresponding to the [001] zone axis of $\text{La}_{4.0}\text{1500-0.5}$ and some reflections reminiscent of the cubic fluorite-type structure. HRTEM images of $\text{La}_{4.0}\text{1500-0.5}$ and cell parameters of the unit cell (s.g. $C12/m1$, $a = 17.070 \text{ \AA}$, $b = 12.204 \text{ \AA}$, $c = 9.742 \text{ \AA}$ and $\beta = 109.58^\circ$) agrees with the reported monoclinic structure. It is important to mention that the monoclinic structure does not present any superstructure like R1 and R2.

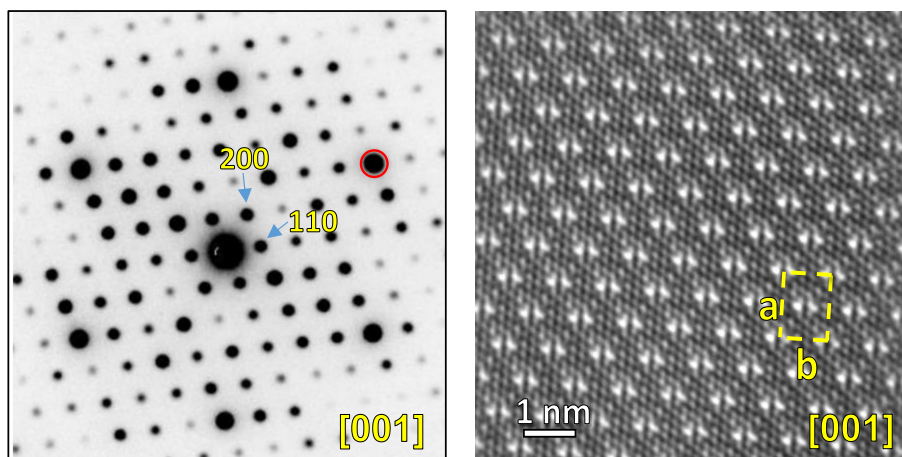


Figure 4.14. SAED patterns (left) and HRTEM (right) images of La_4MoO_9 obtained by heating at 1500°C 1h and cooled down at $0.5^\circ\text{C}\cdot\text{min}^{-1}$. Red circle show reflections reminiscent of cubic fluorite.

4.2.2. Study in depth of the rhombohedral structures.

To fully comprehend the rhombohedral structures of $\text{La}_{5.4}\text{MoO}_{11.1}$ (R1 and R2 phases), we established a collaboration with Prof. Gianguido Baldinozzi from Université Paris-Saclay (France). The enormous unit cell volume (above 6000 \AA^3) and complexity of these structures made it impossible to resolve the structure with “*ab initio*” procedures using exclusively XRPD and NPD data.

In order to solve these structures, firstly, SAED patterns were indexed by the reciprocal vector G by applying the De Wolff’s theory (Janner A. *et al.*, 1983) within the (3+d)-dimensional superspace group approach, because modulated structures often display a set of strong reflections, from the parent structure, and subsets of weaker reflections corresponding to ordered modulations, resulting in:

$$G = ha^* + kb^* + lc^* + m_1q_1 + m_2q_2 + m_3q_3 \quad [28]$$

This reciprocal space vector is uniquely identified with 6 integer indices $(hkl, m_1m_2m_3)$. There are observed different satellite orders when the origin of the modulation is a localized composition fluctuation. The number of independent q_i vectors and their symmetry properties is defined by the superspace group of the crystal. For the R1 and R2 phases, the modulated vectors are commensurate, meaning that they all have a rational relation with the vectors of the average structure.

Figure 4.15, shows the SAED patterns along the $[002]_F$ and $[111]_F$ zone axes for R1 and R2, respectively. Besides the strong reflections corresponding to fluorite structure, weak but quite sharp satellite reflections are also observed. This structure reflections still fulfil the F-lattice extinction rules. These correspond with the strongest reflections observed in the XRPD

patterns and they can be indexed according to the average fluorite-type structure. There is no apparent violation of the F-lattice rule by the set of weaker reflections. This is an interesting point because distortion of the lattice would lift the accidental F-type extinctions leaving only the normal site symmetry reflection conditions.

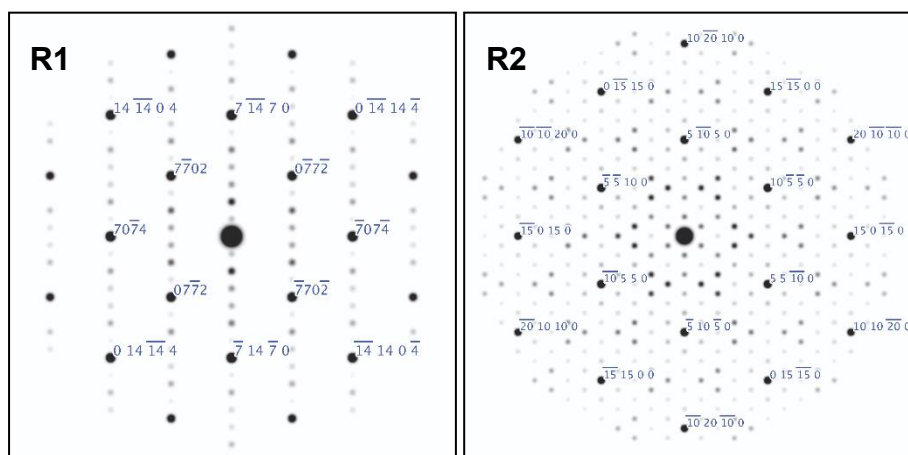


Figure 4.15. SAED patterns of $\text{La}_{5.4}\text{MoO}_{11.1}$; left with an R1 symmetry along the $[002]_F$ zone axis where modulation vectors are of the type $q_{F1} = 1/7 (220)$, and right with an R2 symmetry along the $[111]_F$ zone axis, where modulation vectors are of the type $q_{F1} = 1/5 (220)$.

The satellite reflections in both SAED images can be indexed with rational fractions of the parent structure reciprocal vectors. The satellite reflections in Figure 4.15 (R1), corresponding to the $[002]_F$ zone axis appear to be aligned along with the $[hh0]$ and $[h\bar{h}0]$ directions and can be indexed as $(\alpha\alpha 0)_F$, $(\alpha\bar{\alpha} 0)_F$ with $\alpha = n/7$. This choice of vectors is in good agreement with SAED patterns collected in other zone axes. The satellite reflections in this orientation can be indexed according to a wave vector q_{F1} :

$$q_{F1} = 1/7 \mathbf{a}_F^* + 1/7 \mathbf{b}_F^* \quad [29]$$

The direct lattice transformation from the usual fluorite to the trigonal $R\bar{3}m$ subgroup is:

$$H = \begin{pmatrix} \bar{1}/2 & 0 & 1 \\ 1/2 & \bar{1}/2 & 1 \\ 0 & 1/2 & 1 \end{pmatrix} \quad [30]$$

This subgroup still enforces the previous F-lattice rule on the main reflections. The change of the point groups also opens the possibility to produce 4 ferroelastic variants that might show up as different domains (90°) in the SAEDs. In the $R\bar{3}m$ subgroup, the q_{F1} vector is expressed as $q_{R1} = 1/7 b_R^*$. Considering the point group $R\bar{3}m$, the star of modulation vectors contains 3 branches (e.g., $q_{R2} = 1/7 a_R^*$ and $q_{R3} = \bar{1}/7 a_R^* + \bar{1}/7 b_R^*$). The same analysis can be performed on the R2 polymorph, though with $\alpha = n/5$.

Using this information, we can build supercells of the average $R\bar{3}m$ just multiplying both a_R and b_R by 7 for the R1 and by 5 for the R2 polymorphs. In the case of the $7 \times 7 \times 1$ superstructure the following lattice transformation must be applied to space group $G1 = R\bar{3}m$:

$$P_{R \rightarrow R771} = \begin{pmatrix} 7 & 0 & 0 \\ 0 & 7 & 0 \\ 0 & 0 & 1 \end{pmatrix} \quad [31]$$

This lattice transformation has the effect of generating a space group G3 for the $7 \times 7 \times 1$ supercell that has 1764 symmetry operations. Again, the supplementary elements come from the translation subgroup that now consists of 147 vectors while the point group operations are still the same. The equivalence class of the subgroup $R\bar{3}m$ of G3 consists of 49 cosets to produce the independent atom sites in this large cell. The 20 independent atomic positions of the fluorite structure in the $R\bar{3}m$ space group of the $7 \times 7 \times 1$ supercells are summarized in Table 4.5.

Table 4.5. Independent atoms of the ideal fluorite crystal structure in the $R\bar{3}m$ space group of the $7\times 7\times 1$ supercell.

Atom	x	y	z	Wyckoff	Symmetry
M1	0	0	0	3a	-3m
M2	0	1/7	0	18f	.2
M3	0	2/7	0	18f	.2
M4	0	3/7	0	18f	.2
M5	1/7	2/7	0	18h	.m
M6	1/7	3/7	0	36i	1
M7	1/7	4/7	0	18h	.m
M8	2/7	5/7	0	18h	.m
O1	0	0	1/4	6c	3m
O2	0	1/7	1/4	36i	1
O3	0	2/7	1/4	36i	1
O4	0	3/7	1/4	36i	1
O5	1/7	2/7	1/4	18h	.m
O6	1/7	3/7	1/4	36i	1
O7	1/7	4/7	1/4	18h	.m
O8	2/7	1/7	1/4	18h	.m
O9	2/7	4/7	1/4	18h	.m
O10	3/7	1/7	1/4	36i	1
O11	4/7	1/7	1/4	18h	.m
O12	4/7	2/7	1/4	18h	.m

For the $5 \times 5 \times 1$ superstructure, the first step is to apply the following lattice transformation to the space group $G_1 = R\bar{3}m$:

$$P_{R \rightarrow R551} = \begin{pmatrix} 5 & 0 & 0 \\ 0 & 5 & 0 \\ 0 & 0 & 1 \end{pmatrix} \quad [32]$$

This lattice transformation has the effect of generating a space group G_2 for the $5 \times 5 \times 1$ supercell that has 900 symmetry operations. The supplementary elements come from the translation subgroup that now consists of 75 vectors while the point group operations are still the same. The second step of the process involves a proper choice of the symmetry elements of the translation subgroup compatible with the desired final symmetry that is still $R\bar{3}m$ because the modulated diffraction pattern still respects the F-centre rule. The equivalence class of the subgroup $R\bar{3}m$ of G_2 consists of 25 cosets that are used to produce the independent atom sites in this large cell, differing only by translations. The 12 independent atomic positions of the fluorite structure in the $R\bar{3}m$ space group of the $5 \times 5 \times 1$ supercells are summarized in Table 4.6.

Table 4.6. Independent atoms of the ideal fluorite crystal structure in the $R\bar{3}m$ space group of the $5 \times 5 \times 1$ supercell.

Atom	x	y	z	Wyckoff	Symmetry
M1	0	0	0	3a	-3m
M2	$\bar{2}/15$	$\bar{1}/15$	1/3	18h	.m
M3	$\bar{2}/5$	$\bar{1}/5$	0	18h	.m
M4	0	$\bar{1}/5$	0	18f	.2
M5	$\bar{3}/5$	0	0	18f	.2
O1	0	0	1/4	6c	3m
O2	$\bar{2}/15$	$\bar{1}/15$	1/3 + 1/4	18h	.m
O3	$\bar{2}/5$	$\bar{1}/5$	1/4	18h	.m
O4	0	$\bar{1}/5$	1/4	36i	1
O5	$\bar{1}/5$	$\bar{3}/5$	1/4	18h	.m
O6	$\bar{3}/5$	0	1/4	36i	1
O7	$\bar{8}/15$	$\bar{7}/15$	1/3 + 1/4	18h	.m

The deduced atomic positions for R1 and R2-type structures (Tables 4.5 and 4.6) were used as the initial model for a Rietveld refinement using neutron powder diffraction data (collected at PSI). The proposed structural models were verified by neutron powder diffraction (NPD) because XRPD is not sensible to oxygen atomic ordering. Parameters such as unit cell, scale factor, background, peak shape coefficients, atomic positions, and isotropic displacement parameters were refined. Regarding the type of atom at the

metal positions and occupancy factors, a comprehensive analysis was carried out, where each cation position was tested as lanthanum or molybdenum, adjusting its occupancy to reflect the theoretical formula. The occupancies were freely refined and only those scenarios with reasonable M-O distances and good agreement factors were chosen. Finally, oxygen occupancy factors were refined and those very close to the unit were set to 1 and remained fixed.

Final refinement of the R1 phase (s.g. $R\bar{3}m$, $Z = 3$, $a = 27.9510(9)$ Å, $c = 9.8998(9)$ Å and $V = 6698.1(9)$ Å³) converged to $R_{wp} = 4.09\%$ and $R_F = 3.56\%$. The Rietveld NPD plot, refined atomic parameters and interatomic distances are shown in Figure 4.16, Table 4.7 and 4.8, respectively.

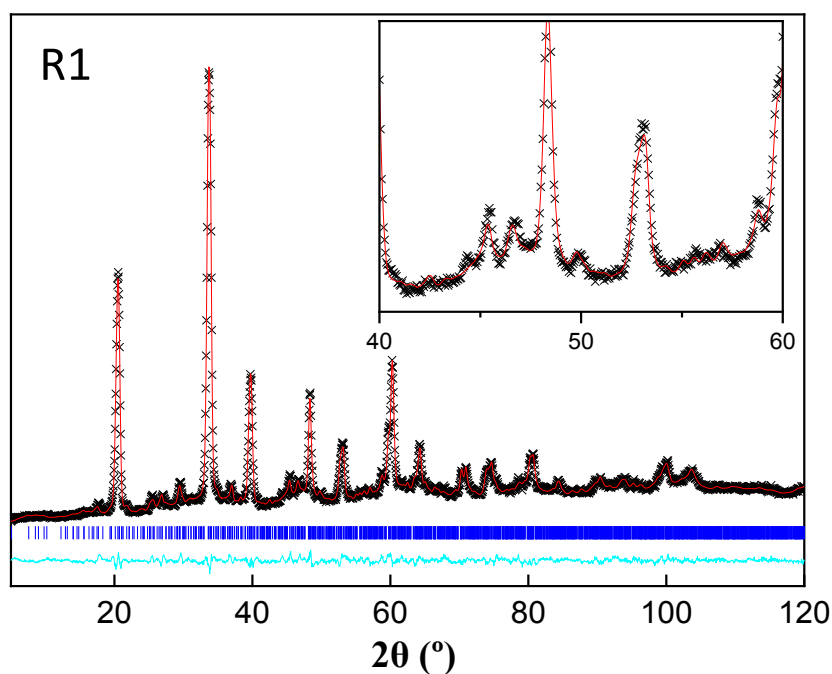


Figure 4.16. Rietveld NPD plot of $\text{La}_{5.4}\text{MoO}_{11.1}$ obtained by heating at 1500 °C 1h and cooled down at 50 °C·min⁻¹ (R1). In the image are represented the experimental data (×××), calculated diagram (—), and difference curve (cyan at the bottom).

Table 4.7. Refined atomic positions, occupancy factors and isotropic atomic displacement parameters of $\text{La}_{5.4}\text{MoO}_{11.1}$ obtained by heating at 1500 °C 1h and cooled down at 50 °C·min⁻¹ (R1) from NPD in $R\bar{3}m$ space group.

Atom	x	y	z	Occ.	Uiso× 100 (Å ²)
Mo1	0	0	0	1(-)	5.4(9)
Mo2	0.1423(4)	0.2846(8)	-0.009(9)	1(-)	0.3(1)
La1	0	0.1431(8)	0	1(-)	3.1(4)
La2	0	0.2727(9)	0	1(-)	12(7)
La3	0	0.4356(9)	0	1(-)	1.8(5)
La4	0.1383(5)	0.4282(5)	0.0083(9)	1(-)	1.5(3)
La5	0.1418(7)	0.5709(4)	-0.017(9)	1(-)	2.0(3)
La6/ Mo3	0.2844(3)	0.7155(4)	0.0150(9)	0.91(3)/0.09(3)	1.2(3)
O1	0	0	0.2127(8)	0.51(7)	0.6(2)
O2	-0.0044(8)	0.1370(8)	0.2646(9)	1(-)	1.4(3)
O3	0.0074(8)	0.3274(8)	0.2787(9)	0.68(3)	8.8(9)
O4	-0.0114(7)	0.4195(7)	0.2429(9)	0.74(3)	5.1(5)
O5	0.1429(9)	0.2859(9)	0.2361(8)	0.65(1)	1.0(4)
O6	0.1523(8)	0.4362(9)	0.2585(8)	1(-)	3.0(4)
O7	0.1500(9)	0.5750(6)	0.2223(9)	0.98(1)	2.3(5)
O8	0.2772(9)	0.1386(6)	0.2455(9)	0.99(1)	5.2(7)
O9	0.2911(6)	0.5823(9)	0.2312(9)	0.77(1)	3.2(7)
O10	0.4199(9)	0.1292(7)	0.2321(9)	1(-)	1.8(3)
O11	0.5716(6)	0.1433(9)	0.2631(9)	1(-)	0.7(3)
O12	0.5788(9)	0.2894(6)	0.2307(9)	0.81(3)	4.7(8)

Table 4.8. Interatomic distances of La_{5.4}MoO_{11.1} obtained by heating at 1500 °C 1h and cooled down at 50 °C·min⁻¹ (R1) from NPD in *R* $\bar{3}$ *m* space group.

Bond	Distance (Å)	Bond	Distance (Å)
(La1-O2)×2	2.62(1)	(La5-O2)×2	2.48(1)
(La1-O10)×2	2.71(1)	La5-O5	2.42(1)
(La1-O11)×2	2.40(1)	(La5-O6)×2	2.26(1)
(La1-O12)×2	2.61(1)	La5-O7	2.38(1)
(La2-O3)×4	2.42(1)	La5-O9	2.85(1)
(La2-O4)×2	2.28(1)	La5-O11	2.43(1)
(La2-O10)×2	2.02(1)	La6-O1	2.54(1)
(La3-O3)×2	2.89(1)	(La6/Mo3-O2)×2	2.29(1)
(La3-O4)×2	2.43(1)	(La6/Mo3)-O7	2.28(1)
(La3-O5)×2	2.34(1)	(La6/Mo3-O9)×3	2.38(1)
(La3-O6)×2	2.60(1)	(La6/Mo3)-O12	2.44(1)
La4-O2	2.48(1)	(Mo1-O1)×2	2.11(1)
La4-O3	2.85(1)	(Mo1-O12)×6	2.36(1)
La4-O4	2.88(1)	(Mo2-O4)×2	2.48(1)
(La4-O6)×2	2.45(1)	Mo2-O5	2.43(1)
La4-O7	2.70(1)	(Mo2-O8)×2	2.48(1)
La4-O8	2.51(1)	(Mo2-O10)×2	2.60(1)
La4-O10	2.39(1)	Mo2-O11	2.42(1)

Mo was placed in two positions, one at the origin of coordinates, M1 (0 0 0), a position confirmed by the shorter M-O distances, indicative of a Mo-O bond; and the other one in M5. On the other hand, M2, M3, M4, M6, and M7 were assigned to lanthanum. All these positions (M1-M7) possess a full occupancy (Table 4.6). The M8 position was split between La and Mo, with final occupancy factors of 0.91(3) and 0.09(3), respectively. Therefore, there are eight MO₈ distorted cubes sharing edges (5 of lanthanum, 2 of molybdenum, and 1 shared by lanthanum and molybdenum), all of them with reasonable bond distances of 2.02-2.89 Å (La-O) and 2.11-2.60 Å (Mo-O) considering the structural complexity, the high number of atoms in the unit cell (402) and the large cell volume, close to 6700 Å³.

Finally, it is important to underline that the crystallographic formula obtained from the refinement (Table 4.7), La_{5.48}MoO_{11.265}, is very close to the correctly balanced stoichiometry, La_{5.48}MoO_{11.22}, and the nominal one, La_{5.4}MoO_{11.1}. Moreover, the crystallographic density (5.834 g·cm⁻³) is quite close to that measured experimentally in dense ceramic pellets (5.811 g·cm⁻³) confirming the validity of the proposed structural model.

The refinement of the R2 phase (s.g. $R\bar{3}m$, $Z = 3$, $a = 20.4941(5) \text{ \AA}$; $c = 9.5183(5) \text{ \AA}$ and $V = 3463.1(8) \text{ \AA}^3$) converged to $R_{wp} = 6.52\%$ and $R_F = 3.84\%$. The Rietveld NPD plot, refined atomic parameters and interatomic distances are shown in Figure 4.17, Table 4.9 and 4.10, respectively.

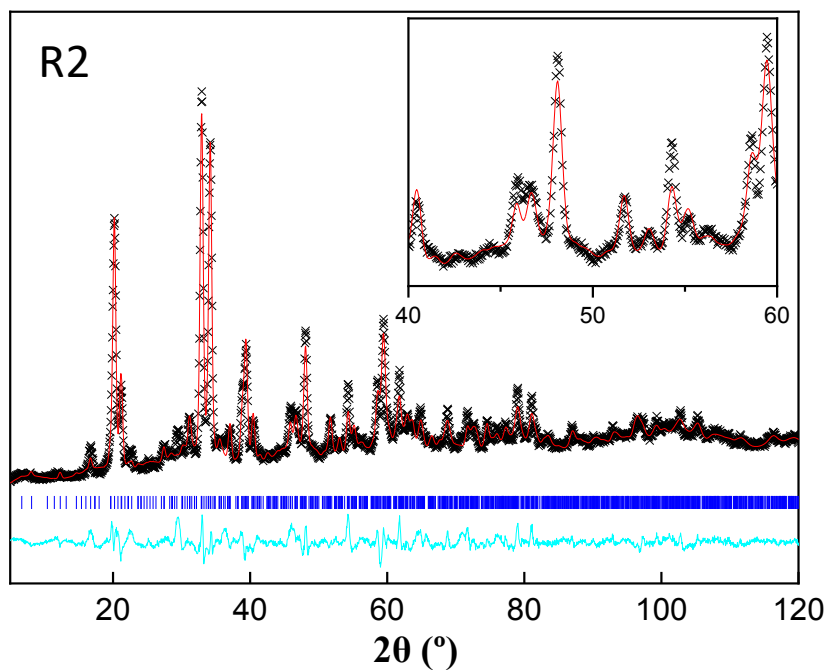


Figure 4.17. Rietveld NPD plot of $\text{La}_{5.4}\text{MoO}_{11.1}$ obtained by heating at $1500 \text{ }^\circ\text{C}$ 1h and cooled down at $0.5 \text{ }^\circ\text{C}\cdot\text{min}^{-1}$ (R2). In the image are represented the experimental data (x×x), calculated diagram (—), and difference curve (cyan at the bottom).

Table 4.9. Refined atomic positions, occupancy factors and isotropic atomic displacement parameters of $\text{La}_{5.4}\text{MoO}_{11.1}$ obtained by heating at 1500 °C 1h and cooled down at 0.5 °C·min⁻¹ (R2) from NPD in $R\bar{3}m$ space group.

Atom	x	y	z	Occ.	Uiso× 100 (Å ²)
Mo1	0	0	0	1(-)	9.7(9)
La1/ Mo2	-0.1328(7)	-0.0664(3)	0.3375(9)	0.53(4)/0.47(4)	0.5(2)
La2	0	-0.2185(5)	0	1(-)	1.7(3)
La3	-0.5883(4)	0	0	1(-)	0.3(1)
La4	-0.4046(3)	-0.2023(5)	0	1(-)	0.8(2)
O1	0	0	¼(-)	0.07(2)	0.5(2)
O2	-0.1180(9)	-0.0590(6)	0.6069(9)	1(-)	2.3(5)
O3	-0.3986(9)	-0.1993(4)	0.2571(8)	1(-)	0.5(2)
O4	0.0017(4)	-0.1961(8)	0.2220(9)	1(-)	5.6(3)
O5	-0.2108(9)	-0.6054(9)	0.2449(4)	1(-)	2.4(3)
O6	-0.6029(9)	-0.0130(8)	0.2663(9)	0.88(2)	2.5(4)
O7	-0.5348(6)	-0.4651(6)	0.5937(9)	0.70(3)	1.2(3)

Table 4.10. Interatomic distances of $\text{La}_{5.4}\text{MoO}_{11.1}$ obtained by heating at 1500 °C 1h and cooled down at 0.5 °C·min⁻¹ (R2) from NPD in $R\bar{3}m$ space group.

Bond	Distance (Å)	Bond	Distance (Å)
(Mo1-O1)×2	2.38(1)	(La2-O4)×2	2.58(2)
(Mo1-O5)×6	2.33(1)	(La2-O6)×2	2.32(1)
(La1/Mo2)-O1	2.50(1)	(La2-O7)×2	2.46(1)
(La1/Mo2-O2)×3	2.40(1)	(La3-O4)×2	2.16(1)
(La1/Mo2)-O3	2.49(1)	(La3-O5)×2	2.89(1)
(La1/Mo2-O4)×2	2.55(1)	(La3-O6)×2	2.37(1)
(La1/Mo2)-O5	2.38(1)	(La3-O7)×2	2.48(1)
La2-O2	2.62(1)	(La4-O3)×2	2.27(1)
La2-O3	2.46(1)	(La4-O4)×2	2.63(1)
		(La4-O6)×4	2.57(1)

Molybdenum is in the origin of coordinates, M1, M3, M4, and M5 were assigned to lanthanum with full occupancy. M2 was split between La and Mo, with final occupancies of 0.53(4) and 0.47(4), respectively. There are five MO_8 distorted cubes sharing edges, 3 of lanthanum, 1 of molybdenum, and 1 shared by lanthanum and molybdenum, with reasonable bond distances of 2.16-2.89 Å (La-O) and 2.33-2.55 Å (Mo-O) considering that the structure has 209 atoms and a cell volume close to 3500 Å³. The crystallographic formula, $\text{La}_{5.52}\text{MoO}_{11.7}$, and density, 5.793 g·cm⁻³, obtained from the refinement is very close to the correctly balanced stoichiometry,

$\text{La}_{5.52}\text{MoO}_{11.28}$, and the experimental density, $5.717 \text{ g}\cdot\text{cm}^{-3}$, suggesting the validity of the R2 model.

Although, despite the accuracy of both models, the broad range in La(Mo)-O distances might indicate a higher level of disorder in the cationic positions, which is difficult to address with diffraction powder techniques, being necessary for the use of single-crystal diffraction studies.

All cationic environments in both models possess an 8-fold cubic coordination, where the cubes are sharing edges. In addition, the cationic distribution of the R1 and R2 phases has been defined for $\text{La}_{5.4}\text{MoO}_{11.1}$, and it can be understood how the different polymorphs are formed by adapting the synthesis-sintering conditions. At a very high temperature, $1500 \text{ }^\circ\text{C}$, due to the thermal agitation, lanthanum and molybdenum are disordered in a single crystallographic position M1 (0,0,0), creating a cubic structure that can only be isolated for this composition by quenching. For that symmetry, each La (Mo) is surrounded by eight oxygens at 2.45 \AA .

However, when the cooling rate is set at a slower rate, the molybdenum ordering becomes quite evident. For R1, which can be obtained for $\text{La}_{5.4}\text{MoO}_{11.1}$ at a cooling rate of $50 \text{ }^\circ\text{C}\cdot\text{min}^{-1}$, molybdenum/dopant (as will be seen in phases where the cationic framework is modified by doping) is in three different positions: the initial one, M1 (0,0,0) and two new ones, M5 ($1/7, 1/7, 0$) and M8 ($2/7, 5/7, 0$) (Table 4.7). The slowest cooling rate, $0.5 \text{ }^\circ\text{C}\cdot\text{min}^{-1}$, favours the most thermodynamically stable structural arrangement, where one molybdenum remains in the M1 position and the other two converge to the new and final M2 position ($-2/15, -1/15, 1/3$) (Table 4.9). The similarities between the three phases are quite evident wherein in any phase transition there is no breaking of chemical bonds, only slight readjustments to efficiently accommodate the molybdenum.

Therefore, each polymorph is convertible into the other two by heating at high temperature and controlling the cooling rate. The structural characterization can be summarized with a polyhedral representation that clarifies the complex rhombohedral structures (Figure 4.18).

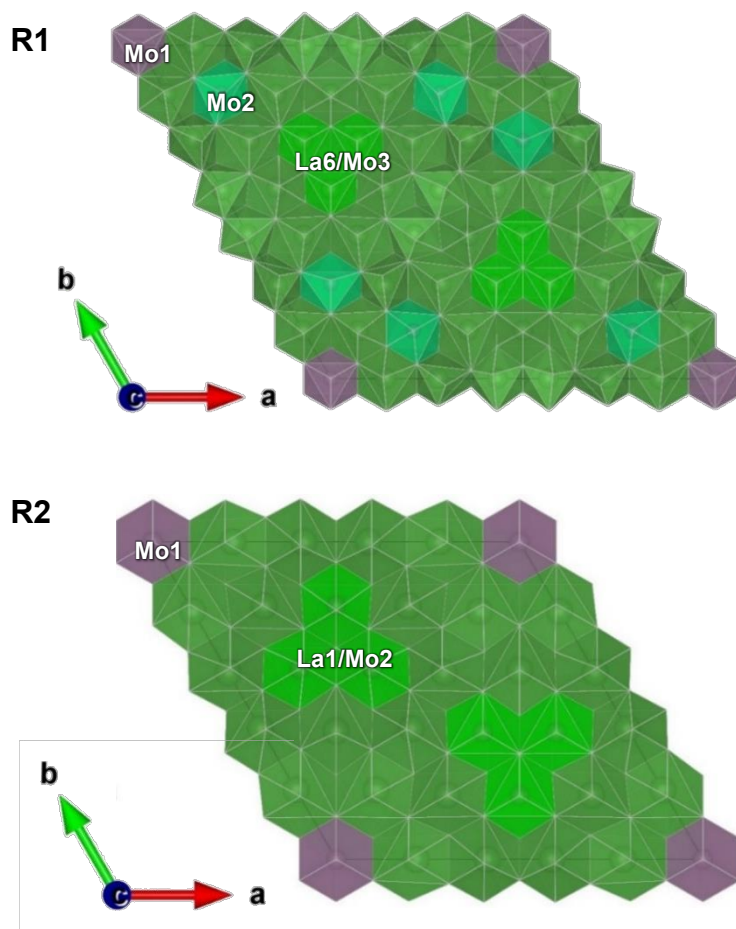


Figure 4.18. c-axis view of the rhombohedral structures of $\text{La}_{5.4}\text{MoO}_{11.1}$ obtained by heating at $1500\text{ }^\circ\text{C}$ 1h and cooled down at 50 and $0.5\text{ }^\circ\text{C}\cdot\text{min}^{-1}$, R1, and R2, respectively. La-Mo coordination spheres are represented by green and purple cubes. Atomic positions occupied by both lanthanum and molybdenum are in lighter green.

On the other hand, as mentioned previously, the monoclinic phase is stable between 1100 and 1300 °C for La_4 , which can be transformed into a cubic fluorite by heating at 1500 °C and cooling by quenching or at $5\text{ °C}\cdot\text{min}^{-1}$. These conditions allow the La/Mo atoms to be completely disordered occupying M1 (0,0,0). The transition between the monoclinic and cubic fluorite is possible and reversible. It is necessary to break down at least all non-8-fold polyhedral by heating at 1500 °C and cooling very slowly at $0.5\text{ °C}\cdot\text{min}^{-1}$, permitting the arrangement of the molybdenum atoms in a pyramidal coordination. A very similar behaviour to that of the R2 phase, where only a very slow cooling permitted the stabilization of that symmetry.

4.3. General characterization and trends of $\text{La}_{6-x}\text{MoO}_{12-\delta}$ single phases.

4.3.1. Structural characterization.

Monophasic cubic compounds belonging to the $\text{La}_{6-x}\text{MoO}_{12-\delta}$ ($0.0 \leq x \leq 3.0$) series (Table 4.2) were further characterized by several techniques to achieve a deeper understanding of the influence of lanthanum content and structures in the final properties.

Unit cell parameters, cell volumes, and agreement factors obtained by XRPD Rietveld refinements are shown in Table 4.11. As has been said before, it is important to mention that the R1 and R2 structures only can be employed with NPD data because XRPD is not sensible to the oxygen ordering in the superstructure. Therefore, samples presenting a R1 or R2 symmetry were analysed by the Le Bail method using basic unit cells.

Table 4.11. Unit cell parameters, cell volumes and agreement factors of $\text{La}_{6-x}\text{MoO}_{12-8}$ ($x = 0.6, 1, 1.5,$ and 2.0) obtained by heating at $1500\text{ }^\circ\text{C}$ 1h and cooled down at different rates (quenching, 5 and $0.5\text{ }^\circ\text{C}\cdot\text{min}^{-1}$) determined by Rietveld refinements of XRPD data.

Samples	a (Å)	V/Z (Å ³)	R _{wp} (%)	R _F (%)
La_{5.4}1500-Q	5.6676(1)	45.51(1)	6.87	3.15
La_{5.0}1500-Q	5.6686(1)	45.54(1)	6.29	3.99
La_{4.5}1500-Q	5.6695(1)	45.56(1)	5.79	3.68
La_{4.5}1500-5	5.6605(1)	45.36(1)	8.40	4.86
La_{4.0}1500-Q	5.6704(1)	45.58(1)	5.51	2.81
La_{4.0}1500-5	5.6621(1)	45.39(1)	7.58	2.13

For quenched samples, $\text{La}_{5.4}$, $\text{La}_{5.0}$, $\text{La}_{4.5}$, and $\text{La}_{4.0}$, the cell volumes are 45.51(1), 45.54(1), 45.56(1), and 45.58(1) Å³, respectively. This variation is small and complex likely due to the interplay of two factors:

- The decrease in lanthanum content should slightly contract the structure.
- The decrease in the oxygen content weakens the framework, allowing its expansion, counterbalancing the volume reduction caused by the lanthanum content.

The small differences in cell volume between samples with the same composition but different cooling conditions might be ascribed to slight deviations in the oxygen content caused by the different rates.

Also, it must be mentioned that XRPD data of $\text{La}_{4.5}1500-5$ and $\text{La}_{4.0}1500-5$ present overlapped peaks corresponding to cubic and rhombohedral domains. To understand these phenomena HRTEM-SAED images were taken of those samples.

HRTEM images of $\text{La}_{4.5}\text{1500-5}$ and $\text{La}_{4.0}\text{1500-5}$ show the complexity of these samples. It can be seen that for both compositions there are cubic and rhombohedral domains cohabiting (Figure 4.19). This is confirmed by SAED calculated from the different domains, which reveal different orderings, in good agreement with the polymorphs previously discussed, as the transition between them just requires minor readjustments of the sublattices.

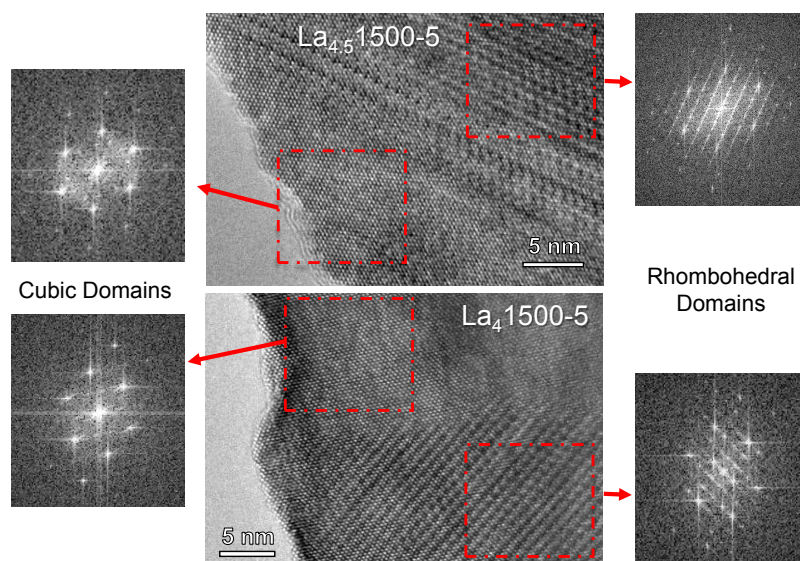


Figure 4.19. HRTEM images and SAED patterns of $\text{La}_{4.5}\text{MoO}_{9.75}$ and La_4MoO_9 compositions obtained by heating at 1500 °C 1h and cooled down at 5 °C·min⁻¹. The images confirmed the co-existence of cubic and rhombohedral domains.

4.3.2. Microstructure of the materials.

Figure 4.20 shows selected SEM micrographs obtained for single phases sintered at 1500 °C for 1h and cooled down at different rates. The samples have low porosity without segregations at the grain boundary. The SEM micrographs were analysed to evaluate the average grain size. On one hand, the grain size increases as the lanthanum content decreases (i.e., from 15.8 to 19.2 μm for La_{5.4}1500-Q to La_{4.0}1500-Q, respectively). On the other hand, samples cooled down at low cooling rates have a higher average grain size, due to fact that these materials remain more time at high temperatures allowing the grain to grow more. The largest average grain size is for the sample La_{5.4}1500-0.5 with values of 21.2 μm , and the lowest average grain size is for La_{5.4}1500-Q with values of 15.8 μm .

Materials were also studied by EDX in different points to determine the La/Mo ratio for all samples. The distribution of lanthanum and molybdenum is homogeneous without any other secondary phase segregations confirming that the samples are monophasic (Figure 4.21). The analysis confirms that the compositions are near to the nominal stoichiometries (Table 4.12).

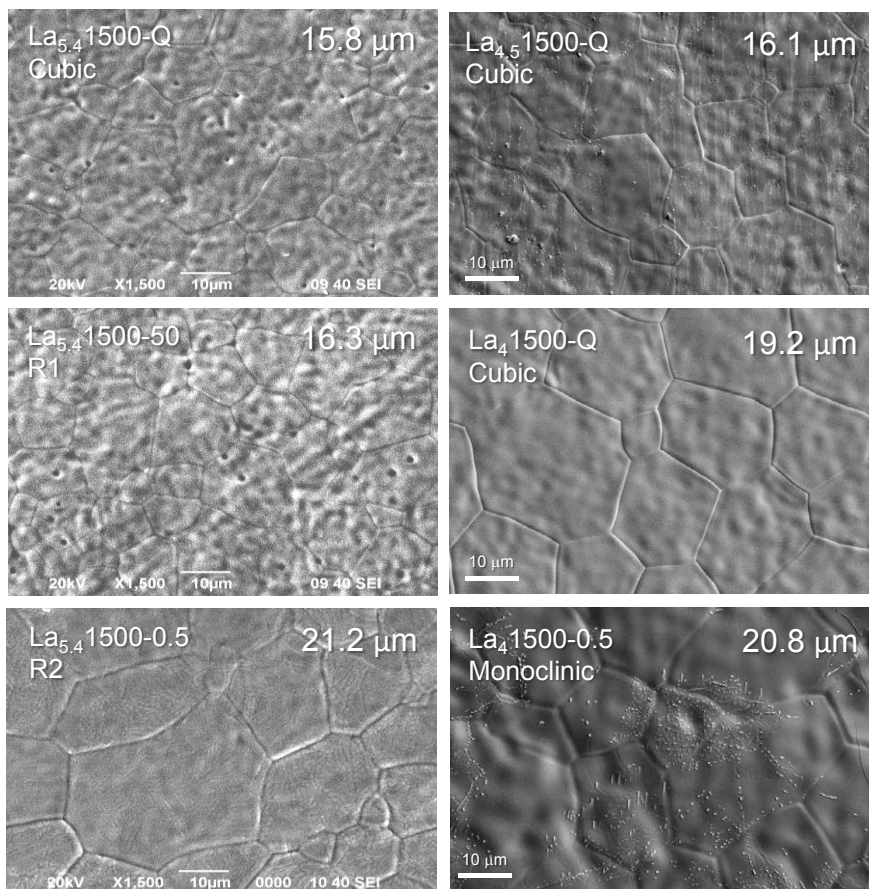


Figure 4.20. SEM micrographs of $\text{La}_{6-x}\text{MoO}_{12-\delta}$ ($x = 0.6, 1.5, 2$) obtained by heating at $1500\text{ }^\circ\text{C}$ 1h and cooled down at different rates, comparing the grain size with each structure obtained.

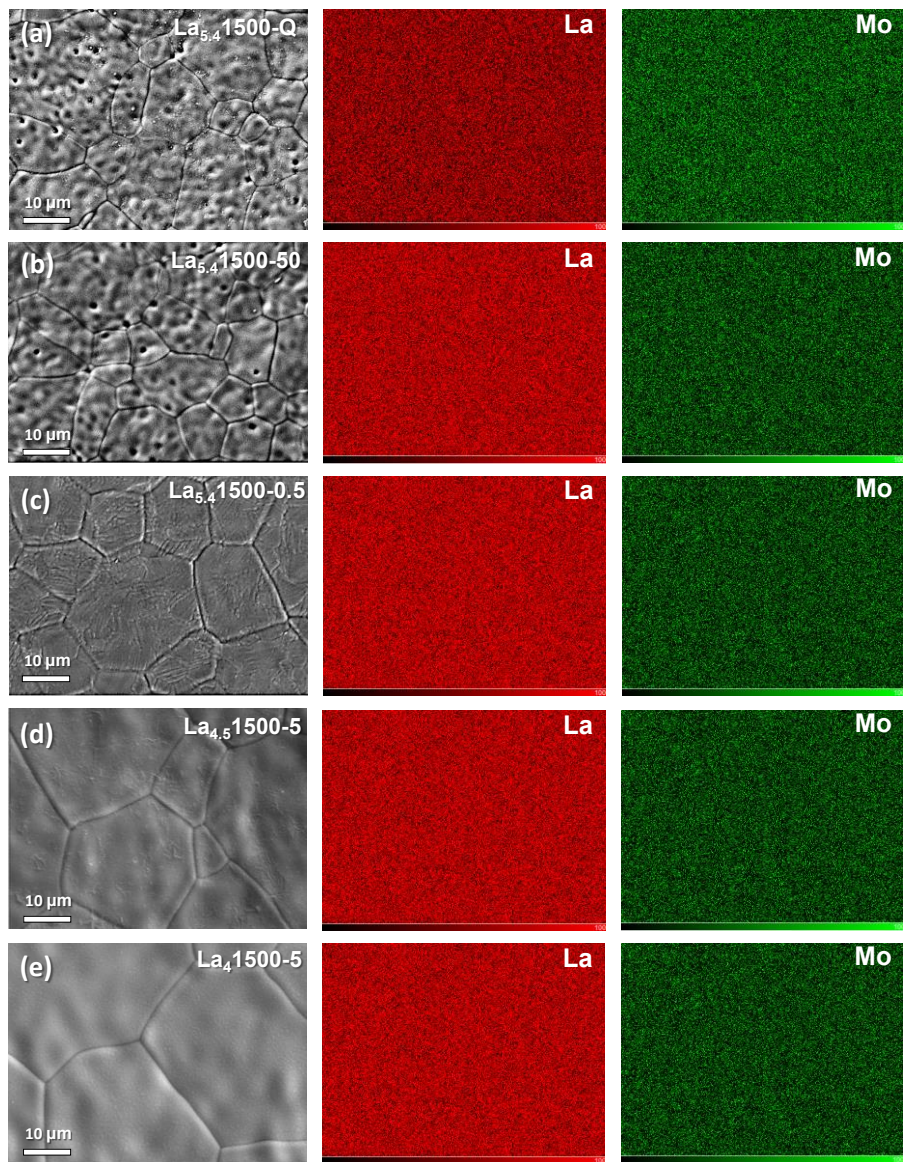


Figure 4.21. EDS images of surfaces and La, Mo elemental mappings of $\text{La}_{6-x}\text{MoO}_{12-\delta}$ ($x = 0.6, 1.5, 2$) obtained by heating at $1500\text{ }^\circ\text{C}$ for 1h and cooled down at different rates.

Table 4.12. Bulk cation concentration (at. %) determined by EDX for $\text{La}_{5.4}\text{MoO}_{11.1}$ obtained by heating at 1500 °C 1h and cooled down at different rates (quenching, 50, and 0.5 °C·min⁻¹).

Sample	La	Mo	La/Mo
La_{5.4}1500-Q	84.1(4)	15.9(1)	5.2(9)
La_{5.4}1500-50	83.9(3)	16.1(2)	5.2(1)
La_{5.4}1500-0.5	84.2(2)	15.8(3)	5.3(2)

In addition, is important to remark that the superficial atomic concentration was also studied by XPS. The obtained results are shown in Appendix 6.2 and confirm that the La/Mo ratios are close to nominal ones, similar to the values obtained from EDX.

4.3.3. Electrical characterization.

To study their electrical properties, the samples were sintered as ceramic pellets of approximately 10 mm in diameter and 1 mm in thickness, prepared at 2 MPa. All exhibit a high relative density (above 95%) compared with the theoretical density obtained by the Rietveld method, as it was discussed in the previous section.

The monophasic samples were analysed by impedance spectroscopy under dry/wet N_2 and wet H_2 , in order to analyse the different contributions to the overall conductivity: ionic, electronic and protonic. Figure 4.22 shows the selected Nyquist plots of $\text{La}_{5.4}\text{1500-Q}$, $\text{La}_{4.5}\text{1500-Q}$, and $\text{La}_{4.0}\text{1500-Q}$. The experimental data was adjusted by equivalent circuits with the Z-View program.

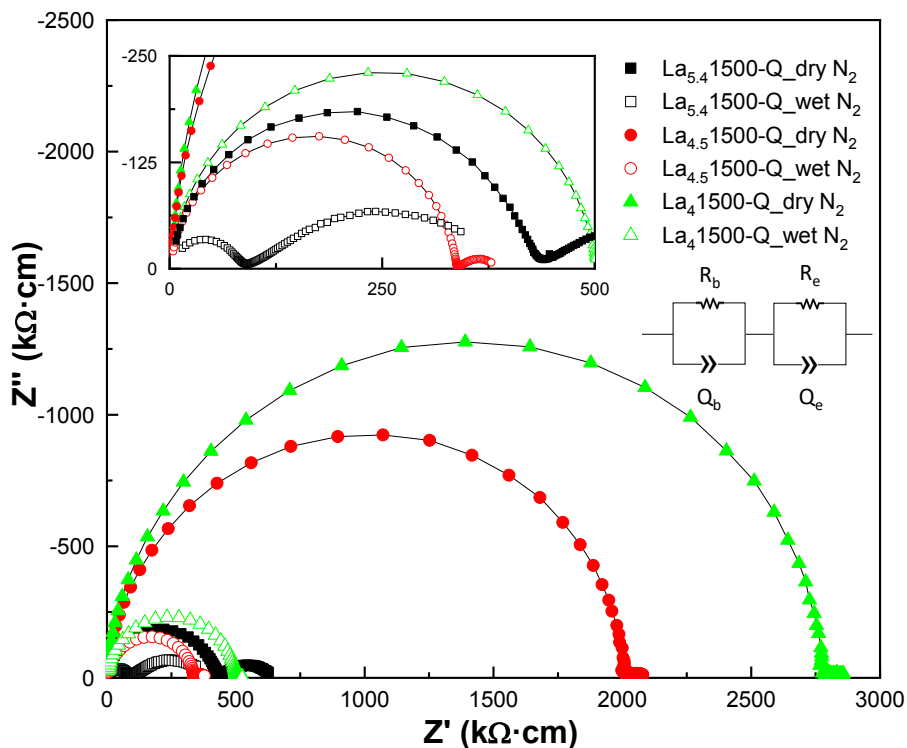


Figure 4.22. Representative impedance spectra at 400 °C of $\text{La}_{6-x}\text{MoO}_{12-\delta}$ ($x = 0.6, 1.5,$ and 2.0) obtained by heating at 1500 °C 1h and cooled down by quenching, under dry and wet N_2 atmospheres.

As can be seen, there are two separated contributions ascribed to the grain interior conduction and electrode processes with capacitance values of $\sim\text{pF}\cdot\text{cm}^{-1}$ and $\sim\mu\text{F}\cdot\text{cm}^{-1}$, respectively. The contribution at high frequencies is fitted with an (RQ) equivalent circuit, where Q is a constant phase element and can be assigned to the bulk conduction. At intermediate frequencies, the grain boundary contribution is not observed for any of the samples, likely due to the large grain size and the absence of phase segregations in this region.

The Arrhenius plots of the samples (Figure 4.23) show the behaviour of the conductivity against the temperature in different atmospheres (dry N_2 , wet N_2 and wet 5% $\text{H}_2\text{-Ar}$).

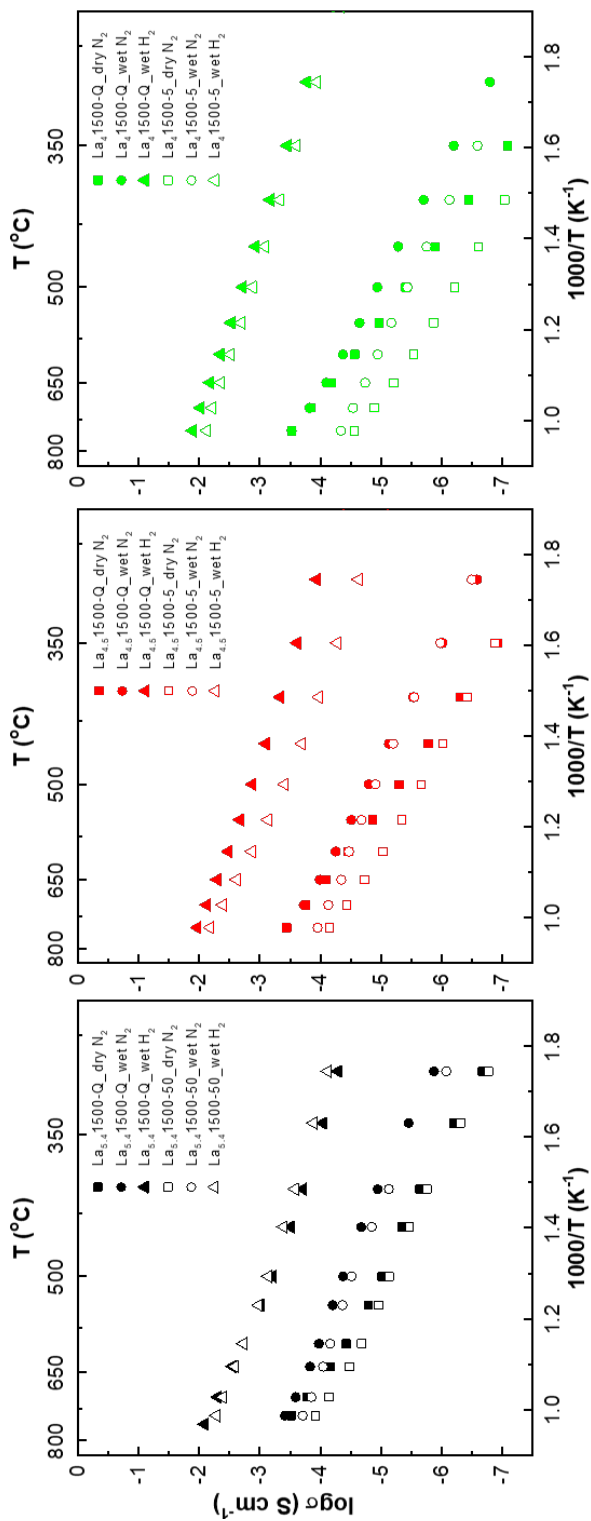


Figure 4.23. Arrhenius plots of (a) $\text{La}_{0.4}\text{MoO}_{9.75}$, (b) $\text{La}_{4.5}\text{MoO}_{9.75}$ and (c) $\text{La}_{4.4}\text{MoO}_9$ obtained by heating at 1500°C 1h and cooled down at different rates under dry and wet N_2 and wet $5\% \text{H}_2\text{-Ar}$ atmospheres.

In general, all samples present an increase of conductivity in wet vs dry conditions, due to the presence of a proton contribution to the overall conductivity in the low-temperature range ($T < 800$ °C) that is more significant under 650 °C. In addition, above this temperature the conductivity values are very similar in dry and wet gases, suggesting that the oxide ion conduction is dominant in this region. In Table 4.13 are summarized the conductivity data for all measured samples.

Table 4.13. Conductivity data obtained for $\text{La}_{6-x}\text{MoO}_{12-\sigma}$ ($x = 0.6, 1.5, \text{ and } 2.0$) obtained by heating at 1500 °C 1h and cooled down at different rates (quenching, 50, 5 and 0.5 °C·min⁻¹), measured at 700 and 400 °C.

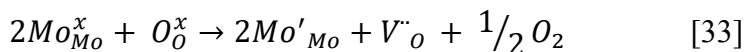
Sample	Dry N ₂ (mS·cm ⁻¹)		Wet N ₂ (mS·cm ⁻¹)		Wet 5% H ₂ -Ar (mS·cm ⁻¹)	
	$\sigma_{700\text{ °C}}$	$\sigma_{400\text{ °C}}$	$\sigma_{700\text{ °C}}$	$\sigma_{400\text{ °C}}$	$\sigma_{700\text{ °C}}$	$\sigma_{400\text{ °C}}$
La_{5.4}1500-Q	$1.7 \cdot 10^{-1}$	$2.3 \cdot 10^{-3}$	$2.5 \cdot 10^{-1}$	$1.1 \cdot 10^{-2}$	5.0	$2.0 \cdot 10^{-1}$
La_{5.4}1500-50	$7.1 \cdot 10^{-2}$	$1.7 \cdot 10^{-3}$	$1.4 \cdot 10^{-1}$	$7.4 \cdot 10^{-3}$	$4.5 \cdot 10^{-1}$	$2.3 \cdot 10^{-2}$
La_{5.4}1500-0.5	$9.0 \cdot 10^{-2}$	$1.7 \cdot 10^{-3}$	$1.8 \cdot 10^{-1}$	$1.9 \cdot 10^{-3}$	$4.5 \cdot 10^{-1}$	$2.3 \cdot 10^{-2}$
La_{4.5}1500-Q	$1.7 \cdot 10^{-1}$	$5.0 \cdot 10^{-4}$	$1.9 \cdot 10^{-1}$	$2.9 \cdot 10^{-3}$	7.5	$4.6 \cdot 10^{-1}$
La_{4.5}1500-5	$3.7 \cdot 10^{-1}$	$3.8 \cdot 10^{-4}$	$7.4 \cdot 10^{-2}$	$2.8 \cdot 10^{-3}$	4.1	$1.1 \cdot 10^{-1}$
La_{4.0}1500-Q	$1.4 \cdot 10^{-1}$	$3.6 \cdot 10^{-4}$	$1.5 \cdot 10^{-1}$	$2.0 \cdot 10^{-3}$	9.5	$6.7 \cdot 10^{-1}$
La_{4.0}1500-5	$1.3 \cdot 10^{-2}$	$9.1 \cdot 10^{-5}$	$4.6 \cdot 10^{-2}$	$7.4 \cdot 10^{-4}$	6.0	$4.7 \cdot 10^{-1}$
La_{4.0}1500-0.5	$1.8 \cdot 10^{-1}$	$3.5 \cdot 10^{-3}$	$2.6 \cdot 10^{-1}$	$5.0 \cdot 10^{-2}$	1.6	$3.9 \cdot 10^{-2}$

In a N₂ atmosphere, where the only contributions to the conductivity are ionic (proton and oxide), it can be seen that at any temperature, the

conductivity decreases as the lanthanum content becomes smaller. For instance, for La_{5.4}1500-Q, La_{4.5}1500-Q and La_{4.0}1500-Q, the values are $2.5 \cdot 10^{-1}$, $1.9 \cdot 10^{-1}$ and $1.5 \cdot 10^{-1}$ mS cm⁻¹, respectively, at 700 °C (oxide ion mobility dominance) in wet N₂. At 400 °C (proton mobility dominance) and the same atmosphere the values for those compositions are $1.1 \cdot 10^{-2}$, $2.9 \cdot 10^{-3}$ and $2.0 \cdot 10^{-3}$ mS cm⁻¹, respectively. This is due to an increasing number of oxide vacancies disrupt the ionic conduction pathways, hindering the oxide and proton mobility. On the other hand, for a same composition but different symmetry, cubic samples present improved conductivity values respect to the rhombohedral ones due to their higher symmetry and more straight conduction pathways. For instance, La_{5.4}1500-Q, La_{5.4}1500-50 and La_{5.4}1500-0.5 show values of $2.5 \cdot 10^{-1}$, $1.4 \cdot 10^{-1}$ and $1.8 \cdot 10^{-1}$ mS cm⁻¹, respectively, at 700 °C in wet N₂. The highest conductivity of La_{5.4}1500-0.5 respect to La_{5.4}1500-50 might be ascribed to its significantly higher average grain size.

The influence of humidity is also manifest in the activation energies, with values of ~ 1.05 and 0.80 eV, in dry and wet N₂ atmospheres, respectively, for the quenched samples. A decrease originated by the increase of the proton oxide mobility.

In a 5% H₂-Ar atmosphere the conductivity was enhanced due to an n-type contribution, caused by a minor reduction of Mo⁶⁺ to Mo⁵⁺, following this reaction:



It should be noticed that in reducing atmosphere, for samples obtained in the same conditions, the conductivity increases as the lanthanum content decreases. For instance, the conductivity values for La_{5.4}1500-Q, La_{4.5}1500-

Q, and La_{4.0}1500-Q at 700 °C, are 5.0, 7.5, and 9.5 mS·cm⁻¹, respectively. This behavior is the opposite found in dry/wet N₂ and is likely due to the higher reducibility of the samples with lower La/Mo ratios and the decrease in the cell volumes, which makes the molybdenum atoms to be closer to each other, facilitating the electronic conduction by electron hopping. It is worth mentioning that this increase in conductivity is more significant in the low-temperature range, dominated by the proton conduction when compared to the high-temperature region, dominated by the oxide and electron conduction. In addition, a decrease in the activation energies is also observed as the lanthanum content decreases, with values of 0.72, 0.55, and 0.51 eV for La_{5.4}1500-Q, La_{4.5}1500-Q, and La_{4.0}1500-Q, respectively, due to the higher electronic conductivity contribution. On the other hand, the lower conductivity values are observed for La_{4.0}1500-0.5, with 1.6 mS·cm⁻¹ at 700 °C and 3.9·10⁻² at 400 °C, due to the less symmetric monoclinic phase, which hinders the conducting pathways.

The dependence of the conductivity versus the oxygen partial pressure for La_{5.4}1500-Q, La_{4.5}1500-Q, and La_{4.0}1500-Q is plotted in Figure 4.24. It can be seen an increase in conductivity as the oxygen partial pressure decreases due to a very important n-type electronic contribution, more significant for La_{4.0}1500-Q in comparison to La_{5.4}1500-Q, where the difference between the ionic plateaus and the most reduced points is higher for the former.

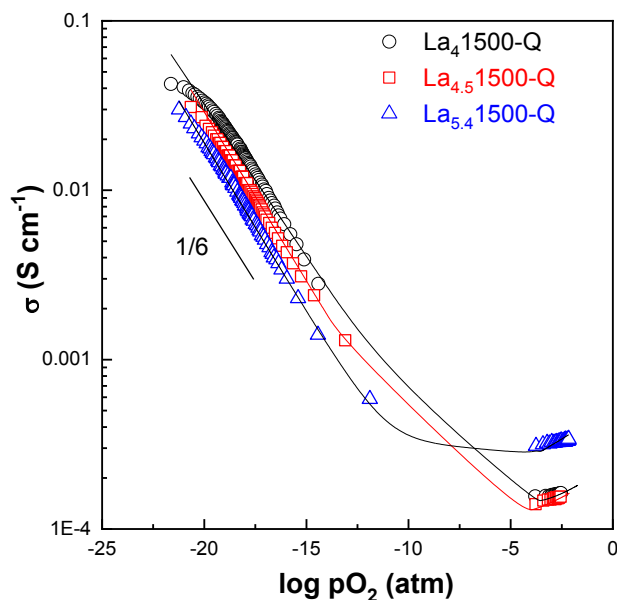


Figure 4.24. Conductivity vs oxygen partial pressure at 800 °C for $\text{La}_{5.4}\text{1500-Q}$, $\text{La}_{4.5}\text{1500-Q}$, and $\text{La}_{4.0}\text{1500-Q}$. The solid lines show curves fitting.

The n-type branches of the plots show a dependence on the conductivity following the next equation:

$$\sigma = \sigma_o + \sigma_n (\text{pO}_2)^{-1/6} + \sigma_p (\text{pO}_2)^{1/6} \quad [34]$$

where σ_o is the ionic conductivity, and σ_n and σ_p are the partial n-type and p-type electronic conductivity, respectively. As can be observed, the n-type contribution is the main conduction mechanism at low oxygen partial pressure and a small p-type contribution is observed at high pO_2 values. These curves confirm that samples with high La-content exhibit higher ionic conductivity with a plateau region at intermediate pO_2 values; however, samples with low La-content exhibit lower ionic conductivity and higher n-type and p-type electronic conductivities.

4.4. Modification of the cationic-anionic framework.

Influence of the preparation conditions.

In order to optimize the properties of the studied materials, an aliovalent substitution in the cationic-anionic framework was carried out. For the sake of comparison, synthesis and properties of the doped materials were addressed in a similar way to the undoped compositions.

4.4.1. Substitution in the lanthanum position, $\text{La}_{5.3}\text{A}_{0.10}\text{MoO}_{11.05}$ (A = Ca, Sr and Ba) series.

The influence of the cooling rate was analyzed by heating the samples at 1500 °C for 1h and cooling down at different rates (quenching, 50 and 0.5 °C·min⁻¹). The materials from now on will be named $\text{A}_{0.10}$ (A = Ca, Sr and Ba). XRPD patterns for selected samples and a summary of the phases obtained are shown in Figure 4.25 and Table 4.14, respectively.

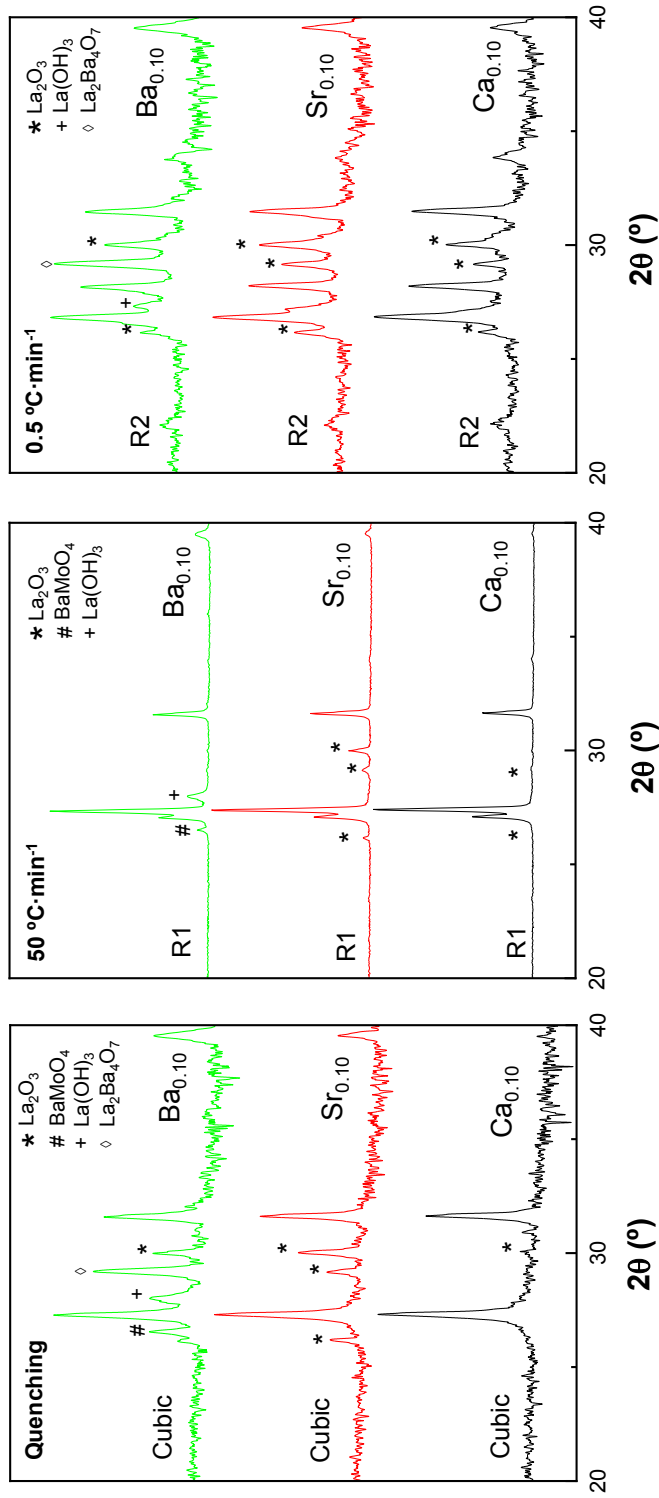


Figure 4.25. XRPD patterns of $\text{La}_{45.3}\text{A}_{0.10}\text{MoO}_{11.05}$ (A = Ca, Sr and Ba) series obtained by heating at 1500 °C 1h and cooled down at different rates (quenching, 50 and 0.5 °C·min⁻¹). The major phase for each sample is denoted at the bottom left of the diffraction patterns and the minor secondary phases are labelled.

Table 4.14. Summary of $\text{La}_{5.3}\text{A}_{0.10}\text{MoO}_{11.05}$ (A = Ca, Sr, and Ba) phases obtained by heating at 1500 °C 1h and cooling down at different rates (quenching, 50 and 0.5 °C·min⁻¹). The mayor phase is in bold letters.

Sample	Cooling rate		
	Quenching	50 °C·min ⁻¹	0.5 °C·min ⁻¹
Ca_{0.10}	Cubic La ₂ O ₃	R1 La ₂ O ₃	R2 La ₂ O ₃
Sr_{0.10}	Cubic La ₂ O ₃	R1 La ₂ O ₃	R2 La ₂ O ₃ La(OH) ₃
Ba_{0.10}	Cubic La ₂ O ₃ BaMoO ₄ La(OH) ₃ La ₂ Ba ₄ O ₇	R1 BaMoO ₄ La(OH) ₃	R2 La ₂ O ₃ La(OH) ₃ La ₂ Ba ₄ O ₇

On one hand, all samples cooled down by quenching present a cubic fluorite structure with segregations of La₂O₃. Ba_{0.10} also presents secondary phases of BaMoO₄ (PDF 00-002-0449), La(OH)₃ (PDF 00-006-0585), and La₂Ba₄O₇ (PDF 00-052-1324). On the other hand, Ca_{0.10} and Sr_{0.10} cooled down at 50 °C·min⁻¹ present a R1 structure with segregations of La₂O₃, while Ba_{0.10} shows additional phases of BaMoO₄ and La(OH)₃. Finally, samples cooled down at 0.5 °C·min⁻¹ crystallize with the rhombohedral structure R2, and for all samples are observed segregations of La₂O₃, except Ba_{0.10}, which also presents La(OH)₃, and La₂Ba₄O₇.

The number of secondary phases increases with the ionic radii of the alkaline-earth metal, in the following order: Ca_{0.10} < Sr_{0.10} < Ba_{0.10}. The ionic radii of Ca²⁺ (1.12 Å), Sr²⁺ (1.26 Å), and Ba²⁺ (1.42 Å), in an 8-fold

coordination (Shannon, 1976), make difficult their introduction in the La^{3+} (1.16 Å) position, due to their great size, being challenging the obtention of single phases. Therefore, Ca^{2+} , with the smaller size is the sample with fewer impurities.

All attempts to optimize the synthesis conditions to obtain monophasic materials (varying the temperature from 800 to 1500 °C) were unsuccessful. Consequently, samples doped in the lanthanum position were not further studied, shifting the focus to doping in the molybdenum position.

4.4.2. Substitution in the molybdenum position, $\text{La}_{5.4}\text{Mo}_{0.90}\text{B}_{0.10}\text{O}_{11.1-\delta}$ (B = Ti, Zr and Nb) series.

This study began heating the precursor from 1200 to 1400 °C 1h cooling at $5\text{ °C}\cdot\text{min}^{-1}$, and at 1500 °C cooling at $50\text{ °C}\cdot\text{min}^{-1}$ for analyze the influence of the sintering temperature in properties of materials. XRPD patterns for selected samples are shown in Figure 4.26. The materials from now on will be named $\text{B}_{0.10}$ (B = Ti, Zr and Nb).

As can be seen in Figure 4.26, at 1200 °C samples present an R2 structure with segregations of La_2O_3 (for Ti and Zr-doped) and traces of R1 and La_2O_3 (for Nb doped). Materials heated between 1300-1400 °C crystallize with a R1 structure with La_2O_3 segregations. By heating at 1500 °C, Ti and Nb-doped samples are monophasic with a R1 structure. $\text{Zr}_{0.10}$ also presents a R1 structure, but La_2O_3 is detected as secondary phase.

Secondly, the influence of the cooling rate in the synthesis was also analysed. XRPD patterns of $\text{La}_{5.4}\text{Mo}_{0.90}\text{B}_{0.10}\text{O}_{11.1-\delta}$ (B = Ti, Zr, and Nb) series heated at 1500 °C for 1h and cooled at different rates (quenching, 50 and $0.5\text{ °C}\cdot\text{min}^{-1}$) and a summary of the resulting phases are shown in Figure 4.27 and Table 4.15, respectively.

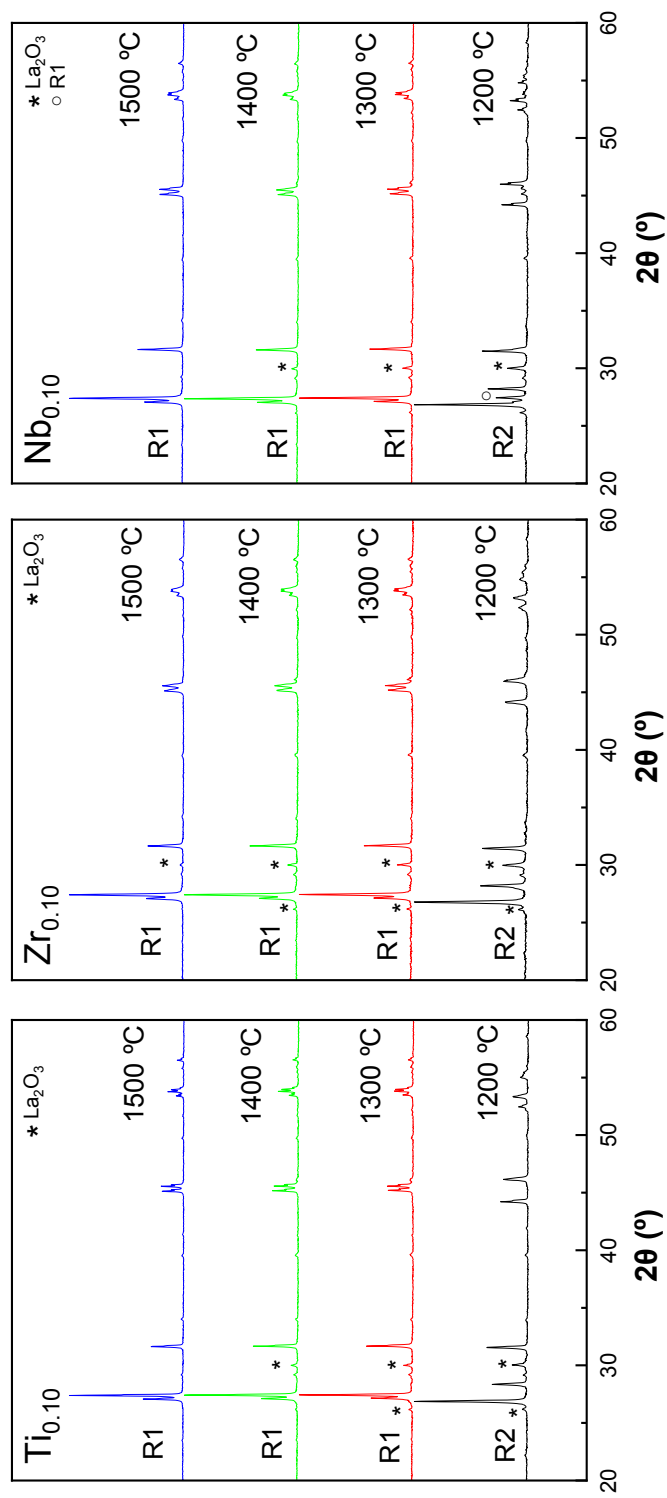


Figure 4.26. XRPD patterns of $\text{La}_{0.4}\text{M}_{0.90}\text{B}_{0.10}\text{O}_{1.1-\delta}$ (B = Ti, Zr and Nb) samples obtained by heating 1h between 1200 and 1500 °C and cooled down at 50 °C·min⁻¹. The major phase for each sample is denoted at the bottom left of diffraction patterns and the minor secondary phases are labelled.

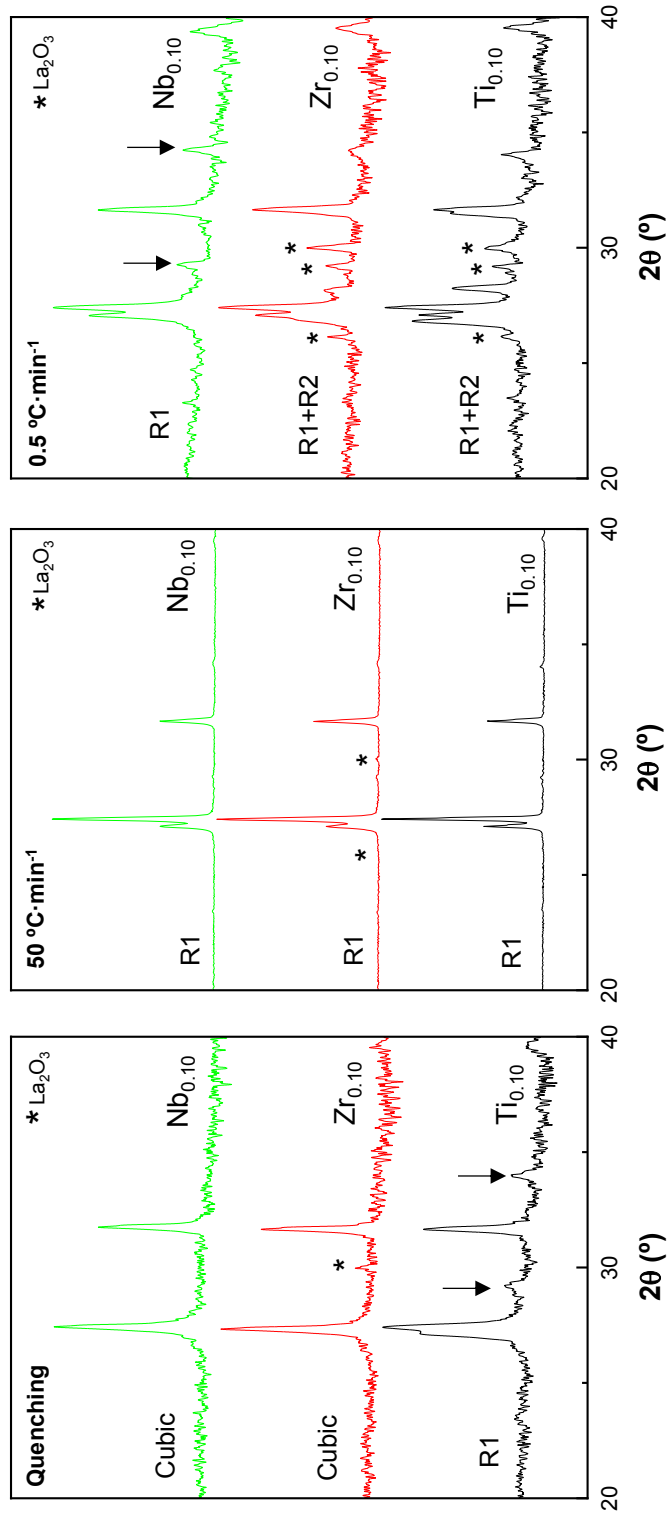


Figure 4.27. XRPD patterns of $\text{La}_{0.54}\text{Mo}_{0.90}\text{B}_{0.10}\text{O}_{1.1+\delta}$ (B = Ti, Zr and Nb) series obtained by heating at 1500 °C 1h and cooled down at different rates (quenching, 50 and 0.5 °C·min⁻¹). The major phase for each sample is denoted at the bottom left of diffraction patterns and the minor secondary phases are labelled. Superstructure peaks are marked with arrows for single-phase.

Table 4.15. Summary of $\text{La}_{5.4}\text{Mo}_{0.90}\text{B}_{0.10}\text{O}_{11.1-\delta}$ (B = Ti, Zr, and Nb) phases obtained by heating at 1500 °C 1h and cooled down at different rates (quenching, 50 and 0.5 °C·min⁻¹). The mayor phase is in bold letter.

Sample	Cooling rate		
	Quenching	50 °C·min ⁻¹	0.5 °C·min ⁻¹
Ti _{0.10}	R1	R1	R1 R2 La ₂ O ₃
Zr _{0.10}	Cubic La ₂ O ₃	R1 La ₂ O ₃	R1 R2 La ₂ O ₃
Nb _{0.10}	Cubic	R1	R1

Samples cooled by quenching crystallize with monophasic R1 and cubic structures for Ti and Nb, respectively, while the Zr sample crystallize with a cubic structure but presents La₂O₃ segregations. On the other hand, samples cooled down at 50 °C·min⁻¹ present a R1 type-structure without impurities, with the exception of Zr that shows La₂O₃. Finally, samples cooled down at 0.5 °C·min⁻¹ have mixtures of R1 and R2 with La₂O₃ segregations, but the Nb-doped material crystallizes in a monophasic R1 structure, instead of the R2 structure formed by the undoped material in the same conditions. These data indicate that metal-doping on the molybdenum position tends to stabilize the R1 polymorph, but only Nb-doped materials present pure compounds. To simplify this section Appendix 6.3 shows other results regarding stability studies for these materials.

XRPD data of Ti_{0.10} cooled at 50 °C·min⁻¹ was analysed by the Le Bail method using the basic unit cell of La_{5.4} as initial parameters (Figure 4.28).

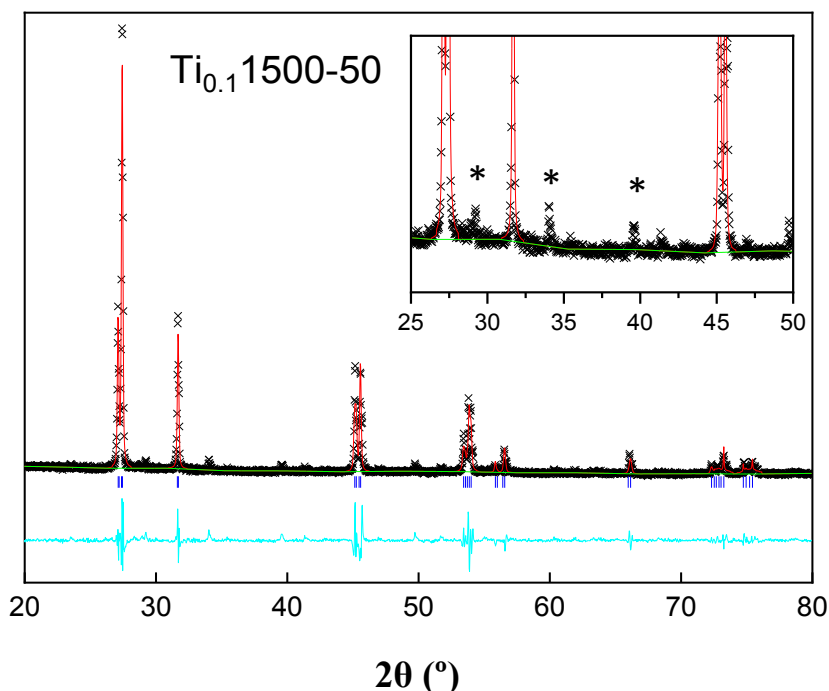


Figure 4.28. Le Bail XRPD plots of $\text{La}_{5.4}\text{Mo}_{0.90}\text{Ti}_{0.10}\text{O}_{11.05}$ obtained by heating at $1500\text{ }^{\circ}\text{C}$ 1h and cooled down at $50\text{ }^{\circ}\text{C}\cdot\text{min}^{-1}$ with rhombohedral structure R1. In the image are represented the experimental data ($\times\times\times$), calculated pattern (—), and difference curve (cyan at the bottom). Asterisks show the superstructure reflections.

The patterns (as the undoped samples) present a superstructure that can be indexed as a $7a \times 7a \times c$ superstructure (see marks at inset of Figure 4.28) from the basic cell parameters determined by XRPD ($a = 3.99\text{ \AA}$ and $c = 9.88\text{ \AA}$) with acceptable R_{wp} (12.9%). In addition, a decrease in the cell volume is observed for the Ti-doped sample ($\sim 45.3\text{ \AA}^3$) in comparison to the undoped material ($\sim 45.5\text{ \AA}^3$), due to the smaller size of Ti^{4+} (0.74 \AA) in comparison to that of Mo^{6+} (1.02 \AA). Ti and Zr-doping did not stabilize single phase cubic structures, even by quenching, so only the niobium samples were further studied, preparing the $\text{La}_{5.4}\text{Mo}_{1-x}\text{Nb}_x\text{O}_{11.1-x/2}$ series ($0 \leq x \leq 0.25$) and analysing the influence of the Nb content in the structure and electrical properties of materials (see next section).

4.4.3. Study of $\text{La}_{5.4}\text{Mo}_{1-x}\text{Nb}_x\text{O}_{11.1-x/2}$ ($0 \leq x \leq 0.25$) series.

XRPD patterns of $\text{La}_{5.4}\text{Mo}_{1-x}\text{Nb}_x\text{O}_{11.1-x/2}$ ($x = 0, 0.05, 0.10, 0.15, 0.20$ and 0.25) series heated at $1500\text{ }^\circ\text{C}$ for 1h and cooled down at different rates (quenching, 50 and $0.5\text{ }^\circ\text{C}\cdot\text{min}^{-1}$) and a summary of the conditions to obtain single phases are showed in Figure 4.29 and Table 4.16, respectively.

$\text{La}_{5.4}\text{Mo}_{1-x}\text{Nb}_x\text{O}_{11.1-x/2}$ ($x \leq 0.20$) samples cooled by quenching and $50\text{ }^\circ\text{C}\cdot\text{min}^{-1}$ are cubic and R1 single phases, respectively. However, a different behaviour is observed for samples prepared at $0.5\text{ }^\circ\text{C}\cdot\text{min}^{-1}$. The undoped material presents a monophasic R2 structure, which fully evolves to a R1 single phase with a niobium content of $x = 0.1$. $\text{Nb}_{0.15}$ and $\text{Nb}_{0.20}$ also present a R1 symmetry, but La_2O_3 is detected as secondary phase. When Nb-doping is higher or equal to 0.25 segregates LaNbO_4 (PDF 00-022-1125) due to the excess of Nb in the material. This indicates that under the synthetic conditions used, the Nb doping limit for these materials is close to $x = 0.20$.

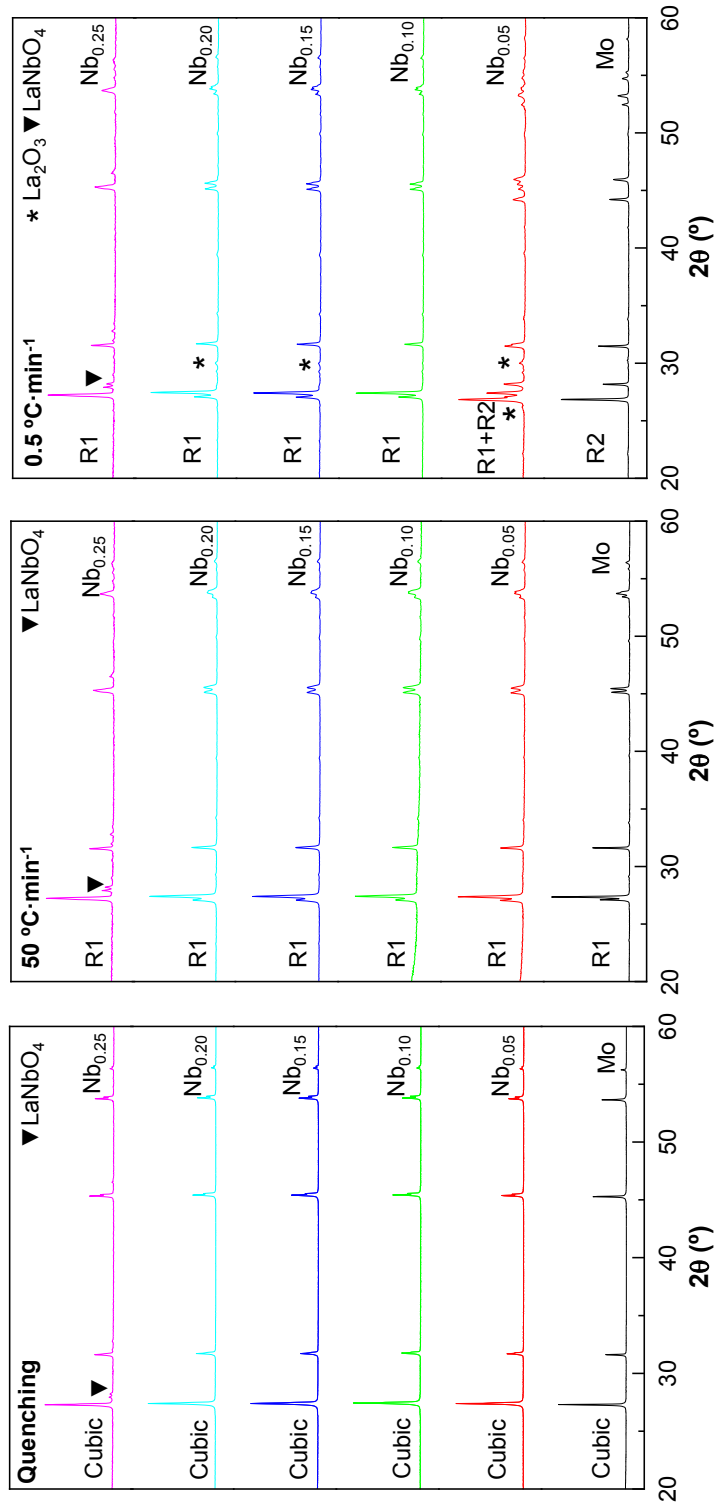


Figure 4.29. XRPD patterns of $\text{La}_{5.4}\text{Mo}_{1-x}\text{Nb}_x\text{O}_{11.1-x/2}$ ($x = 0, 0.05, 0.10, 0.15, 0.20$ and 0.25) series obtained by heating at $1500\text{ }^\circ\text{C}$ 1h and cooled down at different rates (quenching, 50 and $0.5\text{ }^\circ\text{C}\cdot\text{min}^{-1}$). The major phase for each sample is denoted at bottom left of diffraction patterns and the minor secondary phases are labelled.

Table 4.16. Summary of cooling rates needed to obtain $\text{La}_{5.4}\text{Mo}_{1-x}\text{Nb}_x\text{O}_{11.1-x/2}$ ($0 \leq x \leq 0.20$) single phases by heating the precursors at 1500 °C 1h. Empty cells correspond to conditions that did not lead to single phases*.

Sample	Cooling rate		
	Quenching	50 °C·min ⁻¹	0.5 °C·min ⁻¹
Undoped	Cubic	R1	R2
Nb_{0.05}	Cubic	R1	-
Nb_{0.10}	Cubic	R1	R1
Nb_{0.15}	Cubic	R1	-
Nb_{0.20}	Cubic	R1	-

*The composition range is reduced compared to the original series. Only monophasic samples are shown in this Table.

$\text{La}_{5.4}\text{Mo}_{1-x}\text{Nb}_x\text{O}_{11.1-x/2}$ ($0 \leq x \leq 0.25$) single phases (Table 4.16) were studied by the Rietveld (cubic) and Le Bail (rhombohedral) methods using XRPD data (Table 4.17). The unit cell volume of the quenched samples decreases linearly as the niobium content increases, according to Vegard's law, due to the smaller ionic radii of Nb^{5+} (0.74 Å) in 8-fold coordination, in comparison to those of La^{3+} (1.16 Å) and Mo^{6+} (1.02 Å) in the same environment (Table 4.17).

It is important to mention that in samples cooled by quenching, Ti^{4+} and Nb^{5+} have the same ionic radii, but the final materials do not have the same cell volumes. This is due to the different oxygen contents generated by the aliovalent doping of Ti^{4+} and Nb^{5+} , where the former creates 1 vacancy per mol of dopant, and the latter, half a vacancy per mol of dopant, leading to different oxygen contents and, hence, not equal cell volumes (45.29(1) Å³ for Ti and 45.51(1) Å³ for Nb).

On other hand, for samples cooled down at $50\text{ }^{\circ}\text{C}\cdot\text{min}^{-1}$, as the unit cell volume decreases with increasing Nb-doping except for the undoped compounds that exhibit a value somewhat lower than the expected one (Figure 4.30).

Table 4.17. Unit cell parameters, volumes and agreement factors of $\text{La}_{5.4}\text{Mo}_{1-x}\text{Nb}_x\text{O}_{11.1-x/2}$ ($x = 0, 0.05, 0.10, 0.15$ and 0.20) series obtained by heating at $1500\text{ }^{\circ}\text{C}$ 1h and cooled down at different rates (quenching, 50 and $0.5\text{ }^{\circ}\text{C}\cdot\text{min}^{-1}$) determined by Rietveld (cubic) and Le Bail (rhombohedral) refinements of XRPD data.

Cooling rate		Undoped	Nb _{0.05}	Nb _{0.10}	Nb _{0.15}	Nb _{0.20}
Quenching	a (Å)	5.6676(1)	5.6649(1)	5.6615(1)	5.6574(1)	5.6533(1)
	V/Z (Å ³)	45.51(1)	45.44(1)	45.36(1)	45.26(1)	45.17(1)
	R _{wp} (%)	6.87	8.75	5.13	5.51	5.27
	R _F (%)	3.15	2.08	2.53	3.06	3.48
50 °C·min ⁻¹	a (Å)	3.9904(1)	3.9919(1)	3.9908(1)	3.9904(1)	3.9899(1)
	c (Å)	9.8759(2)	9.8970(2)	9.8989(2)	9.8978(3)	9.8966(4)
	V/Z (Å ³)	45.40(1)	45.53(1)	45.51(1)	45.50(1)	45.48(1)
	R _{wp} (%)	10.05	7.80	7.91	8.62	9.06
0.5 °C·min ⁻¹	a (Å)	4.0996(1)	4.1114(1)/ 3.9846(3)	3.9873(1)	3.9848(1)	3.9830(1)
	c (Å)	9.5204(2)	9.5045(3)/ 9.8846(1)	9.9007(1)	9.8973(4)	9.8971(2)
	V/Z (Å ³)	46.19(1)	46.38(1)/ 45.47(1)	45.44(1)	45.37(1)	45.32(1)
	R _{wp} (%)	9.39	9.02	10.43	11.06	11.95

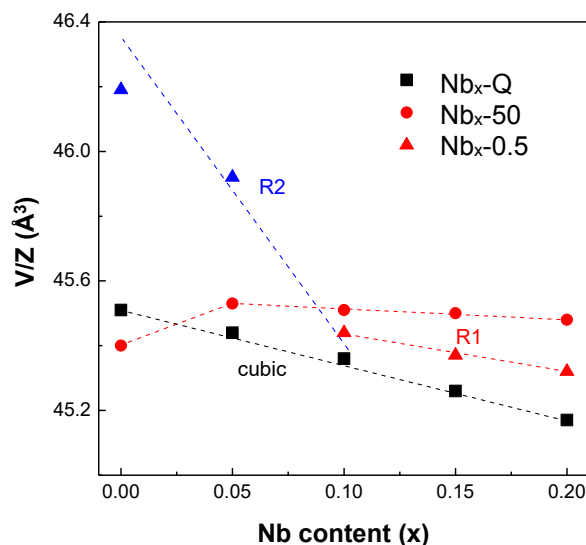


Figure 4.30. Unit cell volume versus niobium content of $\text{La}_{5.4}\text{Mo}_{1-x}\text{Nb}_x\text{O}_{11.1-x/2}$ series cooled down at different rates (quenching, 50 and $0.5\text{ }^\circ\text{C}\cdot\text{min}^{-1}$). Samples with the same polymorphism are shown in the same color: black, red, and blue for cubic fluorite, R1, and R2, respectively.

In contrast, this linear dependence is not observed for the samples prepared at a low cooling rate ($0.5\text{ }^\circ\text{C}\cdot\text{min}^{-1}$), which can be explained by the structural phase transition from the R2 to R1 polymorph with Nb-doping and the presence of a minor secondary phase of La_2O_3 for $x \geq 0.15$. These results indicate that not only does the cooling rate have a significant effect on the polymorphism of $\text{La}_{6-x}\text{MoO}_{12-\delta}$ but also does the incorporation of different aliovalent dopants, which introduces extrinsic oxide ion vacancies in the lattice, suggesting that the local structure of the different polymorphs is similar and the differences are mainly associated with modifications in the oxygen sublattice as previously observed for related materials, such as the fast ionic conductor $\text{La}_2\text{Mo}_2\text{O}_9$ with an α -monoclinic \rightarrow β -cubic structural phase transition from a static to a dynamic distribution of the oxygen defects. However, additional measurements are necessary to confirm this hypothesis, such as neutron atomic pair distribution function (PDF) analysis.

The cubic structure of selected quenched Nb-doped materials, $\text{La}_{5.4}\text{Mo}_{1-x}\text{Nb}_x\text{O}_{11.1-x/2}$ ($x = 0, 0.10, 0.20$), were studied by a combined Rietveld refinement of XRPD and TOF-NPD data, using a single fluorite-type structure as the starting structural model. La, Mo, and Nb were placed in the same crystallographic position and occupancy factors were initially set to the nominal stoichiometry, with their isotropic displacement parameters constrained to be the same. Parameters such as unit cell, scale factor, background, peak shape coefficients, and isotropic displacement parameters were refined as usual. Occupancy factors were refined freely, without any constraint, and La, Mo, and Nb remained practically unaltered from the nominal values, indicating that the experimental stoichiometry is very close to the nominal one. Therefore, cation occupancy factors were fixed to the nominal values.

Figure 4.31 shows the Rietveld XRPD and TOF-NPD plots of $\text{Nb}_{0.10}$, and Table 4.18 displays relevant crystallographic data obtained from the refinements. As it can be seen, the results are quite satisfactory, with low disagreement factors, and R_F and R_{wp} values between 2-3 and 5-8, respectively, confirming that all quenched samples crystallize as a single cubic fluorite structure. This result confirms that refinement of the oxygen occupancy factors yields a higher concentration of oxygen vacancies with increasing in Nb-doping as expected (Table 4.18).

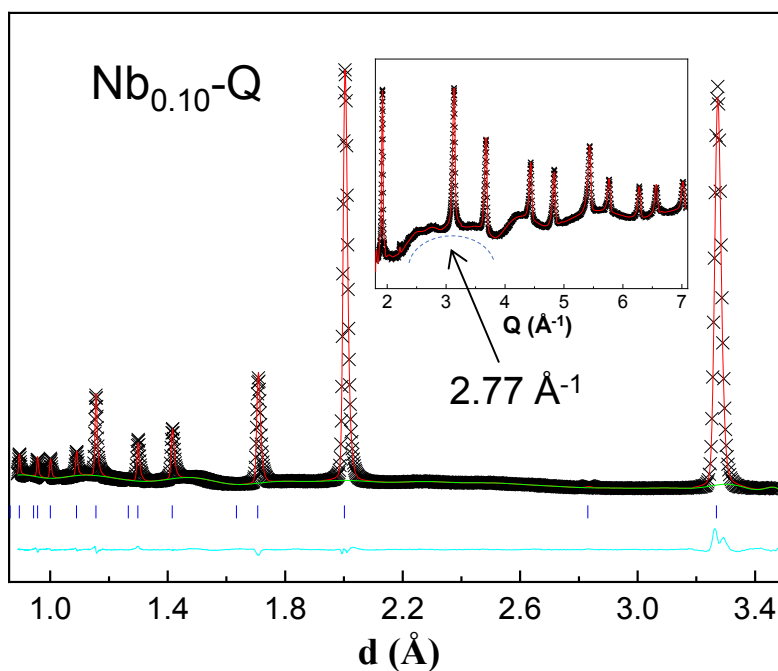
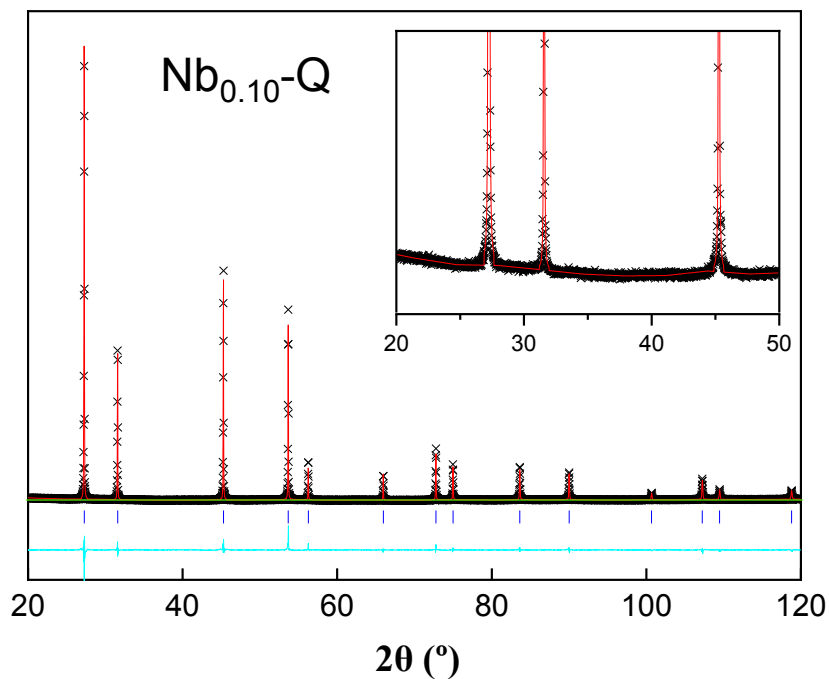


Figure 4.31. Rietveld XRPD (top) and TOF-NPD (bottom) plots of $\text{La}_{5.4}\text{Mo}_{0.90}\text{Nb}_{0.10}\text{O}_{11.05}$ obtained by heating at $1500\text{ }^\circ\text{C}$ 1h and cooled down by quenching. In the images are represented the experimental data ($\times\times\times$), calculated pattern (—), and difference curve (cyan at the bottom).

Table 4.18. Unit cell parameters, cell volumes, Rietveld agreement factors, atomic positions, isotropic atomic displacement parameters and occupancy factors of $\text{La}_{5.4}\text{Mo}_{1-x}\text{Nb}_x\text{O}_{11.1-x/2}$ ($x = 0, 0.10, \text{ and } 0.20$) obtained by heating at $1500\text{ }^\circ\text{C}$ 1h and cooled down by quenching determined by TOF-NPD Rietveld refinements using different data banks (4, 5, and 6).

	Undoped	Nb _{0.10}	Nb _{0.20}
a (Å)	5.6661(1)	5.6606(1)	5.6540(1)
V(Å³)	45.48(1)	45.34(1)	45.18(1)
R_{wp}^{N4}/R_{wp}^{N5}/ R_{wp}^{N6} (%)	3.85/3.14/3.45	3.37/2.93/3.76	3.22/3.09/3.30
R_p^{N4}/R_p^{N5}/R_p^{N6} (%)	3.46/2.45/2.86	3.21/2.19/2.87	2.94/2.21/2.42
R_F^{N4}/R_F^{N5}/R_F^{N6} (%)	2.19/2.17/3.32	3.20/3.20/2.53	3.83/3.57/2.77
Atom	La/Mo/Nb, 4a, (0, 0, 0)		
Uiso × 100 (Å²)	2.8(1)	2.6(1)	2.5(1)
Occupancy factor La/Mo/Nb	0.7714(-)/ 0.1428(-)	0.7714(-)/ 0.1286(-)/ 0.0143(-)	0.7714(-)/ 0.1143(-)/ 0.0286(-)
Atom	O, 8c, (1/4, 1/4, 1/4)		
Uiso × 100 (Å²)	4.2(1)	4.5(1)	4.5(1)
Occupancy factor O	0.72(1)	0.71(1)	0.69(1)

Rietveld refinements of TOF-NPD data show a significant undulation of the background (inset of Figure 4.31). This behavior has already been reported for other oxide ion conductors, such as $\text{La}_2\text{Mo}_2\text{O}_{9-\delta}$, $\text{Bi}_{26}\text{Mo}_{10}\text{O}_{69-\delta}$, and Bi_2O_3 -based materials, and is ascribed to a contribution of local static structural disorder in the anionic sublattice, caused by fast oxide ion diffusion, to the elastic diffuse scattering.

The nature of this disorder can be ascertained by the first undulation maximum of the background, where a very significant contribution to its

intensity comes from the static structural disorder. According to the Debye formula, the preferred pair distance characteristic of the short-range order can be deduced from this first marked maximum. In the Debye formula, Q_{\max} is the first undulation maximum and d_{\max} is a preferred pair distance for this (Corbel *et al.*, 2005):

$$Q_{\max} = \frac{2\pi \times 1.23}{d_{\max}} \quad [35]$$

In the inset of Figure 4.31 (bottom) for $\text{Nb}_{0.10}\text{-Q}$, the maximum is about 2.77 \AA^{-1} , corresponding to $d_{\max} \approx 2.79 \text{ \AA}$, the typical O-O distance in an 8-fold environment coordination. Similar pair distances are obtained for $\text{Nb}_{0.10}\text{-Q}$ and $\text{Nb}_{0.20}\text{-Q}$. This confirms that the modulation observed in the patterns can be ascribed to the distribution of the oxygen defects. Similar results are reported in the literature for related molybdates, i.e., Q_{\max} of 2.75 and 2.8 \AA^{-1} , for $\text{Bi}_{26}\text{Mo}_{10}\text{O}_{69}$ and $\text{La}_2\text{Mo}_2\text{O}_9$, respectively.

The structure of the materials was further characterized by combined selected area electron diffraction (SAED) and high-resolution TEM images. The pictures obtained for the quenched samples are showed in Figure 4.32.

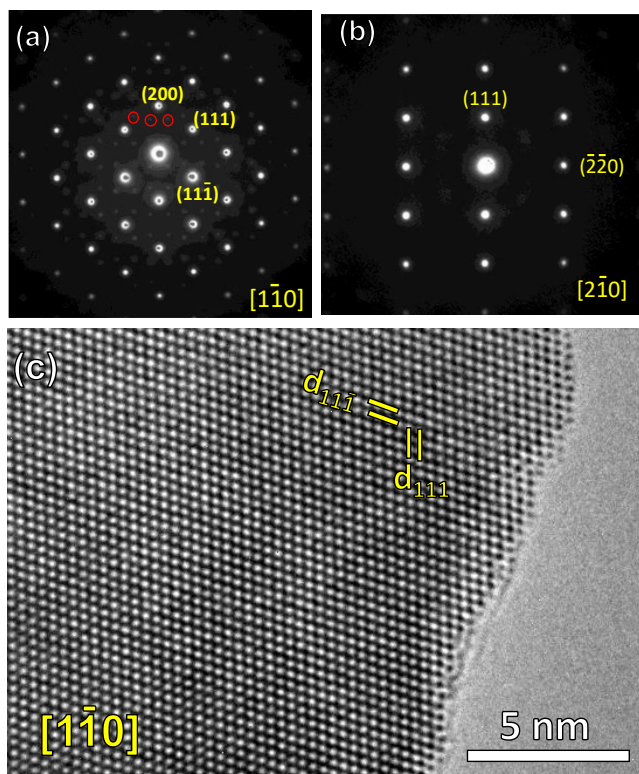


Figure 4.32. SAED patterns of $\text{La}_{5.4}\text{Mo}_{0.90}\text{Nb}_{0.10}\text{O}_{11.05}$ obtained by heating at 1500 °C 1h and cooled down by quenching along a) $[1\bar{1}0]$ and b) $[2\bar{1}0]$ zone axes. Red circles indicate weak satellite reflections due to structure modulations. c) HRTEM image in the $[1\bar{1}0]$ zone axis.

The main reflections of the SAEDs can be indexed based on a cubic fluorite-type structure with cell parameter $a = 5.67 \text{ \AA}$, in agreement with the XRPD and NPD results that are shown in Table 4.18. However, certain crystallographic directions show weak satellite reflections, consistent with an incommensurate modulation due to the local oxygen ordering as was observed by the neutron diffraction measurements. HRTEM images further confirm the cubic structure of this sample, where the interplanar distances are like those obtained by diffraction techniques.

SAED patterns for the sample cooled down at $0.5\text{ }^{\circ}\text{C}\cdot\text{min}^{-1}$ ($\text{Nb}_{0.10}\text{1500-0.5}$), reveal the presence of a superstructure characteristic of a R1 structure. This is observed in the $[001]$ zone axis that is shown in Figure 4.33.

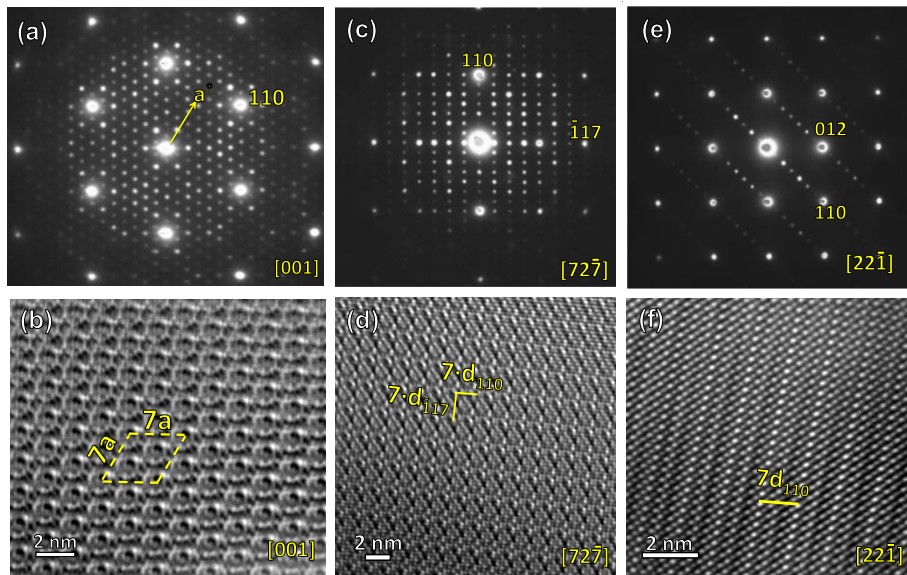


Figure 4.33. SAED patterns and HRTEM images of $\text{La}_{5.4}\text{Mo}_{0.90}\text{Nb}_{0.10}\text{O}_{11.05}$ obtained by heating at $1500\text{ }^{\circ}\text{C}$ 1h and cooled down at $0.5\text{ }^{\circ}\text{C}\cdot\text{min}^{-1}$ along (a,b) $[001]$, (c,d) $[72\bar{7}]$ and (e,f) $[22\bar{1}]$ zone axes.

4.4.4. Substitution in the oxygen position via fluorination, $\text{La}_{5.4}\text{Mo}_{1-x}\text{B}_x\text{O}_{11.1-y/2-\delta}\text{F}_y$ ($x = 0$ and 0.10 ; $\text{B} = \text{Ti}, \text{Zr}$ and Nb ; $y = 1, 3$ and 6).

As it was mentioned in section 1.6.4, the substitution of oxygen with fluorine can modify the final structure and electrical properties of the materials. Firstly, it was optimized the fluorine content in the undoped lanthanum molybdate following the procedure described in section 1.7.5. XRPD patterns of $\text{La}_{5.4}\text{MoO}_{11.1-y/2}\text{F}_y$ ($y = 1, 3$, and 6) heated at $1500\text{ }^{\circ}\text{C}$ for 1h and cooled down at $5\text{ }^{\circ}\text{C}\cdot\text{min}^{-1}$ are shown in Figure 4.34a.

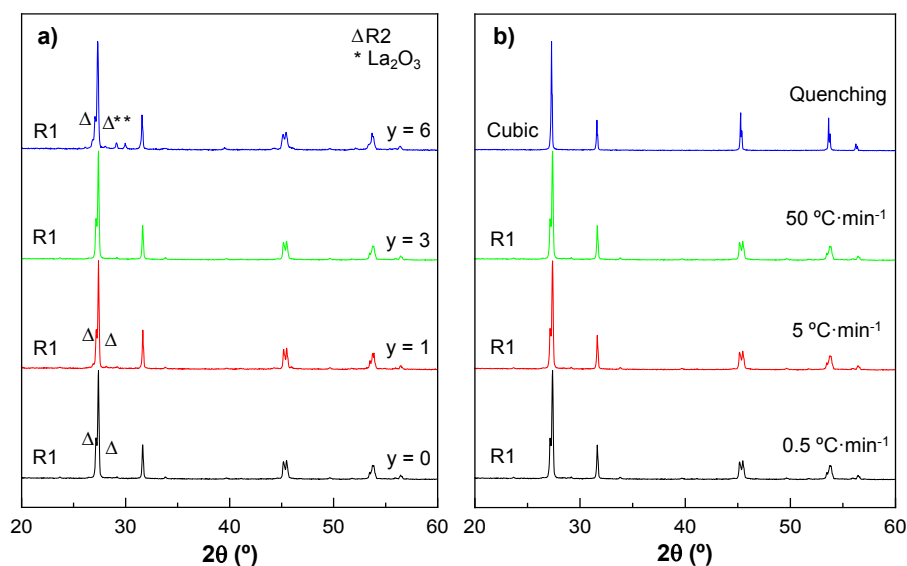


Figure 4.34. a) XRPD patterns of $\text{La}_{5.4}\text{MoO}_{11.1-y/2}\text{F}_y$ ($y = 0, 1, 3$ and 6) series obtained by heating at $1500\text{ }^\circ\text{C}$ 1h and cooled down at $5\text{ }^\circ\text{C}\cdot\text{min}^{-1}$. b) XRPD patterns of $\text{La}_{5.4}\text{MoO}_{11.1-y/2}\text{F}_y$ ($y = 3$) heated at $1500\text{ }^\circ\text{C}$ 1h and cooled down at different rates (quenching, $50, 5$ and $0.5\text{ }^\circ\text{C}\cdot\text{min}^{-1}$). The main phase for each sample is denoted at the bottom left of the diffraction patterns and the minor secondary phases are labeled.

The addition of a small amount of fluorine ($y = 1$) has no stabilizing effect since the sample presents the same mixture of R1 and R2 phases that the undoped sample. Increasing the amount of fluorine, $y = 3$, leads to a single R1 phase. Finally, if the fluorine content is higher than 3, there is observed a mixture of R1 and R2 and La_2O_3 as secondary phases. Therefore, the fluorine content of $y = 3$ is the most adequate to study the effect of fluorine doping in lanthanum molybdates. The influence of the cooling rate on fluorinated samples was also studied. All cooling rates lead to a R1 symmetry, with the exception of quenching that leads to cubic one, confirming the introduction of fluorine in the anionic framework. It is worth to remember that $\text{La}_{5.4}$, when cooled at $5\text{ }^\circ\text{C}\cdot\text{min}^{-1}$ is a mixture of R1 and R2, and at $0.5\text{ }^\circ\text{C}\cdot\text{min}^{-1}$ is R2,

which is further evidence of the beneficial effect of the incorporation of fluorine into the structure.

Finally, the effect of the sintering temperature was also studied. XRPD patterns of $\text{La}_{5.4}\text{MoO}_{11.1-y/2}\text{F}_y$ ($y = 3$) heated between 800 and 1500 °C for 1h and cooled down at 5 °C·min⁻¹ are shown in Figure 4.35.

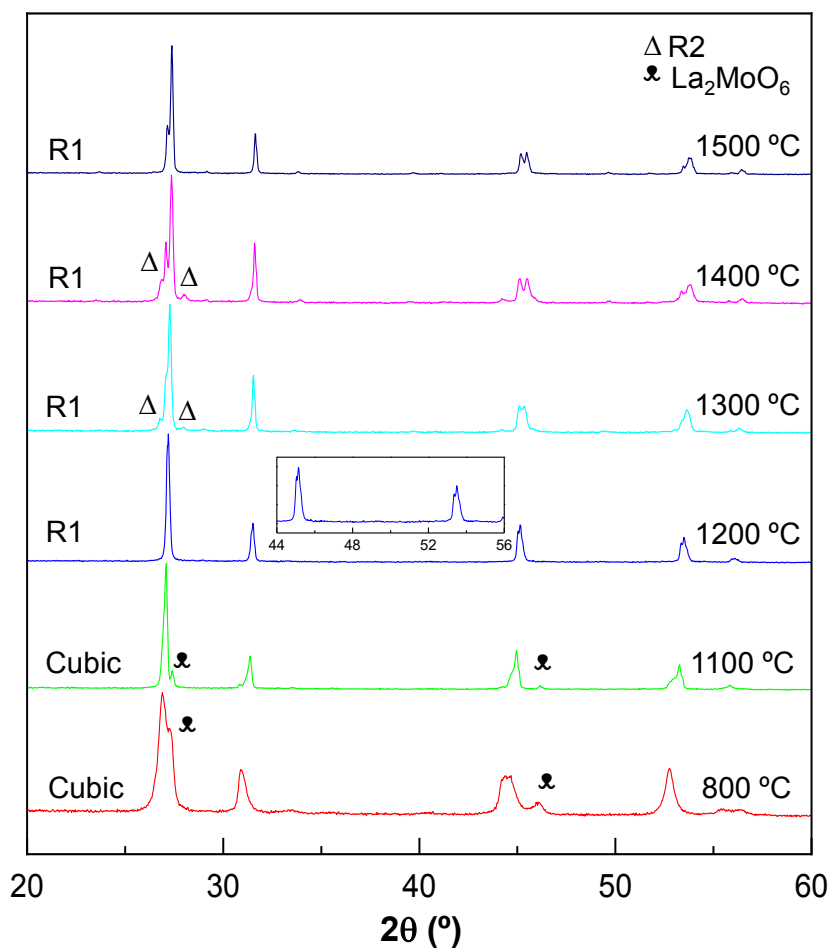


Figure 4.35. XRPD patterns of $\text{La}_{5.4}\text{MoO}_{11.1-y/2}\text{F}_y$ ($y = 3$) obtained by heating 1h between 800 and 1500 °C and cooled down at 5 °C·min⁻¹. The major phase of each sample is denoted at the bottom left of the diffraction patterns and the minor secondary phases are labeled.

At low temperatures ($T \leq 1100$ °C), XRPD patterns show La_2MoO_6 as secondary phase, a phenomenon not observed for the undoped samples. At 1200 °C the sample seems to present a cubic structure, but a close inspection of the XRPD patterns (see inset) reveals a splitting of the diffraction peaks, indicating that the sample is R1. At sintering temperatures between 1300 and 1400 °C, the samples are a mixture of rhombohedral polymorphs, and the R1 phase is only stabilized at 1500 °C. These results indicate that fluorination and the concomitant modification of the anionic framework have a significant effect on the polymorphism of lanthanum molybdates. In addition, it must be mentioned that no F-containing species are detected in the whole range of temperatures, likely due to the incorporation of fluorine to the different phases.

Once it has been verified that the fluorination of lanthanum molybdates is possible and that its effect is beneficial, this study was extended to Mo-site doped materials (previously studied in section 4.4.2 and 4.4.3). XRPD patterns of $\text{La}_{5.4}\text{Mo}_{0.90}\text{B}_{0.10}\text{O}_{11.1-y/2-\delta}\text{F}_y$ ($\text{B} = \text{Ti}, \text{Zr}, \text{and Nb}, y = 3$) heated for 1h between 1200 and 1500 °C and cooled down at 5 °C·min⁻¹ are shown in Figure 4.36.

At 1200 °C, for the fluorinated Ti and Zr-doped molybdates, the samples are a mixture of $\text{LaOF}/\text{La}_3\text{Mo}_2\text{O}_{10}$ (PDF 00-023-0315) and $\text{R1}/\text{La}_2\text{MoO}_6$ (PDF 00-007-0041), respectively. However, for the Nb-doped material, fluorination leads to a monophasic cubic structure, a drastic change from the non-fluorinated sample, which is R2 with minor side phases of R1 and La_2O_3 . In the other hand, all samples sintered between 1300-1500 °C for 1h present a R1 structure without secondary phases, where all their non-fluorinated counterparts showed secondary phases (Figure 4.26).

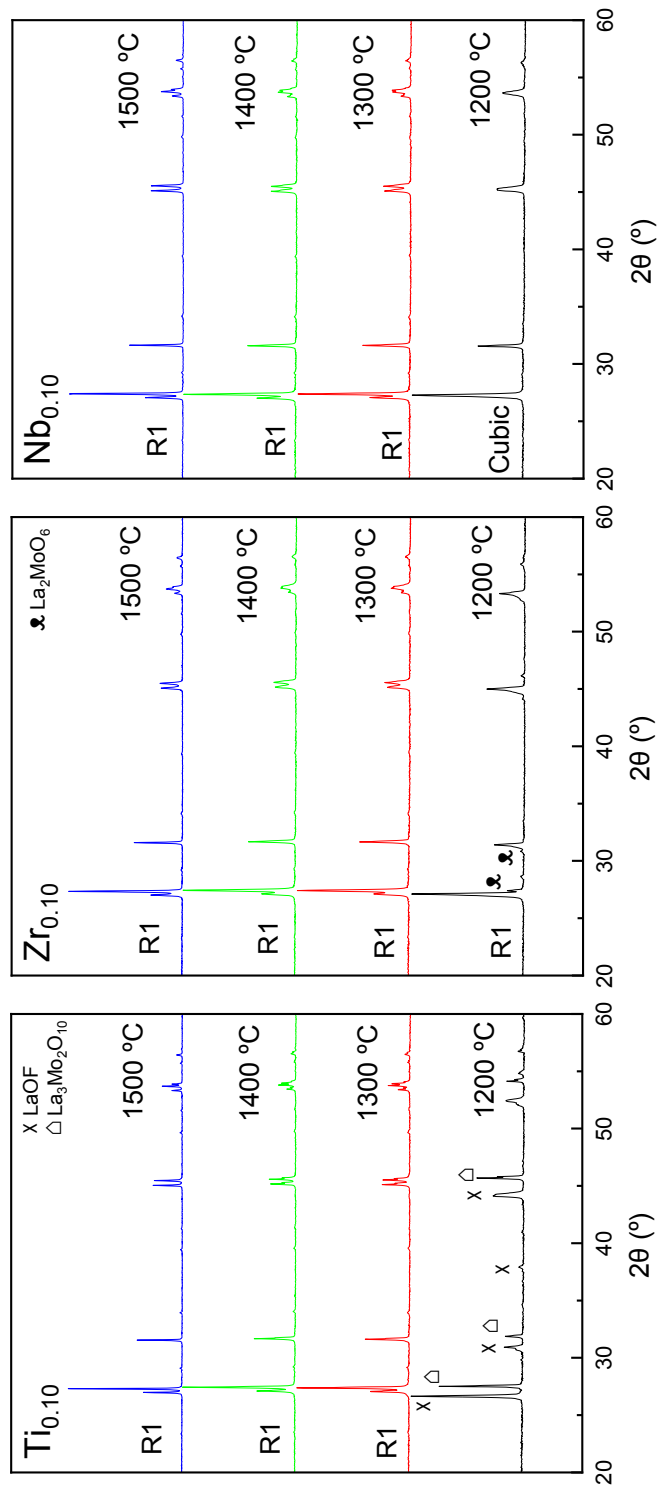


Figure 4.36. XRPD patterns of $\text{La}_{5.4}\text{Mo}_{0.90}\text{B}_{0.10}\text{O}_{11.05-y/2-3F_y}$ (B= Ti, Zr and Nb, y = 3) obtained by heating 1h between 1200 and 1500 °C and cooled down at 5 °C·min⁻¹. The major phase for each sample is denoted at the bottom left of the diffraction peak and the minor secondary phases are labelled.

Once the fluorination method was fine-tuned, the fluorine content was determined by ion chromatography (Table 4.19). In general, there is a low incorporation of fluorine respect to the theoretical value added (~ 16 atom % for $y = 3$), a fact that is accentuated when the sintering temperature increases due to F evaporation. A possible mechanism for this process is proposed in the following equation since the fluorination was not carried out in a dry atmosphere:



Table 4.19. Atomic and weight percentage of fluorine obtained by ion-chromatography and calculated formulas for $\text{La}_{5.4}\text{Mo}_{1-x}\text{B}_x\text{O}_{11.1-y/2-3}\text{F}_y$ ($x = 0, 0.10$; $B = \text{Ti, Zr, Nb}$; $y = 3$) heated 1h between 1200-1400 °C and cooled down at 5 °C·min⁻¹.

Sample	[F] (atom %)	[F] (weight %)	Calc. formula
Mo1200-F₃	0.26	0.085	$\text{La}_{5.4}\text{MoO}_{11.07}\text{F}_{0.045}$
Ti_{0.10}1300-F₃	0.08	0.026	$\text{La}_{5.4}\text{Mo}_{0.90}\text{Ti}_{0.10}\text{O}_{10.993}\text{F}_{0.014}$
Ti_{0.10}1400-F₃	0.01	0.004	$\text{La}_{5.4}\text{Mo}_{0.90}\text{Ti}_{0.10}\text{O}_{10.998}\text{F}_{0.012}$
Zr_{0.10}1300-F₃	0.09	0.03	$\text{La}_{5.4}\text{Mo}_{0.90}\text{Zr}_{0.10}\text{O}_{10.992}\text{F}_{0.016}$
Zr_{0.10}1400-F₃	0.02	0.006	$\text{La}_{5.4}\text{Mo}_{0.90}\text{Zr}_{0.10}\text{O}_{10.998}\text{F}_{0.003}$
Nb_{0.10}1200-F₃	0.8	0.26	$\text{La}_{5.4}\text{Mo}_{0.90}\text{Nb}_{0.10}\text{O}_{10.98}\text{F}_{0.14}$
Nb_{0.10}1300-F₃	0.1	0.034	$\text{La}_{5.4}\text{Mo}_{0.90}\text{Nb}_{0.10}\text{O}_{11.041}\text{F}_{0.018}$
Nb_{0.10}1400-F₃	0.02	0.006	$\text{La}_{5.4}\text{Mo}_{0.90}\text{Nb}_{0.10}\text{O}_{11.048}\text{F}_{0.003}$

In this table, data are only shown for temperatures below 1400 °C because at higher sintering temperatures the fluorine content is under the detection limit of the technique. The chemical formulas have been calculated to take into consideration the fluorine incorporation, resulting, for example,

$\text{La}_{5.4}\text{MoO}_{11.077}\text{F}_{0.045}$ and $\text{La}_{5.4}\text{Mo}_{0.90}\text{Nb}_{0.10}\text{O}_{10.98}\text{F}_{0.14}$ for $\text{La}_{5.4}1200\text{-F}_3$ and $\text{Nb}_{0.10}1200\text{-F}_3$, respectively. Moreover, it can be clearly seen that an increase of the sintering temperature for the same nominal composition leads to a decrease of the fluorine content by evaporation.

$\text{La}_{5.4}\text{Mo}_{0.90}\text{Nb}_{0.10}\text{O}_{11.05-y/2}\text{F}_y$ ($y = 3$) obtained at $1200\text{ }^\circ\text{C}$, which is cubic, was studied by a combined Rietveld refinement of XRPD and NPD data to confirm the fluorine incorporation after the simultaneous cation and anion doping. Data were also collected for the nonfluorinated materials prepared at $1500\text{ }^\circ\text{C}$ and quenched from that temperature, $\text{Nb}_{0.10}1500\text{-Q}$. All refinements were performed with a single fluorite-type structure with an $Fm\bar{3}m$ space group as starting structural model. Occupancy factors were initially set to the nominal stoichiometry, where La, Mo, and Nb were in the same crystallographic positions, and their isotropic displacement parameters were constrained to be the same. Refinement of the occupancy factors led to values close to the theoretical values; therefore, these were maintained. Fluorine was not included in the structural model, as oxygen and fluorine are not distinguishable by neutron powder diffraction. Rietveld XRPD and NPD plots, unit cell parameters, cell volumes, agreement factors, atomic displacement, occupancy factors and interatomic distances are showed in Figure 4.37 and Table 4.20.

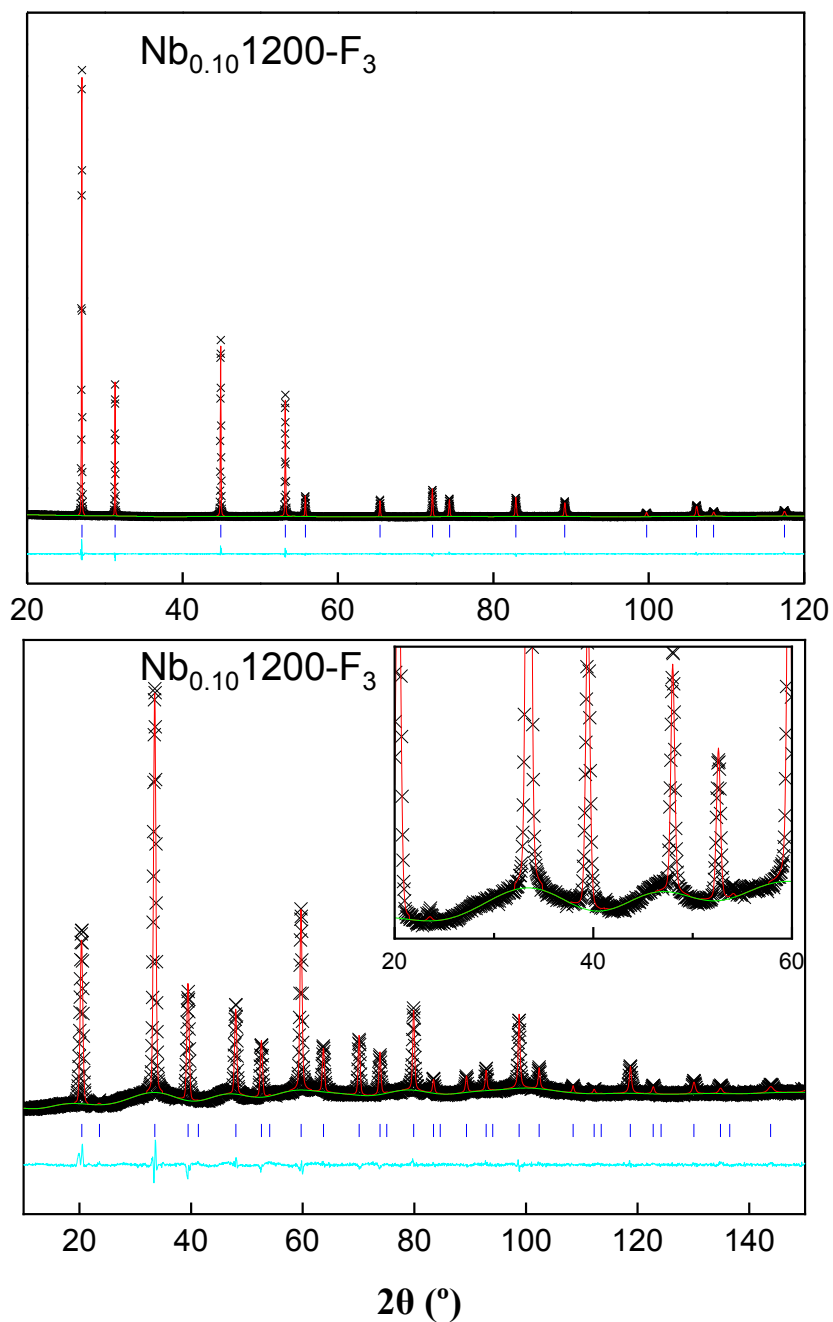


Figure 4.37. Rietveld XRPD (top) and NPD (bottom) plots of $\text{La}_{5.4}\text{Mo}_{0.90}\text{Nb}_{0.10}\text{O}_{11.05}\text{F}_y$ ($y = 3$) obtained by heating at 1200 h and cooled down at $5\text{ }^\circ\text{C}\cdot\text{min}^{-1}$. In the images are represented the experimental data ($\times\times\times$), calculated pattern (—), and difference curve (cyan at the bottom).

Table 4.20. Unit cell parameters, cell volumes, agreement factors, atomic displacement, occupancy factors, and O(F)-O(F) distances determined from a combined XRPD-NPD Rietveld refinement of $\text{La}_{5.4}\text{Mo}_{0.90}\text{Nb}_{0.10}\text{O}_{11.05-y/2}\text{F}_y$ ($y = 3$) obtained by heating at 1200 °C 1h and cooled at 5 °C·min⁻¹. Data for $\text{Nb}_{0.10}\text{1500-Q}$ are also included.

	Nb_{0.10}1200-F₃	Nb_{0.10}1500-Q
a (Å)	5.6993(1)	5.6607(1)
V/Z (Å³)	46.28(1)	45.35(1)
R_{wp}^{XRPD}/R_{wp}^{NPD} (%)	4.00/3.96	4.99/3.89
R_F^{XRPD}/R_F^{NPD} (%)	1.97/4.72	3.54/4.53
Atom	La/Mo/Nb, 4a, (0, 0, 0)	
U_{iso}×100 (Å²)	2.65(1)	2.58(1)
Occupancy factor La/Mo/Nb	0.7714(-)/0.1286(-) /0.0143(-)	0.7714(-)/0.1286(-) /0.0143(-)
Atom	O, 8c, (1, 1, 1)	
U_{iso}×100 (Å²)	2.91(1)	4.84(1)
Occupancy factor O	0.767(2)	0.732(3)
d(O(F)-O(F)) (Å)	2.85(1)	2.83(1)

As can be seen, refinements are quite good with low disagreement factors. An expansion in the cell volume for the fluorinated samples is observed in comparison with the nonfluorinated one, despite the size of F⁻ in a tetrahedral coordination, 1.31 Å, is lower than that of O²⁻ (1.38 Å) in the same environment. This is due to the replacement of one oxygen with two fluorine that produces a concomitant increase in the electrostatic repulsions in the anionic network. The expansion of the unit cell due to the electrostatic repulsions is further confirmed by analysing the O(F)-O(F) distances, which are larger in the anion-doped samples. The high values of the atomic displacement parameters reveal the local disorder of these

materials in both cationic and anionic sublattices. This disorder is also displayed as an undular background of the NPD pattern, as happened with non-fluorinated compounds.

Rhombohedral samples obtained between 1200 and 1500 °C, $\text{La}_{5.4}\text{Mo}_{1-x}\text{B}_x\text{O}_{11.05-y/2-\delta}\text{F}_y$ ($x = 0, 0.1$ and $y = 3$) and cooled down at $5\text{ °C}\cdot\text{min}^{-1}$, were analysed by the Le Bail method (because the R1 and R2 structural models are not applicable for XRPD analysis). Parameters such as unit cell, scale factor, background, and peak shape coefficients were refined and are showed in Table 4.21.

Table 4.21. Unit cell parameters, cell volumes and agreement factors of $\text{La}_{5.4}\text{Mo}_{1-x}\text{B}_x\text{O}_{11.1-y/2-\delta}\text{F}_y$ ($x = 0, 0.1$; $B = \text{Ti, Zr and Nb}$; $y = 3$) series obtained by heating between 1200-1500 °C 1h and cooled down at $5\text{ °C}\cdot\text{min}^{-1}$ determined by Le Bail refinements of XRPD data. A.G.S. column presents the Average Grain Size of samples determined from SEM images that will be shown in the next section.

Sample	a (Å)	c (Å)	V/Z (Å ³)	R _{wp} (%)	A.G.S. (µm)
Mo1200-F₃	3.9936(2)	9.8855(4)	45.30(1)	7.30	1.8
Ti_{0.10}1300-F₃	3.9956(2)	9.9110(5)	45.68(1)	8.65	6.2
Ti_{0.10}1400-F₃	3.9901(1)	9.8937(4)	45.47(1)	9.12	12.1
Ti_{0.10}1500-F₃	3.9808(1)	9.8801(4)	45.20(1)	8.53	16
Zr_{0.10}1300-F₃	3.9949(1)	9.9077(5)	45.64(1)	9.31	4.9
Zr_{0.10}1400-F₃	3.9893(1)	9.8952(5)	45.46(1)	8.56	15.6
Zr_{0.10}1500-F₃	3.9845(1)	9.8834(1)	45.30(1)	7.32	18
Nb_{0.10}1300-F₃	3.9940(1)	9.8853(5)	45.52(1)	9.57	4.3
Nb_{0.10}1400-F₃	3.9919(1)	9.8835(5)	45.46(1)	9.93	13.4
Nb_{0.10}1500-F₃	3.9851(1)	9.8938(3)	45.36(1)	6.23	20.9

The general tendency with the introduction of fluorine is an increase of the cell volumes. In Table 4.21 a decrease in cell volumes is observed when the sintering temperature increases, hence the amount of fluorine is lower. This is due to the preservation of the electroneutrality by the substitution of two fluorines, which increases the anion content. The extra fluorine anion is incorporated into an oxide vacancy position of the lattice, leading to an enlargement of the electrostatic repulsion in the anionic framework that increase the volume. For example, it can be seen for $\text{Nb}_{0.10}\text{1300-F}_3$ and $\text{Nb}_{0.10}\text{1400-F}_3$, with values of 45.52 and 45.46 \AA^3 , respectively.

Finally, the local structure was examined by SAED and HRTEM images to confirm the results obtained by XRPD and NPD (Figure 4.38).

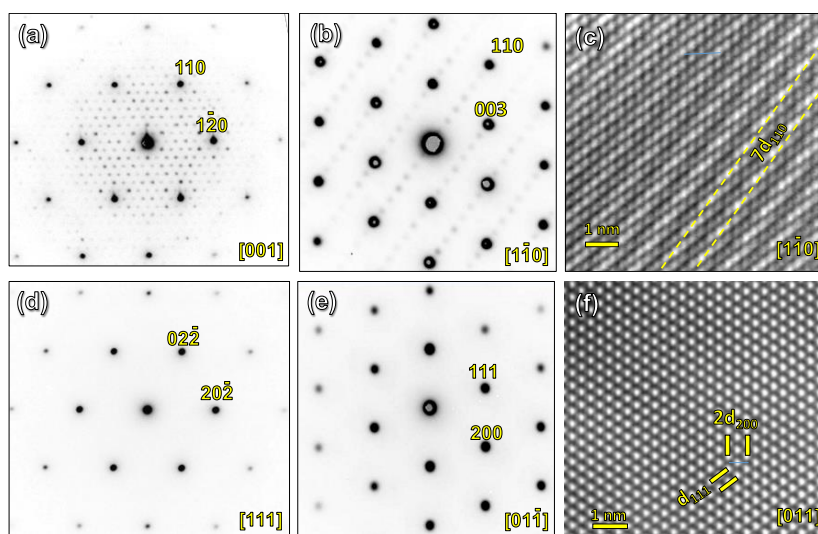


Figure 4.38. SAED patterns and HRTEM images of: (a-c) $\text{La}_{5.4}\text{MoO}_{11.1-2/2}\text{F}_y$ ($y = 3$) obtained by heating at 1500 $^{\circ}\text{C}$ 1h and cooled down at 5 $^{\circ}\text{C}\cdot\text{min}^{-1}$; and (d-f) $\text{La}_{5.4}\text{Mo}_{0.90}\text{Nb}_{0.10}\text{O}_{10.05-2/2}\text{F}_y$ ($y = 3$) obtained by heating at 1200 $^{\circ}\text{C}$ 1h and cooled down at 5 $^{\circ}\text{C}\cdot\text{min}^{-1}$ along different zone axes.

$\text{La}_{5.4}\text{1500-F}_3$ shows intense reflections, which are reminiscent of the fluorite type structure, but additional reflections are observed along a certain crystallographic axis, indicating the formation of a supercell. The SAED

patterns of this specimen (Figure 4.38) have been indexed considering the basic rhombohedral unit cell determined by XRPD data (space group $R\bar{3}$, $a = 3.98 \text{ \AA}$ and $c = 9.88 \text{ \AA}$). In the [001] zone axis a 7×7 superstructure is observed, but these superstructure reflections are not observed along the [003] direction which indicates the real cell is a $7a \times 7a \times c$ superstructure relative to the rhombohedral basic unit cell determined by XRPD. In addition, HR images show this periodicity that remarks the presence of this superstructure. For Nb_{0.10}1200-F₃, HRTEM and SAED images of (Figure 4.38 d, e, f) shows the characteristic reflections of a cubic fluorite structure (s.g. $Fm\bar{3}m$) with a lattice cell parameter of $a_F = 5.6 \text{ \AA}$ without the formation of superstructures, modulations, clusters, or defects.

4.4.5. Microstructural characterization of doped materials.

SEM images (Figure 4.39) reveal that the Nb-doped samples are very dense and the average grain size increases with the dopant content.

For example, the grain size diameter for quenched samples increases from 15.8 to 33.5 μm for La_{5.4}1500-Q and Nb_{0.10}1500-Q, respectively. Although, the grain size increases as the cooling rate decreases due to longer dwelling times at high temperatures, growing the grain size, for example, from 33.5 μm for Nb_{0.10}1500-Q to 54 μm for Nb_{0.10}1500-0.5.

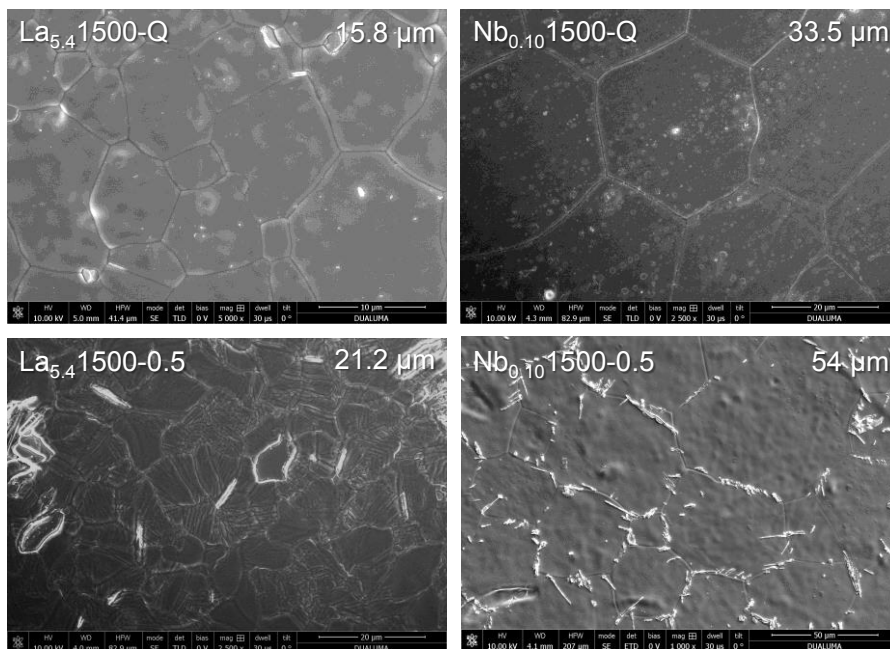


Figure 4.39. SEM images of $\text{La}_{5.4}\text{Mo}_{1-x}\text{Nb}_x\text{O}_{11.1-x/2}$ ($x = 0$ and 0.10) obtained by heating at $1500\text{ }^\circ\text{C}$ 1h and cooled down by quenching and $0.5\text{ }^\circ\text{C}\cdot\text{min}^{-1}$, comparing the grain size with each treatment and showing that the Nb content increases the grain size. In the picture of the sample, $\text{Nb}_{0.10}1500-0.5$ have observed segregations of $\text{La}(\text{OH})_3$ present in the grain boundary, but these segregations are minimal and do not appears in XRPD.

Fluorinated samples sintered at $1500\text{ }^\circ\text{C}$ (Figure 4.40) presented high density. The samples sintered at $1200\text{ }^\circ\text{C}$ present some residual porosity and a relative density close to 90% because of the low sintering temperature. In addition, the average grain size is also smaller, with values of 1.8 and $1.2\text{ }\mu\text{m}$ for $\text{La}_{5.4}1200\text{-F}_3$ and $\text{Nb}_{0.10}1200\text{-F}_3$, respectively. On the other hand, is remarkable the increase of average grain size due the fluorine introduction, as can be seen comparing $\text{La}_{5.4}1500\text{-F}_3$ ($16.3\text{ }\mu\text{m}$, Figure 4.20) and $\text{La}_{5.4}1500\text{-F}_3$ ($30\text{ }\mu\text{m}$).

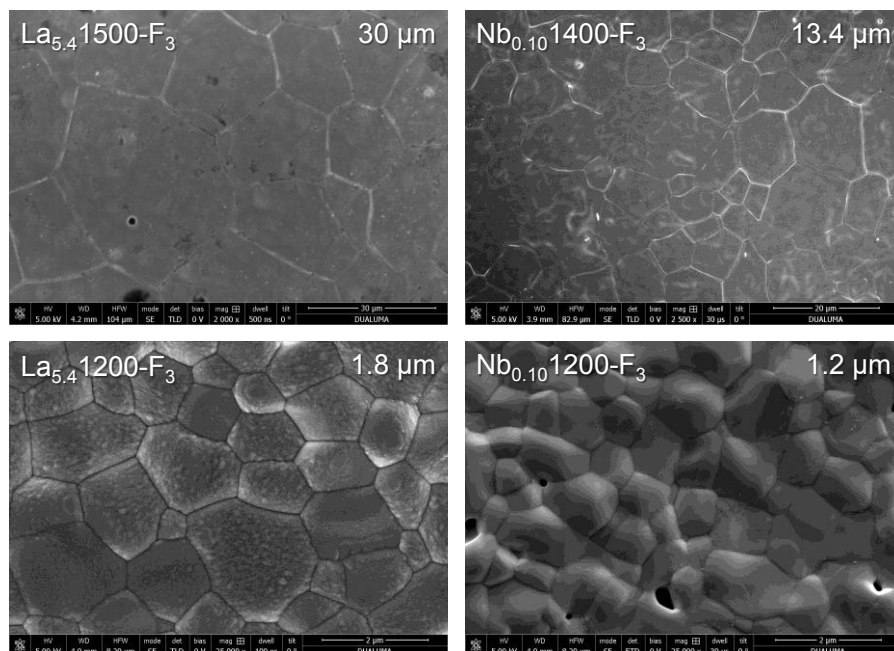


Figure 4.40. SEM micrographs of $\text{La}_{5.4}\text{Mo}_{1-x}\text{Nb}_x\text{O}_{11.1-y/2-5}\text{F}_y$ ($x = 0, 0.10$ and $y = 3$) obtained by heating at different temperatures 1h and cooled down at 5°C min^{-1} . Average grain sizes are included within the micrographs.

In addition, in Table 4.20 are showed the values of average grain size for Ti, Zr and Nb-doped materials. These data demonstrate that at higher sintering conditions, it was observed a decrease in the average grain size obtaining values of 12.1, 15.6, and 13.4 μm for $\text{Ti}_{0.10}1400\text{-F}_3$, $\text{Zr}_{0.10}1400\text{-F}_3$, and $\text{Nb}_{0.10}1400\text{-F}_3$, respectively, comparing with $\text{La}_{5.4}1500\text{-F}_3$ (30 μm). Finally, EDS mapping of $\text{Nb}_{0.10}1200\text{-F}_3$ (Figure 4.41) confirms the homogeneity of sample without liquid phases or segregations. Similar elemental mappings are obtained for other doped samples.

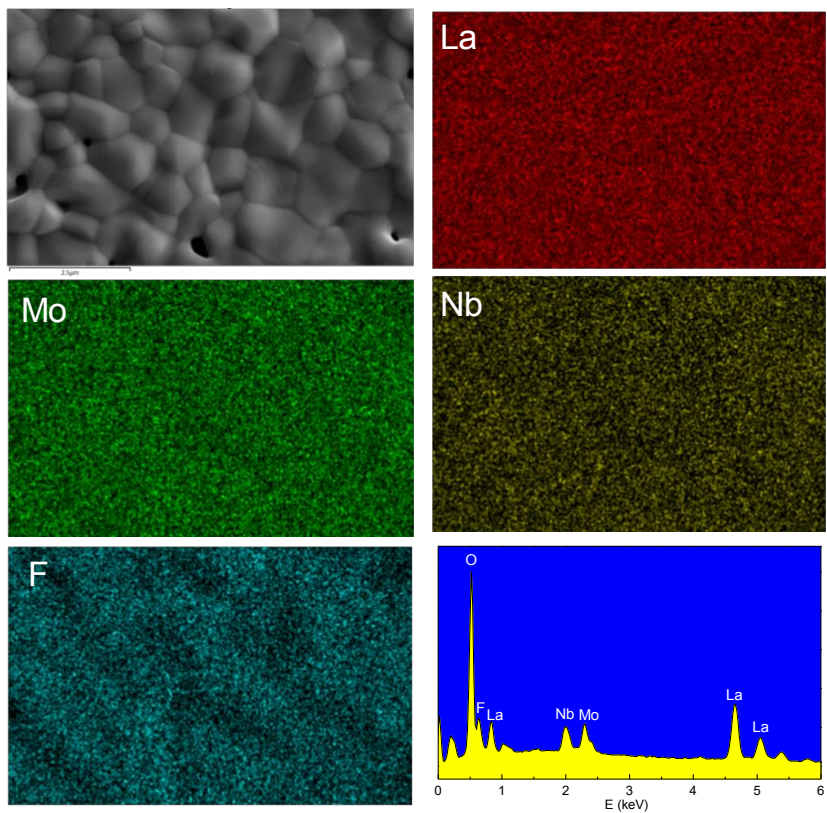


Figure 4.41. SEM-EDS elemental mappings of the surface of $\text{La}_{5.4}\text{Mo}_{0.90}\text{Nb}_{0.10}\text{O}_{11.05-2/2}\text{F}_y$ ($y = 3$) sintered at 1200 °C for 1 h.

4.5. Electrical characterization of doped materials.

The influence of doping on the conductivity was studied; for that, the materials were pelletized and the different contributions to the overall conductivity were characterized by impedance spectroscopy under several atmospheres (dry N₂, wet N₂ and wet 5% H₂-Ar). All spectra show similar characteristics, independently of the composition, atmosphere, and cooling rate employed during the synthesis as can be seen in representative spectra for La_{5.4}Mo_{1-x}Nb_xO_{11.1-y/2-δ}F_y (x = 0, 0.10 and y = 0, 3) shown in Figure 4.42.

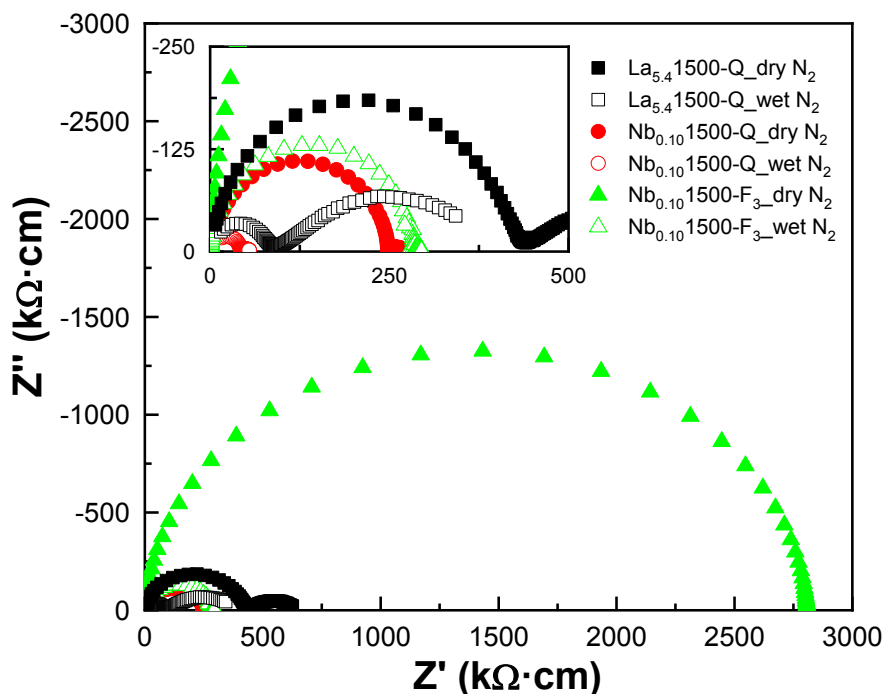


Figure 4.42. Representative impedance spectra at 400 °C of La_{5.4}Mo_{1-x}Nb_xO_{11.1-y/2-δ}F_y (x = 0, 0.10 and y = 0, 3) obtained by heating at 1500 °C 1h and cooled down by quenching (5 °C·min⁻¹ in case of fluorinated samples) under dry/wet N₂ and wet 5% H₂-Ar gases at 400 °C.

Two processes are distinguished in the spectra; the dominant one, at high frequency, with a capacitance of ~pF·cm⁻¹ is associated with the grain interior conduction. The low-frequency contribution with higher values of

capacitance, $\sim \text{mF}\cdot\text{cm}^{-1}$, is attributed to the electrode response. Thus, no grain boundary contribution to the conductivity is detected for any sample or sintering temperature, due to the large grain size of the sample and the absence of phase segregations, as it was also discussed for the undoped compositions. The impedance spectra were simulated by an equivalent circuit model: $(R_b Q_b)(R_e Q_e)$, where R is resistance and Q is a pseudocapacitance, and b and e denote the grain interior and electrode responses, respectively.

The conductivity of undoped and Nb-doped samples heated at 1500 °C 1h, cooled at different rates were represented in Arrhenius and isotherms plots showed in Figures 4.43 and 4.44.

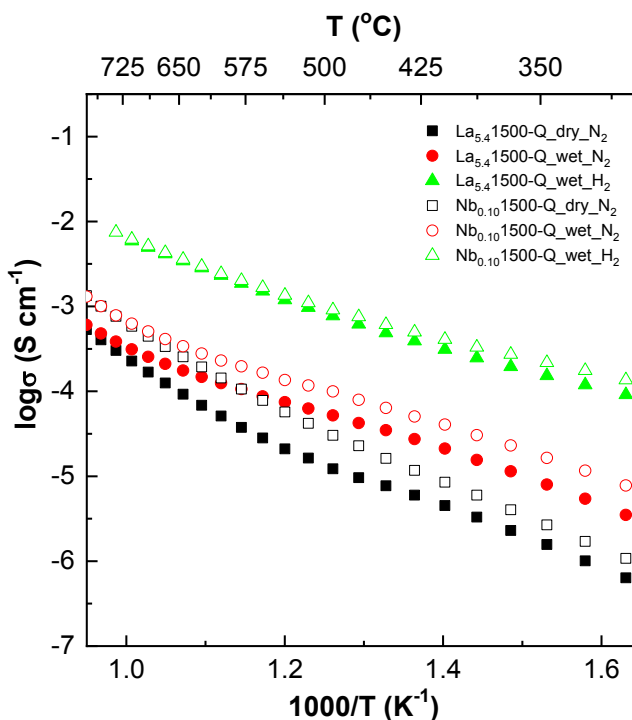


Figure 4.43. Arrhenius plots of the overall conductivity of $\text{La}_{5.4}\text{Mo}_{1-x}\text{Nb}_x\text{O}_{11.1-x/2}$ ($x = 0, 0.10$) obtained by heating at 1500 °C 1h and cooled down by quenching, measured in dry/wet N_2 and wet 5% H_2 -Ar.

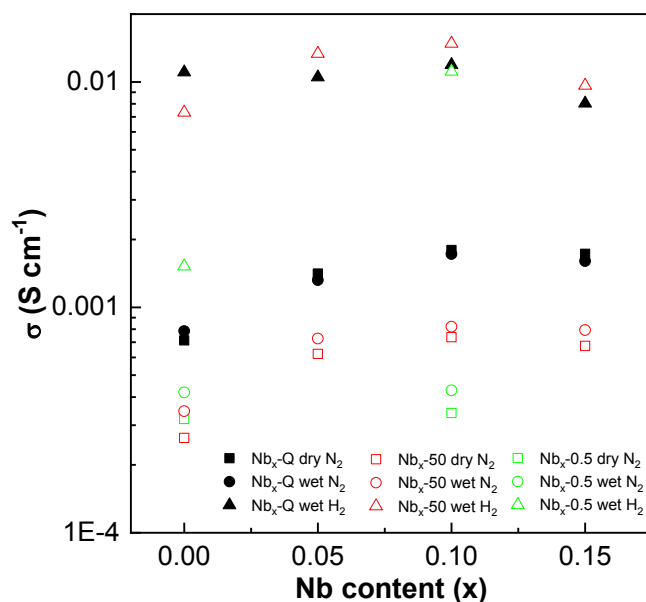


Figure 4.44. Conductivity of $\text{La}_{0.54}\text{Mo}_{1-x}\text{Nb}_x\text{O}_{11.1-x/2}$ ($x = 0, 0.10$) obtained by heating $1500\text{ }^\circ\text{C}$ 1h and cooled by quenching, 50 and $0.5\text{ }^\circ\text{C}\cdot\text{min}^{-1}$ measured at $800\text{ }^\circ\text{C}$ in dry/wet N_2 and wet 5% H_2 -Ar.

Arrhenius plots show a very significant increase of the conductivity in wet atmospheres at low temperatures ($T < 600\text{ }^\circ\text{C}$) for both the cubic and rhombohedral polymorphs, due to a significant proton contribution to the overall conductivity. As expected, the proton conductivity decreases as the temperature increases due to the release of water and a reduction in the proton concentration, being the values similar in dry and wet conditions over $700\text{ }^\circ\text{C}$. In general, the quenched samples exhibit higher conductivity values than those prepared at low cooling rates, which could be explained by the higher structural symmetry and improved mobility of the charge carriers

For cubic Nb-doped materials (Figure 4.44), the overall conductivity increases with Nb-doping due to the generation of extrinsic oxide ion vacancies in the lattice when Mo^{6+} is partially substituted by Nb^{5+} . The maximum conductivity is observed for $x = 0.10$, with a value of $1.7\text{ mS}\cdot\text{cm}^{-1}$

at 800 °C in wet N₂, which is a significant improvement respect to the undoped compound $\sim 0.71 \text{ mS}\cdot\text{cm}^{-1}$. A similar trend is observed in the low-temperature range ($T < 600 \text{ }^\circ\text{C}$), where the conductivity is dominated by the proton contribution. Therefore, Nb-doping enhances both oxide ion and proton conductivity in La_{5.4}MoO_{11.1}-based compounds up to $x = 0.10$. An increase of Nb-substitution above $x > 0.15$ leads to an excessive oxygen vacancy concentration in the lattice and their possible association; consequently, no further improvement of the conductivity is observed.

Regarding the Nb_x1500-0.5 series, a decrease in conductivity is observed for Nb_{0.10}1500-0.5 in comparison with the undoped compound, which change on doping from R2 to R1. No other members of this series were analyzed by impedance spectroscopy due to the segregation of La₂O₃ and the disruptive expansion of the pellets.

In addition, the conductivity of fluorine-doped samples was also studied, and it is represented as an Arrhenius plot in Figure 4.45.

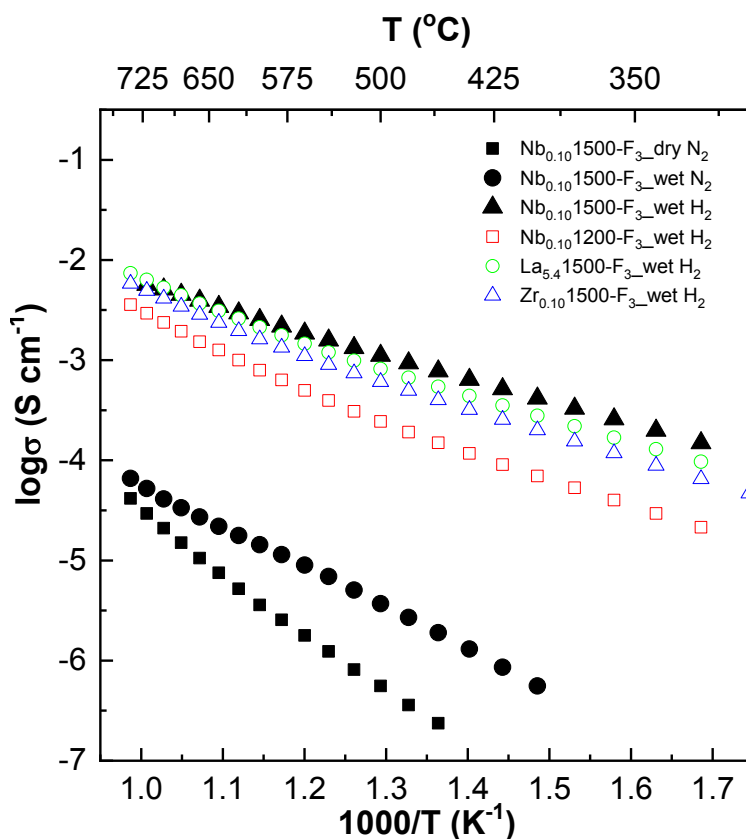


Figure 4.45. Arrhenius plots of the overall conductivity $\text{La}_{5.4}\text{Mo}_{0.90}\text{Nb}_{0.10}\text{O}_{11.05-y/2}\text{F}_y$ ($y = 3$) were sintered at $1500\text{ }^{\circ}\text{C}$ for 1h and cooled at $5\text{ }^{\circ}\text{C}\cdot\text{min}^{-1}$ under different flowing atmospheres. Other selected samples measured under wet 5% H_2 -Ar are also shown.

It must be mentioned that a significant drop in conductivity is observed for $\text{Nb}_{0.10}1500\text{-F}_3$ respect to $\text{Nb}_{0.10}1500\text{-50}$, from 0.21 to $0.02\text{ mS}\cdot\text{cm}^{-1}$ at $700\text{ }^{\circ}\text{C}$, in dry N_2 . Moreover, for $\text{Nb}_{0.10}1500\text{-50}$, the activation energies in the low-temperature range are 0.81 and 0.72 eV under dry and wet conditions, respectively, whereas for $\text{Nb}_{0.10}1500\text{-F}_3$ these values are 1.07 and 0.89 eV , respectively, in the same range. This drop in the conductivity and activation energies increase might be due to the minor filling of the oxide vacancies by fluorine atoms, hindering the oxide ion conduction mechanism because of the

loss of oxide vacancies, as it was demonstrated by NPD studies. Under reducing conditions, the conductivity increases due to a significant n-type contribution, caused by a minor reduction of Mo^{6+} to Mo^{5+} , reaching values like those reported for nonfluorinated samples (demonstrating that the small incorporation of fluorine into the anionic framework does not modify the molybdenum oxidation state).

Comparing the Arrhenius plots for other cation-doped samples with rhombohedral symmetry sintered at 1500 °C, at temperatures lower than 600 °C, $\text{Nb}_{0.10}1500\text{-F}_3$ exhibits slightly higher conductivity than $\text{La}_{5.4}1500\text{-F}_3$, with values of 1.1 and 0.81 $\text{mS}\cdot\text{cm}^{-1}$, respectively, at 500 °C, due to a higher number of oxide vacancies. However, $\text{Zr}_{0.10}1500\text{-F}_3$ shows the lowest conductivity, 0.61 $\text{mS}\cdot\text{cm}^{-1}$ at 500 °C, likely due to the smaller average grain size. In addition, $\text{Nb}_{0.10}1200\text{-F}_3$, despite its high symmetry, presents lower conductivity values than the other samples, 0.24 $\text{mS}\cdot\text{cm}^{-1}$ at 500 °C, likely due to its low sintering temperature and lower relative density, as mentioned in the microstructure section.

Finally, the stability of these materials in separation membranes working conditions was studied in Appendix 6.3, being stable and showing potential to be used as hydrogen separation membranes. Hence, these materials are proton conductors under oxidizing and wet conditions; however, they are predominantly n-type electronic conductors under reducing atmospheres. In Appendix 6.4, are showed preliminary hydrogen permeability experiments that evaluate the performance of these materials as hydrogen separation membranes.

5. CONCLUSIONS.

From the work carried out in this thesis, the following conclusions can be drawn:

1) $\text{La}_{6-x}\text{MoO}_{12-\delta}$ ($0.6 \leq x \leq 2$) compounds were synthesized by the freeze-drying precursor method and the calcination conditions were optimized in order to obtain single phase materials. Several cooling rates were applied to all samples after heating them at 1500 °C 1h, obtaining different polymorphs: a simple cubic fluorite-type (space group $Fm\bar{3}m$) for all samples cooled by quenching, two different rhombohedral phases for the samples with high lanthanum contents ($x = 0.6, 1$) cooling at 50 and 0.5 °C min^{-1} (denominated as R1 and R2, respectively) and a monoclinic symmetry for low lanthanum content samples ($x = 2$) cooled at 0.5 °C $\cdot \text{min}^{-1}$.

2) The crystal structures of the R1 and R2 polymorphs for $\text{La}_{5.4}\text{MoO}_{11.1}$ have been deduced from HRTEM images and SAED patterns using the superspace formalism and the Rietveld method with neutron powder diffraction data. For R1, a model with eight cationic positions and 12 for oxygen was proposed. The R2 model consisted of five cationic positions and seven for oxygen. Rietveld refinements of both models presented good agreement factors, reasonable bond distances and experimental formula and densities very close to the theoretical ones.

3) In order to optimize the properties of the materials, an aliovalent substitution in the cationic-anionic framework was carried out, $\text{La}_{5.4}\text{Mo}_{1-x}\text{B}_x\text{O}_{12-y/2-\delta}\text{F}_y$ ($\text{B} = \text{Ti, Zr, Nb}$; $x = 0, 0.1$; $y = 0, 3$). It was observed that the cationic-doping favours the formation of the R1 phase over R2, specially for Nb-doping, which fully stabilizes the R1 form. Modification of the anionic framework through fluorination also leads to stabilization of high symmetry forms and leads to single phases where their nonfluorinated

counterparts presented secondary phases. Chemical analysis by ionic chromatography and neutron powder diffraction confirm that fluorine is introduced in the crystalline structure.

4) Microstructural analysis by scanning electron microscopy and energy-dispersive X-ray spectroscopy revealed that all samples present a very low porosity without segregations at the grain boundary and a high homogeneity. Average grain sizes are high and significantly increase for lower lanthanum content and cation/anion doped samples.

5) The electrical characterization of the samples by impedance spectroscopy showed no grain boundary contribution to the total conductivity, only grain interior due to the high average grain sizes. For all samples, it is detected an important proton contribution to the overall conductivity at temperatures lower than 650 °C. Above that temperature the conductivity is dominated by the oxide ion mobility. In general, the samples with higher symmetry present improved electrical properties.

6) For the $\text{La}_{6-x}\text{MoO}_{12-\delta}$ ($0 \leq x \leq 3$) series the ionic conductivity in N_2 atmospheres decreases for lower lanthanum contents due to excessive formation of oxide ion vacancies. However, on the other hand, the electronic conductivity in 5% H_2 -Ar atmospheres improves due to the lowering of the Mo-Mo distances, facilitating the electron hopping.

7) The doped samples, $\text{La}_{5.4}\text{Mo}_{1-x}\text{B}_x\text{O}_{12-y/2-\delta}\text{F}_y$ ($\text{B} = \text{Ti, Zr, Nb}$; $x = 0, 0.1$; $y = 0, 3$) present an improvement in conductivity for cation co-doping, due to the oxygen vacancies generated by the aliovalent substitution. Oppositely, fluorine-doping leads to a decrease of the ionic conductivity due to the filling of the oxide vacancies, but to an improvement of the electronic contribution due to decrease of cell volume on fluorine doping.

6. APPENDIXES.

6.1. Phase stability and thermal characterization of $\text{La}_{5.4}\text{MoO}_{11.1}$.

The stability of the samples was evaluated by XRPD after annealing the powders between 800 and 1000 °C for 48h in air and 5% H_2 -Ar. At 800 °C in air and 5% H_2 -Ar, all samples retain the original structure without any evidence of secondary phases. Cell parameters were obtained by Rietveld XRPD refinements for these samples after treatments are shown in Table 6.1 and the resulting XRPD plots are shown in Figure 6.1.

Table 6.1. Unit cell parameters of $\text{La}_{5.4}\text{MoO}_{11.1}$ heated at 1500 °C 1h and cooled down at different rates (quenching, 50 and 0.5 °C·min⁻¹) after annealing the powders at 800 °C 48h in air and 5% H_2 -Ar.

La_{5.4}1500-Q	a (Å)		V/Z (Å³)	R_{wp} (%)	R_F (%)
As prepared	5.6676(1)		45.51(1)	6.87	3.15
800°C 48h (air)	5.6729(2)		45.64(1)	8.75	2.02
800°C 48h (5%H_2-Ar)	5.6671(2)		45.50(1)	7.53	2.15
La_{5.4}1500-50	a (Å)	c (Å)	V/Z (Å³)	R_{wp} (%)	
As prepared	3.9914(1)	9.8715(2)	45.40(1)	10.35	
800°C 48h (air)	3.9934(1)	9.8747(4)	45.46(1)	10.17	
800°C 48h (5%H_2-Ar)	3.9922(1)	9.8814(4)	45.46(1)	8.48	
La_{5.4}1500-0.5	a (Å)	c (Å)	V/Z (Å³)	R_{wp} (%)	
As prepared	4.0996(1)	9.5204(2)	46.19(1)	9.39	
800°C 48h (air)	4.1089(2)	9.4933(6)	46.27(2)	10.17	
800°C 48h (5%H_2-Ar)	4.1083(2)	9.5007(6)	46.29(2)	8.71	

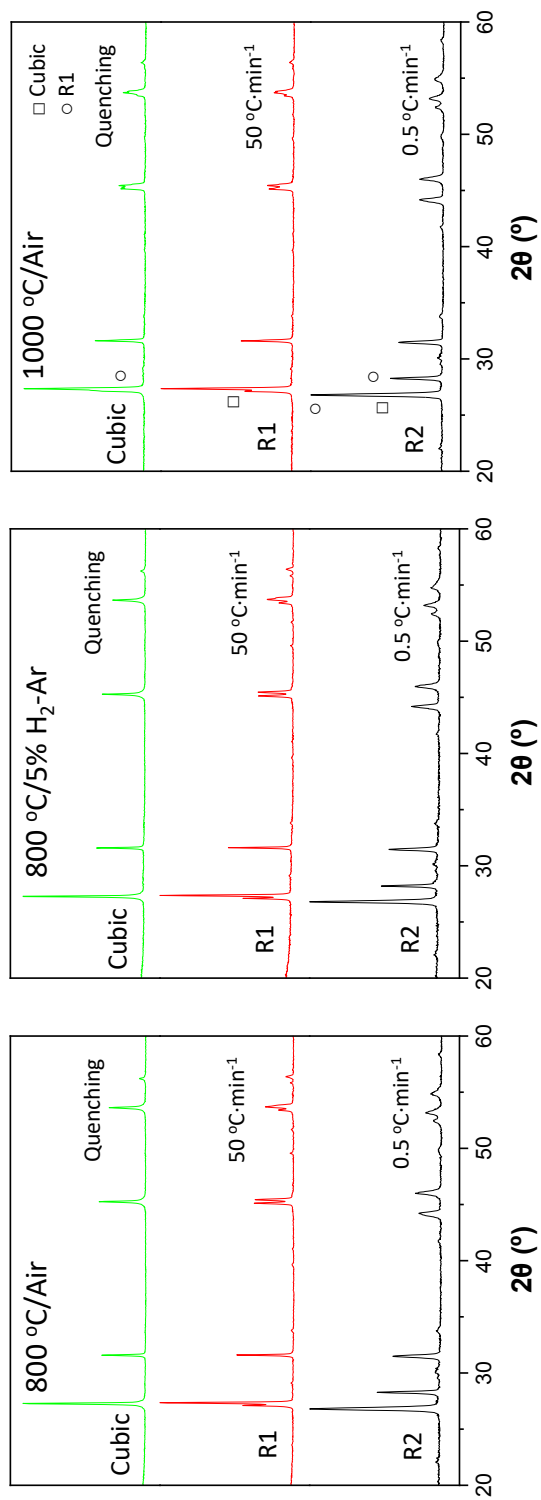


Figure 6.1. XRPD patterns of $\text{La}_{0.54}\text{MoO}_{11.1}$ obtained by heating at 1500 °C 1h and cooled down at different rates (quenching, 50 and 0.5 °C·min⁻¹) after annealing for 48 h in air at 800 °C and air at 1000 °C. The major phase for each sample is denoted at the bottom left of the diffraction patterns and secondary phases are labelled.

As can be seen all materials, maintain the crystalline structure before being in working conditions, confirming their stability and application for hydrogen separation membrane. In addition, no significative change is observed in the cell parameters, indicating the stability of materials. At higher temperatures (1000 °C) all samples are stables, except La_{5.4}1500-Q which suffers a partial degradation after 48h, leading to a mixture of cubic and rhombohedral polymorphs.

Also, the materials were analyzed by HT-XRPD, and no phase transformation was observed between RT and 1000 °C (Figure 6.2).

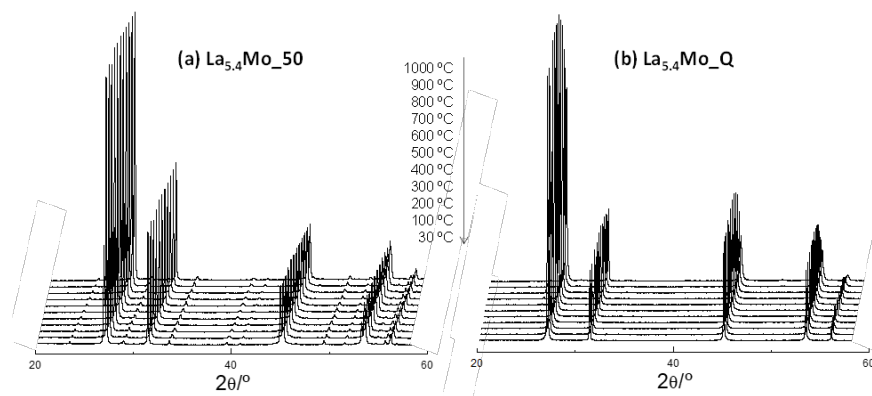


Figure 6.2. HT-XRPD for La_{5.4}MoO_{11.1} that were cooled down by (a) 50 °C·min⁻¹ and (b) quenching, measured at temperatures between 30°C and 1000 °C.

At temperatures over 1000 °C the materials are not stable. Hence, it can be concluded that the different polymorphs of La_{5.4}MoO_{11.1} are structurally stable, and therefore suitable for potential applications at temperatures below 800 °C. The thermal expansion coefficients, determined by the HT-XRPD data, were $10.5 \cdot 10^{-6} \text{ K}^{-1}$ for La_{5.4}1500-Q and $12.0 \cdot 10^{-6} \text{ K}^{-1}$ for La_{5.4}1500-0.5. The values are like those reported for lanthanum tungstates, i.e., $11 \cdot 10^{-6} \text{ K}^{-1}$ for La_{5.4}WO_{11.1} (Magrasó *et al.*, 2013 and Zayas-Rey *et al.*, 2014) having thermomechanical compatibility for separation membranes applications.

For $\text{La}_{5.4}$, the water uptake was monitored by thermogravimetric analysis as a function of the temperature to indirectly determine the concentration of oxygen vacancies available for hydration. The thermogravimetric curves, collected under humidified air, were reproducible on both heating and cooling cycles. For the sake of comparison, only the curves taken on cooling are shown in Figure 6.3.

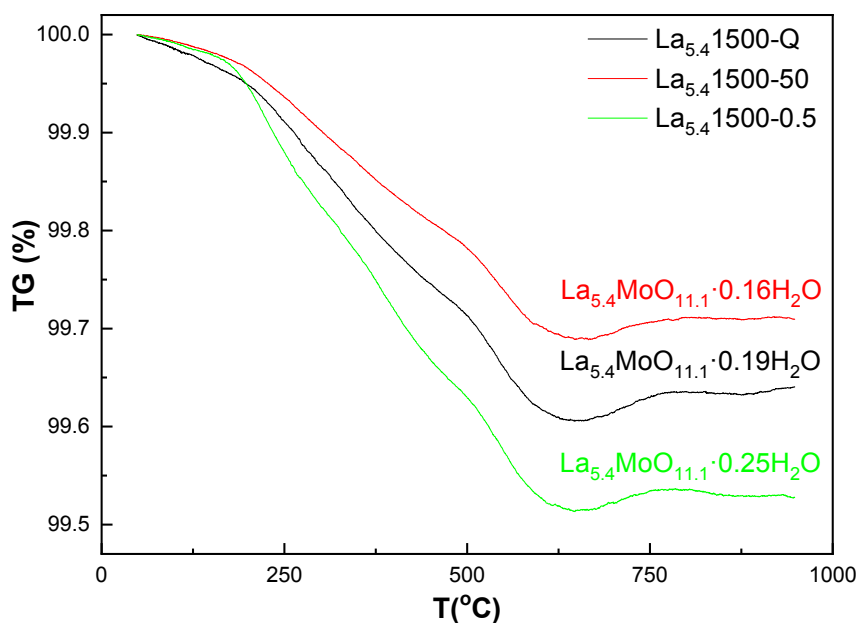


Figure 6.3. Thermogravimetric curves for $\text{La}_{5.4}\text{MoO}_{11.1}$ calcinated at 1500 °C 1h and cooled down at different rates (quenching, 50 and 0.5 °C·min⁻¹) performed under humidified air from room temperature to 1000 °C on cooling. The numbers of water molecules per mole of lanthanum molybdate are shown over the curves.

All samples have the typical weight increase upon cooling due to water uptake and the formation of protonic defects of proton-conducting material, according to the exothermic hydration of oxygen vacancies:



The water uptake starts approximately at 650 °C, a temperature similar to that of lanthanum tungstates (Zayas-Rey et al., 2013). Therefore, these materials are expected to be predominantly proton conductors below 650 °C. As can be seen, the highest water uptake is for La_{5.4}1500-0.5, with 0.25 mol (H₂O)/mol (La_{5.4}MoO_{11.1}), and the lowest one is for La_{5.4}1500-50, with 0.16 mol (H₂O)/mol (La_{5.4}MoO_{11.1}).

6.2. X-ray photoelectronic spectroscopy characterization.

La_{5.4}MoO_{11.1} was studied by X-ray photoelectron spectroscopy to analyze superficial atomic concentration as well as the possible oxidation states of the molybdenum. Table 6.2, show the estimated atomic concentration of each sample, as well as the La/Mo atomic ratios. The superficial La/Mo ratio is similar for all samples, about 4.8, but is lower than the nominal one, 5.4, indicating that the material surface is slightly lanthanum deficient, although the limited precision of this technique for cation quantification should be considered.

Table 6.2. Surface atomic concentration (at. %) of La_{5.4}MoO_{11.1} heated at 1500 °C 1h and cooled down at different rates (Q, 50 and 0.5 °C·min⁻¹).

Sample	O 1s	C 1s	La 3d	Mo 3d	La/Mo
La _{5.4} 1500-Q	55.8	29.2	12.3	2.6	4.7
La _{5.4} 1500-50	56.8	27.0	13.5	2.8	4.8
La _{5.4} 1500-0.5	56.6	26.9	13.7	2.8	4.9

Figure 6.4, show the O 1s core level was decomposed into three different contributions at binding energies (BEs) of 528.5, 530.8, and 532.1 eV. The relative intensity of these components varied for each sample. The main contribution (O_I), located at 530.8 eV, is close to that reported for MoO_3 , ~ 530.9 eV and for La_2O_3 oxide, ~ 530.5 eV, and hence, this is ascribed to the lanthanum molybdenum mixed oxide. Moreover, the band at 532.1 eV (O_{III}) is assigned to adsorbed oxygen or OH groups. This contribution is more important for those samples as the cooling rate is slower. This contribution is more important for those samples prepared at a lower cooling rate and could be related to superficial OH species due to water uptake. The third contribution at lower binding energies (O_{II}), 528.5 eV, is also observed for $La_{5.4}1500-50$ and $La_{5.4}1500-0.5$ samples, which becomes more important as the cooling rate is slower. This contribution, which is not observed for the cubic $La_{5.4}1500-Q$ sample, is also detected in the Mo 3d and La 3d signals and might be related to the different crystal symmetry of the structures. These contributions are shown in Figure 6.4.

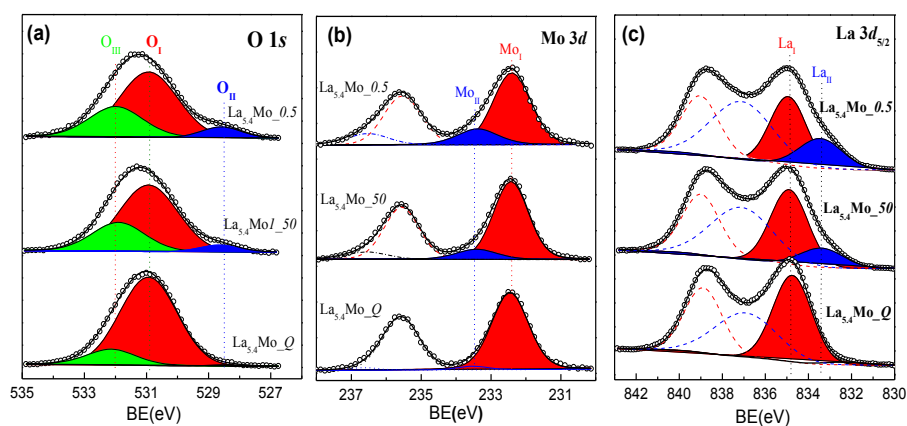


Figure 6.4. XPS spectra for O 1s, Mo 3d and La 3d_{5/2} for samples $La_{5.4}1500-Q$, $La_{5.4}1500-50$, $La_{5.4}1500-0.5$.

The Mo 3d core level consists of two doublets, Mo 3d_{5/2} and Mo 3d_{3/2}, separated by 3.16 eV, with a similar area ratio of Mo 3d_{5/2} / Mo 3d_{3/2}. The Mo 3d_{5/2} signal was considered to identify the molybdenum oxidation states. All of them showed a main contribution at 232.4 eV, assigned to Mo⁶⁺ species. A small contribution is discernible at higher BE, about 233.4 eV, which cannot be assigned to molybdenum in lower oxidation states. This contribution is not observed for the cubic polymorph and becomes more important for those samples prepared at lower cooling rates, indicating that this is possibly related to Mo⁶⁺ species in different chemical environments.

Lanthanum spectra show strong satellite peaks; their intensity and energy separation depend on the ligand atom due to a charge transfer from the valence band of the ligand atom. This fact makes the La 3d spectrum difficult to decompose. In the present work, only the La 3d_{5/2} component was studied. Dashed lines correspond to satellite peaks. The main peak is located at 834.8 eV, is observed for those samples prepared at a slower cooling rate and assigned to a new chemical environment for the La³⁺ in the rhombohedral polymorphs.

The XPS spectra of the cubic polymorph, previously reduced in 5% H₂-Ar at 800 °C for 24h, were also acquired to study the possible reduction of molybdenum. The Mo 3d core level is like that of the oxidized sample, indicating that only a small and undetectable fraction of Mo⁶⁺ is reduced to lower oxidation states (Figure 6.5). This result is in good agreement with the nearly constant unit cell volume of the samples treated in air and hydrogen (see Table 6.1.).

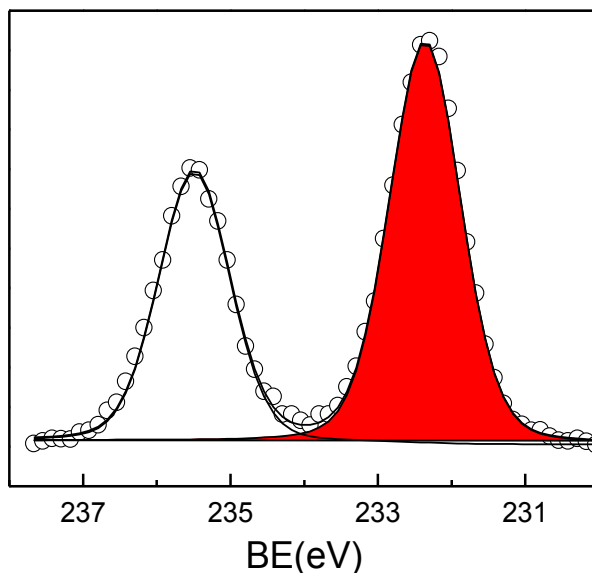


Figure 6.5. XPS spectra of Mo 3d core level for La_{5.41500}-Q treated in 5% H₂-Ar for 24h. Mo⁶⁺ is only observed.

6.3. Phase stability of doped compounds under reducing conditions.

To ensure the reliability of these materials under reducing conditions, and their application as hydrogen separation membranes, a stability test was performed for single-phase compounds. The fluorinated samples were annealed at 800 °C for 48h under flowing 5% H₂-Ar and analyzed afterward by XRPD which are resumed in Figure 6.6.

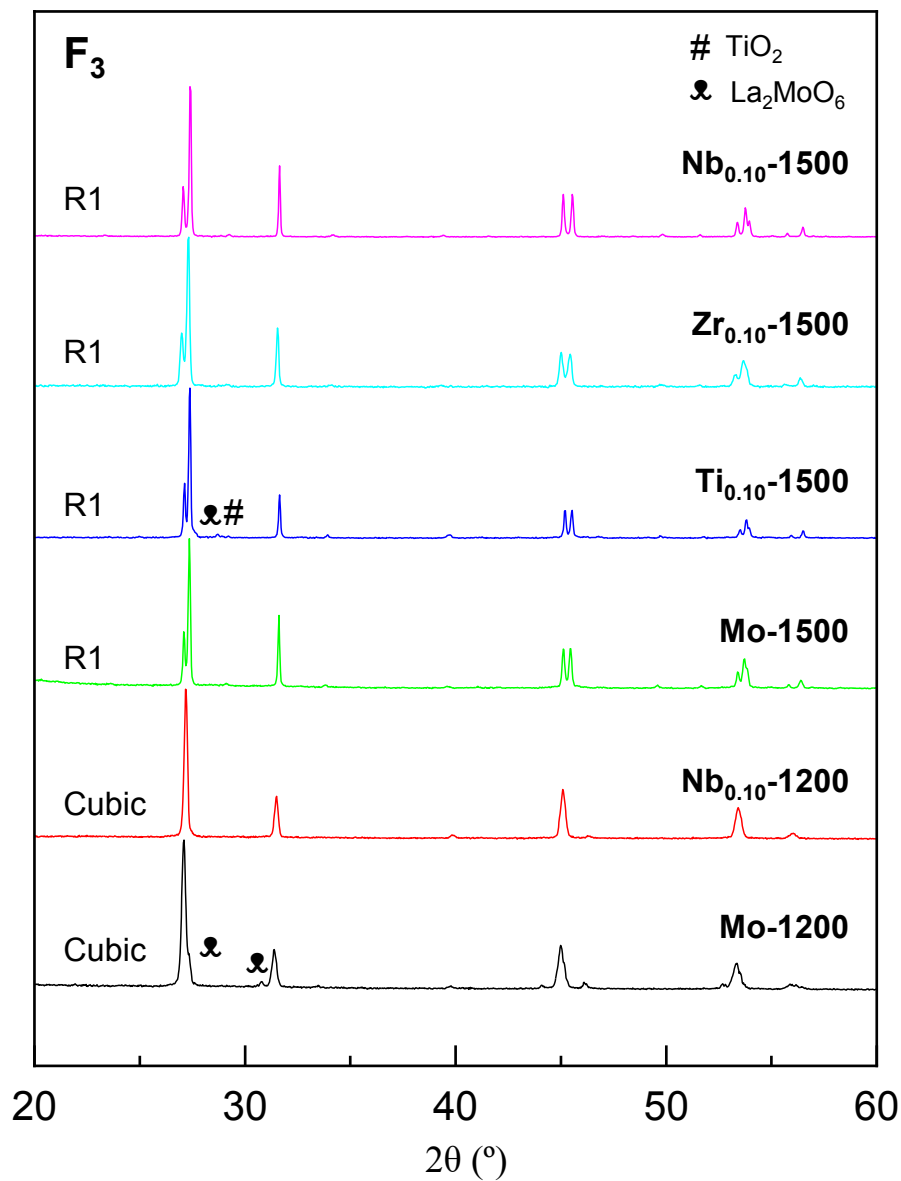


Figure 6.6. XRPD patterns of cubic and rhombohedral $[La_{5.4}Mo_{1-x}B_xO_{11.1-y/2-\delta}F_y]$ ($x = 0, 0.10$; $B = Ti, Zr, Nb$; $y = 3$) samples, obtained at 1200 and 1500 °C, respectively; after annealing the powders at 800 °C for 48 h in 5% H_2 -Ar. The main phase for each sample is denoted at the bottom left of the diffraction patterns and the diffraction peaks of the minor secondary phases are labeled.

The materials remain stable after the treatment under reducing conditions, maintaining an R1 or cubic symmetry. However, for Mo1200-F₃ and Ti_{0.10}1500-F₃, segregations of La₂MoO₆ and TiO₂ have been detected.

6.4. Hydrogen separation membrane test.

These materials were tested in hydrogen permeation experiments to confirm their applicability as hydrogen separation membrane. This test was performed by Dr. José M. Serra from *Instituto de Tecnología Química* at *Universidad Politécnica de Valencia*. The data obtained are showed in Figure 6.7.

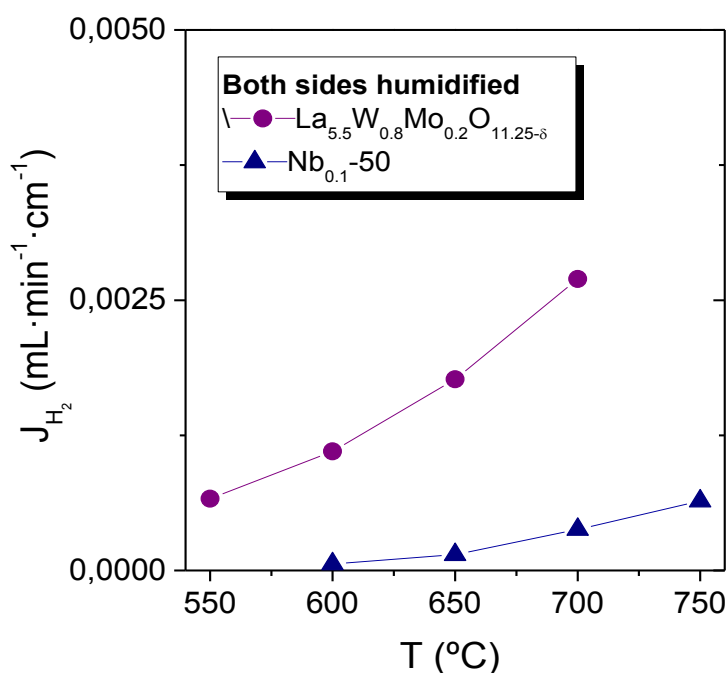


Figure 6.7. Hydrogen permeation for $La_{5.4}Mo_{0.9}Nb_{0.1}O_{11.05}$ obtained by heating at 1500 °C 1h and cooled down at 50 °C·min⁻¹ compared with $La_{5.5}W_{0.8}Mo_{0.2}O_{11.25-\delta}$.

As can be seen, for Nb_{0.1}1500-50 the permeability increases with the temperature, with values of 0.0003 mL·min⁻¹·cm⁻¹ at 700 °C with a feed of 50% H₂-Ar. This is significantly lower than for La_{5.5}W_{0.8}Mo_{0.2}O_{11.25-δ}, with 0.003 mL·min⁻¹·cm⁻¹ in the same conditions (Escolástico *et al.*, 2013b). The results show that much further work is necessary to improve the performance of lanthanum molybdates as hydrogen separation membranes.



7. BIBLIOGRAPHY.

A

- Al-Mamouri M., Edwards P.P., Greaves C. and Slaski M. Synthesis, and superconducting properties of the strontium copper oxy-fluoride $\text{Sr}_2\text{CuO}_2\text{F}_{2+\delta}$. *Nature* **1994**, 369, 382-384.
<https://doi.org/10.1038/369382a0>
- Altomare, A., Carrozzini, B., Giacovazzo, C., Guagliardi, A., Moliterni, A.G.G., and Rizzi, R. Solving crystal structures from powder data. I. The role of the prior information in the two-stage method. *J. Appl. Crystallogr.* **1996**, 29, 667–673.
<https://doi.org/10.1107/S0021889896007467>
- Amezawa K., Tomii Y. and Yamamoto N. High temperature protonic conduction in LaPO_4 doped with alkaline earth metals. *Solid State Ionics* **2005**, 176, 135-141.
<https://doi.org/10.1016/j.ssi.2004.07.003>
- Amsif M., Magrasó A., Marrero-López D., Ruiz-Morales J.C., Canales-Vázquez J. and Núñez P. Mo-substituted lanthanum tungstate $\text{La}_{28-y}\text{W}_{4+y}\text{O}_{54+d}$: a competitive mixed electron–proton conductor for gas separation membrane application. *Chem Mater* **2012**, 24, 3868-3877.
<https://doi.org/10.1021/cm301723a>
- Animitsa I. and Tarasova N. The influence of anionic heterovalent doping on transport properties and chemical stability of F-, Cl-doped brownmillerite $\text{Ba}_2\text{In}_2\text{O}_5$. *J. Alloys Compd.* **2018**, 739, 353-359.
<https://doi.org/10.1016/j.jallcom.2017.12.317>
- Animitsa I., Tarasova N. and Filinkova Y. Electrical properties of the fluorine doped $\text{Ba}_2\text{In}_2\text{O}_5$. *Solid State Ionics* **2012**, 207, 29-37.
<https://doi.org/10.1016/j.ssi.2011.11.015>

B

- BMW. Linde MH and TUM to trial hydrogen forklifts, tow tractors. *Fuel Cells Bull* **2013**, 11, 3.
[https://doi.org/10.1016/S1464-2859\(13\)70367-5](https://doi.org/10.1016/S1464-2859(13)70367-5)
- Berry F.J., Bowfield A.F., Coomer F.C., Jackson S.D., Moore E.A., Slater P.R., Thomas M.F., Wright A.J. and Ren X. Fluorination of perovskite-related phases of composition $\text{SrFe}_{1-x}\text{Sn}_x\text{O}_{3-\delta}$. *J. Phys. Condens. Matter* **2009**, 21, 256001.
<https://doi.org/10.1088/0953-8984/21/25/256001>
- Bolland O. and Undrum H. A novel methodology for comparing CO₂ capture options for natural gas-fired combined cycle plants. *Adv Environ. Res.* **2003**, 7, 901–911.
[https://doi.org/10.1016/S1093-0191\(02\)00085-0](https://doi.org/10.1016/S1093-0191(02)00085-0)
- Boultif A. and Louer D. Powder patterns indexing with the dichotomy method, *J. Appl. Cryst.* **2004**, 37, 724-731.
<https://doi.org/10.1107/S0021889804014876>

C

- Cai M., Liu S., Efimov K., Caro J., Feldhoff A. and Wang H. Preparation and hydrogen permeation of $\text{BaCe}_{0.95}\text{Nd}_{0.05}\text{O}_{3-d}$ membranes. *J Membr Sci* **2009**, 343, 90-96.
<https://doi.org/10.1016/j.memsci.2009.07.011>
- Chen L., Zhuang L., Xue J., Wei Y. and Wang H. Tuning the separation performance of hydrogen permeable membranes using an anion doping strategy. *J. Mater. Chem. A* **2017**, 5, 20482-20490.
<https://doi.org/10.1039/C7TA06030K>
- Chen Y., Liao Q., Li Z., Wang, H., Wei, Y. Feldhoff, A. and Caro, J.A. CO₂-stable hollow-fiber membrane with high hydrogen permeation flux. *AIChE J.* **2015**, 61, 1997-2007.
<https://doi.org/10.1002/aic.14772>

- Corbel G., Laligant Y., Goutenoire F., Suard E. and Lacorre P. Effects of Partial Substitution of Mo⁶⁺ by Cr⁶⁺ and W⁶⁺ on the Crystal Structure of the Fast Oxide-Ion Conductor Structural Effects of W⁶⁺. *Chem. Mater.* **2005**, 17, 4678-4684.
<https://doi.org/10.1021/cm0501214>
- Cros B. and Kerner-Czeskleba H. Synthesis and Characterization of Stable Compounds at 1400 degrees C from the system La₂O₃-MoO₂-MoO₃, *Revue de Chimie Minerale* **1978**, 15, 6, 5210-5218.

D

- Dan Vu T., Krichen F., Barré M., Coste S., Jouanneaux A., Suard E., Fitch A. and Goutenoire F. Ab-initio structure determination of La₃₄Mo₈O₇₅ using powder X-ray and neutron diffraction data. *Cryst. Growth Des.* **2019**, 19, 6074-6081.
<https://doi.org/10.1021/acs.cgd.8b01552>
- De Wolff, P.M. Symmetry operations for displacively modulated structures. *Acta Cryst. A* **1977**, 33, 493-497.
<https://doi.org/10.1107/S0567739477001223>
- Ding D, Li L, Feng K, Liu Z, and Xia C. High performance Ni-Sm₂O₃ cermet anodes for intermediate-temperature solid oxide fuel cells. *J Power Sources* **2009**, 187, 400-402.
<https://doi.org/10.1016/j.jpowsour.2008.11.013>
- Ding D, Liu B, Gong M, Liu X, and Xia C. Electrical properties of samaria-doped ceria electrolytes from highly active powders. *Electrochim. Acta* **2010**, 55, 4529-4535.
<https://doi.org/10.1016/j.electacta.2010.03.005>
- Ding D, Liu B, Zhu Z, Zhou S, and Xia C. High reactive Ce_{0.8}Sm_{0.2}O_{1.9} powders via a carbonate co-precipitation method as electrolytes for low-temperature solid oxide fuel cells. *Solid State Ionics* **2008**, 179, 896-899.
<https://doi.org/10.1016/j.ssi.2007.11.015>

-
- Dong F., Chen Y., Chen D. and Shao Z. Surprisingly High Activity for Oxygen Reduction Reaction of Selected Oxides Lacking Long Oxygen-Ion Diffusion Paths at Intermediate Temperatures: A Case Study of Cobalt-Free $\text{BaFeO}_{3-\delta}$. *ACS Appl. Mater. Interfaces* **2014**, 6, 11180-11189.
<https://doi.org/10.1021/am502240m>

E

- Escolastico S., Seeger J., Roitsch S., Ivanova M., Meulenberg W.A. and Serra J.M. Enhanced H_2 Separation through Mixed Proton-Electron Conducting Membranes Based on $\text{La}_{5.5}\text{W}_{0.8}\text{M}_{0.2}\text{O}_{11.25-\delta}$. *ChemSusChem* **2013b**, 6, 1523-1532.
<https://doi.org/10.1002/cssc.201300091>
- Escolastico S., Solís C. and Serra J.M. Hydrogen separation and stability study of ceramic membranes based on the system $\text{Nd}_5\text{LnWO}_{12}$. *Int J Hydrogen Energy* **2011**, 36, 11946–11954.
<https://doi.org/10.1016/j.ijhydene.2011.06.026>
- Escolástico S., Solís C., Scherb T., Schumacher S. and Serra J.M. Hydrogen separation in $\text{La}_{5.5}\text{WO}_{11.25-\delta}$ membranes. *Journal of Membrane Science* **2013a**, 444, 276-284.
<https://doi.org/10.1016/j.memsci.2013.05.005>
- Escolástico S., Vert V.B. and Serra J.M. Preparation, and characterization of nanocrystalline mixed proton-electronic conducting materials based on the system $\text{Ln}_6\text{WO}_{12}$. *Chem Mater* **2009**, 21, 3079-3089.
<https://doi.org/10.1021/cm900067k>

G

- Guan J., Dorris S.E., Balachandran U. and Liu M.L. Transport properties of $\text{SrCe}_{0.95}\text{Y}_{0.05}\text{O}_{3-d}$ and its application for hydrogen separation. *Solid State Ionics* **1998**, 110, 303-310.
[https://doi.org/10.1016/S0167-2738\(98\)00148-9](https://doi.org/10.1016/S0167-2738(98)00148-9)

H

- Haugrud R. Defects and transport properties in Ln₆WO₁₂ (Ln = La, Nd, Gd, Er). *Solid State Ionics* **2007**, 178, 555-560.
<https://doi.org/10.1016/j.ssi.2007.01.004>
- Ho T. and Vishy K. Hydrogen powered car: two-stage modelling system. *Int J Hydrogen Energy* **2011**, 36, 10065-10079.
<https://doi.org/10.1016/j.ijhydene.2011.05.020>

J

- Janner A., Janssen T. and De Wolff P.M. Wyckoff positions used for the classification of Bravais classes of modulated crystals. *Acta Crystallographica Section A*. **1983**, 39, 667-670.
<https://doi.org/10.1107/S010876738300135X>
- Ji C., Wang S., Zhang B. and Liu X. Emissions performance of a hybrid hydrogen-gasoline engine powered passenger car under the New European Driving Cycle. *Fuel* **2013**, 106, 873-875.
<https://doi.org/10.1016/j.fuel.2013.01.011>

K

- Katahira K., Kohchi Y., Shimura T. and Iwahara H. Protonic conduction in Zr-substituted BaCeO₃. *Solid State Ionics* **2000**, 138, 91-98.
[https://doi.org/10.1016/S0167-2738\(00\)00777-3](https://doi.org/10.1016/S0167-2738(00)00777-3)
- Kitamura N., Amezawa K., Tomii Y. and Yamamoto N. Protonic conduction in rare earth orthophosphates with the monazite structure. *Solid State Ionics* **2003**, 162-163, 161-165.
[https://doi.org/10.1016/S0167-2738\(03\)00219-4](https://doi.org/10.1016/S0167-2738(03)00219-4)

L

- Le Bail. Whole powder pattern decomposition methods and applications: A retrospection. *Powder Diffraction* **2005**, 20, 4.
<https://doi.org/10.1154/1.2135315>
- Lei B., Zhang S.Q., Fang S.M., Zhang L., Gao H.Y. and Meng G.Y. In-situ fabrication of a supported $\text{Ba}_3\text{Ca}_{1.18}\text{Nb}_{1.82}\text{O}_{9-d}$ membrane electrolyte for a proton-conducting SOFC. *J. Am. Ceram. Soc.* **2008**, 91, 3806-3809.
<https://doi.org/10.1111/j.1551-2916.2008.02733.x>

M

- Magrasó A, Frontera C, Marrero-López D and Nuñez P. New crystal structure and characterization of lanthanum tungstate “ $\text{La}_6\text{WO}_{12}$ ” prepared by freeze-drying synthesis. *Dalton Trans* **2009**, 10273.
<https://doi.org/10.1039/B916981B>
- Magrasó A. Transport number measurements and fuel cell test undoped and Mo-substituted lanthanum tungstate. *J Power Sources* **2013**, 240, 583-588.
<https://doi.org/10.1016/j.jpowsour.2013.04.087>
- Magrasó A. and Haugrud R. Effects of the La/W ratio and doping on the structure, defect structure, stability, and functional properties of proton-conducting lanthanum tungstate $\text{La}_{28-x}\text{W}_{4+x}\text{O}_{54+\delta}$. A review. *J. Mater. Chem. A* **2014**, 2, 12630-12641.
<https://doi.org/10.1039/C4TA00546E>
- Magrasó A., Polfus, J.M., Frontera C., Canales-Vázquez J., Kalland L.E., Hervoches C.H., Erdal S., Hancke R., Islam M.S., Norby T. and Haugrud R. *J. Mater. Chem.* **2012**, 22, 5, 1762-1764.
<https://doi.org/10.1039/C2JM14981H>

N

- Nigara Y., Yashiro K., Hong J.O., Kawada T. and Mizusaki J. Hydrogen permeability of YSZ single crystals at high temperatures. *Solid State Ionics* **2004**, 171, 61-67.
[https://doi.org/10.1016/S0167-2738\(03\)00274-1](https://doi.org/10.1016/S0167-2738(03)00274-1)
- Nigara Y., Yashiro K., Kawada T. and Mizusaki J. Hydrogen permeability in $\text{Ce}_{0.8}\text{Yb}_{0.2}\text{O}_{1.9}$ at high temperatures. *Solid State Ionics* **2000**, 136-137, 215-221.
[https://doi.org/10.1016/S0167-2738\(00\)00313-1](https://doi.org/10.1016/S0167-2738(00)00313-1)
- Nigara Y., Yashiro K., Kawada T. and Mizusaki J. Hydrogen permeability in $(\text{CeO}_2)_{0.9}(\text{GdO}_{1.5})_{0.1}$ at high temperatures. *Solid State Ionics* **2003**, 159, 135-141.
[https://doi.org/10.1016/S0167-2738\(02\)00919-0](https://doi.org/10.1016/S0167-2738(02)00919-0)
- Niknam T., Bornapour M. and Gheisari A. Combined heat, power, and hydrogen production optimal planning of fuel cell power plants in distribution networks. *Energy Convers Manage* **2013**, 66, 11-25.
<https://doi.org/10.1016/j.enconman.2012.08.016>
- Norby T. and Larring Y. Concentration and transport of proton and oxygen defect in oxides. *Inst Mater* **1996**, 83-93.
[https://doi.org/10.1016/S1359-0286\(97\)80051-4](https://doi.org/10.1016/S1359-0286(97)80051-4)

P

- Park Y., Kang J., Moon D., Suk Jo Y. and Lee C. Parallel and series multi-bed pressure swing adsorption processes for H_2 recovery from a lean hydrogen mixture. *Chemical Engineering Journal* **2021**, 408, 15, 127299.
<https://doi.org/10.1016/j.cej.2020.127299>
- Penner S.S. Steps toward the hydrogen economy. *Energy* **2006**, 31, 33-43.
<https://doi.org/10.1016/j.energy.2004.04.060>

-
- Phair J.W. and Badwal S.P.S. Review of proton conductors for hydrogen separation. *Ionics* **2006**, 12, 103-115.
<https://doi.org/10.1007/s11581-006-0016-4>

Q

- Qi X. and Lin Y.S. Electrical conduction and hydrogen permeation through mixed proton-electron conducting strontium cerate membranes. *Solid State Ionics* **2000**, 130, 149-156.
[https://doi.org/10.1016/S0167-2738\(00\)00281-2](https://doi.org/10.1016/S0167-2738(00)00281-2)

R

- Roark S.E., Mackay R. and Sammells A.F. Hydrogen separation membranes for VISION 21 energy plants. In: Proceedings of the 27th international technical conference on coal utilization and fuel systems, Clearwater, FL, March **2002**.
<https://citeseerx.ist.psu.edu/viewdoc/download?doi=10.1.1.562.1148&rep=rep1&type=pdf>

S

- Savvin S.N., Avdeev M., Kolbanev I.V., Kharitonova E.P., Shcherbakova L.G., Shlyakhtina A.V. and Nuñez, P. Stability against reduction of fluorite-like rhombohedral $\text{La}_{5.5}\text{MoO}_{11.25}$ and $\text{Ho}_{5.4}\text{Zr}_{0.6}\text{MoO}_{12.3}$ fluorite: Conductivity and neutron diffraction study. *Solid State Ionics* **2018**, 319, 148-155.
<https://doi.org/10.1016/j.ssi.2018.02.001>
- Savvin S.N., Shlyakhtina A.V., Borunova A.B., Shcherbakova L.G., Ruiz-Morales J.C. and Núñez, P. Crystal structure and proton conductivity of some Zr-doped rare-earth molybdates. *Solid State Ionics* **2015**, 271, 91-97.
<https://doi.org/10.1016/j.ssi.2014.12.003>

- Savvin S.N., Shlyakhtina A.V., Kolbanev I.V., Knotko A.V., Belov D.A., Shcherbakova L.G. and Nuñez P. Zr-doped samarium molybdates potential mixed electron–proton conductors. *Solid State Ionics* **2014**, 262, 713-718.
<https://doi.org/10.1016/j.ssi.2017.01.020>
- Serra J.M., Escolastico S., Ivanova M., Meulenberg W.A., Buchkremer H.P. and Stöver D. German Patent DE102010027645.6, WO 2012/010386 A1, **2010**.
- Shannon R.D. Revised Effective Ionic Radii and Systematic Studies of Interatomic Distances in Halides and Chalcogenides. *Acta Crystallographica* **1976**, A32, 751-67.
<https://doi.org/10.1107/S0567739476001551>
- Shimura T., Fujimoto S. and Iwahara H. Proton conduction in non-perovskite-type oxides at elevated temperatures. *Solid State Ionics* **2001**, 143, 117-123.
[https://doi.org/10.1016/S0167-2738\(01\)00839-6](https://doi.org/10.1016/S0167-2738(01)00839-6)
- Shlyakhtina A.V., Avdeev M., Abrantes J.C.C., Gomes E., Lyskov N.V., Kharitonova E.P., Kolbaneva I.V. and Shcherbakova L.G. Structure and conductivity of Nd₆MoO₁₂-based potential electron–proton conductors under dry and wet redox conditions. *Inorg. Chem. Front.*, **2019**, 6, 566.
<https://doi.org/10.1039/C8QI01142G>
- Shlyakhtina A.V., Savvin S.N., Knotko A.V., Shcherbakova L.G. and Núñez P. Electrical Conductivity of Ln_{6-x}Zr_xMoO_{12+δ} (Ln = La, Nd, Sm; x = 0.2, 0.6) Ceramics during Thermal Cycling. *Inorg. Mater.* **2016**, 52, 1055-1062.
<https://doi.org/10.1134/S0020168516100149>
- Shlyakhtina A.V., Savvin S.N., Lyskov N.V., Belov D.A., Shchegolikhin A.N., Kolbanev I.V., Karyagina O.K., Chernyak S.A., Shcherbakova L.G. and Núñez P. Sm_{6-x}MoO_{12-δ} (x = 0, 0.5) and Sm₆WO₁₂ - Mixed electron-proton conducting materials. *Solid State Ionics* 302, **2017B**, 143-151.
<https://doi.org/10.1016/j.ssi.2017.01.020>

-
- Shlyakhtina A.V., Savvin S.N., Lyskov N.V., Kolbanev I.V., Karyagina O.K., Chernyak S.A., Shcherbakova L.G. and Núñez, P. Polymorphism in the Family of $\text{Ln}_{6-x}\text{MoO}_{12-\delta}$ ($\text{Ln} = \text{La}, \text{Gd} - \text{Lu}; x = 0, 0.5$) Oxygen Ion- and Proton-Conducting Materials. *J. Mater. Chem. A* **2017A**, 5, 7618-7630.
<https://doi.org/10.1039/C6TA09963G>
 - Slater P.R. Poly(vinylidene fluoride) as a reagent for the synthesis of K_2NiF_4 -related inorganic oxide fluorides. *J. Fluorine Chem.* **2002**, 117, 43-45.
[https://doi.org/10.1016/S0022-1139\(02\)00166-5](https://doi.org/10.1016/S0022-1139(02)00166-5)
 - Song S.J., Wachsman E.D., Dorris S.E. and Balachandran U. Defect structure and n-type electrical properties of $\text{SrCe}_{0.95}\text{Eu}_{0.05}\text{O}_{3-\delta}$. *J. Electrochem Soc* **2003**, 150, A1484-1490.
<https://doi.org/10.1149/1.1614796>
 - Song S.J., Wachsman E.D., Rhodes J., Dorris S.E. and Balachandran U. Hydrogen permeability of $\text{SrCe}_{1-x}\text{M}_x\text{O}_{3-d}$ ($x = 0.05, \text{M} = \text{Eu}, \text{Sm}$). *Solid State Ionics* **2004**, 167, 99-105.
<https://doi.org/10.1016/j.ssi.2003.12.010>
 - Sorensen B. Assessing current vehicle performance and simulating the performance of hydrogen and hybrid cars. *Int J. Hydrogen Energy* **2007**, 32, 1597-1604.
<https://citeseerx.ist.psu.edu/viewdoc/download?doi=10.1.1.620.3143&rep=rep1&type=pdf>
 - Speight, J. G. *Heavy Oil Recovery and Upgrading*, **2019**.
<https://doi.org/10.1016/C2016-0-04682-X>
 - Sun W., Shi Z. and Liua W., Considerable Hydrogen Permeation Behavior through a Dense $\text{Ce}_{0.8}\text{Sm}_{0.2}\text{O}_{2-\delta}$ (SDC) Asymmetric Thick Film. *Journal of The Electrochemical Society*, **2013**, 160 (6) F585-F590.
<https://doi.org/10.1149/2.073306jes>
 - Sushil A. and Sandun F. Hydrogen membrane separation techniques. *Ind. Eng. Chem Res* **2006**, 45, 875-881.
<https://doi.org/10.1021/ie050644l>

T

- Tao Z., Yan L., Qiao J., Wanga B., Zhang L. and Zhang J. A review of advanced proton-conducting materials for hydrogen separation. *Progress in Materials Science* **2015**, 74, 1-50.
<https://doi.org/10.1016/j.pmatsci.2015.04.002>
- Toyota® Mirai operating principles, **2015**.
<https://www.toyota-europe.com/world-of-toyota/feel/environment/better-air/fuel-cell-vehicle>

V

- Verweij H. Ceramic membranes: morphology and transport. *J Mater Sci* **2003**, 38, 4677-4695.
<https://doi.org/10.1023/A:1027410616041>
- Vøllestad E., Vigen C.K., Magrasó A. and Haugsrud R. Hydrogen permeation characteristics of $\text{La}_{27}\text{Mo}_{1.5}\text{W}_{3.5}\text{O}_{55.5}$. *J. Membr. Sci.* **2014**, 461, 81–88.
<https://doi.org/10.1016/j.memsci.2014.03.011>

W

- Wang B., Yi J., Winnubst L. and Chen C. Stability, and oxygen permeation behavior of $\text{Ce}_{0.8}\text{Sm}_{0.2}\text{O}_{2-d}-\text{La}_{0.8}\text{Sr}_{0.2}\text{CrO}_{3-d}$ composite membrane under large oxygen partial pressure gradients. *J Membr Sci* **2006**, 286, 22-25.
<https://doi.org/10.1016/j.memsci.2006.06.009>
- Wang D., Chen S., Changchun X. and Xiang W. Energy, and energy analysis of a new hydrogen-fueled power plant based on calcium looping process. *Int J Hydrogen Energy* **2013**, 38, 5389-5400.
<https://doi.org/10.1016/j.ijhydene.2013.02.060>
- Wang J.D., Xie Y.H., Zhang Z.F., Liu R.Q. and Li Z.H. Protonic conduction in Ca^{2+} -doped $\text{La}_2\text{M}_2\text{O}_7$ (M = Ce, Zr) with its application to ammonia synthesis electrochemically. *Mater Res Bull* **2005**, 40, 1294-1302.
<https://doi.org/10.1016/j.materresbull.2005.04.008>

Y

- Yi J., Zuo Y., Liu W., Winnubst L. and Chen C. Oxygen permeation through a $\text{Ce}_{0.8}\text{Sm}_{0.2}\text{O}_{2-d}-\text{La}_{0.8}\text{Sr}_{0.2}\text{CrO}_{3-d}$ dual-phase composite membrane. *J Membr Sci* **2006**, 280, 849-855.
<https://doi.org/10.1016/j.memsci.2006.03.011>
- Yoshimura M. and Rouanet A. High temperature phase relation in the system $\text{La}_2\text{O}_3-\text{WO}_3$. *Materials Research Bulletin* **1976**, 11, 2, 151-158.
[https://doi.org/10.1016/0025-5408\(76\)90070-2](https://doi.org/10.1016/0025-5408(76)90070-2)

Z

- Zhang K., Sunarso J., Pham G., Wang S. and Liu S. External short circuit-assisted proton conducting ceramic membrane for H_2 permeation. *Ceram Int* **2014**, 40, 791-797.
<https://doi.org/10.1016/j.ceramint.2013.06.069>
- Zayas-Rey M.J., dos Santos-Gómez L., Cabeza A., Marrero-López D. and Losilla E.R. Proton conductors based on alkaline-earth substituted $\text{La}_{28-x}\text{W}_{4+x}\text{O}_{54+3x/2}$. *Dalton Trans.*, **2014**, 43, 6490.
<https://doi.org/10.1039/C3DT53604A>
- Zayas-Rey M.J., dos Santos-Gómez L., Marrero-López D., León-Reina L., Canales-Vázquez J. and Aranda M.A.G. Structural and conducting features of niobium-doped lanthanum tungstate, $\text{La}_{27}(\text{W}_{1-x}\text{Nb}_x)_5\text{O}_{55.55-d}$. *Chem Mater* **2013**, 25, 448-456.
<https://doi.org/10.1021/cm304067d>
- Zhu J., Liu G., Liu Z., Chu Z., Jin W. and Xu N. Unprecedented Perovskite Oxyfluoride Membranes with High-Efficiency Oxygen Ion Transport Paths for Low-Temperature Oxygen Permeation. *Adv. Mater.* **2016**, 28, 3511-3515.
<https://doi.org/10.1002/adma.201505959>

- Zhu Z.W., Yan L.T., Liu H.W., Sun W.P., Zhang Q.P. and Liu W. A mixed electronic and protonic conducting hydrogen separation membrane with asymmetric structure. *Int J Hydrogen Energy* **2012**, 37, 12708-12713.
<https://doi.org/10.1016/j.ijhydene.2012.06.033>



Permissions.

Effect of Preparation Conditions on the Polymorphism and Transport Properties of La_{6-x}MoO_{12-δ} (0 ≤ x ≤ 0.8)



Author: Adrián López-Vergara, José M. Porras-Vázquez, Antonia Infantes-Molina, et al
Publication: Chemistry of Materials
Publisher: American Chemical Society
Date: Aug 1, 2017

Copyright © 2017, American Chemical Society

PERMISSION/LICENSE IS GRANTED FOR YOUR ORDER AT NO CHARGE

This type of permission/license, instead of the standard Terms & Conditions, is sent to you because no fee is being charged for your order. Please note the following:

- Permission is granted for your request in both print and electronic formats, and translations.
- If figures and/or tables were requested, they may be adapted or used in part.
- Please print this page for your records and send a copy of it to your publisher/graduate school.
- Appropriate credit for the requested material should be given as follows: "Reprinted (adapted) with permission from (COMPLETE REFERENCE CITATION). Copyright (YEAR) American Chemical Society." Insert appropriate information in place of the capitalized words.
- One-time permission is granted only for the use specified in your request. No additional uses are granted (such as derivative works or other editions). For any other uses, please submit a new request.

BACK

CLOSE WINDOW

Metal-Doping of La_{5.4}MoO_{11.1} Proton Conductors: Impact on the Structure and Electrical Properties



Author: Adrián López-Vergara, José M. Porras-Vázquez, Einar Vøllestad, et al
Publication: Inorganic Chemistry
Publisher: American Chemical Society
Date: Oct 1, 2018

Copyright © 2018, American Chemical Society

PERMISSION/LICENSE IS GRANTED FOR YOUR ORDER AT NO CHARGE

This type of permission/license, instead of the standard Terms & Conditions, is sent to you because no fee is being charged for your order. Please note the following:

- Permission is granted for your request in both print and electronic formats, and translations.
- If figures and/or tables were requested, they may be adapted or used in part.
- Please print this page for your records and send a copy of it to your publisher/graduate school.
- Appropriate credit for the requested material should be given as follows: "Reprinted (adapted) with permission from (COMPLETE REFERENCE CITATION). Copyright (YEAR) American Chemical Society." Insert appropriate information in place of the capitalized words.
- One-time permission is granted only for the use specified in your request. No additional uses are granted (such as derivative works or other editions). For any other uses, please submit a new request.

BACK

CLOSE WINDOW

Synergic Effect of Metal and Fluorine Doping on the Structural and Electrical Properties of La_{5.4}MoO_{11.1}-Based Materials



Author: Adrián López-Vergara, Marta Bergillos-Ruiz, Javier Zamudio-García, et al
Publication: Inorganic Chemistry
Publisher: American Chemical Society
Date: Jan 1, 2020

Copyright © 2020, American Chemical Society

PERMISSION/LICENSE IS GRANTED FOR YOUR ORDER AT NO CHARGE

This type of permission/license, instead of the standard Terms & Conditions, is sent to you because no fee is being charged for your order. Please note the following:

- Permission is granted for your request in both print and electronic formats, and translations.
- If figures and/or tables were requested, they may be adapted or used in part.
- Please print this page for your records and send a copy of it to your publisher/graduate school.
- Appropriate credit for the requested material should be given as follows: "Reprinted (adapted) with permission from (COMPLETE REFERENCE CITATION). Copyright (YEAR) American Chemical Society." Insert appropriate information in place of the capitalized words.
- One-time permission is granted only for the use specified in your request. No additional uses are granted (such as derivative works or other editions). For any other uses, please submit a new request.

BACK

CLOSE WINDOW

Unravelling Crystal Superstructures and Transformations in the La6-xMoO12-δ (0.6 ≤ x ≤ 3.0)
Series: A System with Tailored Ionic/Electronic Conductivity



Author: Adrián López-Vergara, Lucía Vázquez-Anaya, José M. Porras-Vázquez, et al
Publication: Chemistry of Materials
Publisher: American Chemical Society
Date: Aug 1, 2020

Copyright © 2020, American Chemical Society

PERMISSION/LICENSE IS GRANTED FOR YOUR ORDER AT NO CHARGE

This type of permission/license, instead of the standard Terms & Conditions, is sent to you because no fee is being charged for your order. Please note the following:

- Permission is granted for your request in both print and electronic formats, and translations.
- If figures and/or tables were requested, they may be adapted or used in part.
- Please print this page for your records and send a copy of it to your publisher/graduate school.
- Appropriate credit for the requested material should be given as follows: "Reprinted (adapted) with permission from (COMPLETE REFERENCE CITATION). Copyright (YEAR) American Chemical Society." Insert appropriate information in place of the capitalized words.
- One-time permission is granted only for the use specified in your request. No additional uses are granted (such as derivative works or other editions). For any other uses, please submit a new request.

BACK

CLOSE WINDOW

License Number 5320220014496

[Printable Details](#)

License date Jun 01, 2022

Licensed Content

Order Details

Licensed Content Publisher Elsevier
Licensed Content Publication Chemical Engineering Journal
Licensed Content Title Parallel and series multi-bed pressure swing adsorption processes for H₂ recovery from a lean hydrogen mixture
Licensed Content Author Yongha Park, Jun-Ho Kang, Dong-Kyu Moon, Young Suk Jo, Chang-Ha Lee
Licensed Content Date Mar 15, 2021
Licensed Content Volume 408
Licensed Content Issue n/a
Licensed Content Pages 1

Type of Use reuse in a thesis/dissertation
Portion figures/tables/illustrations
Number of figures/tables/illustrations 1
Format both print and electronic
Are you the author of this Elsevier article? No
Will you be translating? Yes, including English rights
Number of languages 1

About Your Work

Additional Data

Title Lanthanum Molybdates: a comprehensive study for hydrogen separation membranes
Institution name Universidad de Málaga
Expected presentation date Sep 2022

Portions 1.4
Specific Languages English, Spanish

Requestor Location

Tax Details

Mr. Adrian Lopez-Vergara
Avda. Cervantes, 2

Publisher Tax ID GB 494 6272 12

Requestor Location

Málaga, 29071
Spain
Attn: Mr. Adrian Lopez-Vergara

Price

.

Your confirmation email will contain your order number for future reference.

License Number 5320220451085

[Printable Details](#)

License date Jun 01, 2022

Licensed Content

Licensed Content Publisher Elsevier
Licensed Content Publication Ceramics International
Licensed Content Title External short circuit-assisted proton conducting ceramic membrane for H₂ permeation
Licensed Content Author Kun Zhang, Jaka Sunarso, Gia Hung Pham, Shaobin Wang, Shaomin Liu
Licensed Content Date Jan 1, 2014
Licensed Content Volume 40
Licensed Content Issue 1
Licensed Content Pages 7

Order Details

Type of Use reuse in a thesis/dissertation
Portion figures/tables/illustrations
Number of figures/tables/illustrations 1
Format both print and electronic
Are you the author of this Elsevier article? No
Will you be translating? Yes, including English rights
Number of languages 1

About Your Work

Title Lanthanum Molybdates: a comprehensive study for hydrogen separation membranes
Institution name Universidad de Málaga
Expected presentation date Sep 2022

Additional Data

Portions Figure 1.6
Specific Languages English, Spanish

Requestor Location

Requestor Location Mr. Adrian Lopez-Vergara
Avda. Cervantes, 2
Málaga, 29071
Spain
Attn: Mr. Adrian Lopez-Vergara

Tax Details

Publisher Tax ID GB 494 6272 12

License Number 5320220650206

[Printable Details](#)

License date Jun 01, 2022

Licensed Content

Licensed Content Publisher Elsevier
Licensed Content Publication Materials Research Bulletin
Licensed Content Title Protonic conduction in Ca²⁺-doped La₂M₂O₇ (M=Ce, Zr) with its application to ammonia synthesis electrochemically
Licensed Content Author Ji-De Wang, Ya-Hong Xie, Zheng-Fang Zhang, Rui-Quan Liu, Zhi-Jie Li
Licensed Content Date Aug 11, 2005
Licensed Content Volume 40
Licensed Content Issue 8
Licensed Content Pages 9

Order Details

Type of Use reuse in a thesis/dissertation
Portion figures/tables/illustrations
Number of figures/tables/illustrations 1
Format both print and electronic
Are you the author of this Elsevier article? No
Will you be translating? Yes, including English rights
Number of languages 1

About Your Work

Title Lanthanum Molybdates: a comprehensive study for hydrogen separation membranes
Institution name Universidad de Málaga
Expected presentation date Sep 2022

Additional Data

Portions Figure 1.7
Specific Languages English, Spanish

Requestor Location

Requestor Location Mr. Adrian Lopez-Vergara
Avda. Cervantes, 2
Málaga, 29071
Spain
Attn: Mr. Adrian Lopez-Vergara

Tax Details

Publisher Tax ID GB 494 6272 12

Price

Your confirmation email will contain your order number for future reference.

License Number 5320220818278 [Printable Details](#)

License date Jun 01, 2022

Licensed Content

Licensed Content Publisher Elsevier
Licensed Content Publication Solid State Ionics
Licensed Content Title Defects and transport properties in Ln6WO12 (Ln=La, Nd, Gd, Er)
Licensed Content Author Reidar Haugsrud
Licensed Content Date Apr 1, 2007
Licensed Content Volume 178
Licensed Content Issue 7-10
Licensed Content Pages 6

Order Details

Type of Use reuse in a thesis/dissertation
Portion figures/tables/illustrations
Number of figures/tables/illustrations 1
Format both print and electronic
Are you the author of this Elsevier article? No
Will you be translating? Yes, including English rights
Number of languages 1

About Your Work

Title Lanthanum Molybdates: a comprehensive study for hydrogen separation membranes
Institution name Universidad de Málaga
Expected presentation date Sep 2022

Additional Data

Portions Figure 1.8
Specific Languages English, Spanish

Requestor Location

Mr. Adrian Lopez-Vergara
Avda. Cervantes, 2

Requestor Location
Málaga, 29071
Spain
Attn: Mr. Adrian Lopez-Vergara

Tax Details

Publisher Tax ID GB 494 6272 12

Price

Your confirmation email will contain your order number for future reference.

License Number 5320220972406 [Printable Details](#)

License date Jun 01, 2022

Licensed Content

Licensed Content Publisher Elsevier
Licensed Content Publication Materials Research Bulletin
Licensed Content Title High temperature phase relation in the system La2O3□W03
Licensed Content Author Masahiro Yoshimura,Alain Rouanet
Licensed Content Date Feb 1, 1976
Licensed Content Volume 11
Licensed Content Issue 2
Licensed Content Pages 8

Order Details

Type of Use reuse in a thesis/dissertation
Portion figures/tables/illustrations
Number of figures/tables/illustrations 1
Format both print and electronic
Are you the author of this Elsevier article? No
Will you be translating? Yes, including English rights
Number of languages 1

About Your Work

Title Lanthanum Molybdates: a comprehensive study for hydrogen separation membranes
Institution name Universidad de Málaga
Expected presentation date Sep 2022

Additional Data

Portions Figure 1.9
Specific Languages English, Spanish

Requestor Location

Mr. Adrian Lopez-Vergara
Avda. Cervantes, 2

Requestor Location
Málaga, 29071
Spain
Attn: Mr. Adrian Lopez-Vergara

Tax Details

Publisher Tax ID GB 494 6272 12

Price

Order Date	06Jun-2022	Type of Use	Republish in a thesis/dissertation
Order License ID	1229147-1	Publisher	ROYAL SOCIETY OF CHEMISTRY
ISSN	1477-9234	Portion	image/photo/illustration

LICENSED CONTENT

Publication Title	Dalton transactions	Rightholder	Royal Society of Chemistry
Article Title	New crystal structure and characterization of lanthanum tungstate "La6WO12" prepared by freeze-drying synthesis.	Publication Type	eJournal
Author/Editor	Royal Society of Chemistry (Great Britain)	Start Page	10273
Date	01/01/2003	End Page	10283
Language	English	Issue	46
Country	United Kingdom of Great Britain and Northern Ireland	Volume	0

REQUEST DETAILS

Portion Type	image/photo/illustration	Distribution	Worldwide
Number of images / photos / illustrations	1	Translation	Original language plus one translation
Format (select all that apply)	Print, Electronic	Copies for the disabled?	No
Who will republish the content?	Author of requested content	Minor editing privileges?	No
Duration of Use	Life of current edition	Incidental promotional use?	No
Lifetime Unit Quantity	Up to 499	Currency	USD
Rights Requested	Main product		

NEW WORK DETAILS

Title	Lanthanum Molybdates: a comprehensive study for hydrogen separation membranes.	Institution name	Universidad de Málaga
Instructor name	Enrique Ramírez Losilla	Expected presentation date	2022-09-01

ADDITIONAL DETAILS

Order reference number	N/A	The requesting person / organization to appear on the license	Adrián López Vergara
------------------------	-----	---	----------------------

REUSE CONTENT DETAILS

Title, description or numeric reference of the portion(s)	Figure 1.10	Title of the article/chapter the portion is from	New crystal structure and characterization of lanthanum tungstate "La6WO12" prepared by freeze-drying synthesis.
Editor of portion(s)	Magrasó, Anna; Frontera, Carlos; Marrero-López, David; Núñez, Pedro	Author of portion(s)	Magrasó, Anna; Frontera, Carlos; Marrero-López, David; Núñez, Pedro
Volume of serial or monograph	0	Issue, if republishing an article from a serial	46
Page or page range of portion	10273-10283	Publication date of portion	2009-12-14

Order Date	13-Jun-2022	Type of Use	Republish in a thesis/dissertation
Order License ID	1229150-1	Publisher	ROYAL SOCIETY OF CHEMISTRY,
ISSN	1364-5501	Portion	Image/photo/illustration

LICENSED CONTENT

Publication Title	Journal of materials chemistry	Publication Type	e-Journal
Article Title	Complete structural model for lanthanum tungstate: a chemically stable high temperature proton conductor by means of intrinsic defects	Start Page	1762
		End Page	1764
		Issue	5
Author/Editor	Royal Society of Chemistry (Great Britain)	Volume	22
Date	01/01/1991	URL	http://firstsearch.rsc.org
Language	English		
Country	United Kingdom of Great Britain and Northern Ireland		
Rightsholder	Royal Society of Chemistry		

REQUEST DETAILS

Portion Type	Image/photo/illustration	Distribution	Worldwide
Number of images / photos / illustrations	1	Translation	Original language plus one translation
Format (select all that apply)	Print, Electronic	Copies for the disabled?	No
Who will republish the content?	Author of requested content	Minor editing privileges?	No
Duration of Use	Life of current edition	Incidental promotional use?	No
Lifetime Unit Quantity	Up to 499	Currency	USD
Rights Requested	Main product		

NEW WORK DETAILS

Title	Lanthanum Molybdates: a comprehensive study for hydrogen separation membranes.	Institution name	Universidad de Málaga
Instructor name	Enrique Ramírez Losilla	Expected presentation date	2022-09-01

ADDITIONAL DETAILS

Order reference number	N/A	The requesting person / organization to appear on the license	Adrián López Vergara
------------------------	-----	---	----------------------

REUSE CONTENT DETAILS

Title, description or numeric reference of the portion(s)	Figure 1.11.	Title of the article/chapter the portion is from	Complete structural model for lanthanum tungstate: a chemically stable high temperature proton conductor by means of intrinsic defects
Editor of portion(s)	Magrasó, Anna; Polfus, Jonathan M.; Frontera, Carlos; Canales-Vázquez, Jesús; Kalland, Liv-Elisif; Hervoches, Charles H.; Erdal, Sigmund; Hancke, Ragnhild; Islam, M. Saiful; Norby, Truls; Haugrud, Reidar	Author of portion(s)	Magrasó, Anna; Polfus, Jonathan M.; Frontera, Carlos; Canales-Vázquez, Jesús; Kalland, Liv-Elisif; Hervoches, Charles H.; Erdal, Sigmund; Hancke, Ragnhild; Islam, M. Saiful; Norby, Truls; Haugrud, Reidar
Volume of serial or monograph	22	Issue, if republishing an article from a serial	5
Page or page range of portion	1762-1764	Publication date of portion	2012-01-10

Your confirmation email will contain your order number for future reference.

License Number	5322960934775
License date	Jun 06, 2022

[Printable Details](#)

Licensed Content

Licensed Content Publisher	Elsevier
Licensed Content Publication	Journal of Power Sources
Licensed Content Title	Transport number measurements and fuel cell testing of undoped and Mo-substituted lanthanum tungstate
Licensed Content Author	Anna Magrasó
Licensed Content Date	Oct 15, 2013
Licensed Content Volume	240
Licensed Content Issue	n/a
Licensed Content Pages	6

Order Details

Type of Use	reuse in a thesis/dissertation
Portion	figures/tables/illustrations
Number of figures/tables/illustrations	1
Format	both print and electronic
Are you the author of this Elsevier article?	No
Will you be translating?	Yes, including English rights
Number of languages	1

About Your Work

Title	Lanthanum Molybdates: a comprehensive study for hydrogen separation membranes
Institution name	Universidad de Málaga
Expected presentation date	Sep 2022

Additional Data

Portions	Figure 1.12.
Specific Languages	English, Spanish

Requestor Location

Requestor Location	Mr. Adrian Lopez-Vergara Avda. Cervantes, 2
	Málaga, 29071 Spain Attn: Mr. Adrian Lopez-Vergara

Tax Details

Publisher Tax ID	GB 494 6272 12
------------------	----------------

§ Price